X-ray Study of Dynamical Evolution in Clusters of Galaxies

Tae Furusho

Department of Physics, Tokyo Metropolitan University
1-1 Minami-Ohsawa, Hachioji, Tokyo 192-0397, Japan

Submitted to Tokyo Metropolitan University
for the Degree of Doctor of Philosophy (Physics)
January 2001

Thie wortk is based on analysis of data from the ISAS
satellite ASCA in collaboration with ASCA team.

Present address:
Code 662, NASA/GSFC, Greenbelt, MD 20771, USA
E-mail: furusho@olegacy.gsfc.nasa.gov

Abstract

We present two-dimensional temperature maps of four nearby bright clusters of galaxies A1060, AWM7, the Centaurus cluster, and the Perseus cluster, based on multi-pointing observations with the *ASCA* GIS. The pointing fields cover the whole cluster regions of 1 – 1.8° corresponding to about 2–3 h_{50}^{-1} Mpc. The temperatures were derived from hardness ratios, including corrections for the effects of the XRT response. The central cool components were subtracted for the Centaurus and the Perseus clusters, and metallicity gradients in AWM7, the Centaurus and the Perseus clusters were also corrected.

The intracluster medium in A1060 and AWM7 is almost isothermal from the center to the outer regions with temperatures of 3.3 and 3.9 keV, respectively. The Centaurus cluster exhibits remarkable hot region within about $30'$ south-east from the cluster center, showing a temperature increase of +0.8 keV from the surrounding level of 3.5 keV. There are also some cool regions with lower temperatures by −1.3 keV toward the cluster edge. The temperature map of the Perseus shows more complex structure in the whole cluster region. There is an extended cool region with a diameter of $\sim 20'$ and $kT \sim 5$ keV at about $20'$ east from the cluster center. This region also shows higher surface brightness, and is surrounded by a large ring-like hot region with $kT \gtrsim 7$ keV. Another extended cool region is extending outward from the IC 310 subcluster.

The observed results indicate that A1060 and AWM7 have not experienced merging processes for recent a few Gyr. The southeast hot region near the cluster center of the Centaurus corresponds to a galaxy subcluster region from optical observations. These features suggest that a strong merger has occurred in the recent ~ 1 Gyr, and that the central cool component has survived it. For the Perseus cluster, the presence of several other hot and cool blobs suggests that this rich cluster has been formed as a result of a repetition of many subcluster mergers.

Main results of this thesis have been published as 2 papers: Furusho et al. 2001, PASJ, 53, 421 (for A1060, AWM7, and Centaurus), and Furusho et al. 2001, ApJ, 561, L165 (for Perseus)

Contents

List of Figures

List of Tables

Chapter 1

Introduction

Clusters of galaxies have been regarded as the largest virialized systems in the universe with dimensions of 1–5 Mpc across. Since the time-scale for the cluster evolution is comparable to the age of the universe, $\sim$ 10 Gyr, their properties should reflect the initial condition and the evolutional history over the cosmological time scale.

The constituents of clusters are divided into three components: galaxies , intracluster medium (ICM), and dark matter. The galaxies are mainly observed in the optical band with the number of about a few hundreds a cluster. The ICM is a diffuse, X-ray emitting hot plasma with temperatures of typically $\times 10^{7-8}$ K. Their masses are heavier than the stellar mass by a factor of 3–5, and the distributions generally trace the gravitational potential. The dark matter occupies around 80% of the total cluster mass of $10^{14-15} M_{\odot}$. The primary energy source of the ICM is considered to be the kinetic energy released through the gas infall into the gravitational potential of the dark matter. The heating mechanism is, however, not yet fully understood. Numerical simulations based on a bottom-up formation scenario predict that shock heatings caused by mergers of smaller groups and subclusters are the important process. If mergers are playing a major role in the cluster evolution, their footprints on the ICM, in the form of morphology, temperature and metallicity, can be studied with X-ray observations.

Recent X-ray observations have shown various evidences indicating that the clusters are still evolving. Einstein and ROSAT have shown that some clusters suggest external disturbances in their irregular morphologies, and ASCA has shown two-dimensional temperature maps of nearby cluster with remarkable structures. The temperature structure persist over several Gyr even after the surface brightness distribution has been almost smoothed out with a time-scale of $\lesssim$ several hundreds Myr. Also, ASCA shows that radial profiles of metallicity in the ICM can be classified into several types that depend on such as the age, gas mixing, and cluster size. The metals are considered to be ejected from the galaxies into the ICM via galactic winds, or ram pressure stripping mainly during the starburst phase of more than several Gyr ago. These characters enable us to perform, to some extent, a time sliced study of the cluster evolution.

To reach consistent understanding of the evolutionary process of clusters, we need to look into the morphology, temperature, and metallicity structures for different richness systems in a systematic manner with enough spatial resolution. In particular, constraining the temperature structures in apparently relaxed systems that have smooth surface brightnesses is very important to know the past history in the evolution of average clusters. Since nearby clusters with $z \lesssim 0.02$ cannot be covered in the field of view of the GIS instrument on ASCA, we have to devise an analysis method to correctly handle multi-pointing data. Little effort has so far been made for such a study, mainly because of the technical difficulty. We carry out here the first attempt on the sensitive studies of the temperature and metallicity distributions for a sample of nearby clusters.

ASCA provides superior energy resolution and high sensitivity over a wide energy band 0.5–10.0 keV. These enable us to map out the temperature structure in nearby clusters with a spatial resolution of less than 100 kpc. This thesis presents temperature maps of Abell 1060, AWM7, the Centaurus cluster, and the Perseus cluster, based on the multi-pointing observations from ASCA. These clusters are all located closely to us ($z = 0.0104 - 0.0183$), emitting intense X-ray fluxes with the ICM temperatures $kT = 3 - 6$ keV. The clusters are markedly different in the strength of the central cool component, and in the shape of the metallicity profile, which would reflect different past histories of the cluster evolution. Comparison of temperature maps and metallicity distributions among the four clusters should, therefore, bring us a new important knowledge about the history of dynamical evolution as well as its connection with the central structure.

Throughout this thesis, we assume $H_0 = 50$ km s^{-1} Mpc^{-1} and $q_0 = 0.5$. The solar number abundance of Fe relative to H is taken as 4.68×10^{-5} (Anders and Grevesse 1989).

Chapter 2

The Structure and Evolution of Clusters

The hierarchical structure formation in the universe forms the basis of our study. In this chapter, we briefly review the current scenario of the structure formation, its effects on the cluster evolution, and the theoretical background. We also summarize relevant past results observed in X-rays, and previous observed properties of the hot gas and member galaxies on the four clusters studied in this thesis.

2.1 Scenario of the evolution in the universe

The evolution of the universe is divided broadly into the structure formation and the chemical evolution. The former is a dynamical process of celestial objects, and the latter represents the production of heavy elements in galaxies. Clusters of galaxies are useful probes to study both evolutions by mainly three reasons: 1) Since the dynamical time-scale of clusters is close to Hubble time, clusters retain the cosmological initial conditions well, 2) Clusters can be approximated that they consist of galaxies, hot gas, and dark matter in a spherical shape, thus they are easy to deal with, 3) Although a part of metals produced in galaxies run away into intragalactic medium, they do not escape from intracluster medium (ICM), hence we can obtain the total metal abundance without omission. In order to look into the properties of clusters, X-ray observations are particularly suited, because the X-ray emitting gas gives us the physical parameters such as temperature, mass, and metal abundance.

2.1.1 Dynamical evolution

At present, the hierarchical clustering scenario is widely supported, because it is naturally expected from the cold dark matter model. In fact, the galaxies at redshifts of ~ 5 have been observed, whereas the most distant observed clusters is at $z \sim 1$. That indicates the bottom-up scenario where small systems have been formed first. According to the scenario, large-scale structures of the universe have been formed from infinitesimally small density perturbations at the early universe through the gravitational interaction. A number of numerical simulations for the structure formation have shown producing the large-scale structures and clusters. Following an early work by White's 700-body simulations (1976), recent calculations (e.g. Eke et al. 1998) include N-body/gasdynamical simulations as shown in figure 2.1. Their results show hierarchical clustering for the hot gas and dark matter, and indicate that the clusters are formed through subcluster mergers and/or absorption of groups of galaxies.

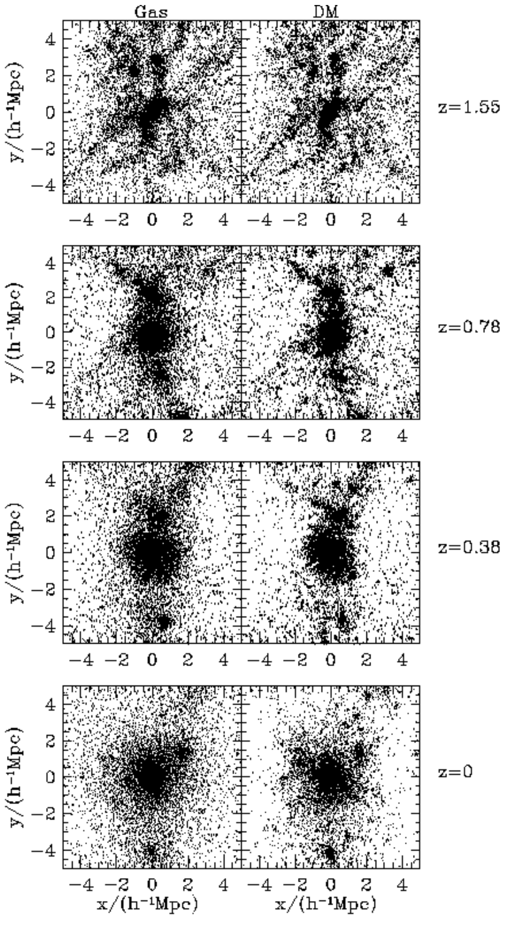

Figure 2.1: Dot plots showing the projected particle positions in cubes of physical size 10 h^{-1} Mpc centered on a cluster at different times (Eke et al. 1998).

Figure 2.2 shows how the radii of overdense spheres behave during the expansion of the universe. For a large initial overdensity, the expansion is stopped at an early stage and the system collapses into a virialized system. A system which is now virialized must have an overdensity $\rho/\rho_{\rm crit} > 200$, and clusters of galaxies just satisfies this condition. Those which are now infalling must have $\rho/\rho_{\rm crit} > 5$ that corresponds to dense parts of superclusters of galaxies. This gives clusters of galaxies a very special place in the hierarchy of structures in the universe.

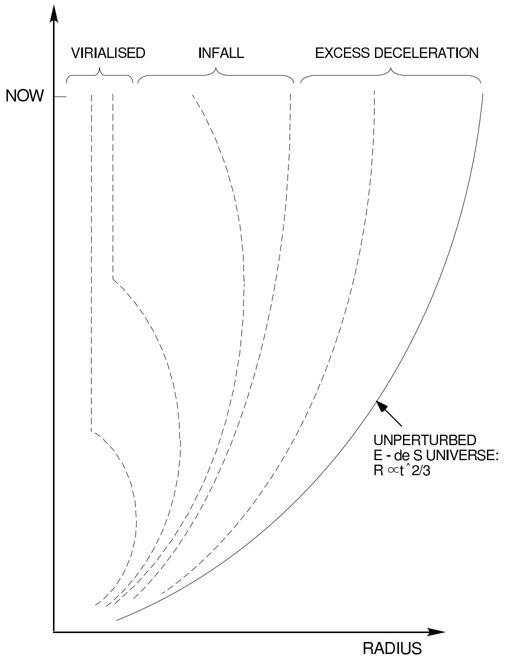

Figure 2.2: The dynamics of overdense spheres in the expanding universe. The larger initial overdensity, the earlier the sphere's expansion halts (Rees 1992).

2.1.2 Chemical evolution

The existence and distribution of the chemical elements and their isotopes are a consequence of nuclear processes that have taken place in the Big Bang, and subsequently in stars and interstellar medium. First, the gas collapses into a star by the gravitational potential of dark matter, and heavy elements produced in stars. Secondly, they are scattered into the surrounding gas through supernovae (SN). Thirdly, the gas including the heavy elements collapses into a star. The chemical evolution means a change of the total metal abundance in a galaxy through repeat of the above process.

Based on the optical observations, the element and star formation history of the universe are derived as shown in figure 2.3 (Madau 1999). The results appear an existence of a decline in the universal metal production rate at the redshift of $z < 1$ whether uncorrected or corrected for dust extinction. On the other hand, X-ray observations give the metal abundances for the elements in the ICM. Since part of metals are transfered into the ICM by galactic wind or ram pressure stripping, the total metal abundances are obtained from X-ray spectroscopy.

2.2 Observational studies of cluster evolution

Main subjects of clusters obtained from X-ray observations are morphology, temperature structure, central cool component, and metal distribution. Here we briefly summarize relevant past results from X-ray observations.

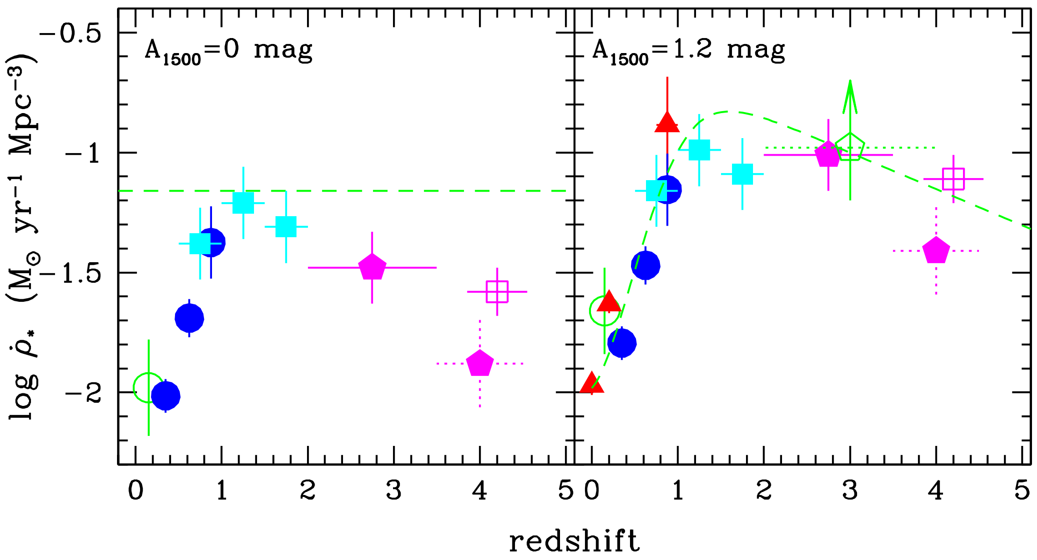

Figure 2.3: *left:* Mean comoving density of star formation as a function of cosmic time. The data points with error bars have been inferred from the UV-continuum luminosity densities. The dotted line shows the fiducial rate, $< \dot{\rho}_* >= 0.054 M_\odot$ yr^{-1} Mpc^{-3}, required to generate the observed extragalactic background light. *right:* dust corrected values ($A_{1500} = 1.2$ mag). The Hα determinations (filled triangles) together with the SCUBA lower limit (empty pentagon) have been added for comparison (Madau 1999).

2.2.1 Morphology

Figure 2.4 shows the X-ray images of A1367 and A754 in the 0.5–2.0 keV band with ROSAT PSPC. A1367 is a typical irregular cluster without a central concentration, it suggests to be a young cluster ongoing subcluster mergers. The X-ray images of A754 obviously indicates that these clusters are under a major merger. A754 also shows significant temperature structure regarding the morphology (Markevitch et al. 2000). We can expect a merging cluster based on substructures in X-ray surface brightness. However, the time-scale of apparently irregular morphology is shorter than that of temperature structure, and most of clusters show circularly symmetric surface brightness.

2.2.2 Temperature structure

Recent experiments made possible to obtain spatially resolved spectra of clusters, and are revealing the temperature structure. Markevitch et al. (1998) analyzed spatially resolved X-ray spectra of 30 nearby clusters with ASCA and ROSAT. They reported that most of them show a similar temperature decline at large radii, and about a half of the sample shows signs of merging. Determination of the dynamical structure of the clusters can constrain cosmological models because clusters should be dynamically more relaxed in a

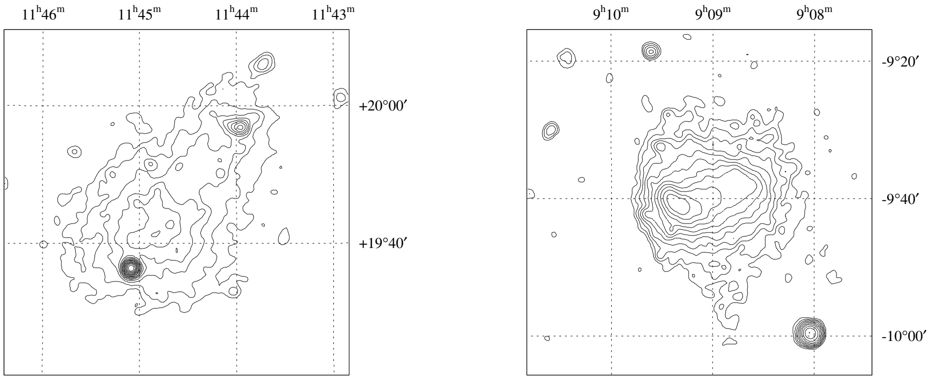

A1367

A754

Figure 2.4: The X-ray morphology of A1367 (left) and A754 (right) several clusters of galaxies with ROSAT PSPC.

low-density universe than in a high-density one (e.g. Richstone et al. 1992). Comparing the temperature profiles with the results of cluster hydrodynamic simulations, Markevitch et al. (1998) found the low Ω ($\lesssim 0.3$) cosmological models are suitable to explain the temperature profiles.

For example, we cite two instances of 2-dimensional temperature structures of the Coma cluster. Figure 2.5 shows color-coded temperature map of the Coma cluster obtained from ASCA (Watanabe et al. 1999) and XMM-Newton (Arnaud et al. 2000). The extended north-west region is clearly hotter than the surrounding regions. The result indicates evidence of a recent merger in the Coma cluster. It is interesting to see no substructure in the X-ray image around the hot region. Hence, the temperature structure gives us much information of mergings, which is not given by the morphology only. Note that the Coma cluster also shows that the abundance distribution is almost uniform. This probably mean that the metals in the Coma cluster are mixed by mergers.

2.2.3 Central cool component

Another important feature in clusters is the existence of a cool gas at the cluster center. The presence and intensity are recognized either from central narrow peaks in the surface brightness profiles or from X-ray spectra. Their origin has often been interpreted in terms of cooling flow models that requires a multi-phase temperature structure (e.g. Fabian 1994a), whereas extensive cluster studies from ASCA spectroscopy have shown the co-existence of hot ($kT \gtrsim 3$ keV) and cool ($kT \sim 1$ keV) components in several systems (Ikebe et al. 1999). It is important to know when and how these cool components have been created in the course of cluster evolution.

If there is no strong concentration in the central region, that indicates the cluster is too young or poor to reach enough high density to start radiative cooling, or the cool com-

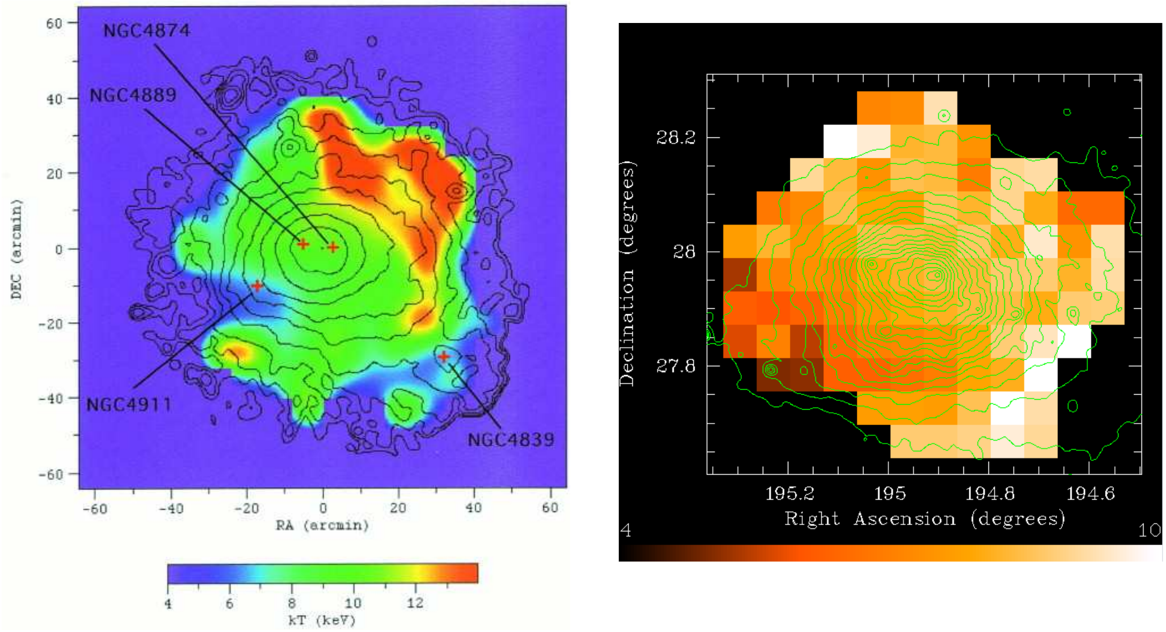

Figure 2.5: Color coded temperature map of the Coma cluster with ASCA (Watanabe et al. 1999) and XMM-Newton (Arnaud et al. 2000).

ponent might be disrupted by mergers. The presence of strong cool component suggests that there is no merger recently. However, when the central excess is enough strong, and subcluster is very small, it is possible to survive under a merger. It is important to know when and how these cool components have been created in the course of cluster evolution, though the expectation is very difficult.

Note that XMM Reflection Grating Spectrometers observation recently discoveries that the volume emission measure of cool component for A1795 ($z = 0.0631$), which is one of the strong cooling flow clusters, is less than a few % of the hot component at the center (Tamura et al. 2001). Also, A1835 ($z = 0.2523$) which is a strong cooling flow cluster with a $kT \sim 8$ keV shows that the emission measure of the cool gas below $kT = 2.7$ keV is much lower than expected from standard cooling flow models (Peterson et al. 2001). These results suggest that the explanation of central cool component by cooling flow model is very difficult. The detailed feature mechanism of cool component is still mysterious.

2.2.4 Metal distribution

Since heavy elements can be produced only by thermonuclear reactions in stars and supernovae, the presence of the emission lines found in the spectra from the ICM implies that heavy elements processed in galaxies largely contaminate the ICM.

Koyama et al. (1991) discovered Fe abundance increases at the center of the Virgo cluster with Ginga. From the ASCA observation, similar central abundance increases were found in several clusters (Fukazawa et al. 1994; David et al. 1996; Xu et al. 1997; Kikuchi et al. 1999). Moreover, the metal profiles are roughly divided into three types: 1) central concentration, 2) large-scale gradient, and 3) constant. For example, the metal profiles of Virgo and Centaurus cluster (Figure 2.16, Ikebe et al. 1999) are represented by the first type. They show extremely concentrated cool component associated with the cD galaxy at the cluster center. The central region is considered to survive mergers sometimes which mixed metals in the outer region. Next, a large scale gradient in the metal abundance (over 500 kpc) is detected in AWM7 (Figure 2.13, Ezawa et al. 1997) and Perseus cluster (Figure 2.4.5, Ezawa et al. 2001). These features suggest that the gas injected from individual galaxies is not efficiently mixed in the cluster space, and traces the distribution of galaxies, so that implies that the merging processes occured before starburst phase. Finally, Abell 1060 (Figure 2.10, Tamura et al. 1996) and Coma cluster show very flat metal abundance distributions. This suggests that the metals are well mixed by mergers after starburst phase. Hence, the observed metal abundance distribution enables us to study the chemical evolution related with merging history.

2.3 Theoretical background

We briefly describe here the X-ray emission mechanism, shock heating due to a merger, and characteristic time-scales as the basic theoretical background to study the cluster evolution.

2.3.1 X-ray emission from hot plasma

The ICM, having low gas density ($\sim 10^{-3}$ cm^{-3}) and a high temperature ($\sim 10^{8}$ K) radiates predominantly in the X-ray band. The emitted X-rays consist of thermal Bremsstrahlung continuum and various atomic emission lines.

The plasma volume emissivity, i.e. X-ray radiation energy emitted from a unit volume in a unit time, is given as

$$\epsilon = n_{\rm g}^2 \Lambda(T, Z). \tag{2.1}$$

The quantity $n_{\rm g}$ is the number density of the gas, and $\Lambda(T, Z)$ is the cooling function, with T and Z representing the plasma temperature and the heavy element abundance, respectively. Figure 2.6 shows the cooling function as a function of the plasma temperature assuming the cosmic abundances. The contribution of the bremsstrahlung continuum to Λ increases as $\propto T^{1/2}$. In contrast, the line contribution to Λ monotonously decreases with temperature above $T \sim 10^7$ K.

We can obtain the total X-ray luminosity by integrating equation 2.1. It is useful to define the emission integral as

$$EI = \int n_{\rm g}^2 \, dV, \tag{2.2}$$

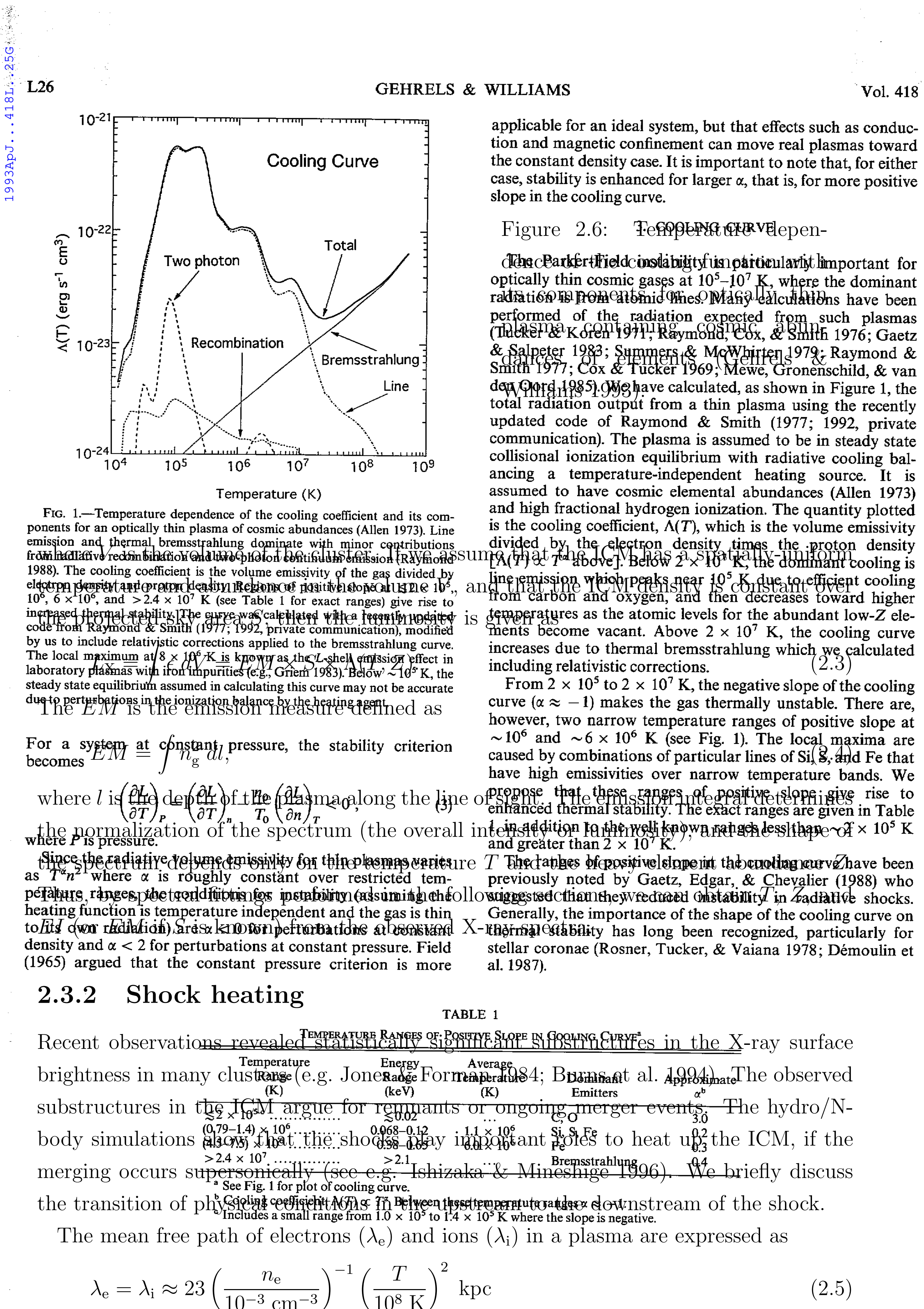

L26 GEHRELS & WILLIAMS Vol. 418

FIG. 1.—Temperature dependence of the cooling coefficient and its components for an optically thin plasma of cosmic abundances (Allen 1973). Line emission and thermal bremsstrahlung dominate with minor contributions from radiative recombination and two-photon continuum emission (Raymond 1988). The cooling coefficient is the volume emissivity of the gas divided by electron density and proton density. Regions of positive slope at $\lesssim 2 \times 10^5$, 10^6, 6×10^6, and $>2.4 \times 10^7$ K (see Table 1 for exact ranges) give rise to increased thermal stability. The curve was calculated with a recently updated code from Raymond & Smith (1977; 1992, private communication), modified by us to include relativistic corrections applied to the bremsstrahlung curve. The local maximum at 8×10^6 K is known as the *L*-shell emission effect in laboratory plasmas with iron impurities (e.g., Griem 1983). Below $\sim 10^5$ K, the steady state equilibrium assumed in calculating this curve may not be accurate due to perturbations in the ionization balance by the heating agent.

For a system at constant pressure, the stability criterion becomes

$$\left(\frac{\partial L}{\partial T}\right)_P = \left(\frac{\partial L}{\partial T}\right)_n - \frac{n_0}{T_0}\left(\frac{\partial L}{\partial n}\right)_T < 0 , \qquad (3)$$

where *P* is pressure.

Since the radiative volume emissivity for thin plasmas varies as $T^\alpha n^2$ where α is roughly constant over restricted temperature ranges, the conditions for instability (assuming the heating function is temperature independent and the gas is thin to its own radiation) are $\alpha < 0$ for perturbations at constant density and $\alpha < 2$ for perturbations at constant pressure. Field (1965) argued that the constant pressure criterion is more applicable for an ideal system, but that effects such as conduction and magnetic confinement can move real plasmas toward the constant density case. It is important to note that, for either case, stability is enhanced for larger α, that is, for more positive slope in the cooling curve.

3. COOLING CURVE

The Parker-Field instability is particularly important for optically thin cosmic gases at 10^5–10^7 K, where the dominant radiation is from atomic lines. Many calculations have been performed of the radiation expected from such plasmas (Tucker & Koren 1971; Raymond, Cox, & Smith 1976; Gaetz & Salpeter 1983; Summers & McWhirter 1979; Raymond & Smith 1977; Cox & Tucker 1969; Mewe, Gronenschild, & van den Oord 1985). We have calculated, as shown in Figure 1, the total radiation output from a thin plasma using the recently updated code of Raymond & Smith (1977; 1992, private communication). The plasma is assumed to be in steady state collisional ionization equilibrium with radiative cooling balancing a temperature-independent heating source. It is assumed to have cosmic elemental abundances (Allen 1973) and high fractional hydrogen ionization. The quantity plotted is the cooling coefficient, $\Lambda(T)$, which is the volume emissivity divided by the electron density times the proton density [$\Lambda(T) \propto T^\alpha$ above]. Below 2×10^7 K, the dominant cooling is line emission which peaks near 10^5 K due to efficient cooling from carbon and oxygen, and then decreases toward higher temperatures as the atomic levels for the abundant low-*Z* elements become vacant. Above 2×10^7 K, the cooling curve increases due to thermal bremsstrahlung which we calculated including relativistic corrections.

From 2×10^5 to 2×10^7 K, the negative slope of the cooling curve ($\alpha \approx -1$) makes the gas thermally unstable. There are, however, two narrow temperature ranges of positive slope at $\sim 10^6$ and $\sim 6 \times 10^6$ K (see Fig. 1). The local maxima are caused by combinations of particular lines of Si, S, and Fe that have high emissivities over narrow temperature bands. We propose that these ranges of positive slope give rise to enhanced thermal stability. The exact ranges are given in Table 1, in addition to the well known ranges less than $\sim 2 \times 10^5$ K and greater than 2×10^7 K.

The ranges of positive slope in the cooling curve have been previously noted by Gaetz, Edgar, & Chevalier (1988) who suggested that they reduced instability in radiative shocks. Generally, the importance of the shape of the cooling curve on thermal stability has long been recognized, particularly for stellar coronae (Rosner, Tucker, & Vaiana 1978; Démoulin et al. 1987).

TABLE 1

TEMPERATURE RANGES OF POSITIVE SLOPE IN COOLING CURVE[a]

Temperature Range (K)	Energy Range (keV)	Average Temperature (K)	Dominant Emitters	Approximate α[b]
$\lesssim 2 \times 10^5$[c]	$\lesssim 0.02$	...	C, O	3.0
$(0.79$–$1.4) \times 10^6$	0.068–0.12	1.1×10^6	Si, S, Fe	0.2
$(4.5$–$7.5) \times 10^6$	0.38–0.65	6.0×10^6	Fe	0.3
$>2.4 \times 10^7$	>2.1	...	Bremsstrahlung	0.4

[a] See Fig. 1 for plot of cooling curve.

[b] Cooling coefficient $\Lambda(T) \propto T^\alpha$. Between these temperature ranges $\alpha \approx -1$.

[c] Includes a small range from 1.0×10^5 to 1.4×10^5 K where the slope is negative.

Figure 2.6: Temperature dependence of the cooling function with its components for optically thin plasma containing cosmic abundances of elements (Gehrels & Williams 1993).

where V_X is the volume of the cluster. If we assume that the ICM has a spatially-uniform temperature and abundance in the volume V_X, and that the ICM density is constant over the projected sky area S, then the luminosity is given as

$$L_X = \int \epsilon \, dV = EM \times S \times \Lambda(T, Z). \qquad (2.3)$$

The EM is the emission measure defined as

$$EM = \int n_g \, dl, \qquad (2.4)$$

where l is the depth of the plasma along the line of sight. The emission integral determines the normalization of the spectrum (the overall intensity or luminosity), and the shape of the spectrum depends only on the temperature T and the heavy element abundance Z. Thus, by spectral fittings performed in the following sections, we can obtain T, Z, and EI (or EM if S is known) from the observed X-ray spectra.

2.3.2 Shock heating

Recent observations revealed statistically significant substructures in the X-ray surface brightness in many clusters (e.g. Jones & Forman 1984; Burns et al. 1994). The observed substructures in the ICM argue for remnants or ongoing merger events. The hydro/N-body simulations show that the shocks play important roles to heat up the ICM, if the merging occurs supersonically (see e.g. Ishizaka & Mineshige 1996). We briefly discuss the transition of physical conditions in the upstream to the downstream of the shock.

The mean free path of electrons (λ_e) and ions (λ_i) in a plasma are expressed as

$$\lambda_e = \lambda_i \approx 23 \left(\frac{n_e}{10^{-3}\ \mathrm{cm}^{-3}}\right)^{-1} \left(\frac{T}{10^8\ \mathrm{K}}\right)^2\ \mathrm{kpc} \qquad (2.5)$$

(Sarazin 1988, p. 156), where n_e is the number density of electrons. If the region of interest has a much larger scale than the mean free path, we may consider that the physical parameters shown in figure 2.7 satisfy the 'jump' condition. It is called as Rankine-Hugoniot jump condition (e.g. Shu 1992). The mass, momentum, and energy conservation equations are expressed as

$$\rho_1 v_1 = \rho_2 v_2, \tag{2.6}$$

$$\rho_1 v_1^2 + p_1 = \rho_2 v_2^2 + p_2, \tag{2.7}$$

$$\frac{1}{2}v_1^2 + \frac{\gamma}{\gamma-1}\frac{p_1}{\rho_1} = \frac{1}{2}v_2^2 + \frac{\gamma}{\gamma-1}\frac{p_2}{\rho_2}, \tag{2.8}$$

where ρ, v, and p indicate the density, velocity, and pressure, respectively, measured from the rest frame of the shock. The suffixes of 1 and 2 represent the upstream and downstream of the shock, respectively, and γ is the ratio of specific heats. From the above equations, we find

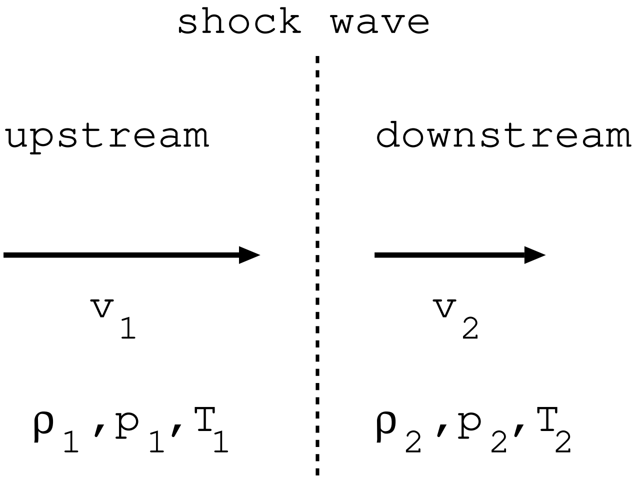

Figure 2.7: Schematic representation of the transition region for a shock wave measured in the rest frame of the shock. Upstream gas properties are transformed to downstream ones.

$$\frac{\rho_2}{\rho_1} = \frac{(\gamma+1)\mathcal{M}_1^2}{(\gamma-1)\mathcal{M}_1^2+2}, \tag{2.9}$$

$$\frac{p_2}{p_1} = \frac{2\gamma\mathcal{M}_1^2-(\gamma-1)}{\gamma+1}, \tag{2.10}$$

$$\frac{T_2}{T_1} = \frac{p_2\cdot\rho_1}{p_1\cdot\rho_2} = \frac{[2\gamma\mathcal{M}_1^2-(\gamma-1)][(\gamma-1)\mathcal{M}_1^2+2]}{(\gamma+1)^2\mathcal{M}_1^2}, \tag{2.11}$$

where $\mathcal{M}$ indicates the Mach number.

In the limit of a weak shock, $p_1 \approx p_2$, the shock wave travels with a velocity which is close to the speed of sound, and is practically the same as an acoustic compression wave (Zel'dovich & Raizer 1966). On the other hand, in the limit of a strong shock, $p_2 \gg p_1$, $\mathcal{M}_2$ approaches a constant value $\mathcal{M}_2 \rightarrow [(\gamma-1)/2\gamma]^{1/2}$, and p_2 is expressed as

$$p_2 \approx \frac{2(\gamma-1)}{(\gamma+1)^2}\rho_2 v_1^2. \tag{2.12}$$

Thus, for the strong shock, the gas can be heated up to $kT_2 \approx (3/16)\mu m_{\rm p} v_1^2$, where $\mu \approx 0.6$ is a mean molecular weight and $m_{\rm p}$ is a proton mass, assuming $\gamma = 5/3$.

2.3.3 Characteristic time scale

We summarize here characteristic time-scales that are important indicators to study cluster evolution.

Hubble time: $t_{\rm Hubble}$

The age of the universe is estimated from the Hubble constant:

$$t_{\rm Hubble} \equiv \frac{1}{H_0} = 2.0 \times 10^{10} \ {\rm yr}, \tag{2.13}$$

where H_0 is taken a value of 50 km s^{-1} Mpc $^{-1}$. This time scale becomes an upper limit on the age of the clusters of galaxies.

Crossing time: $t_{\rm cr}$

According to the hierarchical clustering scenario, we expect the initial state of material in the protocluster to be irregular. Thus the relaxation of the cluster involves the spatial motion of the galaxies, and a lower limit is the crossing time given as

$$t_{\rm cr} \equiv \frac{r}{\sigma_r} \approx 10^9 \left(\frac{\sigma_r}{10^3 {\rm km/s}}\right)^{-1} \left(\frac{r}{\rm Mpc}\right) \ {\rm yr}, \tag{2.14}$$

where the radial velocity dispersion σ_r has been substituted for the radial velocity v_r.

Two-body relaxation time: $t_{\rm rel}$

Thermodynamic equilibrium could results from elastic collisions between galaxies. The most important elastic two-body collisions in clusters are gravitational. The two-body relaxation time is

$$\begin{aligned} t_{\rm rel} &= \frac{3\sigma_r^3}{4\sqrt{\pi} G^2 m m_{\rm f} n_{\rm f} \ln \Lambda} \\ &\simeq 2 \times 10^{10} {\rm yr} \left[\left(\frac{\sigma_r}{10^3 {\rm km\ s^{-1}}}\right)^3 \left(\frac{m}{10^{12} M_\odot}\right)^{-1} \left(\frac{m_{\rm f}}{10^{12} M_\odot}\right)^{-1} \right. \\ &\quad \left. \times \left(\frac{n_{\rm f}}{10^3 {\rm galaxies\ Mpc^{-3}}}\right)^{-1} (\ln \Lambda)^{-1} \right] \end{aligned} \tag{2.15}$$

for the relaxation of a galaxy of mass m in a background field of galaxies of mass $m_{\rm f}$ and number density $n_{\rm f}$. Λ is ratio of maximum to minimum impact parameters of collisions which contribute to the relaxation.

Free-Fall time: $t_{\rm ff}$

If we consider heating of the ICM only due to an infall of the primordial gas into the cluster and the compression, the heating time scale is equal to the free-fall time scale given as

$$t_{\rm ff} \approx (G < \rho >)^{-1/2} \approx 3.1 \times 10^9 \left(\frac{D}{1 {\rm Mpc}}\right)^{3/2} \left(\frac{M_{\rm total}}{10^{14}\ M_\odot}\right)^{-1/2} \ {\rm yr}, \tag{2.16}$$

where D is the cluster diameter, and $M_{\rm total}$ is the total mass of the cluster.

Cooling time: $t_{\rm cool}$

The primary cooling process for the ICM is radiative cooling due to free-free emission, expressed as

$$t_{\rm cool} = \frac{U}{\epsilon} = \frac{3nkT}{n^2\Lambda(T,Z)} \tag{2.17}$$

where U and ϵ are the internal energy and volume emissivity, and $n = n_{\rm e} = n_{\rm p}$ is the number density in a fully ionized plasma, and Λ is the cooling function. The total emissivity through thermal bremsstrahlung is

$$\epsilon^{ff} \approx 3.0 \times 10^{-27} T^{1/2} n^2 \ {\rm erg\,cm^{-3}s^{-1}}, \tag{2.18}$$

assuming solar abundances and velocity averaged Gount factor of 1.1 in a fully ionized plasma with a temperature of $> 3 \times 10^7$ K (Sarazin 1988, p. 148). Then, the cooling time is calculated as

$$\approx 8.5 \times 10^{10} \left(\frac{n}{10^{-3}\ {\rm cm^{-3}}}\right)^{-1} \left(\frac{T}{10^8\ {\rm K}}\right)^{1/2} \ {\rm yr}. \tag{2.19}$$

Thus the cooling time is longer than the Hubble time for most of the clusters except for the central region.

Ionization equilibration time scale: $t_{\rm ie}$

The time-scale for collisional ionization equilibrium with the plasma calculated by Masai (1994) is

$$t_{\rm ie} \approx 10^{12} n_{\rm e}^{-1} = 3.3 \times 10^8 \left(\frac{n_{\rm e}}{10^{-3}\ {\rm cm^{-3}}}\right)^{-1} \ {\rm yr}. \tag{2.20}$$

Here $n_{\rm e}$ is the electron density.

Equipartition time: $t_{\rm eq}$

If a homogeneous plasma is created in a state in which the particle distribution is non-Maxwellian, elastic collisions will cause it to relax to a Maxwellian distribution on a time scale determined by the mean free paths (Spitzer, 1956, 1978). Electrons will achieve this equipartition on a time scale set roughly by $t_{\rm eq} \equiv \lambda_{\rm e} / < v_{\rm e} >_{rms}$,

$$t_{\rm eq}(e,e) = \frac{3 m_{\rm e}^{1/2} (kT_{\rm e})^{3/2}}{4\pi^{1/2} n_{\rm e} e^4 \ln\Lambda} \approx 3.1 \times 10^5 \left(\frac{\ln\Lambda}{40}\right)^{-1} \left(\frac{T}{10^8 {\rm K}}\right)^{3/2} \left(\frac{n_{\rm e}}{10^{-3}{\rm cm^{-3}}}\right)^{-1} \ {\rm yr}, \tag{2.21}$$

where $T_{\rm e}$ is the electron temperature, and ln Λ is the Coulomb logarithm. The time scale for protons to equilibrate among themselves is $\sqrt{m_{\rm p}/m_{\rm e}} \sim 43$ times longer than the value in $t_{\rm eq}(e,e)$: $t_{\rm eq}(p,p) = 1.3 \times 10^7$ yr. The time scale for the electrons and ions to reach equipartition $T_{\rm e} = T_{\rm i}$ is $t_{\rm eq}(p,e) = (m_{\rm p}/m_{\rm e}) t_{\rm eq}(e,e) = 5.7 \times 10^8$ yr.

Conduction time: $t_{\rm cond}$

It is useful to define a conduction time-scale as $t_{\rm cond} \equiv -(d \ln T_{\rm e}/dt)^{-1}$, which can be approximated to $(n_{\rm e} l/\kappa)$ with the scale length of temperature gradient $l \equiv T_{\rm e}/|\nabla T|$ (Sarazin 1988, p.157). Heat conduction is most effective in the cluster core, and $t_{\rm cond}$ increases vary rapidly with radius. The central value to the conduction time scale is given by

$$\begin{aligned} t_{\rm cond}(0) &\approx \frac{n_{\rm e} k}{\kappa}\left(\frac{T}{|\nabla T|}\right)^2 \\ &\approx 5.6 \times 10^7 \left(\frac{n_{\rm p}}{10^{-3}\ {\rm cm}^{-3}}\right)\left(\frac{T_e}{10^8\ {\rm K}}\right)^{-5/2}\left(\frac{\ln \Lambda}{40}\right)\left(\frac{T/|\nabla T|}{0.25\ {\rm Mpc}}\right)^2 {\rm yr}, \quad (2.22) \end{aligned}$$

where $n_{\rm p}$ is the central proton density, and solar abundances have been assumed. Thus heat conduction may be relatively effective in the core of a cluster. At outer radii $r \gtrsim 2r_{\rm c}$, the conduction time is typically 10^2 times longer, and conduction is only marginally effective in the outer parts of the cluster.

Drift time for heavy ions: $t_{\rm drift}$

Heavy ions that diffuse toward the cluster center rapidly reach a drift velocity at which gravitational acceleration is balanced by the slowing effect of collisions (Fabian and Pringle 1977). The time to drift in a small distance dr is then $dt = dr/v_{\rm D}$, where $v_{\rm D}$ is the drift velocity, given as

$$\begin{aligned} t_{\rm drift} \approx\ & 1.2 \times 10^{11}\left(\frac{A}{56}\right)^{-1}\left(\frac{Z}{26}\right)^2\left(\frac{T_{\rm e}}{10^8\ {\rm K}}\right)^{-3/2} \\ & \left(\frac{n_{\rm e}}{10^{-3}\ {\rm cm}^{-3}}\right)\left(\frac{\ln \Lambda}{40}\right)\left(\frac{\sigma_r}{10^3 {\rm km/s}}\right)^{-2}\left(\frac{r_{\rm c}}{0.25 {\rm Mpc}}\right)^2 {\rm yr}. \quad (2.23) \end{aligned}$$

Rephaeli (1978) has found that the drift time from radii greater than 4 core radii into 1 core radius is always greater than 10^{11} yr the cluster parameters in above equation, with the gas density and temperature evaluated at the cluster center. Since this means the drift time is generally at least ten times the probable age of the cluster, the settling of iron into the cluster center is unlikely to occur. However, this does not mean that the metal abundance is necessarily uniform, because heavy elements might be concentrated in the cluster core if they were injected into the intracluster gas in the center.

Mixing time due to galaxy motions: $t_{\rm mix}$

Motions of galaxies through the intracluster gas may mix the gas. This process has not been treated in any great detail in the literature. It might be reasonable to assume that each galaxy mixes the gas within a wake of radius $R_{\rm W}$. Very roughly, the gas within the whole cluster would be mixed on a time scale given by

$$t_{\rm mix} \approx \frac{1}{n_{\rm gal}\sigma_{\rm r}\pi R_{\rm W}^2}\left(\frac{r_{\rm c}}{R_{\rm W}}\right)^2 , \tag{2.24}$$

where $n_{\rm gal}$ is the number density of galaxies, $\sigma_{\rm r}$ is their velocity dispersion, and $r_{\rm c}$ is the cluster core radius. Depending on whether the galaxy contained any interstellar medium or not, the radius might be $\approx$ 10 kpc. The resulting value of $t_{\rm mix}$ is generally much longer than $\sim 10^{11}$ yr for any reasonable values of the cluster parameters, and mixing due to galaxy motions is not very important.

Time scale for ram pressure stripping of a galaxy: $t_{\rm rp}$

Sarazin (1979) gave a semi-analytic treatment of the stripping of gas from spherical galaxies, using basically the same formulation as Tarter (1975). Assuming that the ram pressure is much greater than a critical pressure of $2\rho_{\rm ISM}\sigma_*^2$ derived by numerical hydrodynamic simulations, the time-scale for ram pressure stripping of a galaxy, defined as $t_{\rm rp} \equiv (d\ln M_{\rm ISM}/dt)^{-1}$, is

$$\begin{aligned} t_{\rm rp} &\approx \frac{R}{v}\left(\frac{2\rho_{\rm ISM}}{\rho_{\rm g}}\right)^{1/2} \\ &\approx 3\times10^7\left(\frac{\rho_{\rm ISM}}{\rho}\right)^{1/2}\left(\frac{v}{10^3{\rm km/s}}\right)^{-1}\left(\frac{R}{20{\rm kpc}}\right)\ {\rm yr}, \end{aligned} \tag{2.25}$$

where $\rho_{\rm ISM}$ is the average interstellar gas density, ρ_g is the intracluster gas density, and v is the galaxy velocity. The calculations of Tarter and Sarazin assume that there are no sources of gas in the galaxy.

2.4 Clusters studied

2.4.1 Selection criteria

For our study, closeness and brightness of a system become much important. Good photon statistics allow ASCA to resolve the temperature structures less than 100 kpc in a whole cluster region. We therefore selected four clusters, Abell 1060 (A1060 for short), AWM 7, the Centaurus cluster and the Perseus cluster with following criteria:

- X-ray bright ($L_{\rm X} \gtrsim 10^{43}$ erg s^{-1})
- nearby ($D_L \lesssim 100$ Mpc which corresponds to $z \lesssim 0.017$)
- rather low temperature ($kT \lesssim 5$ keV)
- axially symmetric X-ray morphology

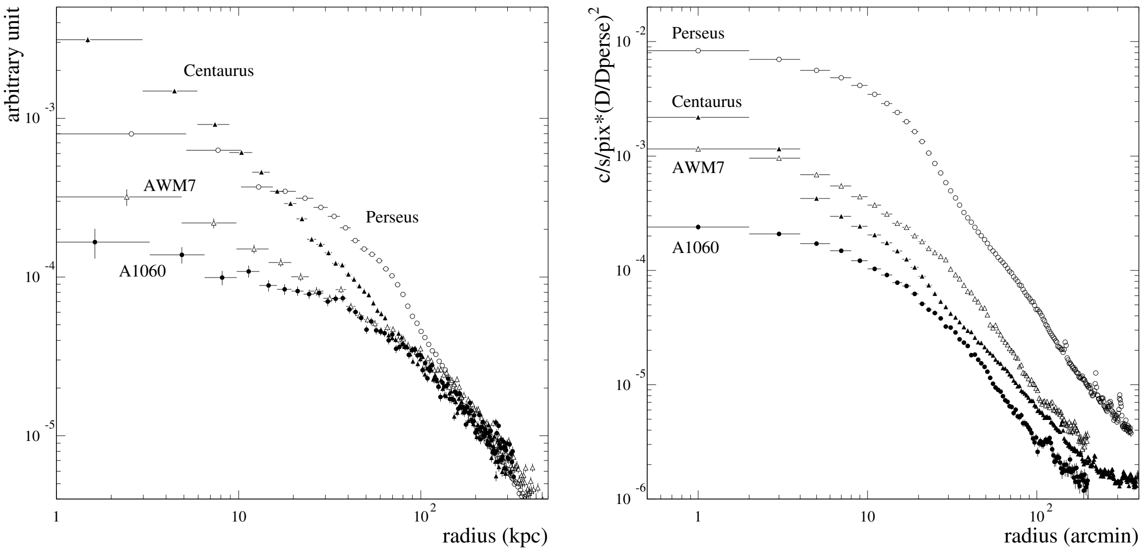

Figure 2.8: X-ray surface brightness profiles of the 4 clusters from the HRI data (left) and PSPC data (right). The HRI profiles are arbitrarily scaled for comparison between their central features. For the PSPC profiles, the intensity is multiplied by the ratio square of the luminosity distance to the distance of the Perseus cluster to help comparison with the intrinsic luminosity.

General properties and previous X-ray results of the 4 clusters are summarized in Table 2.1. They are all nearby (z =0.0104–0.0183), and X-ray bright clusters with the average ICM temperatures kT =3–6 keV. The clusters, however, are markedly different regarding the strength of the central cool component. Figure 2.8 shows the surface brightness profiles of the 4 clusters from the ROSAT HRI (normalized for comparison) and PSPC data. The Centaurus cluster shows very sharp central peak in the surface brightness profile. The Perseus cluster and AWM7 also show central excess features, but it is not as narrow nor intense as the Centaurus. In contrast, A1060 does not have such a narrow peak, and the size and mass of the cD galaxy is smaller than typical cD galaxies from optical observations. Since the cool component is believed to grow in the course of cluster evolution, the feature of the cool component is a good indicator to examine structure formation of clusters. Their metal distributions also have marked individuality as described in the following subsection.

2.4.2 Abell 1060

A1060 (Hydra I cluster) is the nearest cluster after the Virgo, Fornax, and Centaurus clusters among X-ray luminous ones at a redshift of $z = 0.0114$ (Abell et al. 1989). X-ray emission from this cluster has been observed and studied with *Einstein* (Fitchett and

Table 2.1: General properties for A1060, AWM7, the Centaurus cluster, and the Perseus cluster.

		A1060	AWM7	Centaurus	Perseus
Redshift		0.0114	0.0172	0.0104	0.0183
Luminosity Dist.	Mpc	69	104	63	108
BM/RS[†]		III/C	II?/L?	I-II/cD	II-III/L
Population		103	179	$\gtrsim$ 198	$\gtrsim$ 170
Velocity dispersion	km s^{-1}	676	727	586, 280	$\sim$ 5500
cD galaxy		NGC 3311	NGC 1129	NGC 4696	NGC 1275
R.A.(J2000)[‡]		$10^{h}36^{m}42.6^{s}$	$2^{h}54^{m}27.5^{s}$	$12^{h}48^{m}49.3^{s}$	$3^{h}19^{m}48.2^{s}$
Decl.(J2000)[‡]		$-27^{\circ}31'42.9''$	$+41^{\circ}34'42.5''$	$-41^{\circ}18'40.0''$	$+41^{\circ}30'42.1''$
l (J2000)	degrees	269.601549	146.336897	302.403583	150.5758384
b (J2000)	degrees	26.486301	−15.635096	21.557991	−13.2611465
$kT_{\rm hot}$ [a]	keV	$3.3^{+0.4}_{-0.3}$	3.6 ± 0.2	3.6 ± 0.4	5.5 ± 0.5
$kT_{\rm hot}$ [b]	keV	3.25 ± 0.05	3.76 ± 0.08	3.75 ± 0.07	6.79 ± 0.11
$L_{\rm X(2-10\ keV)}$ [a]	10^{44} erg s^{-1}	0.25 ± 0.01	1.2 ± 0.07	0.58 ± 0.02	10.0 ± 1.0
$L_{\rm X(0.5-10\ keV)}$ [b]	10^{44} erg s^{-1}	0.41	2.1	0.97	18
Cooling flow rate [c]	$M_{\odot}$ yr^{-1}	15^{+5}_{-7}	41^{+6}_{-6}	30^{+10}_{-5}	556^{+33}_{-24}
$r_{\rm cool}$ [c]	kpc	79^{+15}_{-26}	103^{+5}_{-8}	81^{+23}_{-18}	185^{+11}_{-11}
$t_{\rm cool}$ [c]	Gyr	$4.7^{+0.4}_{-0.3}$	$1.9^{+0.2}_{-0.2}$	$0.8^{+0.0}_{-0.0}$	$0.9^{+0.0}_{-0.0}$

[†] BM: Bautz-Morgan type, RS: Rood-Sastry type. [‡] Positions of cD galaxy taken from NED. [a] EXOSAT results from Edge and Stewart (1991) [b] ASCA results from Fukazawa et al. (1998) [c] The ROSAT PSPC results from Peres et al. (1998)

Merritt 1988), EXOSAT (Singh et al. 1988), ROSAT, and ASCA (Tamura et al. 1996, 2000). Figure 2.9 shows the PSPC image of the A1060 in the 0.5–2 keV band, the X-ray image is circularly symmetric. The central cool component is very weak or absent in an X-ray spectrum, and cooling flow rate is estimated to be $\dot{M} \lesssim 15 M_{\odot}$ yr^{-1} (Peres et al. 1998). As shown in figure 2.10, the previous study for the central $r < 20'$ region with ASCA shows that the ICM temperature is quite isothermal at around 3.2 keV and the metal abundance is almost flat at $\sim$ 0.3 solar (Tamura et al. 1996, 2000; Finoguenov et al. 2000).

Richter et al. (1982, 1987) and Hamabe (1993) compiled catalogs of member galaxies of A1060. 103 galaxies have redshifts ranging from 2300 to 5200 km s^{-1}, and can be considered as member galaxies of the cluster. The radial velocity histogram shows that this cluster appears to be isolated in redshift space of 60–70 Mpc. From a Gaussian fit to the radial velocity histogram, the systematic velocity is determined to be 3414 km s^{-1} with an average line-of-sight velocity dispersion of 657 km s^{-1} (Richter et al. 1987). At the center, there are two bright elliptical galaxies NGC 3311($z = 0.0120$) regarded as a cD

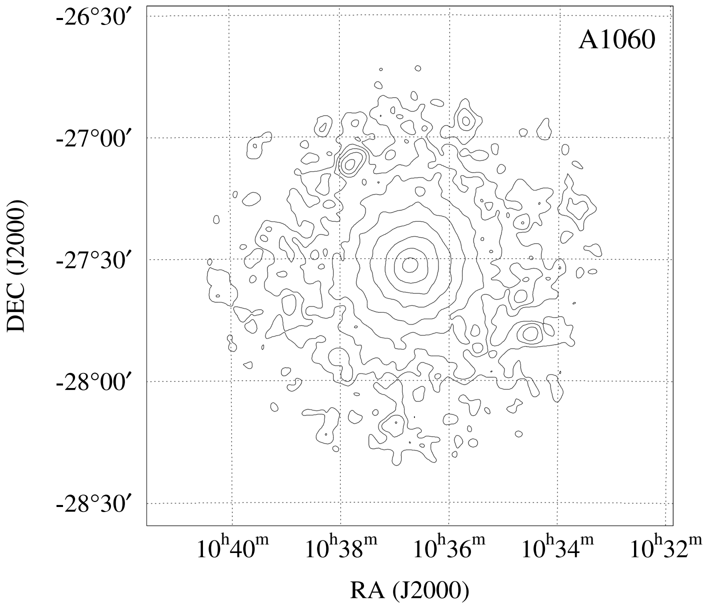

Figure 2.9: The PSPC image of the A1060 in the energy range 0.5–2.0 keV.

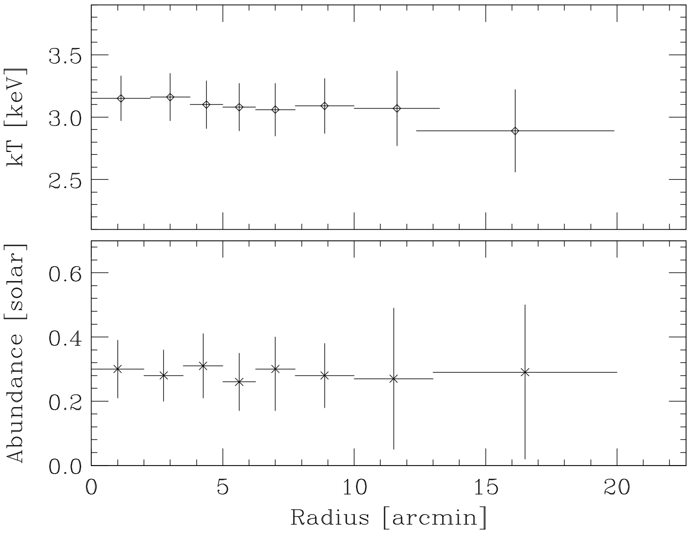

Figure 2.10: Temperature and abundance distributions of A1060 within a radius of 20′ obtained from ASCA (Tamura et al. 1996).

galaxy, and NGC 3309 ($z = 0.0136$). However, both the size and the mass of NGC 3311 are smaller than the typical cD galaxies. In the southeast near the cluster center, there might be a small foreground group of 3 galaxies from HI observations (McMahon et al. 1992).

2.4.3 AWM7

AWM7 ($z = 0.0172$) is a poor cluster that is not listed in Abell catalog. However, the X-ray luminosity is comparable to other Abell clusters, and it forms part of the Pisces-Perseus supercluster filament at the west of the Perseus cluster. X-ray emission from this cluster has been studied with *Einstein* (Kriss, Cioffi, and Canizares 1983), *Ginga*

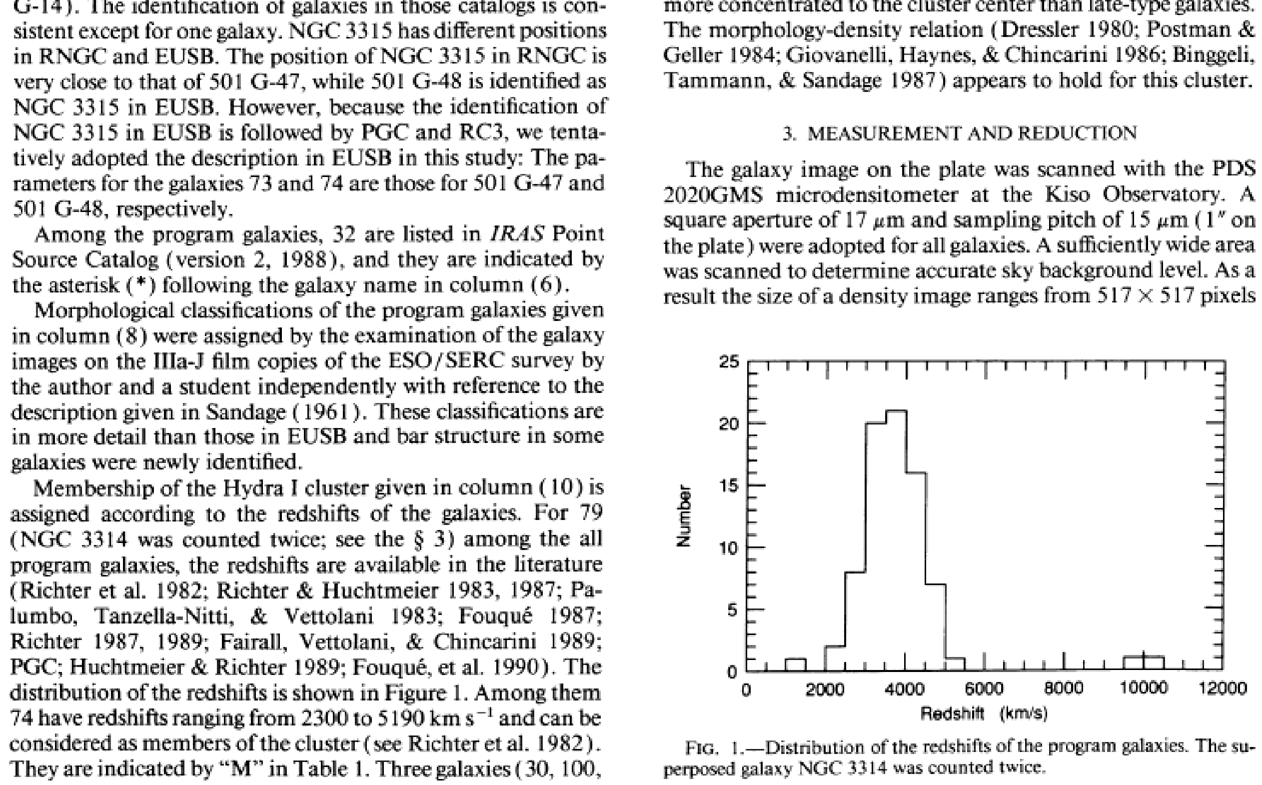

G-14). The identification of galaxies in those catalogs is consistent except for one galaxy. NGC 3315 has different positions in RNGC and EUSB. The position of NGC 3315 in RNGC is very close to that of 501 G-47, while 501 G-48 is identified as NGC 3315 in EUSB. However, because the identification of NGC 3315 in EUSB is followed by PGC and RC3, we tentatively adopted the description in EUSB in this study: The parameters for the galaxies 73 and 74 are those for 501 G-47 and 501 G-48, respectively.

Among the program galaxies, 32 are listed in *IRAS* Point Source Catalog (version 2, 1988), and they are indicated by the asterisk (*) following the galaxy name in column (6).

Morphological classifications of the program galaxies given in column (8) were assigned by the examination of the galaxy images on the IIIa-J film copies of the ESO/SERC survey by the author and a student independently with reference to the description given in Sandage (1961). These classifications are in more detail than those in EUSB and bar structure in some galaxies were newly identified.

Membership of the Hydra I cluster given in column (10) is assigned according to the redshifts of the galaxies. For 79 (NGC 3314 was counted twice; see the § 3) among the all program galaxies, the redshifts are available in the literature (Richter et al. 1982; Richter & Huchtmeier 1983, 1987; Palumbo, Tanzella-Nitti, & Vettolani 1983; Fouqué 1987; Richter 1987, 1989; Fairall, Vettolani, & Chincarini 1989; PGC; Huchtmeier & Richter 1989; Fouqué, et al. 1990). The distribution of the redshifts is shown in Figure 1. Among them 74 have redshifts ranging from 2300 to 5190 km s^{-1} and can be considered as members of the cluster (see Richter et al. 1982). They are indicated by "M" in Table 1. Three galaxies (30, 100,

more concentrated to the cluster center than late-type galaxies. The morphology-density relation (Dressler 1980; Postman & Geller 1984; Giovanelli, Haynes, & Chincarini 1986; Binggeli, Tammann, & Sandage 1987) appears to hold for this cluster.

3. MEASUREMENT AND REDUCTION

The galaxy image on the plate was scanned with the PDS 2020GMS microdensitometer at the Kiso Observatory. A square aperture of 17 μm and sampling pitch of 15 μm (1″ on the plate) were adopted for all galaxies. A sufficiently wide area was scanned to determine accurate sky background level. As a result the size of a density image ranges from 517 × 517 pixels

FIG. 1.—Distribution of the redshifts of the program galaxies. The superposed galaxy NGC 3314 was counted twice.

Figure 2.11: *left* – Distribution of the 137 galaxies in A1060 and seven field stars on the UK Schmit plate V3324. Early-type(E-S0/a), late-type(Sa-Irr), and unknown type are denoted by closed circles, open circles, and triangles, respectively. *right* – Distribution of the redshifts of the galaxies (Hamabe 1993).

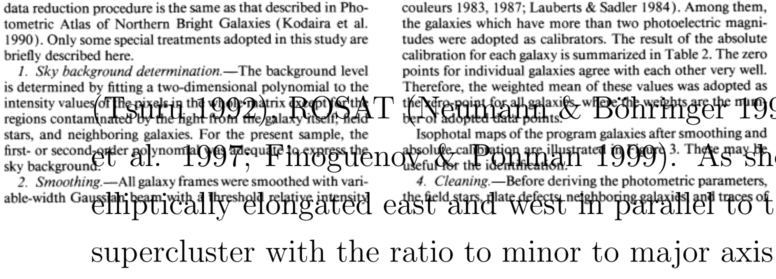

FACOM S-3500 system at the Kiso Observatory. The basic data reduction procedure is the same as that described in Photometric Atlas of Northern Bright Galaxies (Kodaira et al. 1990). Only some special treatments adopted in this study are briefly described here.

1. *Sky background determination.*—The background level is determined by fitting a two-dimensional polynomial to the intensity values of the pixels in the whole matrix except for the regions contaminated by the light from the galaxy itself, field stars, and neighboring galaxies. For the present sample, the first- or second-order polynomial was adequate to express the sky background.

2. *Smoothing.*—All galaxy frames were smoothed with variable-width Gaussian beam with a threshold relative intensity

found in the literature (van den Bergh 1977; Longo & de Vaucouleurs 1983, 1987; Lauberts & Sadler 1984). Among them, the galaxies which have more than two photoelectric magnitudes were adopted as calibrators. The result of the absolute calibration for each galaxy is summarized in Table 2. The zero points for individual galaxies agree with each other very well. Therefore, the weighted mean of these values was adopted as the zero-point for all galaxies, where the weights are the number of adopted data points.

Isophotal maps of the program galaxies after smoothing and absolute calibration are illustrated in Figure 3. These may be useful for the identification.

4. *Cleaning.*—Before deriving the photometric parameters, the field stars, plate defects, neighboring galaxies, and traces of

(Tsuru 1992), ROSAT (Neumann & Böhringer 1995), and ASCA (Xu et al. 1997; Ezawa et al. 1997; Finoguenov & Ponman 1999). As shown in figure 2.12, the X-ray image is elliptically elongated east and west in parallel to the filament structure of Pisces-Perseus supercluster with the ratio to minor to major axis of ~ 0.8. The mapping data of ASCA were previously analyzed by Ezawa et al. (1997). Figure 2.13 shows the radial distribution of temperature, which was found to be fairly flat up to a radius of $40'$. They also found a large-scale metallicity gradient. The cool component in the central region is weak and the GIS data can be fit with a single temperature model (Xu et al. 1997).

From optical data, AWM7 was found as a group of galaxies by Albert, White, and Morgan (1977), and was classified as a richness class 0 galaxy cluster (Kriss et al. 1983). For 33 galaxies redshifts are listed in Beers et al. (1984). Koranyi and Geller (2000) have measured 492 redshifts in the direction of the AWM7, and have identified 179 galaxies as member galaxies. Figure 2.14 shows the distribution of the galaxies. The velocity dispersion within 3.6 Mpc is 727 km s^{-1}.

2.4.4 The Centaurus cluster

The Centaurus cluster (Abell 3526, $z = 0.0104$) is the second X-ray bright (next to Perseus cluster) cluster with a dominant cD galaxy, NGC 4696. Figure 2.15 shows the PSPC image of the Centaurus cluster in the 0.5–2 keV band. The Centaurus cluster has been intensively studied in X-rays with *UHURU* (Giacconi et al. 1972), *HEAO 1* (Mitchell and Mushotzky 1980), *Einstein* (Matilsky, Jones, and Forman 1985), EXOSAT

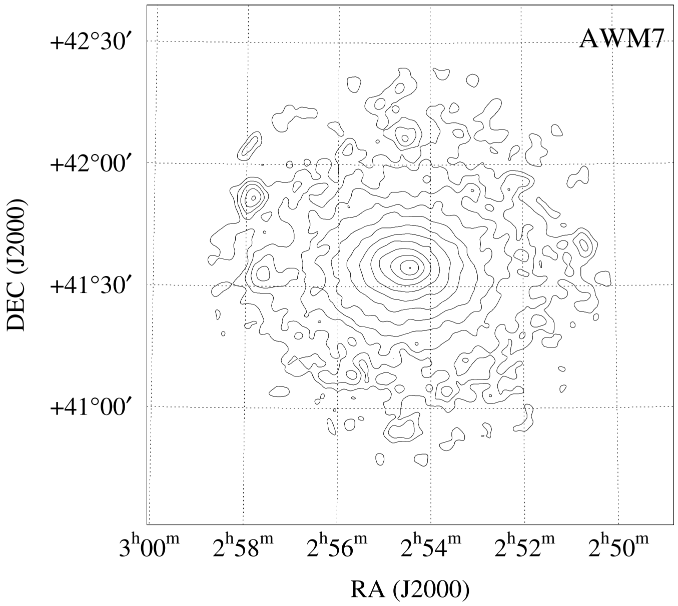

Figure 2.12: The PSPC image of the AWM7 in the energy range 0.5–2.0 keV.

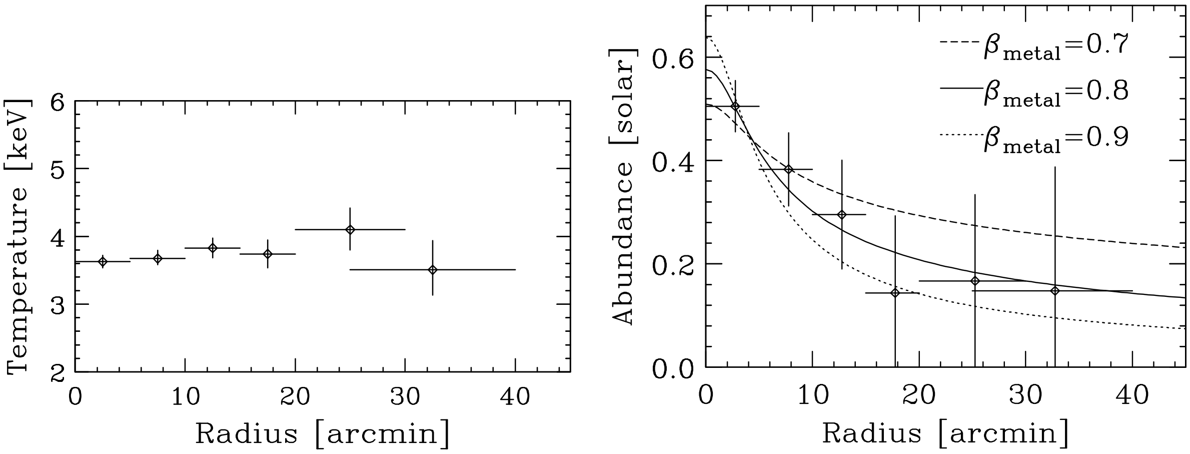

Figure 2.13: Temperature and abundance distributions of AWM7 within a radius of 40′ obtained from ASCA mapping observations (Ezawa et al. 1997).

(Edge and Stewart 1991), *Ginga* (Yamashita 1992), ROSAT (Allen & Fabian 1994), and ASCA (Fukazawa et al. 1994; Ikebe et al. 1999; Churazov et al. 1999). Figure 2.16a shows ASCA results of the emission-measure profiles of the hot and cool component in the central region by Ikebe et al. (1999). The cool component dominates considerably, however, the hot component also exists. The metal abundance profile also shows a central concentration as shown in 2.16b. That significantly implies that the metal distribution accompanies with the cD galaxy.

The presence of the central concentrated cool component suggests that the Centaurus

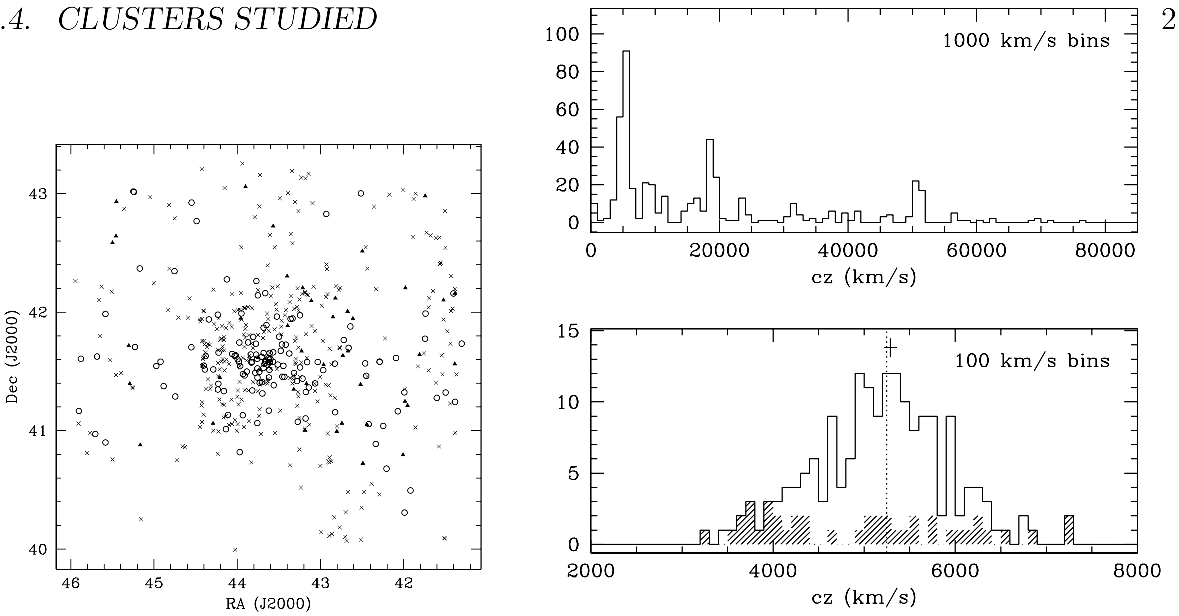

Figure 2.14: *left* – Position of the sky of all objects with measured redshifts. *right* – Distribution of the redshifts of the galaxies. (Koranyi and Geller 2000)

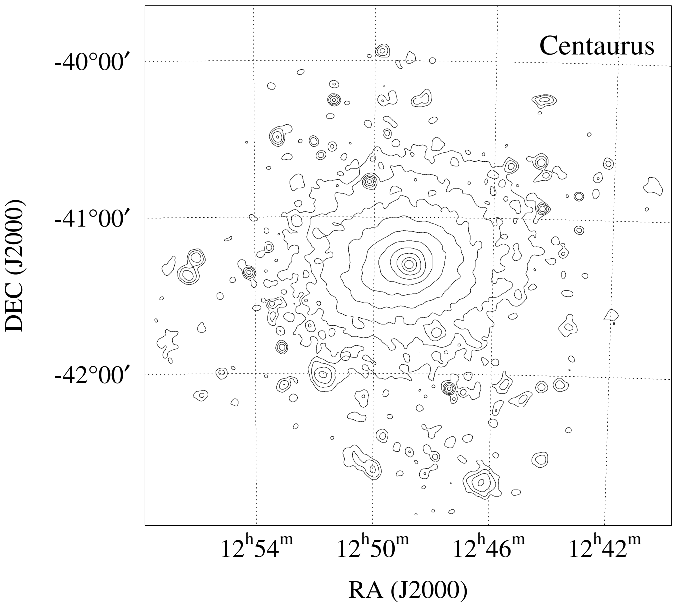

Figure 2.15: The PSPC image of the Centaurus cluster in the energy range 0.5–2.0 keV.

cluster is a relatively relaxed system. However, some results in both optical and X-rays indicate that there is an evidence of merger. Churazov et al. (1999) shows a two-dimensional map of the gas temperature distribution based on the central 4 pointings with ASCA. Figure 2.17 is the temperature map, and there is a remarkable hot region to south-east. The X-ray emission also shows the excess from the surface brightness model at the region. Furthermore, This hot region corresponds to the position of NGC4709, which is the dominant galaxy of the Cen 45 subcluster group. The member galaxies in

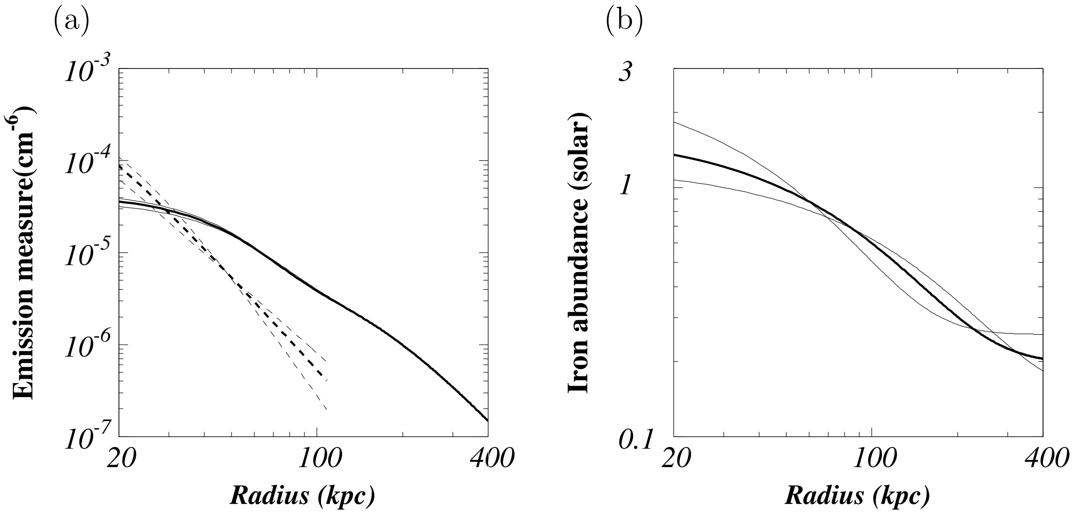

Figure 2.16: (a) Emission-measure profiles of the hot (solid lines) and cool (dashed lines) component, and (b) the iron abundance profile derived from the two-phase model fit. Thick lines show the best-fit models, while thin lines indicate extreme cases at the 90% confidence. (Ikebe et al. 1999).

the Centaurus cluster had been investigated very well by some optical photometric survey. Lucey et al. (1986) discovered a remarkable bimodal velocity distribution in the Centaurus cluster. The two velocity components were found to be roughly centered at about 3000 km s^{-1} and 4500 km s^{-1} and were denoted as Cen30 and cen45, respectively. Figure 2.18 shows the map of member galaxies and the redshift distribution by Stein et al. (1997). The mean velocity and dispersion obtained from the double Gaussian fit are 3397 km s^{-1} and 933 km s^{-1} for Cen30, and 4746 km s^{-1} and 131 km s^{-1} for Cen45. Note that NGC 4696 is at a velocity 2961 ± 26 km s^{-1}. Thus, these results imply the the smaller Cen 45 group is merging with the dominant Cen 30 group.

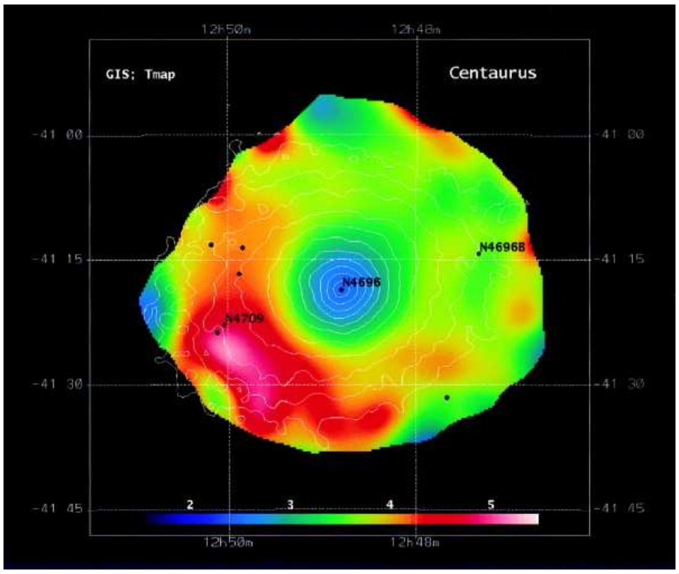

Figure 2.17: Color image of the gas temperature distribution derived from the central 4 pointings with ASCA (Churazov et al. 1999).

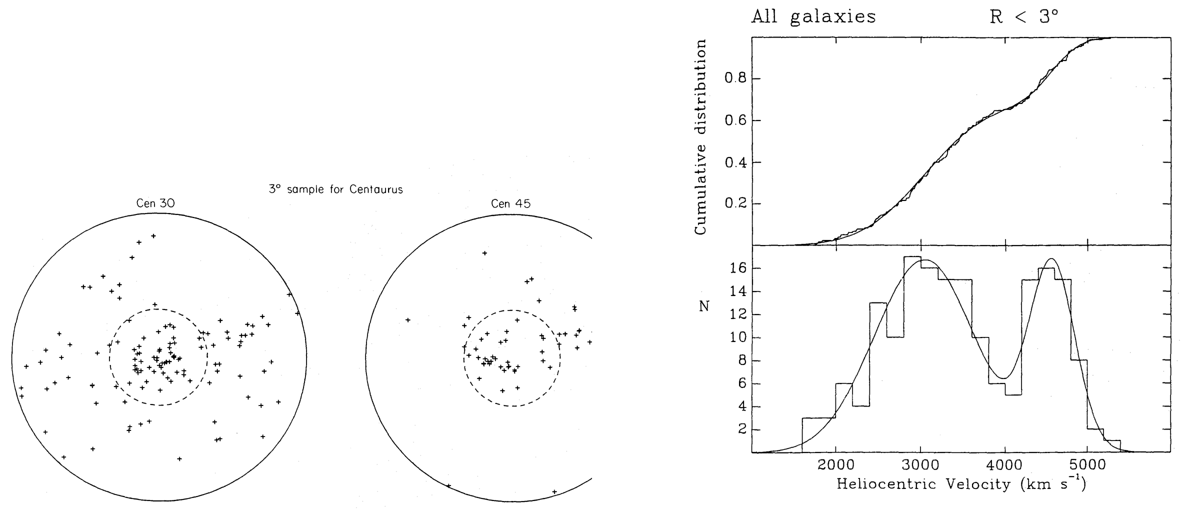

Figure 2.18: *left* – The sky distribution of the two velocity components of Cen30 and Cen45. *right* – The velocity distributions of the 3° sample with 180 galaxies (Lucey et al. 1986).

2.4.5 The Perseus cluster

The Perseus cluster (Abell 426) is the X-ray brightest cluster of galaxies at a distance of $z = 0.0183$. At the center, the cD galaxy NGC1275 is surrounded by a spectacular low-ionization, emission line nebula (Lynds 1970). The Perseus cluster has been extensively studied with the *UHURU* mission (Gursky et al. 1971; Forman et al. 1972), *Ginga* (Allen et al. 1992), SPARTAN-1 detector (Snyder et al. 1990; Kowalski et al. 1993), ROSAT (Ettori et al. 1998), and ASCA (Fabian et al. 1994; Arnaud et al. 1994; Ezawa et al. 2001). Figure 2.19 shows the PSPC image in the 0.5–2.0 keV band. This cluster forms a part of the Pisces-Perseus supercluster, that includes several other clusters, AWM7, A347, and A262. The elongated direction of the X-ray image is in parallel to the filament structure, in the same way as AWM7. Significant substructure in the PSPC image at east from the cluster center has been discussed as evidence that the cluster is not in a relaxed state and in consistent with a recent merger (Schwarz et al. 1992; Ettori et al. 1998). Ezawa et al. (2001) have examined the temperature and metal abundance distribution based on ASCA mapping observations. Figure 2.4.5 shows the temperature drop in the central region even with the 2-temperature model. The abundance distribution shows not central concentration, but large-scale gentle slope.

Kent and Sargent (1983) identified 167 member galaxies of the Perseus cluster. Figure 2.4.5 shows the distribution of radial velocities fitted with a Gaussian function. The mean velocity is found to be 5470±87 km s−1. It is seen that the velocity dispersion drops from ~ 1300 km s^{-1} at the center to ~ 600 km s^{-1} at the radius of $r = 136'$. Brunzendorf and Meusinger (1999) also compiled a catalogue of 660 galaxies within a field of about

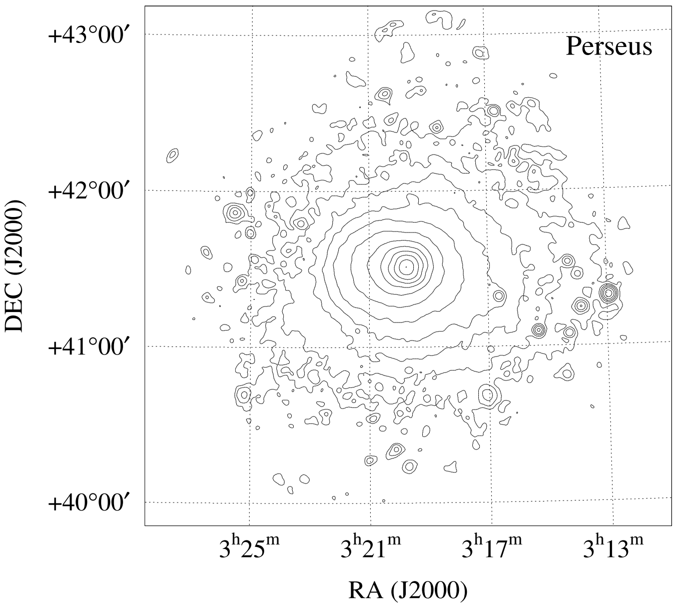

Figure 2.19: The PSPC image of the Perseus cluster in the energy range 0.5–2.0 keV.

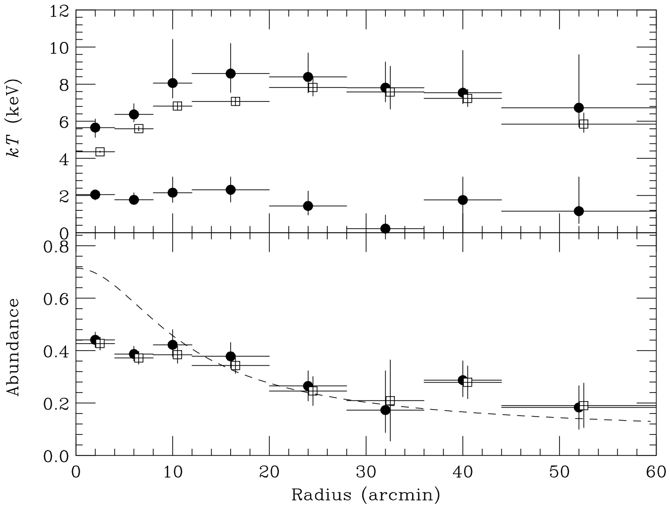

Figure 2.20: Temperature and abundance distributions of Perseus within a radius of 60′ obtained with ASCA (Ezawa et al. 2001). The open and filled circles show the results of the single-temperature and the 2-temperature fit, respectively.

10 square-degrees. In the region of the eastern X-ray excess, they find a significantly higher fraction of spiral and irregular galaxies compared with the morphological mix of the galaxies on the opposite side of the X-ray center.

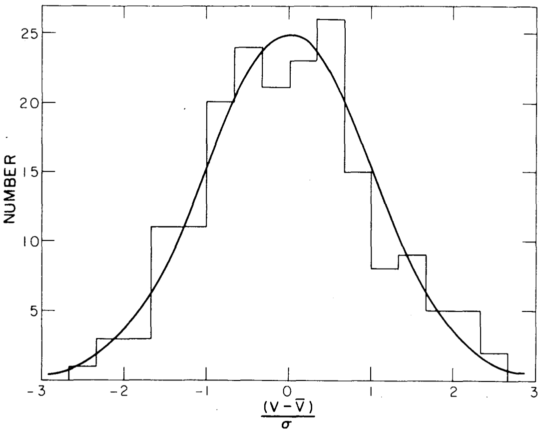

Figure 2.21: The radial velocity distributions in the Perseus cluster normalized to the local velocity dispersion (Kent and Sargent 1983)

Chapter 3

Instrumentation

This thesis is based on analyzing data that were obtained from observations of X-ray astronomy satellite, ASCA. In this chapter, we briefly summarize the design and performance of each instruments onboard ASCA.

3.1 The ASCA Satellite

ASCA (Advanced Satellite for Cosmology and Astrophysics) is the forth Japanese X-ray astronomy satellite (Tanaka et al. 1994) following Hakucho (1979), Tenma (1983) and Ginga (1987). ASCA was launched on February 20, 1993 using the three-stage solid-propellant M-3SII-7 rocket from Kagoshima Space Center of ISAS, and achieved a near-circular orbit with a perigee of 520 km, an apogee of 625 km, and an inclination of 31°. Figure 3.1 shows the in-orbit configuration of ASCA. It weighs 420 kg, and has an octagonal-shaped body of a diameter 1.2 m where six solar panels are attached. ASCA re-entered the atmosphere on March 2, 2001, the day after Prof. Minoru Oda passed away.

ASCA is equipped with four X-ray telescopes (XRTs) at the top of an extendible optical bench. X-rays that the XRTs correct with the large effective areas are focused on four position-sensitive X-ray detectors; two SIS (Solid-state Imaging Spectrometer) detectors called SIS0 and SIS1, and two GIS (Gas Imaging Spectrometer) detectors called GIS2 and GIS3.

3.2 X-ray Telescope (XRT)

The XRT onboard ASCA has enabled cosmic X-ray imaging studies above energies of a few keV up to 10 keV for the first time (Serlemitsos et al. 1995). Soft X-rays are totally reflected off a smooth surface, when their incident angle measured from the surface is shallower than a certain critical value. This phenomenon is known as grazing-incidence reflection. The critical angle, typically of order 1 degree or so, is inversely proportional

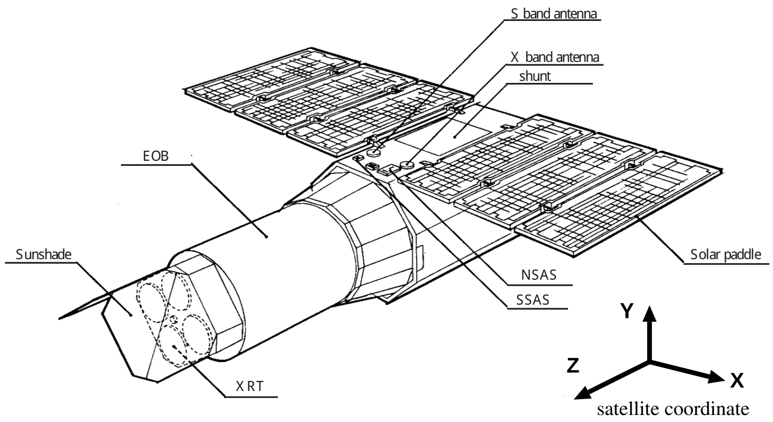

Figure 3.1: In orbit configuration of the ASCA satellite

Table 3.1: Design parameters and performance of the ASCA XRT.

Focal length	3500 mm
Incident angle	0.24° – 0.7°
Geometrical area	558 cm^2 / telescope
Field of view	$\sim 24'$ (FWHM at 1 keV) / $\sim 16'$ (FWHM at 7 keV)
Energy range	$\lesssim$ 10 keV
Effective area of four XRTs	$\sim$ 1300 cm^2 (1 keV) / $\sim$ 600 cm^2 (7 keV)
Half power diameter	$\sim$ 3 arcmin

to the X-ray energy and increases with increasing free electron density of the reflecting material. X-ray telescope mirrors use this mechanism usually in so-called Wolter type I configuration, which employs paraboloid and hyperboloid surfaces as the primary and the secondary mirrors so as to remove the first-order aberration. The two mirrors have a common focus and reflect X-rays in series (double reflection).

The reflector shells of the ASCA XRT are all made of thin (127 μm) aluminum foils, bent in a conical form to approximate paraboloid or hyperboloid. The bent foils are $\sim$ 10 μm lacquer-coated to improve the surface smoothness, and then $\sim$ 50 nm gold-evaporated to increase the reflectivity. The 120 of these foils are closely packed together in an onion-ring configuration with a typical spacing of 1 mm, to cover a large fraction of the mirror aperture. The innermost and the outermost shells have diameters of 120 mm and 345 mm, respectively. In practice, the foils are produced and packed in four quadrants, and aligned by 13 alignment bars into 14 sectors. The first and the last sector is masked because shape error is severe. Four quadrants make up the "paraboloid" section of 100 mm long, and another set of four quadrants make up the "hyperboloid" section. One XRT unit thus fabricated weighs about 9.8 kg. Design parameters and performance of the XRT are shown in table 3.1.

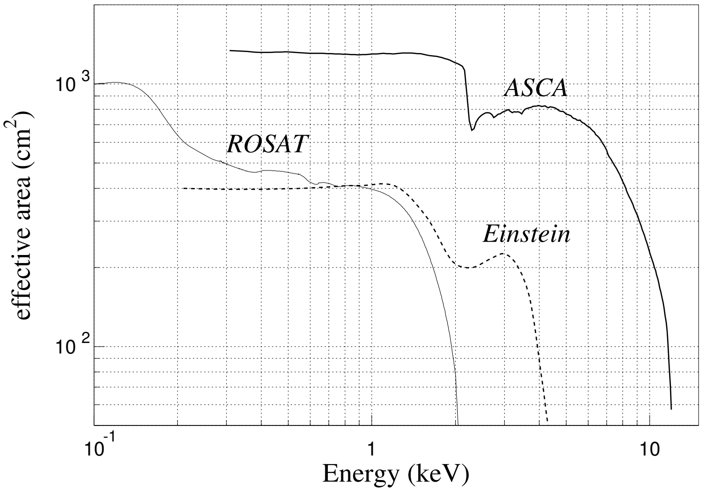

Figure 3.2: Effective area of the ASCA XRT (4 XRTs summed up, on-axis) compared with that of polished mirrors used in previous missions.

The XRT has successfully achieved a very large effective area and a wide energy range, as shown in figure 3.2. When the four units are summed up, the effective area reaches ~ 1100 cm^2 below ~ 2 keV, almost by a factor of 6 and 2 larger than those of Einstein and ROSAT respectively. A sudden drop in the reflectivity at 2.2 keV is caused by the M-edge of the gold used as reflective coating. The XRT maintains a very large reflecting area towards higher energies, e.g. ~ 600 cm^2 at 7 keV, with the upper energy bound as high as ~ 10 keV. X-ray imagery above 3–4 keV has never been achieved by polished mirrors used in previous missions.

Although the XRT has a large effective area even at ~ 10 keV, it sacrifices the imaging quality: large-extended point spread function, and stray light which comes from outside of the field of view caused by abnormal reflection. These effects on our analysis are described in section 4.1.

3.3 Solid-state Imaging Spectrometer (SIS)

The SIS experiment is the first X-ray sensitive charge coupled devices (CCDs) detector system in orbit. Figure 3.3 shows a cross section view of the SIS camera. The SIS system consists of two detectors, SIS0 and SIS1, and each SIS detector is made up of four CCD chips of 11 mm square. The 4 CCD chips are aligned in square with narrow gaps to cover about $20' \times 20'$ square region on the sky. Each chip has 4096 by 4096 pixels of 27 μm square each, and a depletion layer of about 40 μm thick which ensures an improved efficiency for harder X-rays than conventional CCDs. Design parameters and performance of the SIS in brief are summarized in table 3.2.

Figure 3.4a illustrates the quantum efficiency of the SIS as a function of incoming X-ray energy. Thus the SIS sensitivity covers approximately 0.4–10 keV. The CCD chips and preamplifiers are cooled down to -60 °C with a thermo-electric cooler (TEC) from the backside of the chips in order to reduce thermal noise down to $N \sim 5$ electrons level.

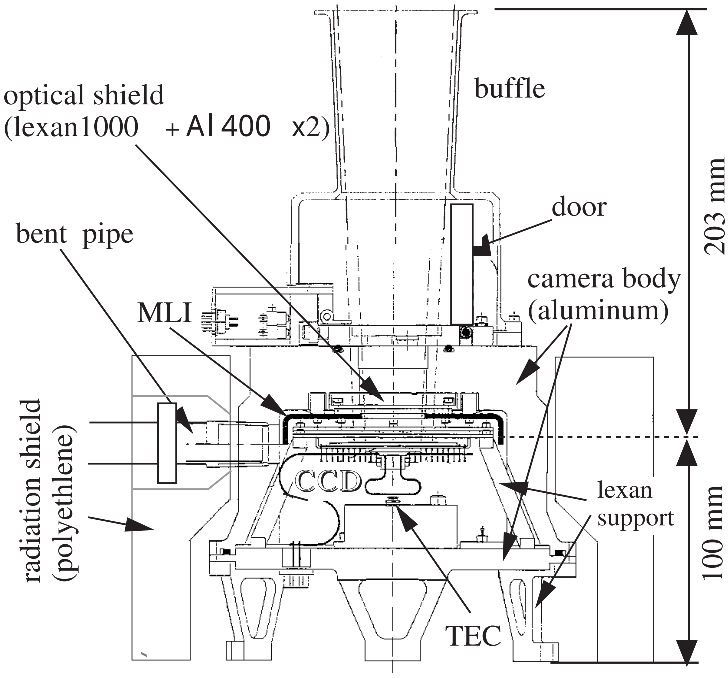

Figure 3.3: Cross section view of the SIS camera

Table 3.2: Design parameters and performance of the SIS

Energy Band	0.4–12 keV
Energy Resolution	2% at 5.9 keV (FWHM)
Effective Area	11×11 mm square per chip
Optical Blocking Filter	100 nm Lexan film coated with 40 nm aluminum
Number of pixels in Image Region	420 pixels × 422 lines per chip
Pixel Size	27 μm
Thickness of Depletion Layer	$\sim$ 40 μm

Thus the SIS achieves an energy resolution of about 150 eV FWHM over the whole energy range (figure 3.4b); this is the best energy resolution ever achieved by non-dispersive X-ray spectrometers so far put into orbit.

3.4 Gas Imaging Spectrometer (GIS)

The GIS is the imaging gas scintillation proportional counter (Makishima et al 1996; Ohashi et al. 1996). The application of the gas scintillator technique to the Japanese X-ray satellite is the second attempt after the successful operation of the SPC experiment on board Tenma (Tanaka et al. 1984; Koyama et al. 1984). The GIS is a general-purpose X-ray imaging spectroscopy system. It consists of the two detector assemblies, namely

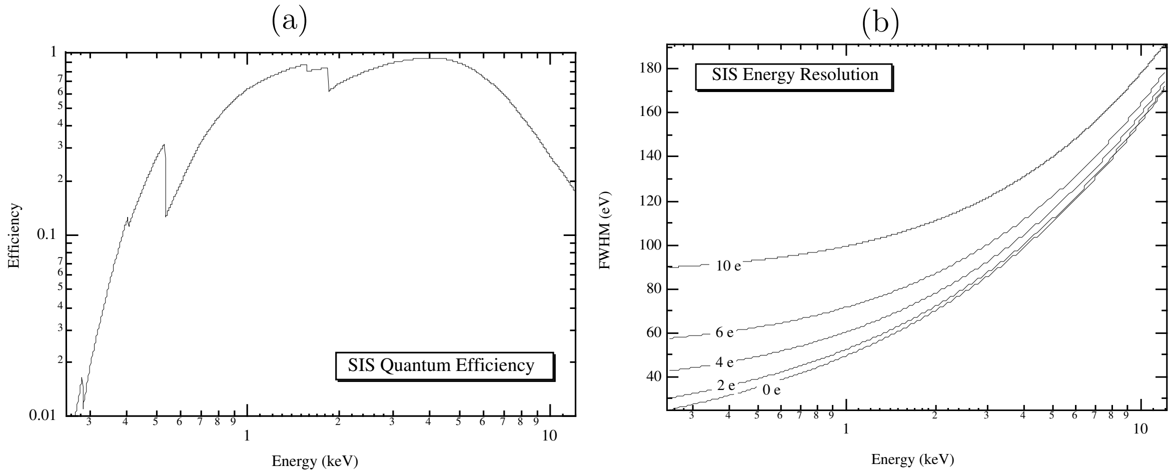

Figure 3.4: (a) Detection efficiency of the SIS as a function of incoming X-ray energy. K-edges of O (0.53keV), Al (1.56keV), and Si (1.84keV) are clearly seen in the figure. This efficiency does not includes optical blocking filter. (b) Energy resolutions of the SIS as a function of incoming X-ray energy for the single event. Energy resolutions with different read-out noise N are plotted ($N \sim 5$ for the SIS). The read-out noise levels are given as the equivalent number of electrons.

GIS2 and GIS3 serving as X-ray detectors. The GIS2 and GIS3 are coupled to two of the four XRTs, and measure pulse-heights and positions of X-rays reflected by the XRTs, photon-by-photon basis.

Figure 3.5 shows a schematic view of the GIS sensor system. X-rays reflected by the XRT enter through the window, whose electric potential is held at −6000 V, and are absorbed in the drift region. Through photo-ionization, primary electrons are generated on average at the rate of one electron per 21.5 eV. The electron cloud thus created slowly drifts to the intermediate mesh (−5300 keV), and then the cloud is accelerated due to the strong field toward the ground mesh which is placed in front of the quartz window. In this process, the electrons excite Xe and produce a large number of UV photons of $\sim$ 170 nm wavelength. The excitation energy for one UV photon is $\sim$ 10 eV. Through the quartz window, these UV photons are collected by the imaging photo-multiplier tube (IPMT) which measures light distribution and the overall intensity of UV flux, which is proportional to the X-ray energy with accuracy of several %. We can obtain the position information from the anode signals, and derive the pulse-hight (PH) and the rise-time (RT) information from the last dynode. Design parameters and performance of the GIS are summarized in table 3.3, and detection efficiency and energy resolution are shown in figure 3.6.

There are a number of monitor data in the GIS system to support monitoring its proper function and to help estimation such as background and dead time (Ohashi et al. 1996). In the PH vs. RT plane, there are 6 scalers which measure the monitor counts (see figure 3.7). The upper PH discriminator sets one threshold line, and lower and upper

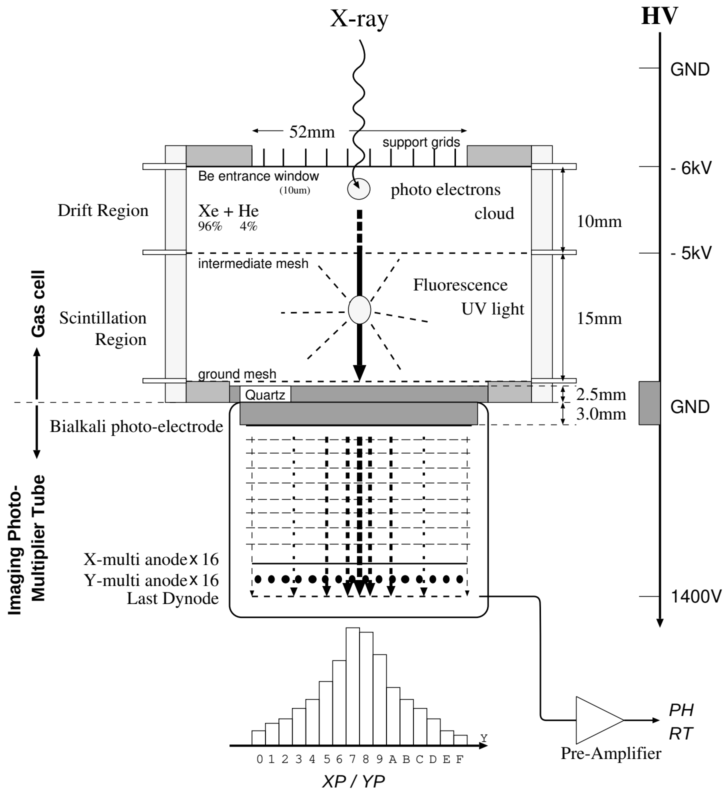

Figure 3.5: Schematic view of the GIS sensor system

Table 3.3: Design parameters and performance of the GIS

Energy Band	0.7–15 keV
Energy Resolution	8% at 5.9 keV (FWHM) ($\propto E^{-0.5}$)
Effective Area	50 mm diameter
Entrance Window	10 μm beryllium
Absorption Material	Xe (96%) + He (4%), 10 mm depth, 1.2 atm at 0 °C
Positional Resolution	0.5 mm at 5.9 keV (FWHM) ($\propto E^{-0.5}$)

RT discriminators make two lines. These discriminators create 6 regions, L0, L1, L2, H0, H1, and H2. The events within the L1 region are allowed as proper X-ray signals by the hard-wired login in the GIS system.

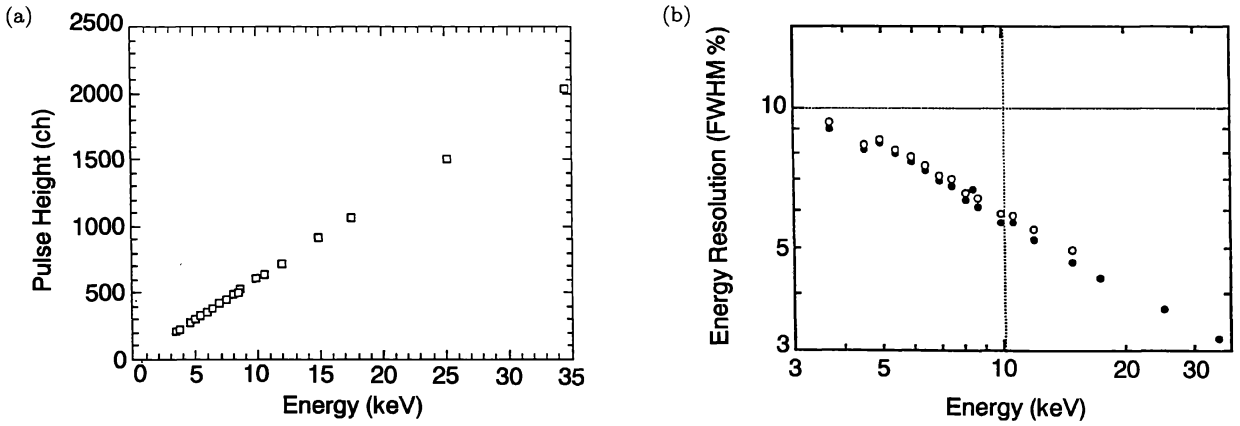

Fig. 10. (a) Linearity and (b) energy resolution are shown as a function of energy. The data were obtained using a pre-flight model detector.

Figure 3.6: (a) Detection efficiency of the GIS as a function of energy. Absorption due to plasma shields in the GIS housing and due to thermal shield in front of the XRT are included in the actual observation. (b) Energy resolutions of the GIS as a function of energy.

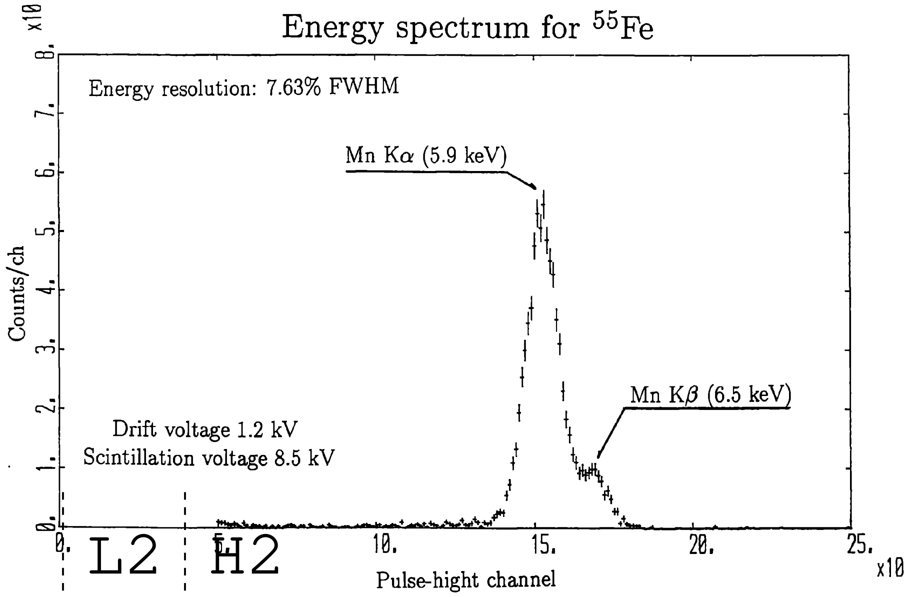

Fig. 11. Pulse-height distribution for 5.9 keV X-rays obtained with a pre-flight detector with a total high voltage of 8.5 kV. The minimal high voltage value used in the orbit is 6 kV.

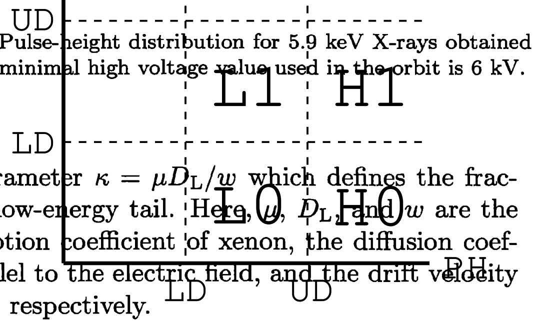

Figure 3.7: Schematic view of the 6 monitor data in the PH vs. RT plane.

and one parameter $\kappa = \mu D_L/w$ which defines the fraction of the low-energy tail. Here, μ, D_L, and w are the mass absorption coefficient of xenon, the diffusion coefficient parallel to the electric field, and the drift velocity of electrons, respectively.

The low-energy tail becomes more prominent for larger values of κ, namely for shorter X-ray mean free path in the gas and slower drift velocity. The model can explain the change of the fraction of the low-energy tail as a function of the high voltage in the gas cell. However, absolute fraction of the tail indicates a three times higher value of κ than that estimated from the diffusion constants given in Dutton (1975). The reason is still unclear. Also, the apparent cut-off feature in the low-energy end (below about 0.3 keV) of the tail is not well-explained by the present model.

In order to minimize the low-energy tail, the field strength in the drift region of the gas cell has been raised within the range that no light emission occurs. The observed pulse-height distributions above 0.5 keV have been successfully modeled by the present model function using empirical κ parameters. As described in Makishima

Chapter 4

Response Construction and Background Estimate

The aim of this thesis is to investigate detailed temperature structure of 4 nearby clusters by a spectral imaging analysis with the ASCA GIS mapping observation data. For such diffuse, extended objects, a complex response of the XRT causes serious problems to obtain exact temperatures, and also a special technique is required to estimate background. In this chapter, we describe ray-tracing simulation and data reduction methods to get over these difficulties on analysis.

4.1 XRT Response for extended sources

The response of ASCA XRT depends on energy and position of incident X-ray photons. Main issues of the XRT imaging capability are the point spread function (PSF) and stray light, which make the analysis of extended sources particularly difficult. The PSF causes artificial temperature and abundance increasing in the data of cluster of galaxies toward outer rings. Furthermore, The spectrum accumulated over specified areas on the detector is more or less contaminated by photons which comes from other areas of the object. To recover those problems, we performed ray-tracing simulations for response reconstruction. In the following subsections, we explain the characteristics of the PSF and the stray light, and how the response is built.

4.1.1 Point Spread Function (PSF)

The PSF of the ASCA XRT has largely extended wings due to waving (shape error) of the thin aluminum foils, as well as to the conical approximations of paraboloid (primary mirror) and hyperboloid (secondary mirror) surfaces. When an observed target is a point source of which angular size is much less than the resolution of the XRT, $\sim 1'$, the extent can be regarded as the XRT PSF.

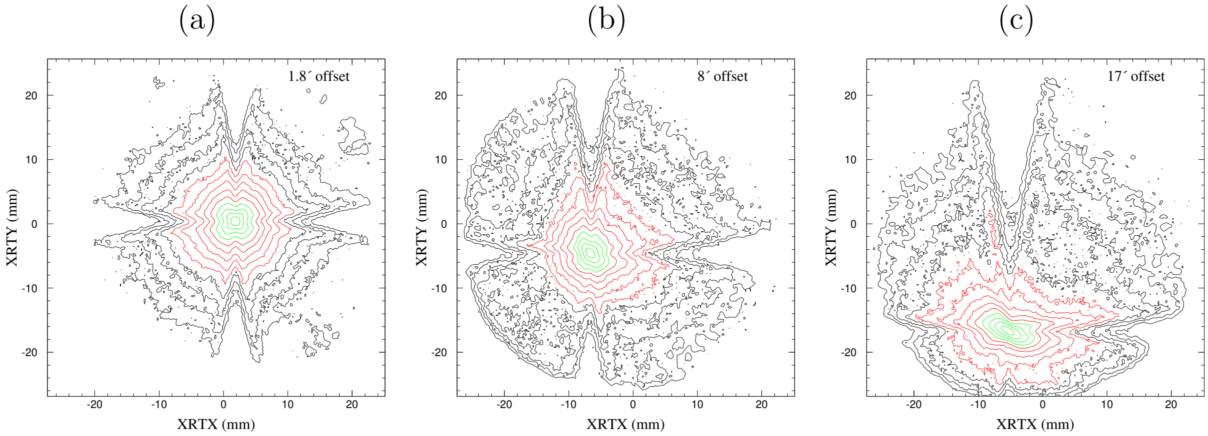

Figure 4.1: Observed Cyg X-1 images taken by GIS2 as examples of the XRT PSF. (a) 1.8′ offset, (b) 8′ offset, and (c) 17′ offset in the 0.5–12 keV energy band. Contour levels are every factor of 2, and origins of the coordinates are the optical axis of GIS2.

Sufficient knowledge of the PSF is an important issue on analysis of the clusters with ASCA. Based on multi-pointing observations of the Cyg X-1, which is one of the brightest point-like source with a hard spectrum, the characteristics of the PSF have been examined (Takahashi et al. 1994; Ikebe 1995; Takahashi et al. 1995; Ikebe et al. 1997). Figure 4.1 show the Cyg X-1 images taken by GIS2. Although the PSF has a more sharply peaked core intrinsically, it is broadened to some extent in the image by the finite position resolution of the GIS. The PSF has four butterfly-like wings, which reflect the quadrant structure of the XRT, with significant flux extending almost over the whole GIS field of view. Horn like structures seen on the edges of the four wings are caused by the large distortion of the conical shape at the outermost sector of each quadrant. As θ (distance from the optical axis) gets larger, the PSF shape is distorted, as characterized by a squeezing into the radial direction and an increase in the fraction of wings. Moreover, these effects are all energy-dependent. The PSF has wider outskirts in the higher energy bands. This is mainly due to the scattering of incident X-rays by the micro-roughness of the foil surface, which generally increases with X-ray energy.

All these properties complicate the analysis of extended sources. Figure 4.2 shows radial profiles of temperature and abundance assuming isothermal clusters, the PSF characteristic causes artificial increase of temperature and abundance values toward outer regions . The temperature increase of 5 keV isothermal cluster is about 60% at $r = 20'$, whereas the maximum fluctuation of the best-fit photon index for Crab offset observations is 2% within a radius of $22'$, as shown in Figure4.3.

In order to correct the PSF effects, we perform ray-tracing simulation, which calculates the position of X-ray photons on the focal plane by inputting energy and incidence angle of Monte-Carlo photons. (Tsusaka et al. 1995; Kunieda et al. 1995) Figure 4.4 shows examples of the radial brightness profile simulated by the ray-tracing, compared with the Cyg X-1 profile. It is confirmed that the ray-tracing images agree with the Cyg X-1 data

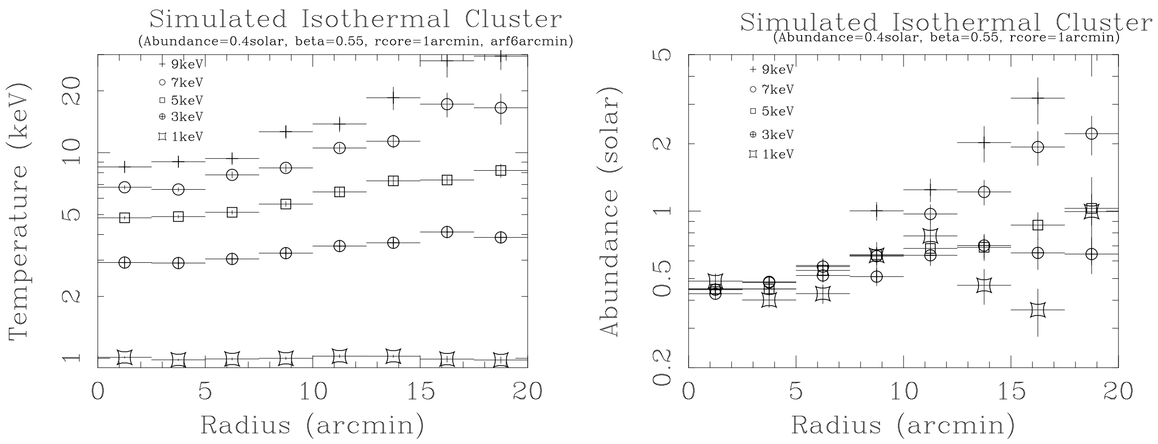

Figure 4.2: The temperature (right) and abundance (left) profiles of simulated clusters with uniform temperature and metal abundance. The spectra are made in the concentric annular regions centered on the cluster, and fitted with conventional procedure which is not taken into account the PSF effect correctly.

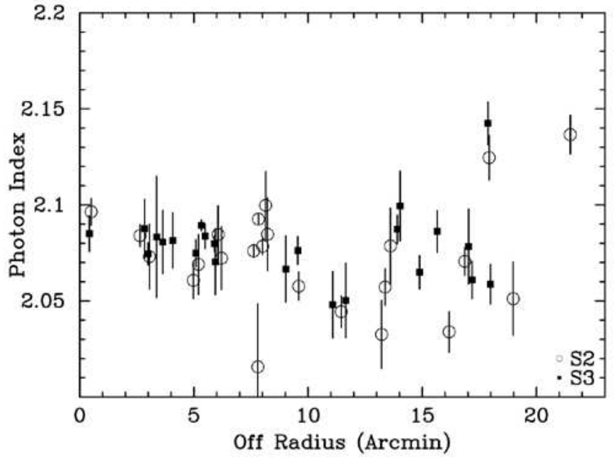

Figure 4.3: The best-fit photon index of the Crab spectra corresponding to different observing positions. Open circles and filled squares indicate GIS2 and GIS3 (Fukazawa et al. 1997).

within ~ 10% level in radial profile (Kunieda et al. 1995). The ray-tracing program is also a reliable tool to estimate the stray light (see section 4.1.2).

In-orbit XRT PSF has been studied mainly based on the multi-pointing observation of Cyg X-1. The image of the Cyg X-1 in low energy band (below 2 keV), however, is considered to be extended possibly due to the X-ray scattering by interstellar dust grains along the line-of-sight to Cyg X-1. Ezawa et al. (1997b) observed Her X-1, which located in a high Galactic latitude with small neutral column density. They confirmed that the Cyg X-1 images are more extended than the actual PSF in low energy band. We compared the radial profile of the cluster simulated by the Her X-1 image as a PSF with the cluster simulated by ray-tracing, and found that the differences between the simulated clusters are almost negligible, as far as the clusters have a extent of $\beta \lesssim 1.0$ and $R_c \gtrsim 1.0'$.

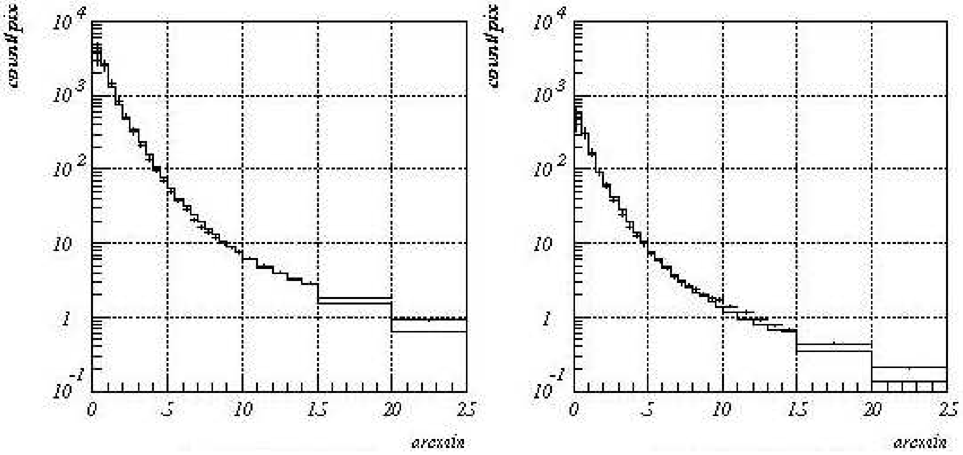

Figure 4.4: Example of radial profile of ray-tracing (solid line) compared with $8'$ offset (1CCD nominal position) Cyg X-1 data (cross) in the 2–6 keV band (left) and 6–12 keV (right) (Kunieda et al. 1995).

4.1.2 Stray light

Stray light is X-ray photons come from outside of the field of view. Those photons reach the focal plane detectors through abnormal paths, such as primary reflection only, secondary reflection only, and multiple reflection, which are not on the assumption of the Wolter type I optics. Note that this phenomenon is somewhat different from the large outskirts of the PSF. The large outskirts of the PSF are mainly due to the waving of the XRT foils, and those photons also undergo the normal sequence of the Wolter type I optics.

The effects of the stray light on the extended source analysis were extensively studied by Ishisaki (1996) for cosmic X-ray background analysis. Figure 4.5(a) shows an example of stray light images taken by GIS3. The Crab nebula is placed at the central position of the circles, $60'$ offset from the optical axis in the direction of $\phi = 45°$, $135°$, and $225°$. A shell-like image is seen spreading over the whole detector plane. The stripes represents the XRT sector structure divided by the alignment bars. X-ray images of the 4 clusters studied in this thesis are extended larger than the GIS field of view, we must take the stray light effect into account for the analysis.

A stray light image has a complex shape as seen in figure 4.5(a), and it is not easy to express it in an analytic formula. Fortunately, stray light patterns are well determined by the foil structure of the XRT. Therefore the ray-tracing program with reliable XRT parameters is expected to reproduce the stray light effects pretty well. Figure 4.5(b) shows a ray-tracing image for $\theta = 60'$ and $\phi = 225°$, which well reproduces the lower right image of figure 4.5(a). Then, using a ray-tracing program, we simulate the effects of stray lights for analysis.

Left panels of figure 4.6 show the observed spectra taken by GIS2 (upper panel) and

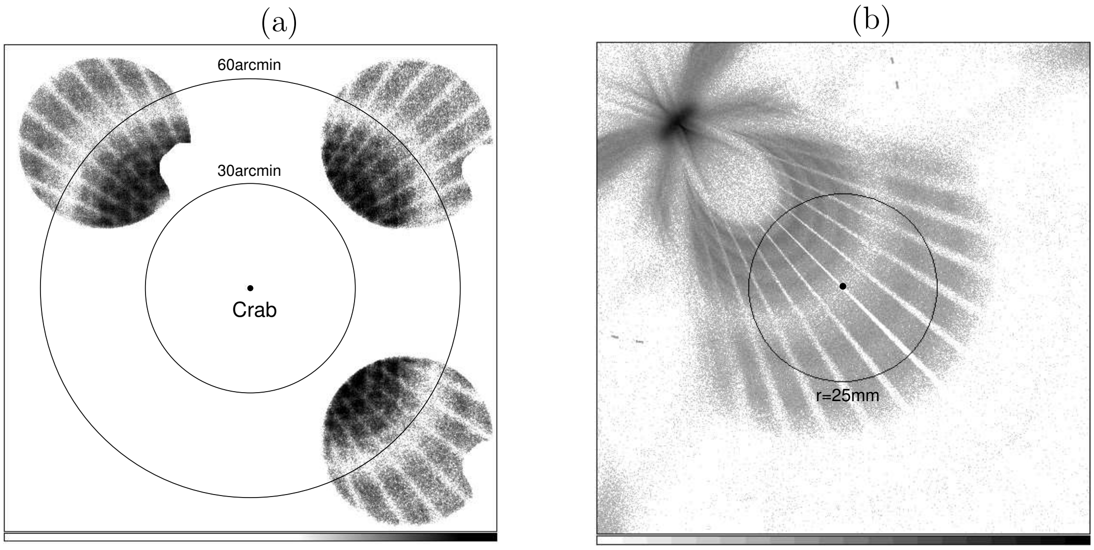

Figure 4.5: (a) Three of the Crab stray light images taken by GIS3 in the 0.7–10 keV band, shifted and superposed on the detector plane so as to reproduce correct angular relations with respect to the Crab nebula. The location of the Crab is indicated with a filled circle, and the optical axis for each observation is offset by $60'$ from the Crab. (b) Ray-tracing image of the stray light pattern at 1 keV for the offset angle $\theta = 60'$ and the azimuthal angle $\phi = 225°$. A filled circle shows a position of the optical axis. A superposed circle of $r = 25$ mm on the image corresponds to the GIS field of view (Ishisaki 1996).

GIS3 (lower panel). Right panels show the simulated spectra using the ray-tracing. We can say that the simulation roughly reproduces the spectral shape and normalization in the range of as much as five orders of magnitude. Figure 4.7 compares the counting rate from the actual observations with those based on the simulation. There seems to exist a systematic difference between GIS2 and GIS3, although the reason is still unclear. However we are thus confident that the systematic error of the simulation is about -30%–$+10\%$ within $\theta \sim 80'$, where the most part of photons come from for extended source analysis.

4.1.3 Formulation of the ASCA response

Here, we mention the response formulation of the XRT+GIS system, with some definitions of the coordinates. Let $F(\theta, \phi, E)$ be a source X-ray distribution, where θ, ϕ are the two-dimensional position on the sky, and E is the X-ray energy. θ and ϕ are defined from the optical axis of the XRT as an offset-angle and an azimuth-angle, respectively. Also, let $D(DETX, DETY, PI)$ denote the observed data, i.e. distribution of detected X-ray photons with pulse-invariant PI (gain corrected pulse-height), and detected position ($DETX$,$DETY$). There also is a coordinate called ($XRTX$,$XRTY$), the scale of which is similar to ($DETX$,$DETY$), but centered on the optical axis of the XRT and the Y-axis

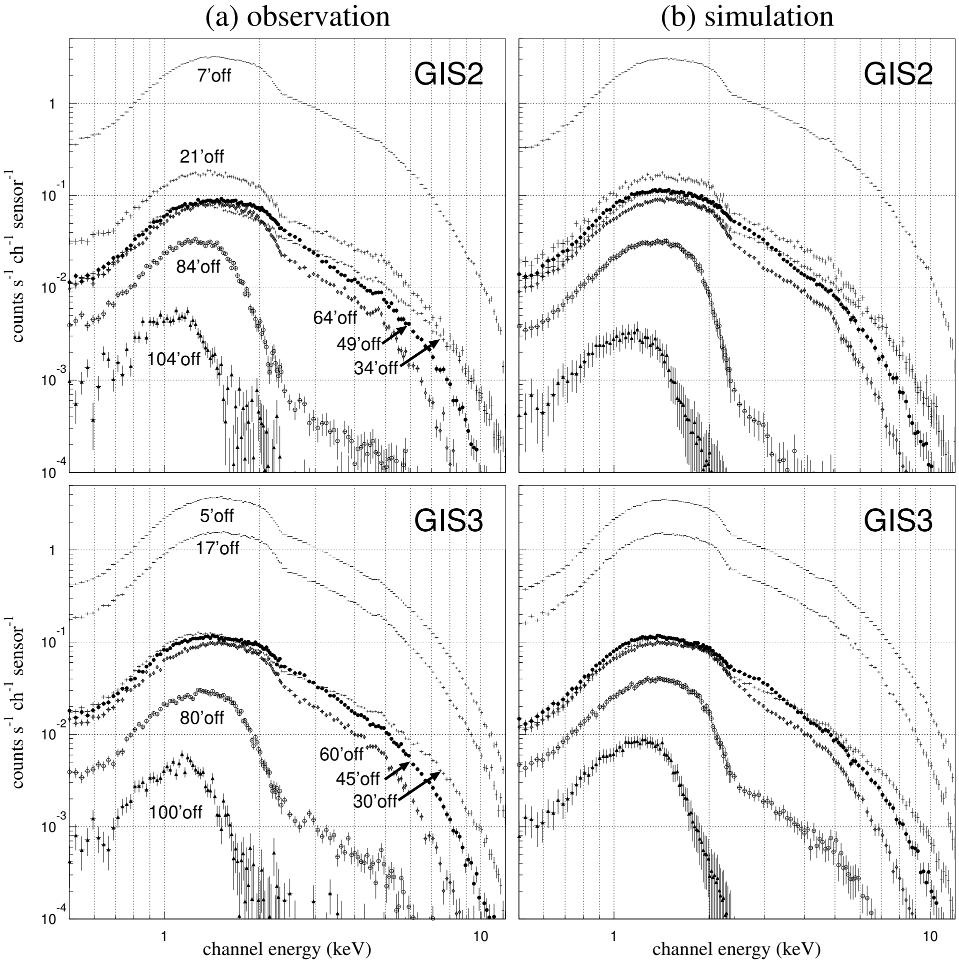
(a) observation

(b) simulation

Figure 4.6: (a) Spectra of the Crab stray observations taken by GIS2 (upper panel) and GIS3 (lower panel) integrated in the radius of 20 mm from the optical axis of each sensor. The Crab has been placed at various offset angles as specified in the figure. The CXB+NXB spectra are subtracted after dead time correction. (b) Simulated spectra of the Crab stray observations. The Crab nebula is assumed to have an absorbed power-law spectrum of $\Gamma = 2.10$, $N_{\rm H} = 3.0 \times 10^{21}$ cm^{-2}, and the power-law normalization of 9.7 c s^{-1} cm^{-2} keV^{-1} at 1.0 keV (Ishisaki 1996).

flipped. Table 4.1 is a summary of these coordinates.

$F(\theta, \phi, E)$ and $D(DETX, DETY, PI)$ are related as

$$\begin{aligned}
&D(DETX, DETY, PI) \qquad (4.1)\\
&\quad = \int dE\ R_{\rm GIS}(E, PI)\\
&\quad \times \int dx\, dy\ P_{\rm GIS}(E, x, y; DETX, DETY)\ A_{\rm GIS}(E, x, y)\\
&\quad \times \int d\theta\, d\phi\ P_{\rm XRT}(\theta, \phi, E; x, y)\ A_{\rm XRT}(\theta, \phi, E)\\
&\quad \times A_{\rm T.S.}(E)\\
&\quad \times F(\theta, \phi, E),
\end{aligned}$$

where (x,y) is the position on the entrance window of the GIS, and the meaning of

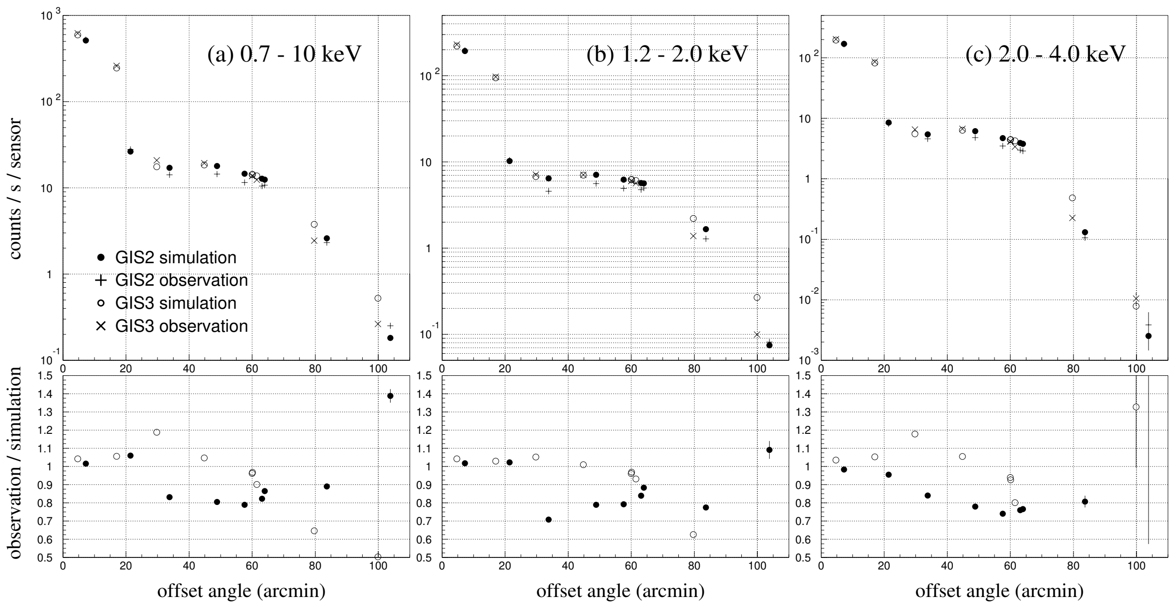

Figure 4.7: Upper panels show counting rates of the Crab stray observations and the ray-tracing simulations in (a) 0.7–10 keV, (b) 1.2–2.0 keV, and (c) 2.0–4.0 keV energy band, plotted versus offset angle of the Crab nebula. Lower panels show the ratios of observation to simulation (Ishisaki 1996).

Table 4.1: Summary of the coordinates

Notation	Figure label	Unit	Comments
E	Energy	keV	Energy of the incident X-ray
PI	channel energy	ch	500 ch = 5.8942 keV, starts from 0 ch
θ	offset angle	arcmin	offset angle from the optical axis
ϕ	azimuth angle	degree	measured clock-wise from X-axis on detector plane
$DETX$	detector coordinates	mm	1 mm = 4 ch = $0.9822'$, centered the detector cen-
$DETY$		ch	ter. (0, 0) mm corresponds to (128.5, 128.5) ch
$XRTX$	XRT coordinates	mm	1 mm = 4 ch = $0.9822'$, centered the optical axis.
$XRTY$		ch	Y-axis flipped to the detector coordinate

each factor constituting the response is summarized in table 4.2. In particular, we usually integrate the data $D(DETX, DETY, PI)$ over a specified area Ω on the detector to obtain a spectrum $H(PI; \Omega)$, as

$$H(PI; \Omega) = \int_{\Omega} dDETX\, dDETY \;\; D(DETX, DETY, PI). \tag{4.2}$$

The method of spectral fitting is a procedure of finding a set of parameters for $F(\theta, \phi, E)$ which give the most similar model spectrum $H(PI; \Omega)$ to the observed PI spectrum.

If the target is a point source or has a uniform spectral shape even the target extended

Table 4.2: Summary of factors constituting the response function

Notation	Description
$A_{\rm T.S.}(E)$	transmission of the thermal shield
$A_{\rm XRT}(\theta,\phi,E)$	effective area of the XRT
$P_{\rm XRT}(\theta,\phi,E;x,y)$	point spread function (PSF) of the XRT
$A_{\rm GIS}(E,x,y)$	quantum efficiency of the GIS
$P_{\rm GIS}(E,x,y;DETX,DETY)$	point spread function (PSF) of the GIS
$R_{\rm GIS}(E,PI)$	energy redistribution matrix for the GIS

in the effective integration region on the sky, $F(\theta,\phi,E)$ can be factorized as $F(\theta,\phi,E) = B(\theta,\phi)\,S(E)$, where $B(\theta,\phi)$ is a surface brightness profile and $S(E)$ is a spectrum. Then, equation (4.1) will have a simpler form of

$$H(PI) = \int dE\ R_{\rm GIS}(E,PI)\ A_{\rm XRT+GIS}(E)\ S(E) \tag{4.3}$$

where:

$$A_{\rm XRT+GIS}(E) = \int_\Omega dDETX\,dDETY \tag{4.4}$$

$$\times\quad A_{T.S.}(E)\int dx\,dy\ P_{\rm GIS}(E,x,y;DETX,DETY)\ A_{\rm GIS}(E,x,y) \tag{4.5}$$

$$\times\quad \int d\theta\,d\phi\ P_{\rm XRT}(\theta,\phi,E;x,y)\ A_{\rm XRT}(\theta,\phi,E)\ B(\theta,\phi) \tag{4.6}$$

$R_{\rm GIS}(E,PI)$ is called an RMF (energy Redistribution Matrix File) and $A_{\rm XRT+GIS}(E)$ is called an ARF (Auxiliary (or Ancillary) Response File). Note that the RMF is determined only by the elementary process of the detector, and that only one RMF for one detector is sufficient for all the analysis. To be accurate, the RMF of the GIS slightly depend on a position of incoming X-rays, but in most case it is negligible. We should rebuild only ARFs when changing the target position or the integration area.

4.1.4 SimARF

As in section 4.1.3, we represent the obtained spectra well in the form of equation 4.3 if the target has a uniform spectral shape. To obtain $A_{\rm XRT+GIS}(E)$ in equation 4.3, we used SimASCA which is an ASCA simulator developed mainly by M. Hirayama, Y. Ishisaki, T. Kotani, and Y. Ogasaka (SimASCA Working Group). We generate a number of Monte-Carlo photons of energy E according to the surface brightness distribution $B(\theta,\phi)$, run the XRT+GIS simulator, and count photons that come into the integration area on the detector plane. We can expect that $D_{\rm XRT}\times(N_{\rm detect}/N_{\rm gen})$ gives the value of $A_{\rm XRT+GIS}(E)$ in equation 4.3, where $N_{\rm gen}$ is number of the generated Monte-Carlo photons, $N_{\rm detect}$ is number of detected photons, and $D_{\rm XRT}$ is geometrical aperture of the XRT. The Monte-Carlo error Δ of this value is expected to be $\Delta/A_{\rm XRT+GIS}(E) =$

$[(N_{\rm gen} - N_{\rm detect})/(N_{\rm gen} \cdot N_{\rm detect})]^{1/2}$. We continue generating the Monte-Carlo photons of energy E, until this error ratio becomes typically less than 5%. M. Hirayama, H. Honda, and R. Shibata (SimARF team) have developed a code doing this procedure, and they named it SimARF. The SimARF has already been used for the analysis of clusters of galaxies, such as Coma, AWM7, Virgo, etc. (Honda et al. 1996; Ezawa et al. 1997; Kikuchi et al. 2000).

The XRT simulator is the key module for making ARFs. We selected the ray-tracing program as the XRT simulator, which can take into account the stray light effects in a natural way. This ray-tracing program is released by the XRT team and also used to make the pre-calculated XRT tables for the effective area and the PSF. As seen in the previous section, the ray-tracing program has sufficient accuracy and reliability in quantifying the stray light effects on the extended source analysis.

Figure 4.8 shows examples of the point source ARFs and the uniformly extended source ARFs created by the SimARF. The main difference is that the extended source ARF has much less effective area in higher energy bands than the ARF at 1CCD nominal position, because of both vignetting and the soft spectra of stray lights. Then, if we fit the spectrum from extended sources using the ARF at 1CCD nominal position, the temperature is underestimated by ~ 0.2 keV for $kT = 2.0$ keV thermal bremsstrahlung, or the photon index is overestimated by ~ 0.2 for $\Gamma = 1.7$ power-law emission.

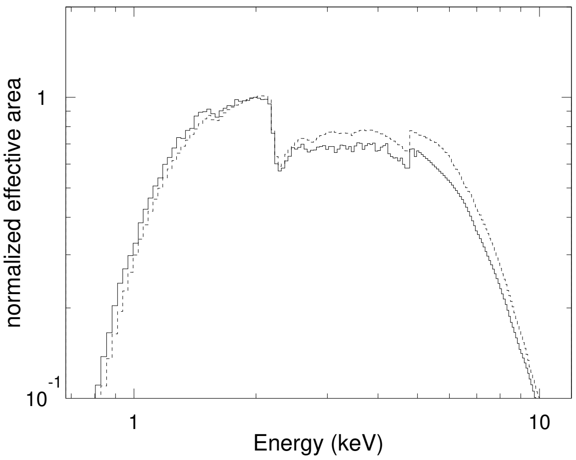

Figure 4.8: Plot of the GIS2 ARF for a point source and uniformly extended source. Solid line shows the uniformly extended source ARF with integration radius 20 mm, and dashed line shows the point source ARFs at 1CCD nominal position with integration radius 6 mm. Both ARFs are normalized to 1.0 at 2.0 keV.

4.2 Background estimate and data reduction

An estimate of the background precisely is essential procedure to derive accurate physical quantities, such as temperature and abundance, in a low surface brightness region. Figure

4.9 shows the average night-earth and the cosmic X-ray background (CXB) spectrum, presented together with the day-earth spectrum. The count rate and spectrum of the GIS background which includes non X-ray background (NXB) and CXB depends on various parameters such as cutoff rigidity, and satellite orbit. The properties of the GIS background have been extensively studied by many people (Kubo 1994; Ikebe 1995; Ishisaki 1996). Based on their results, we could estimate the CXB and NXB with a systematic error of ~ 10 %. In following sections, we briefly summarize the background estimate and subtraction methods.

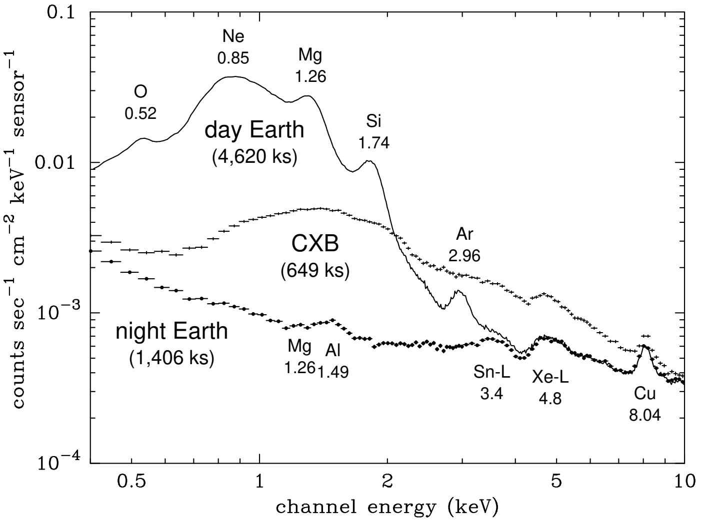

Figure 4.9: Integrated spectra of the day-earth (smooth line), the CXB (crosses), and the night-earth (filled circles) observations taken by the GIS2+3. Each of exposure time is given in the parentheses. The CXB and the day-earth spectra contains NXB. Possible origin of the line feature with the energy in keV are also given in the figure.

4.2.1 Non X-ray Background (NXB)

Since the NXB cannot be distinguished from the real X-ray events, we utilize the night-earth data, i.e. events obtained when the XRT was pointing to the night-side of the Earth, to study the NXB properties. Although there is a possibility of oxygen line or harder X-rays from aurora, we assume that the night-side of the Earth emits no X-rays; hence we believe that the night-earth data consist solely of NXB.

The properties of the NXB is well studied by Ishisaki (1996). For our analysis, we can extract the NXB spectrum based on this method. Since the NXB as a long-term variability, as seen in following section, we reproduced the database of night-earth observation from June 1993 to May 2000, and re-calculated scaling factor for the long-term correction for our analysis.

Flare event cut

Time variation of NXB is predominantly correlated with geomagnetic cutoff rigidity (COR) for cosmic rays along the satellite orbit. COR defines the minimum momentum of charged particles that can penetrate against electro-magnetic force due to terrestrial magnetism. Figure 4.11 shows a correlation between COR and H02 counts (sum of H0 and H2 counts, which are GIS monitor counts described in section 3.4) during the night-earth observations. The H02 count is almost free from signal X-rays in the field of view, even during the on-source observations.

Although COR is a good indicator of NXB, there exists a secondary branch below COR $\sim$ 10 GV on the COR vs. H02 correlation. This is probably due to a slight inaccuracy of the COR-map. If we plot the satellite positions on the Earth, those periods which fall on the secondary branch appear only at the north east region of the map above the north Atlantic Ocean (dots in figure 4.10). The H02 is a good indicator of the NXB, however, there are two more issues known as "hard-flares" and "soft-flares".

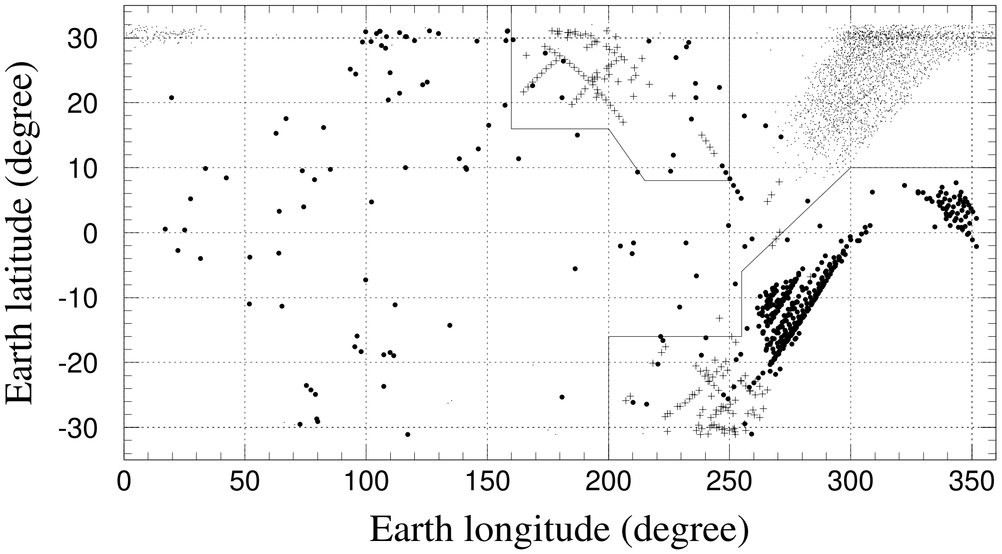

Figure 4.10: Distribution map for three types of phenomena on the Earth surface. The mark "$\cdot$" represents a position when H02 is less than the lower solid line in figure 4.11, where the COR-map is thought to be inaccurate. The mark "$\bullet$" represents a position when H02 is greater than the upper solid line in figure 4.11 (the hard-flares). The mark "+" represents a position when H02 $<$ 1000 c/32 s $=$ 31.25 c/s and NXB $>$ 15 c/32 s $=$ 0.46875 c/s. Two regions surrounded by solid lines define the dangerous areas where we should be cautious of the hard- and the soft-flares.

We can see the hard-flares as a large scatter around COR $\sim 11-12$ GV in figure 4.11. If we plot the satellite positions on the Earth, the hard-flare period are concentrated in the region peripheral to the south Atlantic anomaly (SAA) (filled circles in figure 4.10). SAA is a hole in the geomagnetic field which allows particles trapped in the magnetosphere to

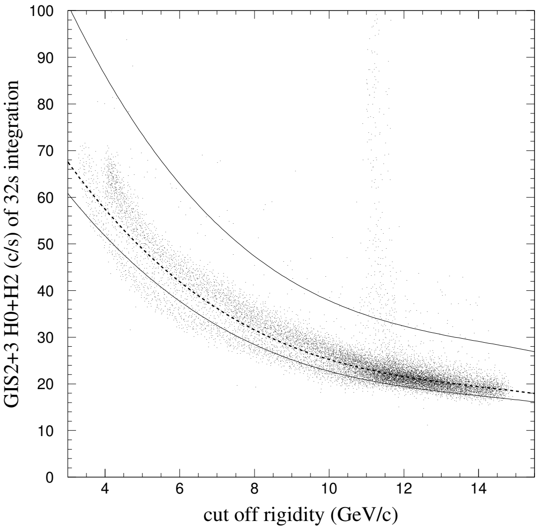

Figure 4.11: Correlation between COR and H02 counts during the night-earth observations. $H02$ is integrated for every 32 s. A dashed line means a function $f(x) = (109.3 - 17.05x + 1.127x^2 - 0.02627x^3)/32$ derived from fitting. Two solid lines below and above show $f(x)$ scaled by 0.9 and 1.5 times, respectively. The flare-cut is not applied.

Table 4.3: Summary of the flare-cut conditions

Condition	Reason
15 c/s $\leq$ H02 $\leq$ 45 c/s	to avoid high NXB
H02 $\leq 1.5 \times f(\mathrm{COR})^{\dagger}$ c/s	for hard flares
RBM $\leq$ 300 c/16 s = 18.75 c/s everywhere	for soft flares
RBM $\leq$ 100 c/16 s = 6.25 c/s in the dangerous areas (figure 4.10)	for soft flares

† $f(x) = 0.5(109.3 - 17.05x + 1.127x^2 - 0.02627x^3)$ c/ 16 s.

come down than usual. The hard-flares are probably caused by particles trapped in SAA. These events can be eliminated by rejecting time intervals when $H02 > 1.5 \times f(COR)$ in figure 4.11.

The soft-flare events appear in two regions: the south west to SAA and above Hawaii (crosses in figure 4.10). During the soft-flares, it is known that the NXB counts increase without an increase of H02. The soft-flares show harder profile than the average spectrum for the entire night-earth observations. Although the soft-flares can be eliminated by masking these regions, masking area is a little too large to ignore a decrease of integration time. To cope with this, we use the RBMCNT, i.e. a counting rate of the radiation belt monitor (RBM) to reject the soft-flares.

From these investigations, we have arrived at the conditions to reject the hard- and soft-flares as summarized in table 4.3. To avoid high NXB periods, we usually restrict H02 in the range of 15–45 c/s, too. We call the procedure to apply these conditions “flare-cut”.

H02-Sorting Method

H02 is a good indicator to predict the NXB variation as described in previous section. We sort the night-earth data which is applied the flare-cut by H02 in every 5 c/s step, i.e. 15–20, 20–25, 25–30 c/s, etc. H02 is counted in the 16 s time interval including the arrival time when the corresponding event is detected. Figure 4.12 shows the residual night-earth spectra corresponding to five H02 intervals. As H02 increases, the spectrum gets softer. We denote each exposure time T_i^{NTE}, and each spectrum $H_i^{NTE}(PI)$, both of which are counted or created on the same condition and in the same detector region as the on-source observations. When T_i^{OBS} is the exposure time in the i-th $H02$ bin during the on-source observation, the NXB spectrum contained in the on-source data is estimated as:

$$H(PI) = \sum_i H_i^{NTE}(PI)\,\frac{T_i^{OBS}}{T_i^{NTE}}. \tag{4.7}$$

We call this method “H02-sorting method”. To check the reproducibility of NXB by the H02-sorting method, we split the entire night-earth data into 480 × 10 ksec intervals.

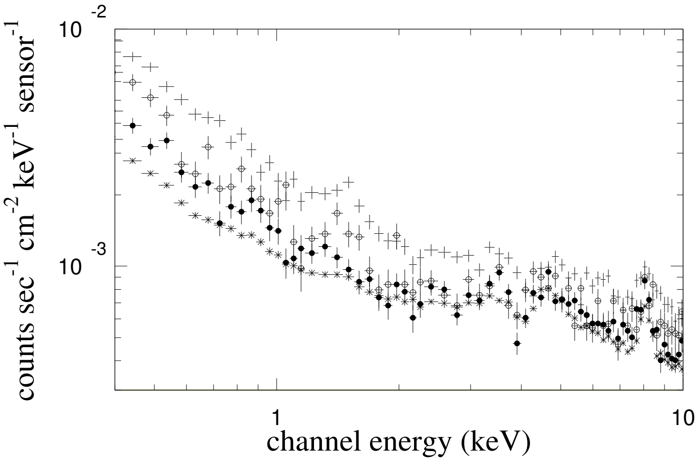

Figure 4.12: H02 sorted spectra during the night-earth observations. The data represents in the H02 range of 50–80 (+), 40–45 (∘), 30–35 c/s (•), and 20–25 c/s (×). H02 are integrated for every 16 s. The flare-cut is applied.

Then we compared the counting rate of each interval with that estimated by H02-sorting method using the entire night-earth data. The resulting NXB reproducibility is shown in figure 4.14. Filled circles in the upper panel show the actual counting rate of each interval, and the middle panel shows the counting rate divided by the prediction. We can see that there is a general trend of increasing counting rate with time until around 1997, and then decreasing. Note that it means that the long-term NXB variation which is seen in figure 4.13 cannot be reproduced by the H02-sorting method.

Correction of the Long-term Variability

A long-term variation of the NXB has been seen by several percent in a year, as shown in figure 4.13. Although the spectral shape has not changed significantly (figure 4.13), it is probably due to a gradual build-up of long-term decay radioisotopes.

We have to adjust the normalization of the NXB estimated by the H02-sorting method with the formula:

$$scaling\ factor \ = \ 1.0$$

$$
\begin{aligned}
&+2.156435 \times 10^{-9} \cdot (ascatime - 70587300)\\
&-6.051379 \times 10^{-18} \cdot (ascatime - 70587300)^2\\
&+8.388631 \times 10^{-26} \cdot (ascatime - 70587300)^3 \qquad (4.8)
\end{aligned}
$$

where *ascatime* represents the time in second from 00:00:00 (UT) on 1 January 1993, and is calculated from the mean observation time.

The standard deviation for a distribution of the ratio of observed to predicted NXB after the flare-cut procedure, the H02-sorting method, and the long-term NXB trend correction is 0.06862, which means 6.9 % rms variation of the NXB counts. This values includes a Poisson error of $\sim$ 3.4 %. Therefore, we conclude that we can achieve a $\sim$ 6.0% rms reproducibility in NXB, by a combined use of the standard background rejection, the flare-cut procedure, the H02-sorting method, and the long-term NXB trend correction. In the following, we quote 6 % as a typical systematic uncertainty associated with the NXB estimation.

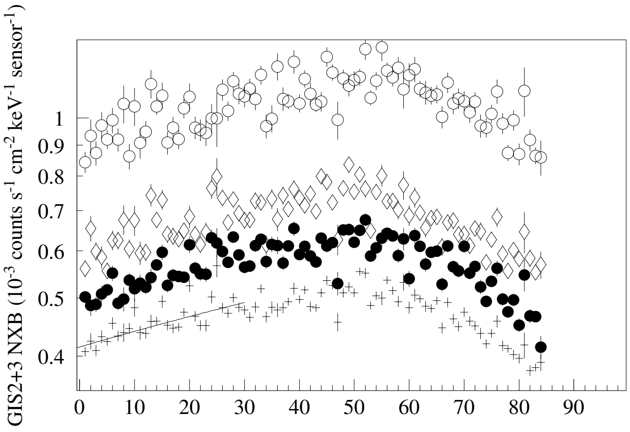

Figure 4.13: Long term (June 1993 – May 2000) variations of the GIS2+GIS3 counting rate during the night-earth observations in the 0.6–1.0 (○), 1.0–2.0 (◇), 2.0–4.0 (●), and 4.0–8.0 (×) keV energy bands, integrated within the radius of 20 mm from the optical axis. The flare-cut is applied.

4.2.2 Cosmic X-ray Background (CXB)

To reproduce the CXB, we use Master Background Database (MBDB) system described in Ikebe (1995). The MBDB consists of the Master Background Photon File (MBPF) and the Master Background Exposure Map (MBEM), based on observation data sets of 4 different blank sky fields; 'Draco', 'NEP', QSF3, and 'SA57'. Table 4.4 shows the observation log of 18 pointings included in the MBDB. After the data screening described in section 4.2.1, we obtained total exposure time of 476 ksec.

An example of GIS2 image is shown in figure 4.15(a). We can recognize that some faint sources are seen in the image. To eliminate faint sources, we apply the MBEM to the image. The MBEM defines an exposure map over the entire GIS field, and the value of MBEM at pixel $(DETX, DETY)$ is calculated as;

$$
\mathrm{MBEM}(DETX, DETY) = \sum_i T_i \times mask_i(DETX, DETY) \qquad (4.9)
$$

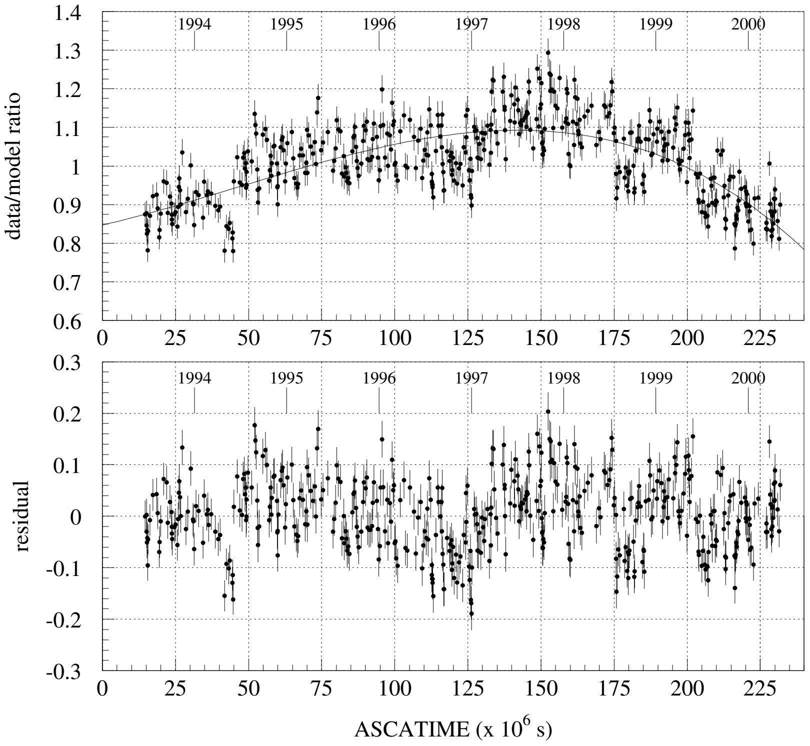

Figure 4.14: Figures to check the NXB reproducibility by H02-sorting method. Upper panel shows the ratios of the NXB to the prediction in the 0.7–7.0 keV energy band, for every 10 ksec exposure. Lower panel shows the ratio of counting rate to the model. The solid line shows the best fit line shown as eq. 4.8.

where T_i is the exposure time of the i-th pointing, and $mask_i$ is the mask image for the i-th pointing. Ikebe (1995) determined the mask image to remove the pixels which have a larger number of counts than a threshold level, considering the PSF of XRT+GIS. Figure 4.15(b) shows an example of the mask image. Although the exposure time varies by position due to the mask, we obtain the CXB with good statistics with minimum value in the summed exposure map is 277 ksec, and maximum is 476 ksec.

Figure 4.16(a) shows the spectra of the four fields, and figure 4.16(b) compares spectrum shape at each fields with Draco spectrum. We can say the spectrum shape dose not vary in the four fields significantly. The fluctuation of the CXB flux is roughly $\sim 10\%$ for the size of GIS field of view (Ishisaki 1996). Thus we estimate the systematic error of 10% for the normalization of the CXB.

Table 4.4: Blank sky observations used for the CXB database

Field Name	Obs. Date † (UT)	Position ‡ (gl, gb)	Exp. Time § (sec)
Draco	1993.06.04	(102.23, 34.13)	21891
	1993.06.05	(102.28, 33.90)	10715
	1993.06.05	(102.33, 33.67)	24812
NEP	1993.07.20	(96.39, 29.81)	10691
	1993.06.10	(96.39, 29.81)	16120
	1993.10.21	(96.39, 29.82)	14733
	1993.08.16	(96.40, 29.98)	17735
	1993.07.02	(96.39, 29.98)	13329
	1993.09.30	(96.38, 29.98)	16132
QSF3	1993.07.11	(250.85, -51.98)	24133
	1993.09.15	(250.86, -51.99)	12494
	1993.09.10	(250.86, -51.98)	12810
	1993.09.21	(250.86, -51.99)	12225
SA57	1993.12.21	(64.25, 85.56)	54119
	1993.12.24	(65.44, 85.65)	41176
	1993.12.28	(63.00, 85.48)	94438
	1994.01.16	(63.15, 85.66)	44129
	1994.01.18	(65.19, 85.47)	33820
Total			475502

†: The start time of observation in year.month.day
‡: Galactic coordinate of the direction of the GIS3 center.
§: Total exposure time after data screening described in section 4.2.1.

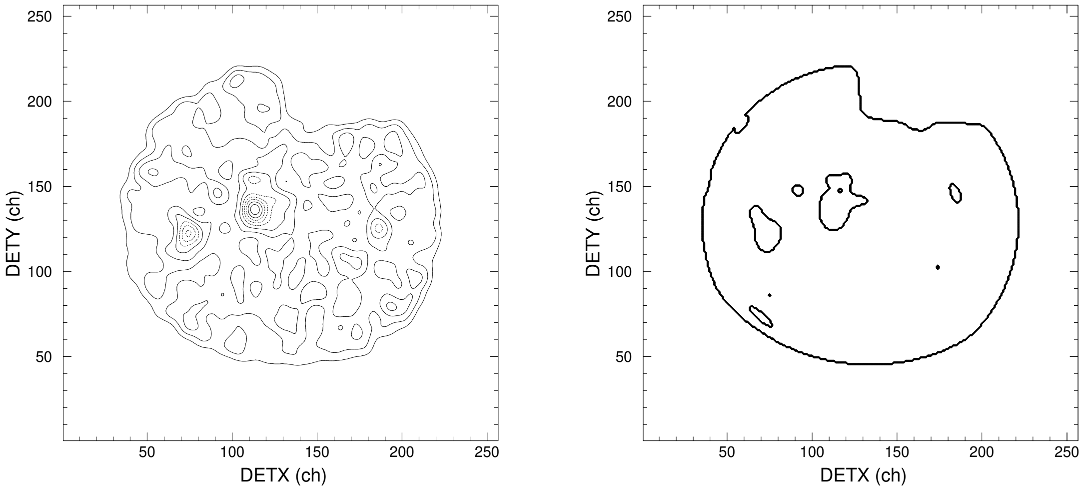
(a) (b)

Figure 4.15: Example of GIS image and mask image. (a) 0.7–10 keV GIS2 image of NEP field observed in July 1993. The image is smoothed by Gaussian of $\sigma = 1'$. The NXB is not subtracted. (b) Mask image for (a).

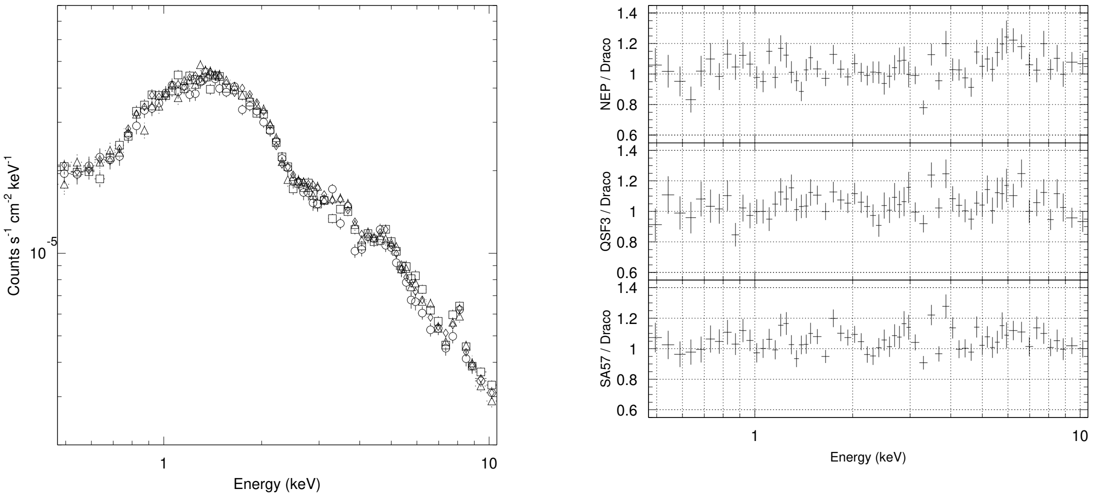

Figure 4.16: Spectra of the Draco, Nep, QSF3, and SA57 fields. The NXB is subtracted. (a) Plot of 4 spectra in counts s^{-1} cm^{-2} keV^{-1}; Draco (circle), NEP (rectangle), QSF3 (triangle), and SA57 (diamond). (b) Comparison of spectrum shape. The spectra of NEP, QSF3, and SA57 are divided by Draco.

Chapter 5

Observation and Analysis

In this chapter, we summarize the observational logs of ASCA and ROSAT, and introduce our analysis method for two-dimensional temperature maps from hardness ratios.

5.1 ASCA observations

All clusters which were selected here have spatial extent larger than the GIS field of view. Therefore, we carried mapping observations for each cluster. The log of ASCA observations is summarized in table 5.1. The numbers of pointings are 7, 6, 11, and 13 for A1060, AWM7, Centaurus, and Perseus, respectively. The observations were performed over a period of five and a half years, from June 1993 to December 1999. Note that two pointings for A1060 have a very small separation angle ($\sim 2'$).

All the GIS data were obtained with the normal PH mode. The SIS data were also obtained, however, we did not use the SIS data in this thesis. The reason is that the field of view of the SIS ($11' \times 11'$) was unable to cover the whole cluster fields, and was not suitable for the present purpose.

We selected the GIS data with a cut-off rigidity > 8 GV and the telescope elevation angle $> 5^\circ$ and 10° from the Earth rim for day and night, respectively. Some of the data for A1060, taken in December 1999, showed significant excess emission in the energy range below 1 keV. The excess is thought to be due to scattered solar X-rays from the earth atmosphere, because a medium-class solar flare occured during the ASCA observation. By setting the elevation angle from the day side of the earth to be $> 20^\circ$, this soft excess was eliminated. This condition was applied to all of the A1060 data. The flare-like events and the article background level are screened out by the H02-sorting methods (Ishisaki 1996) as described in section 4.2.1. The time periods after the attitude maneuver with unsettled pointing directions were also excluded (Ikebe 1995).

Table 5.1: Log of ASCA observations

Cluster	Seq. No.	PI[a]	Date	Coordinates (J2000) R.A.	Decl.	Exp.[b] (s)
A1060	80004000	Day, C.[c]	93 Jun 28	159.42	−27.54	21940
	83024000	Sakima, Y.	94 Dec 12	159.17	−27.08	6582
	83024010	Sakima, Y.	94 Dec 19	159.17	−27.05	10451
	87009000	Ezawa, H.	99 Dec 19	158.53	−27.23	14129
	87010000	Ezawa, H.	99 Dec 20	159.27	−27.64	16385
	87011000	Ezawa, H.	99 Dec 21	158.85	−27.96	10448
	87012000	Ezawa, H.	99 Dec 21	158.39	−27.69	15502
AWM7	80036000	Canizares, C.[c]	93 Aug 7	43.46	41.42	9392
	80037000	Canizares, C.[c]	93 Aug 7	43.06	41.40	14596
	81011000	Ohashi, T.	94 Feb 10	44.27	41.78	7525
	81011010	Ohashi, T.	94 Feb 10	43.32	41.78	13632
	81011020	Ohashi, T.	94 Feb 11	43.88	42.20	12136
	81011030	Ohashi, T.	94 Feb 11	43.88	41.62	10189
Centaurus	80032000	Ohashi, T.[c]	93 Jun 30	192.47	−41.23	11477
	80033000	Ohashi, T.[c]	93 Jul 5	192.55	−40.96	11326
	80034000	Ohashi, T.[c]	93 Jul 5	192.79	−41.32	8999
	83026000	Tawara, Y.	95 Jul 19	192.46	−41.37	45899
	86000000	Ezawa, H.	98 Feb 3	191.98	−40.58	6777
	86001000	Ezawa, H.	98 Feb 3	191.28	−40.78	10580
	86002000	Ezawa, H.	98 Feb 4	191.03	−41.30	7656
	86003000	Ezawa, H.	98 Feb 4	191.31	−41.77	9634
	86004000	Ezawa, H.	98 Feb 4	191.97	−41.87	8206
	86005000	Ezawa, H.	98 Feb 5	192.50	−41.56	7706
	86006000	Ezawa, H.	98 Feb 5	192.50	−41.01	11541
Perseus	80007000	Arnaud, K.[c]	93 Aug 6	50.04	41.63	10307
	80008000	Arnaud, K.[c]	93 Aug 6	49.63	41.54	18014
	80009000	Arnaud, K.[c]	93 Sep 15	49.27	41.55	10959
	81026000	Kowalski, M.	94 Feb 9	49.28	41.41	14973
	81027000	Kowalski, M.	94 Feb 10	48.89	41.26	10896
	83051000	Arnaud, K.	95 Aug 18	50.32	41.54	8818
	83052000	Arnaud, K.	95 Aug 19	50.68	41.54	13949
	83053000	Arnaud, K.	95 Sep 4	50.06	41.29	10604
	85000000	Ezawa, H.	97 Feb 14	50.51	41.96	16905
	85001000	Ezawa, H.	97 Feb 14	49.89	42.10	13663
	85002000	Ezawa, H.	97 Feb 15	49.42	41.93	13444
	85003000	Ezawa, H.	97 Feb 16	50.45	41.02	10659
	85004000	Ezawa, H.	97 Feb 17	49.72	40.93	18809

a. Principal Investigator.

b. The net exposure time after all screening and cleaning procedures.

c. PV (Observation in the Performance Verification phase.)

5.2 ROSAT observations

For spatially extended sources, an analysis of the ASCA data needs proper consideration of the complicated response of the X-ray telescope (XRT; Serlemitsos et al. 1995) as described in the next section. To take these effects into account, we simulated the GIS observations using the ROSAT PSPC data in the 0.5–2 keV band as input images. The higher angular resolution of PSPC than that of ASCA would allow such a substitution.

Table 5.2 shows the log of ROSAT observations and Figure 5.1 shows the PSPC and ASCA field of view superpose on the PSPC image in the 0.5–2 keV band. The images are smoothed by a Gaussian function with $\sigma = 1'$ after the background subtraction and the exposure correction. Both observations of A1060 and AWM7 were performed in January 1992. The single fields of the PSPC almost completely cover the GIS observed regions for these 2 clusters. For the Centaurus cluster and Perseus cluster, we used 5 ROSAT pointings, which were taken in 1992–1993 and 1991–1992, respectively.

Table 5.2: Log of ROSAT/PSPC observations

Cluster	Sequence No.	Date	Coordinates (J2000)		Exposure †
			R.A.	Decl.	(s)
A1060	800200n00	92 Jan 1	159.18	−27.53	13077
AWM7	800168n00	92 Jan 28	43.61	41.59	12200
Centaurus	800192n00	92 Feb 2	192.20	−41.31	7294
	800321a01	93 Jan 18	193.26	−41.57	11781
	800322n00	92 Jul 25	191.15	−41.06	16237
	800323n00	93 Jan 16	192.55	−40.52	19254
	800324a01	93 Jan 18	191.86	−42.11	12862
Perseus	800186n00	92 Feb 2	49.95	41.51	4394
	800032a01	91 Sep 2	48.89	41.28	28699
	800033n00	91 Feb 9	51.01	41.78	12614
	800034a01	91 Aug 19	50.29	40.74	23294
	800035a01	91 Aug 18	49.62	42.31	23562

† The net exposure time after all screening and cleaning procedures.

The data selection was carried out by looking into the time variation of the PSPC count rate in different pulse-height channels. Subtraction of non-cosmic background and correction for the vignetting were performed using the Extended Source Analysis Software package (Snowden et al. 1994; details in appendix A). Assuming the axial symmetry, we fit the surface brightness profile of A1060 and AWM7 in the energy range 0.5 – 2.0 keV with a single β model, defined as

$$S(r) = S_0 \left(1 + \frac{r}{r_{\rm c}}\right)^{-3\beta + \frac{1}{2}} , \tag{5.1}$$

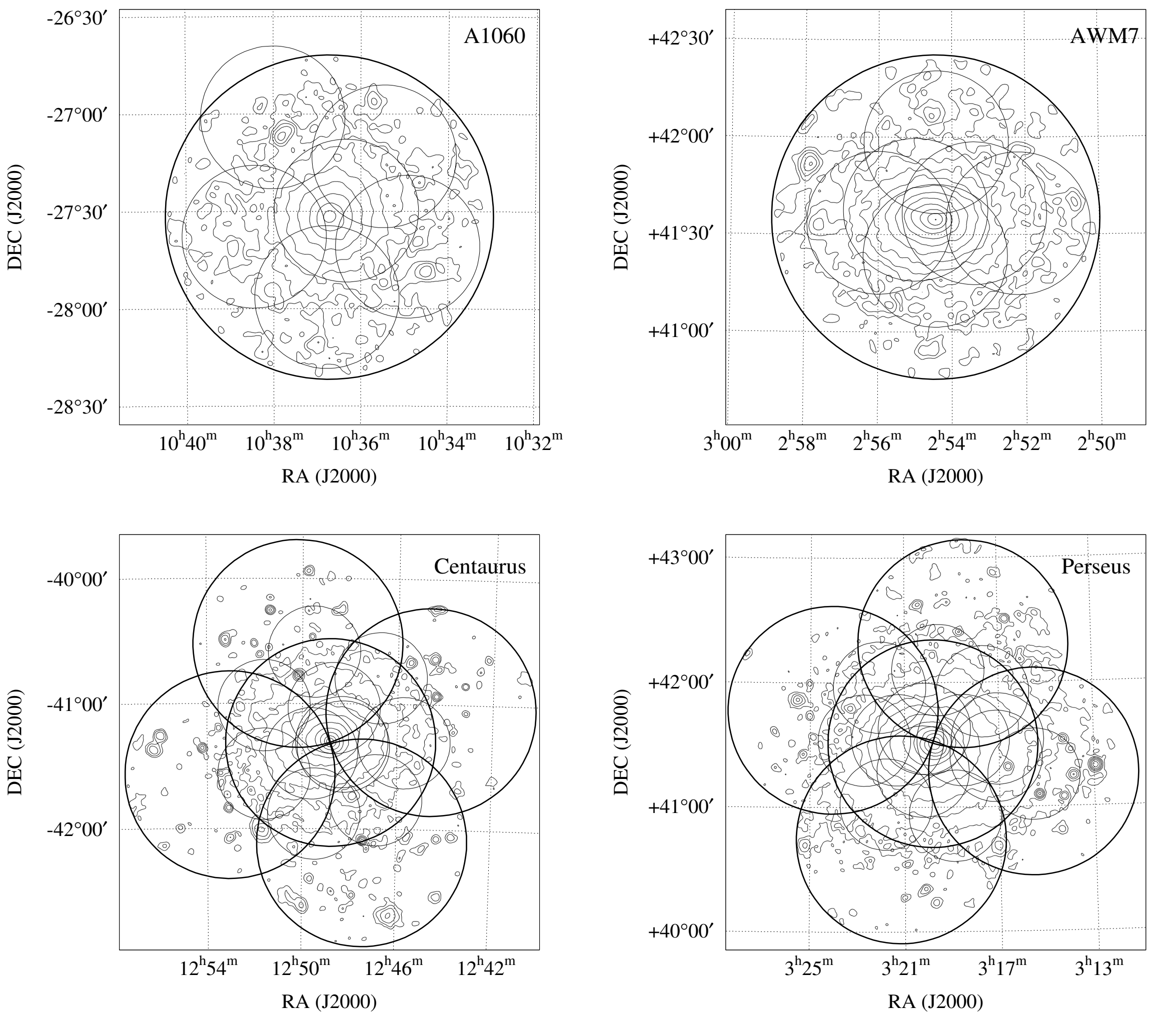

Figure 5.1: The PSPC and GIS field of view superposed on the PSPC images of the A1060, AWM7, Centaurus, and Perseus cluster. The thick and thin circles show the PSPC and GIS field of view with a radius of 50′ and 22′, respectively.

where S_0 is the central brightness, r is the projected radius, $r_{\rm c}$ is the core radius, and β is a slope parameter. Since the surface brightness profiles of the Centaurus and Perseus cluster remarkable excess in the center, the profiles are fitted with double-β model, given by

$$S(r) = S_{0,1}\left(1+\frac{r}{r_{\rm c,1}}\right)^{-3\beta_1+\frac{1}{2}} + S_{0,2}\left(1+\frac{r}{r_{\rm c,2}}\right)^{-3\beta_2+\frac{1}{2}} \quad . \tag{5.2}$$

Here $S_{0,1}, S_{0,2}, r_{\rm c,1}, r_{\rm c,2}, \beta_1$, and β_2 are model parameters; the term with suffix 1 (wider β component) and 2 (narrower β component) represent the emission from the hot component and the central cool component, respectively. We added a constant level which corresponds to the cosmic X-ray background onto the single- or double-β profiles of the 4 clusters. As shown in Table 5.3, the obtained β-model parameters are consistent with the previous results for A1060 by Tamura et al. (2000), AWM7 by Neumann and Böhringer (1995), Centaurus by Ikebe et al. (1999), and Perseus by Ettori et al. (1998), respectively. Note that the bright point sources (HCG 48 for A1060, IC 310 and 1RXS source for the Perseus) are excluded for the fitting.

In order to suppress the statistical fluctuation, the PSPC images used for the GIS simulations were then smoothed by a Gaussian function, whose width was varied width the intensity. We used $\sigma = 60''$ and $15''$ for the intensity levels < 2 and 2–10 cts pix^{-1}, respectively, and no smoothing for > 10 cts pix^{-1}. This preserves the central sharpness of the cluster images. Figure 5.2 shows the surface brightness profiles after the smoothing, cosmic X-ray background subtraction, and exposure correction, with the best-fit β models as shown in Table 5.3.

Table 5.3: Parameters from the β model fit for the PSPC profile.

Cluster	Our results		Previous results		Reference
	r_c (arcmin)	β	r_c (arcmin)	β	
A1060	3.7 ± 0.2	0.53 ± 0.01	3.9 ± 0.1	0.54 ± 0.01	[1]
AWM7	3.2 ± 0.1	0.52 ± 0.01	3.4 ± 0.2	0.53 ± 0.01	[2]
Centaurus ($r > 6'$)	6.4 ± 0.30	0.54 ± 0.01	$7.3^{+2.2}_{-2.0}$	0.57 ± 0.04	[3]
cool	1.2 ± 0.1	0.75 ± 0.01	$1.5^{+4.5}_{-1.3}$	$0.92^{+3.8}_{-0.45}$	[3]
Perseus ($r > 10'$)	10.1 ± 0.3	0.64 ± 0.01	9.5	0.67	[4]
cool	5.0 ± 0.01	1.16 ± 0.01	–	–	

[1] Tamura et al. 2000, [2] Neumann and Böhringer 1995, [3] Ikebe et al. 1999, [4] Ettori et al. 1998.

Note: For the Centaurus cluster, the parameters of the wider β-component are obtained by the single-β model fit to the PSPC profile outside $r > 6'$. Shape parameters of the narrower β-component "cool" are by 2-β model fitting when r_c and β for the wider component are fixed to $7'.3$ and 0.57. For the Perseus cluster, $r > 10'$ The previous results for the Perseus cluster are the parameters derived in the north region, that appears as the most relaxed region in the cluster, and the parameters vary $\beta = 0.61 - 1.10$ and $r_\mathrm{c} = 9.5 - 25.8$ among the north, south, east, and west regions.

5.3 Analysis method

5.3.1 Hardness ratio analysis

We estimated the temperatures from the hardness ratios (*HR*), rather than performing spectral fits, in order to maximize the spatial resolution of the temperature maps. The energy division of the 2 energy bands was chosen so as to minimize the error of the

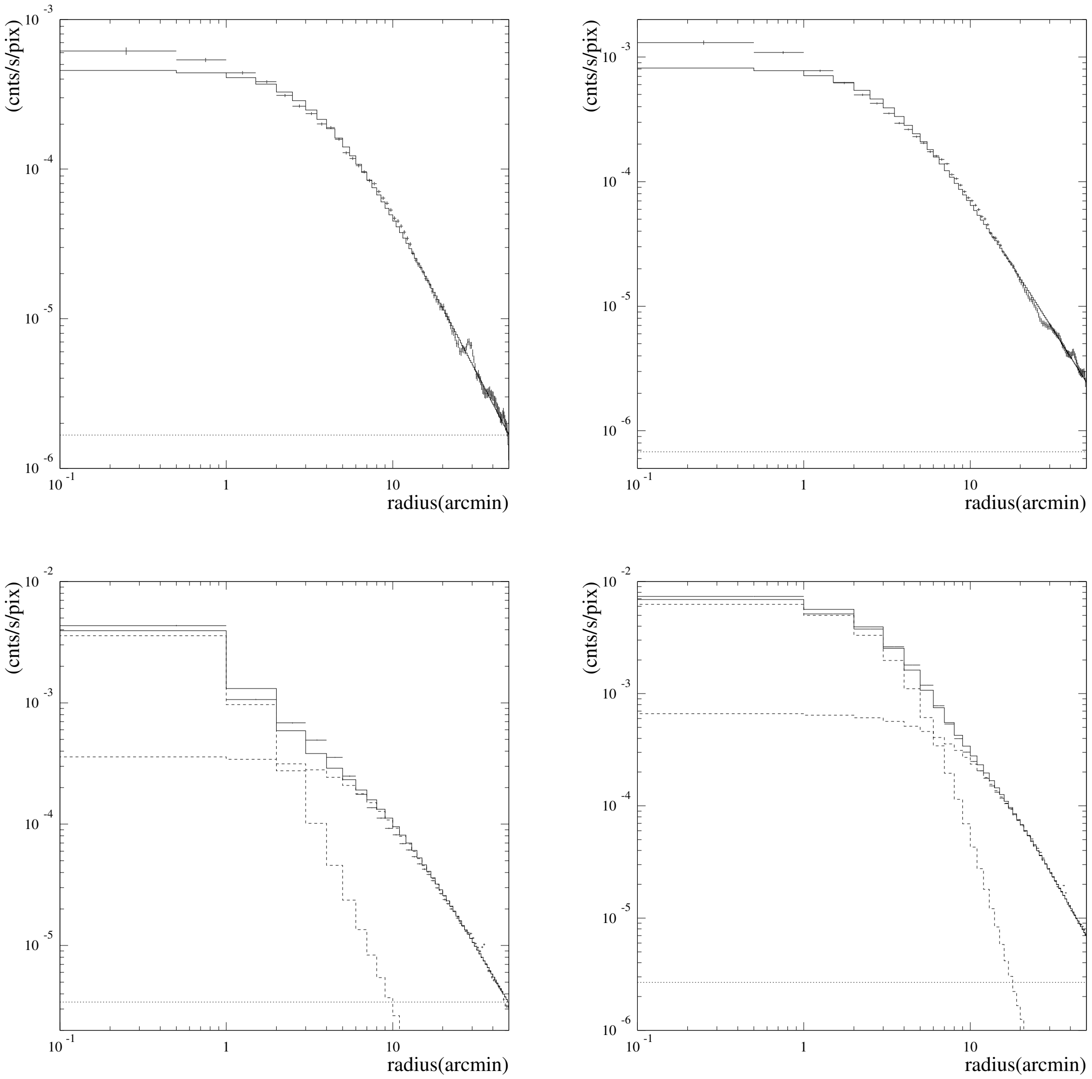

Figure 5.2: The PSPC profiles after the smoothing, cosmic X-ray background subtraction(dotted line), and exposure correction, to use for the GIS ray-tracing simulations. The solid and dotted lines show the best-fit β models obtained from single-β model (for A1060 and AWM7), and 2-β model (for the Centaurus and Perseus cluster) fit with before smoothing and background subtraction profiles to confirm the consistency with the previous results.

resultant temperature for a temperature range of 3–5 keV. By evaluating $HR - kT$ relation for different energy divisions, we chose a common dividing energy of 2 keV for all 4 clusters studied here. The definition of the hardness ratio is $HR = H/S$, where H and S are the count rates in 2–7 keV (2–10 keV for Perseus cluster because of enough statistics and rather high temperature) and 0.7–2 keV, respectively. The *HR*s and their statistical errors were calculated from the background subtracted data which are combined into a large image for each cluster from the ASCA multi-pointing observations. The actual *HR* values are between 0.6 and 1.2 for the 4 clusters.

Table 5.4: Spectral parameters for the $HR-kT$ relations and the ray-tracing simulations.

Cluster	input image	$N_{\rm H}$ 10^{20} cm^{-2}	kT keV	Abundance solar, region
A1060	PSPC 1ptg	3.5†	3.3	0.31
AWM7	PSPC 1 ptg	8.7†	3.6	0.51 – 0.16 (r = 0′-5′-10′-15′-40′)
Centaurus	PSPC 5 ptg	8.8‡	4.0	1.57 – 0.20 (r = 0′-1′-2′-3′-4′-5′-6′-8′-10′-20′)
cool	model ($r_{\rm cutoff}$=5′)^a	8.8‡	1.4	1.0
Perseus	PSPC 5 ptg	14‡	6.0	0.44 – 0.18 (r=0′-4′-8′-12′-20′-28′-36′-44′-60′)
cool	model ($r_{\rm cutoff}$=30′)^b	14‡	2.05	0.44

† The best-fit values from Tamura et al. (2000) and Ezawa et al. (1997) for A1060 and AWM7, respectively.

‡ Galactic value by Stark et al.(1992) and Dickey & Lockman (1999) for Centaurus and Perseus, respectively.

a see section 6.3.2 in more detail.

b see section 6.4.2 in more detail.

The HRs are converted to the temperature based on the $HR-kT$ relation as shown in Figure 5.3. The curves are calculated assuming that the incident spectra to be absorbed MEKAL (Mewe et al. 1985; Mewe et al. 1986; Kaastra 1992; Arnaud & Rothenflug 1985) models based on the previous ASCA results. The spectral parameters are shown in Table 5.4. The same models were also used for the ray-tracing simulations. The parameters for A1060 were taken from Tamura et al. (2000). The $N_{\rm H}$ value is slightly smaller than the Galactic value of 5×10^{20} cm^{-2}, and the metal abundance was fixed at $Z = 0.31$ solar. In AWM7, the metallicity gradient was found by Ezawa et al. (1997) described in section 2.4. We included the effect in the $HR-kT$ relation and the ray-tracing simulation, assuming the abundance values in the 4 concentric annular regions given in table 1 of Ezawa et al. (1997). The best-fit $N_{\rm H}$ value was consistent with the Galactic value. For the Centaurus cluster, the strong concentration of the metal abundance in the central $r < 20'$ region observed by Ikebe et al. (1999). The effect on temperature due to the abundance variation is the largest among the 4 clusters. The difference of temperatures calculated from the $HR-kT$ relations taking at the the maximum and minimum abundance is 0.13 and 0.24 keV at a temperature of 3.6 keV and 3.0 keV, respectively. We divided into 10 concentric annular regions based on the abundance gradient given in equation (5) of Ikebe et al. (1999). The best-fit $N_{\rm H}$ values obtained by Ikebe et al. (1999) differed with spectral

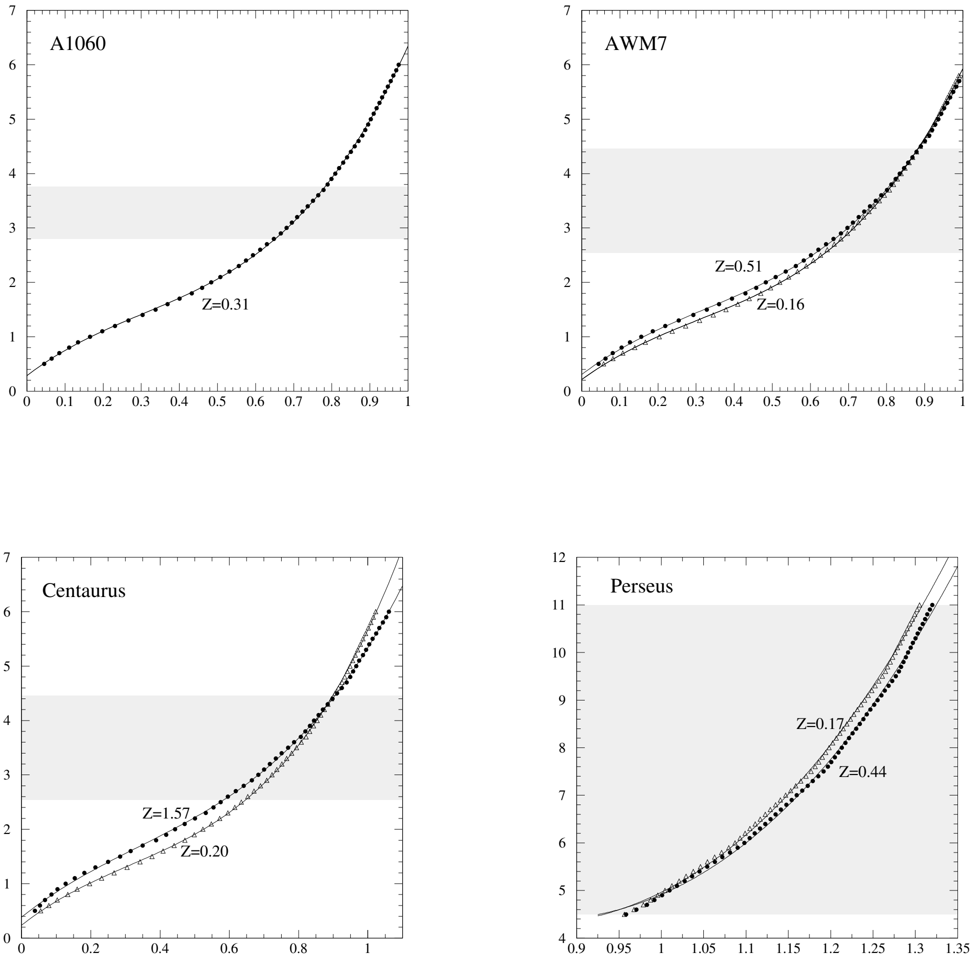

Figure 5.3: Calculated *HR–kT* relations from an absorbed MEKAL model for the 4 clusters with the approximate equation (solid lines). The shaded regions show roughly the temperature range for each cluster.

models, but were consistent with the Galactic value (Stark et al. 1992). We therefore adopted the Galactic value here. For the Perseus cluster, the Galactic $N_{\rm H}$ of 1.4×10^{21} cm^{-2} was accepted by spectral fitting with ASCA, we applied the Galactic value here. The metallicity gradient also has been detected for the Perseus cluster, though the gradient is much gentler than the Centaurus. We included the gradient in the 8 concentric regions in the ray-tracing simulation given in table 2 of Ezawa et al. (2001). The relations can be approximated well with equations of the third degree. We show here the equations taken at the maximum/minimum abundance as shown in Figure 5.3.

A1060 : Z =0.31

$$kT = 0.29 + 5.32\ ({\rm HR}) - 7.83\ ({\rm HR})^2 + 8.56\ ({\rm HR})^3\ \ {\rm keV} \tag{5.3}$$

AWM7 : Z =0.51, 0.16

$$kT = 0.31 + 5.27\ (\mathrm{HR}) - 7.24\ (\mathrm{HR})^2 + 7.46\ (\mathrm{HR})^3\ \ \mathrm{keV} \tag{5.4}$$
$$kT = 0.22 + 5.10\ (\mathrm{HR}) - 7.42\ (\mathrm{HR})^2 + 8.03\ (\mathrm{HR})^3\ \ \mathrm{keV} \tag{5.5}$$

Centaurus : Z =1.57, 0.20

$$kT = 0.39 + 5.08\ (\mathrm{HR}) - 5.54\ (\mathrm{HR})^2 + 5.42\ (\mathrm{HR})^3\ \ \mathrm{keV} \tag{5.6}$$
$$kT = 0.24 + 5.03\ (\mathrm{HR}) - 7.17\ (\mathrm{HR})^2 + 7.56\ (\mathrm{HR})^3\ \ \mathrm{keV} \tag{5.7}$$

Perseus : Z =0.44, 0.18

$$kT = 14.16 - 13.53\ (\mathrm{HR}) - 8.43\ (\mathrm{HR})^2 + 12.71\ (\mathrm{HR})^3\ \ \mathrm{keV} \tag{5.8}$$
$$kT = 13.83 - 13.57\ (\mathrm{HR}) - 8.28\ (\mathrm{HR})^2 + 12.98\ (\mathrm{HR})^3\ \ \mathrm{keV} \tag{5.9}$$

5.3.2 Effect of the XRT response

As described in section 4.1, the XRT on-board ASCA has three main difficulties in performing spatially resolved spectral studies for sources which are extended more than the field of view: 1) a decline of the effective area as a function of an off-axis angle from the optical axis (vignetting), (2) stray light from outside of the field of view (mainly from the bright core of clusters in the present case), and (3) the point spread function (PSF). All of these have energy- and position-dependency.

The first effect is essential factor for our hardness ratio analysis. The effective area of XRT at an off-axis angle of $20'$ from the optical axis decreases to $\sim$ 25% and 10% for 2 and 8 keV, respectively. This difference causes an underestimate of the HR value in the field edge, even if the cluster is completely isothermal. It also complicates the data treatment for overlapping regions of the multi-pointings. Figure 5.4a shows the temperature map calculated from the 3.3 keV isothermal simulation for A1060. The non-uniformity of temperature maps with isothermal cluster simulations are clearly shown. In order to correct for the energy-dependence of vignetting, we ran ray-tracing simulations for isothermal clusters based on the PSPC image.

Second, the emission from outside region of the GIS field of view extended sources bring a problem of the stray light which mixes the X-ray fluxes from different regions as already described in section 4.1.2. In the present case, the bright cluster core mainly contributes the stray light. This effect is also examined with the ray-tracing simulation by tracing back the detected photons to their sky origins. The fractions of photon origin are calculated from the simulated image combined with all pointings for the 4 clusters with a weight of exposure times as shown in Figure 6.3, 6.11, 6.18, and 6.27. In the outer regions $r > 20'$, the photons from the central region $r < 4'$ are completely regarded as the stray light, and the fractions are 2–10% of the detected photons. The difference among the 4 clusters is mainly due to the intensity of the central excess, at the minimum and maximum in the case of A1060 and the Perseus cluster, respectively.

Regarding the last effect, the PSF always produces combination of photons, image distortions, and tails which depend on off-axis angles (see section 4.1.1). For the 4 clusters, the fraction of photons from central $r < 4'$ region in the next ring of $4' - 8'$ is 24–34%, which is almost due to the extent of the bright central peak by the PSF. The same way also holds for the other rings, even the fraction is less than in the $4' - 8'$ ring. On the other hand, the tail of the PSF is more extended in high energies than in lower energies. This effect is, however, almost negligible within $r \lesssim 6'$ from the center of the PSF profile, even when the photon origin is near the field edge at an off-axis angle of $17'$. At $r = 6'$ the source flux drops to about 1/100 as shown in figure 4.4, the energy-dependence of the PSF does not affect in the present analysis. These PSF effects are also corrected by the ray-tracing simulation.

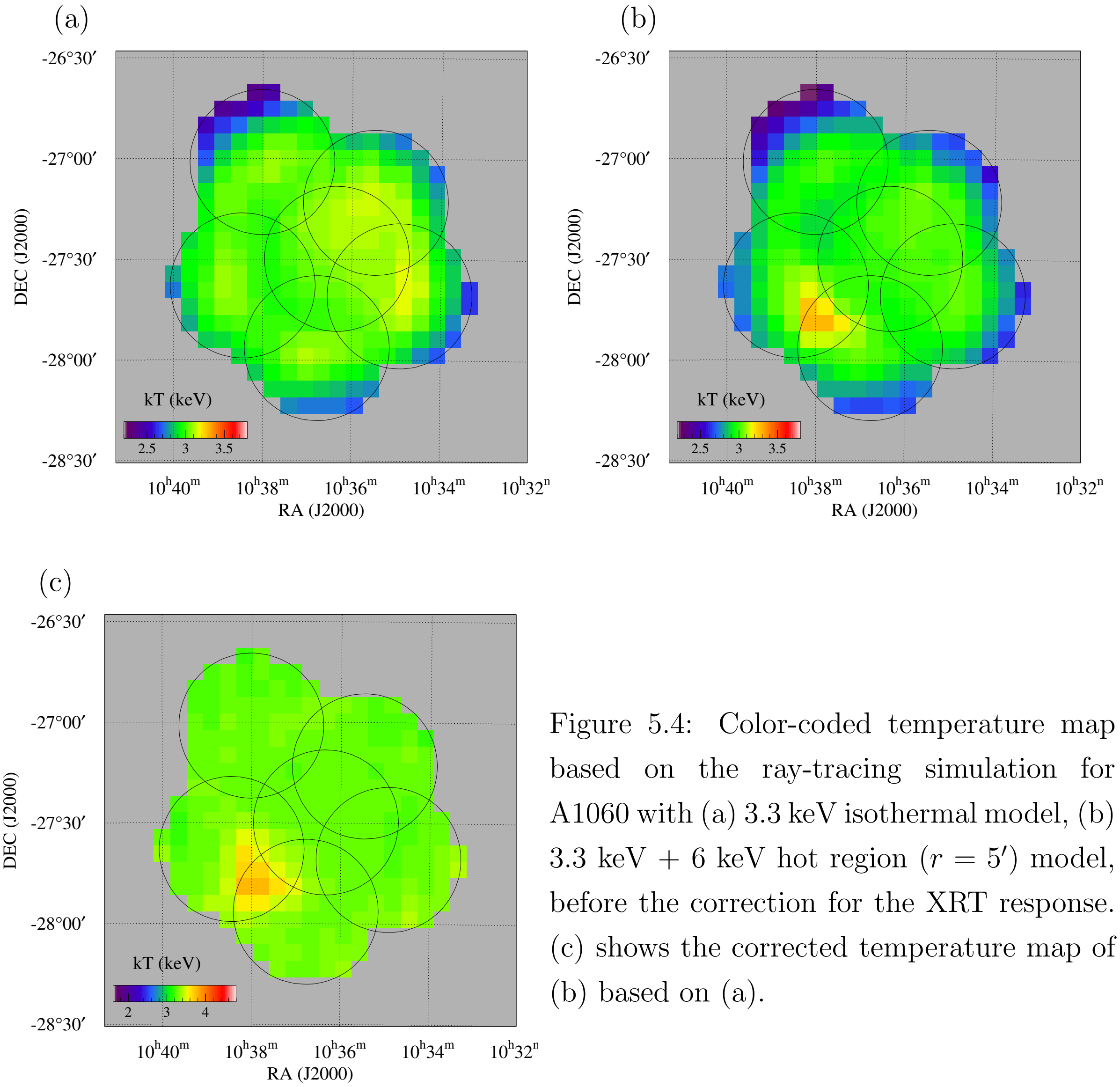

Figure 5.4: Color-coded temperature map based on the ray-tracing simulation for A1060 with (a) 3.3 keV isothermal model, (b) 3.3 keV + 6 keV hot region ($r = 5'$) model, before the correction for the XRT response. (c) shows the corrected temperature map of (b) based on (a).

5.3.3 Correction of *HR* values with simulation

The isothermal simulation is carried out with the PSPC image assuming that the spectrum is an absorbed MEKAL model with the parameters shown in table 5.4. The *HR* values are calculated in each cell of the image obtained from both observed and simulated data. We express them $(HR_{\rm obs})_i$ and $(HR_{\rm sim})_i$, for i-th cell in the image. The ratio of *HR*s between them is taken and normalized by an *HR* value, $HR_{\rm nrm}$, calculated from the $HR - kT$ relation at the temperature taken for the isothermal simulation. We therefore obtain the corrected *HR* value, $(HR_{\rm cor})_i$:

$$(HR_{\rm cor})_i = \frac{(HR_{\rm obs})_i}{(HR_{\rm sim})_i} HR_{\rm nrm} \ . \tag{5.10}$$

Then, the corrected *HR* values are converted to the temperature using an appropriate $HR - kT$ curve for the assumed metal abundance and $N_{\rm H}$. In order to confirm the correctness of this method, we have performed some isothermal simulations in the case of A1060. The adopted temperatures for the simulations are 2.7, 3.0, 3.3, and 3.6 keV. Figure 5.5 shows the difference between the adopted temperature and calculated temperature based on the 3.3 keV simulation as a function of the angle from the cluster center. In the central $r < 5'$, the calculated temperatures based on the 3.3 keV simulation gives the difference of -0.05, -0.02, and $+0.04$ keV for 2.7, 3.0, and 3.6 keV, respectively. These values are comparable to the 1σ statistical error of about 0.05 keV in this case. Within the radius of $45'$, the difference is about 0.07 keV at the most. The systematic error due to the ray-tracing itself is described later. Thus, we have confirmed simply the correctness of calculated temperature.

Second, we have examined an appearance with an intrinsic temperature structure. Since we take a running means of *HR* values to obtain a temperature map as mentioned in the next chapter, temperature structure becomes duller than the original. Figure 5.4b show the case where there is a 6 keV hot region with a radius of $5'$ at $15'$ south-east from the center. The corresponding hot region extends about 2×2 cells ($10' \times 10'$). The corrected temperature map based on 3.3 keV isothermal simulation (figure 5.4a) is shown in figure 5.4c. Thus the hot region is clearly seen compared with the surrounding region of 3.3 keV. However, the highest temperature of the hot region is $kT = 3.9$ keV in the temperature map. Even before taking running mean, the temperature is 4.5 keV. We should be careful not to over- or underestimate an absolute temperature of a hot region corrected with an isothermal simulation of such different temperature ($\Delta T \sim 3$ keV). The discrepancy also depends on statistics and region size. We therefore perform the spectral analysis to confirm the absolute temperature in this thesis. For the Perseus cluster, the isothermal simulation for the XRT correction and $HR-kT$ curve are obviously no longer good assumptions, because the temperature distribution changes widely in the 4–9 keV band. Hence, we have carried out the spectral fitting to obtain more reliable temperature map for the Perseus cluster.

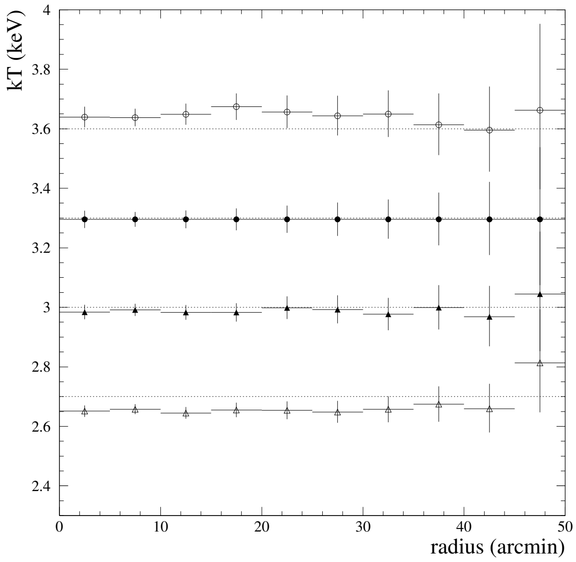

Figure 5.5: The temperature profile calculated from 2.7, 3.0, 3.3, and 3.6 keV isothermal simulations based on the 3.3 keV simulation and $HR - kT$ relation. The error bars show 1σ statistical errors, and the dotted lines show each adopted temperature.

Note that a hard point source also causes the hot region, but we can recognize any contaminations of point sources from the cluster component by either the extent of the temperature map or the excess emission in the X-ray image. For example, two bright point sources in the Perseus cluster show obviously different features in the temperature map as shown in figure 6.28. Also, we have found a hard point source at $35'$ south in the Centaurus cluster (see section 6.3.4). On the other hand, since the extent of the hot region in the Centaurus cluster is considerably larger than the distinguishable size, it is unlikely that the temperature structures for the ICM are strongly affected by point-source contaminations.

5.4 Systematic errors

To confirm the significance of the temperature results, we need to look into any systematic errors in the temperature determination process. There are 3 major origins to be considered: fluctuation of the cosmic and non-X-ray backgrounds, error in the response function, and error in the assumed surface brightness profile.

5.4.1 Background Uncertainty

The influence of the background fluctuation depends on the signal intensity, and outer regions of the cluster are considered to be more affected. Since both CXB and NXB have harder spectra than the observed clusters, their fluctuation can have a significant effect on the temperature results. We have studied this with a simulation by changing the background intensity (details are in section 4.2). The fluctuation amplitude was chosen to be 10% for CXB and 7% for NXB, respectively, which are the typical values for the field to field variation, based on the previous studies (Ishisaki et al. 1997).

Assuming the highest (+10% CXB and +7% NXB) and the lowest (−10% and −7%) background levels, we found that the temperatures at $r > 30'$ of A1060 changes by −0.2 and +0.3 keV on the average. The largest change in a single region ($5' \times 5'$) was −0.6 and +0.8 keV. Since other clusters have higher surface brightness than A1060 in the outer regions, we may take the systematic error of the temperature to be about 0.3 keV in the outermost regions and significantly smaller in the inner regions.

5.4.2 XRT Response

Here, we deal with the systematic errors due to the energy-dependence of the PSF and the effective area, and the stray light. The energy-dependent tail of the PSF has the largest effect on the *HR* at $\sim 6'$ from the cluster center, where the tail is produced by the bright center. Figure 6.3, 6.11, 6.18, and 6.27 show that the flux contamination at $r = 4'$–$8'$ from the inner region is 25–35% of the detected flux. Combining this with the 10% systematic error in our simulation, the effect on the *HR* should be smaller than 3.5%, which corresponds to a temperature error of about 5%.

As for the error on the effective area, offset observations of the Crab nebula with the GIS showed the maximum fluctuation of the photon index to be 2% for off-axis angles smaller than $22'$ as described in section 4.1.1. This corresponds to an *HR* error of 5.3%, resulting in a temperature error of $\lesssim 8\%$. We have also performed several isothermal simulations for A1060 with temperatures of between 2.7 keV and 3.6 keV. The *HR*–*kT* relation at a large offset angle maintains an accuracy of 0.1 keV within a radius of $40'$.

As described in section 4.1.2, the stray light of the XRT was studied well by Ishisaki (1996) based on the Crab observations. The intensity of the stray light predicted by the ray-tracing simulation was shown to have an error of 15–20%. Figure 6.3, 6.11, 6.18, and 6.27 also show that the fraction of stray light coming from offset angles $> 40'$ is at most 50% for all observed regions, causing an intensity error of about a 10%. If all of this intensity falls in the hard band, we would observe 10% higher HR value than the true case. The spectrum of the stray light becomes harder for offset angles $\sim 30'$, and then softer for larger angles, but the spectral change is not very drastic. Considering this spectral behavior, we may assume that the systematic error of the *HR* is ±5% in the worst case. The change in the *HR* value by 5% causes a temperature change of about 10% for kT =3–4 keV. Therefore, 10% of the temperature is the conservative systematic error arising from our response estimation.

5.4.3 Surface Brightness Profile

Since the incident emission-measure profiles in calculating simulated clusters and response functions were based on the PSPC data in the 0.5–2 keV band, the difference in the sensitive energy ranges between PSPC and GIS might have caused some error in the present temperature results. The conversion factor from the PSPC count rate to emission measure varies by about 10% for a temperature range of 3–5 keV (Böhringer 1994). To investigate the systematic error due to the surface brightness profile, we first approximated the PSPC image with a β model and modified the model parameters. The two β models compared here are $\beta = 0.54$ and 0.61, with a common core radius of $3\mathop{.}^{\prime}9$. These parameters are given in table 2 of Tamura et al. (2000); the core radius and the lower β value are the best-fit values for the PSPC image, and the larger β is the maximum boundary value for the GIS fit, respectively. We took A1060 for this study because it has the lowest intensity. The variations of the temperature for the 2 models are 0.05 and 0.01 keV for $r < 30'$ and $r > 30'$, respectively, on the average. The largest difference in a single region ($5' \times 5'$) was 0.13 keV. Therefore, we may say that the error in the surface brightness model causes a fairly small systematic error.

5.4.4 Point Sources

A possible influence from hard point sources to the temperature map was investigated. In figure 4c for the Centaurus cluster, a small hot region is seen at $35'$ south of the cluster center. The extent before taking the running mean is $\sim 2 \times 2$ cells ($5' \times 5'$), which is comparable to the point source image with the XRT response. This peak is barely seen in the 0.7–7 keV band, however, the hard band image above 2 keV shows a clear peak. The position is identified as CCC 032 (Jerjen, Dressler 1997); a galaxy of morphological type Im at a redshift $z = 0.00913$. The temperature derived with an absorbed MEKAL model for the spectrum within a radius of $5'$ is about 7 keV, consistent with the indication of the temperature map. The absorbed X-ray flux in 0.5–10 keV is estimated to be 2.4×10^{-12} erg cm^{-2} s^{-1}. However, about 70% of the flux is thought to be the cluster component according to the excess in the surface brightness. Therefore, the flux of about 7×10^{-13} erg cm^{-2} s^{-1} may have originated from the point source.

On the other hand, a compact group of galaxies, HCG 48, at $29'$ off from the A1060 center shows no significant structure in the temperature map, figure 4a. In fact, a spectral fit gives a temperature of 3.3 keV, consistent with the A1060 ICM. We note that the X-ray emission peak does not correspond to the central elliptical galaxy in HCG 48, but to a Sa galaxy, ESO 501–G 059, at $2.6'$ south.

These results show that we can distinguish contaminations of point sources or galaxy groups with angular sizes $\sim 5'$ in terms of either distinct features in the temperature map or excess emission in the X-ray image. Since the extent of the hot region in Centaurus is considerably larger than the distinguishable size, it is unlikely that the temperature structures of the ICM are strongly affected by source contaminations.

Chapter 6

Results

Based on the hardness ratio analysis as described in the previous chapter, we attempt here to produce two-dimensional temperature maps for the 4 clusters (see figure 6.4, 6.12, 6.19, 6.28). Before carrying out the temperature determination, the images were binned into cells with a size of $5' \times 5'$ for A1060 and AWM7, and $2.5' \times 2.5'$ for Centaurus and Perseus. Table 6.1 summarizes geometrical parameters for each cluster in the present analysis. The latter two clusters are much brighter than the others. The angular scales of the cells correspond to actual sizes of 100, 151, 45, and 78 kpc for A1060, AWM 7, Centaurus, and Perseus, respectively. Furthermore, to suppress the fluctuation, we took an intensity-weighted average for 4×4 cells ($20' \times 20'$ for A1060 and AWM7, $10' \times 10'$ for Centaurus and Perseus), and showed the temperatures by successively shifting the center by one cell. Therefore, the color-coded maps show running means of the temperature, in which sharp structures are suppressed. These running means were only adopted in the color representation of each temperature map, and quantitative analysis was carried out on individual cells or their combinations without taking the running means. The temperature maps are shown for a spatial range where statistical errors in the 4×4 cells are less than 10% for A1060, AWM 7, and Perseus, and less than 15% for Centaurus, respectively.

Table 6.1: Geometrical parameters for the four clusters

	A1060	AWM7	Centaurus	Perseus
redshift	0.0114	0.0172	0.0104	0.0183
angular size of $1'$	19.5 kpc	29.1 kpc	17.8 kpc	30.9 kpc
covered radius	0.6 Mpc	1.2 Mpc	0.9 Mpc	1.8 Mpc
size of 1 cell†	98 kpc	146 kpc	45 kpc	77 kpc
size of 4 cells‡	390 kpc	580 kpc	180 kpc	310 kpc

† The unit size in the temperature maps. ‡ The unit area for the calculation of temperatures.

Since the color-coded maps give no information about the error, we also present the temperature values for 7 concentric annular regions in figure 6.5, 6.13, 6.20, and 6.29. Their radii are $r = 0' - 2' - 4' - 8' - 12' - 20' - 28' - 36'$, and the data points are mutually independent (no running means). Each ring in the radius range of $r > 4'$ into equally divided to 8 azimuthal sections with an opening angle of 45° each, but the inner ring $(2' - 4')$ is azimuthal sections with 90°. The error bars indicate 90% statistical errors.

To obtain detailed spectral information for selected regions, we also carried out spectral fits. The XRT responses for the spectra are produced by the ray-tracing simulation based on the PSPC image with the assumption of the constant temperature. Observed properties of individual clusters are described in detail in the following sections.

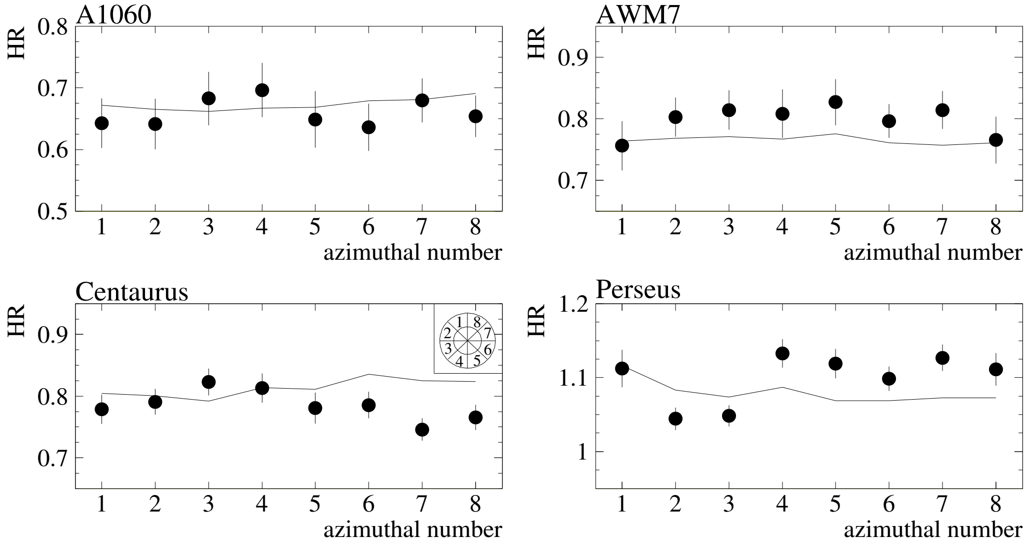

Figure 6.1: Variation of the *HR* in the azimuthal direction with radius $10' - 20'$ for the four clusters. The filled circles indicate the observed values, and the solid lines show the simulated values for isothermal clusters. The error bars show 90% confidence levels for a single parameter.

Examples of the *HR*s are shown in figure 6.1, in which observed *HR* profiles in an azimuthal direction are compared with simulated values for a radius of $10' - 20'$ for the four clusters. The error bars of the data are 90% statistical errors. For the simulated clusters, we assume an isothermal ICM with the average temperature for the hot component based on the previous ASCA results. The assumed spectral parameters are listed in table 5.4. Because of the XRT response, even the simulated *HR*s vary by about 5% from position to position. We note that the simulated isothermal clusters also included the abundance gradients which are significantly detected for AWM 7, Centaurus, and Perseus as described in section 2.3.

6.1 Abell 1060

Figure 6.2 shows the GIS2 image in the 0.7–7 keV band. The image is smoothed by a Gaussian function with $\sigma = 1'$ after subtraction of the non X-ray and the cosmic X-ray backgrounds and exposure correction. The X-ray image shows good circular symmetry, and does not show a narrow peak at the center, such as that in the Centaurus. An X-ray source seen at 29′ north-east of the cluster center is the compact group of galaxies, HCG 48, which has the similar line-of-sight distance as A1060 ($z = 0.0094$ for HCG 48). The right panels in figure 6.2 show the surface profiles projected onto RA and DEC axes. At about 30′ away from the cluster center, the level of the cluster component becomes comparable to the background consisting of NXB and CXB.

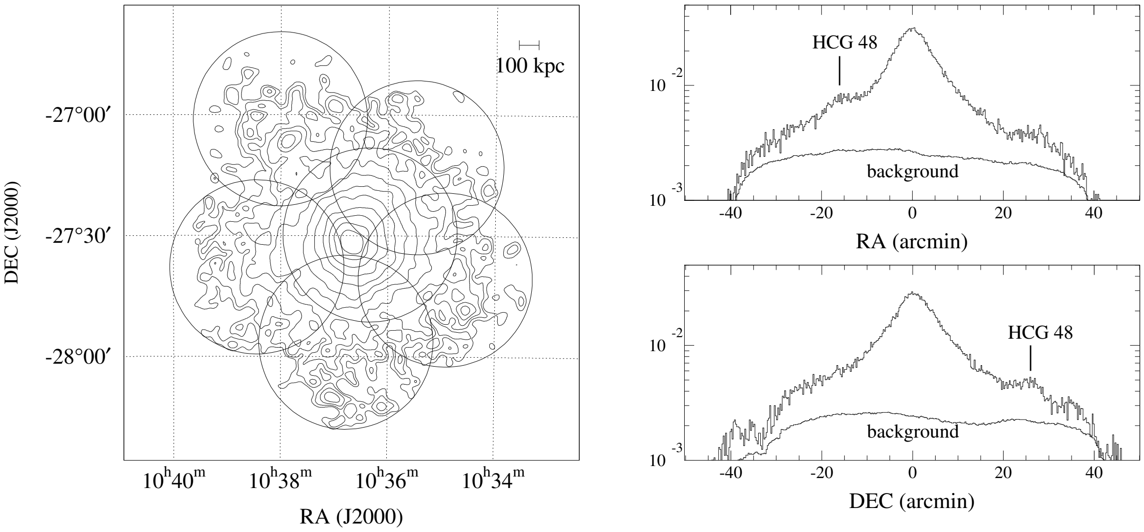

Figure 6.2: *left* – The GIS2 image of the A1060 in the energy range 0.7–7.0 keV. Circles with radii of 22′ show the GIS field of view. *right* – The profiles projected on the RA (upper) and DEC (lower) axes compared with the background.

6.1.1 Temperature structure

First, we have carried out the ray-tracing simulation to correct for the effects on the XRT response. Fractions of photon origins for the simulated isothermal cluster are shown in figure 6.3a in 7 concentric ring regions $r = 0' - 4' - 8' - 12' - 20' - 28' - 36' - 44'$. The temperature map for the isothermal cluster is shown in figure 6.3b. Because hardness ratios become lower toward the edge of the GIS field, the apparent temperature shows artificial variations in the mapping field. Results in figure 6.3a and b are derived for the full image by combining all pointings with a weight of exposure times. In the central region, 80% of the detected photons have their origin ("direct") in the corresponding sky

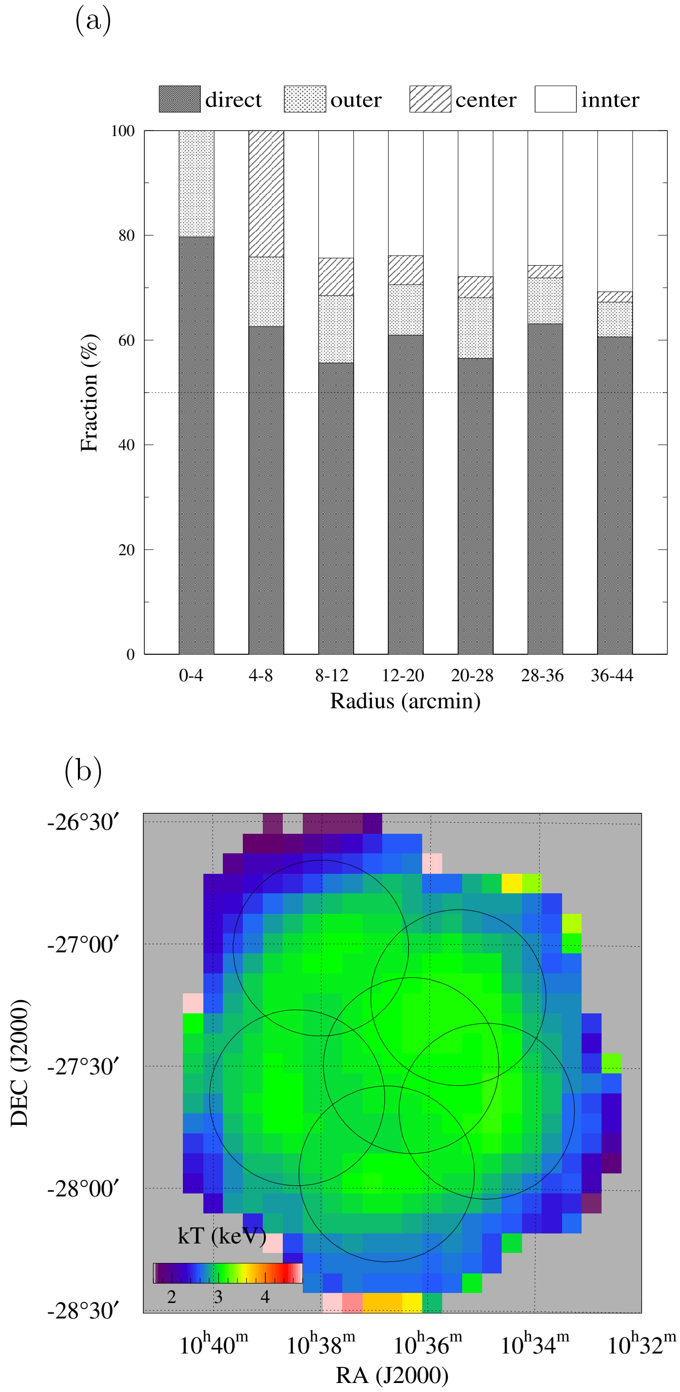

Figure 6.3: (a) Fractions of the photon origin and (b) color-coded temperature map for A1060 estimated from the isothermal simulation. "center" indicates the photons coming from the central $r < 4'$ region.

region . For other regions, the fraction of the direct photons accounts for about 60% of the detected photons even in the $r = 36' - 44'$ ring. The fraction of photons from the central $r < 4'$ region shown as "center" is only few percent for the outer regions $r > 20'$. As shown in figure 6.3b, the lack of complete uniformity in the temperatures is mainly caused by the energy-dependence of the effective area with an off-axis angle from the

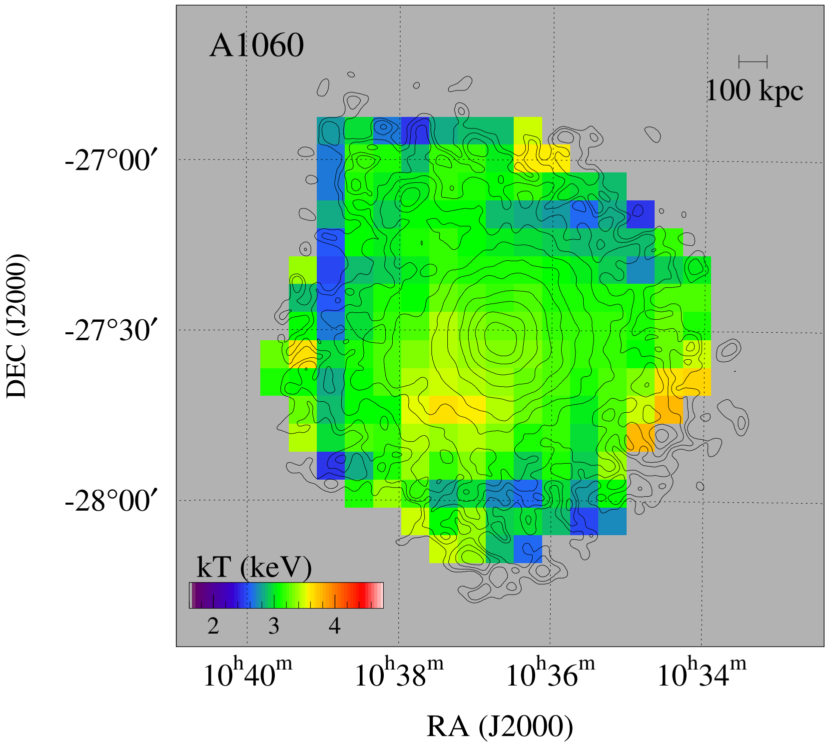

Figure 6.4: Color-coded temperature map for A1060. X-ray intensity with the GIS2 is shown with contours.

optical axis.

As mentioned in Chapter 4, we have calculated the hardness ratios and derived the temperatures from the $HR - kT$ relation after taking the ratios of the observed HRs to the simulated HRs. Figure 6.4 shows the color-coded temperature map for the observed A1060 data, suggesting that the temperature variation in A1060 is less than 15% of the average value in the whole cluster region. The temperature structure looks almost isothermal at 3.2 keV, but the region at $\sim 15'$ south-east from the cluster center seems slightly hot. There is no significant temperature rise or drop at the group of galaxies HCG 48.

The isothermality is also examined by the azimuthal plot of the temperature in the 7 concentric annuli. The azimuthal variation of temperatures are shown in figure 6.5. The observed and simulated HR values and the calculated temperature values are listed in table 6.2. The maximum and minimum temperatures are about 5 keV and 2 keV. The errors show 90% confidence level of only the statistical error. Fitting a model with a constant value to the data in figure 6.5 gives a mean temperature of 3.26 ± 0.06 keV with $\chi^2/\nu = 57.2/44$. The error corresponds to $\Delta\chi^2 = 2.706$ for the statistical errors only. The mean temperature is consistent with the previous result of 3.3 ± 0.1 keV based on the spectral fitting within the central $r < 5'$ region by Tamura et al. (1996, 2000).

Table 6.2: The observed and simulated *HR* values and the corrected temperatures for A1060 shown in fig 6.5.

radius	azimuth	data *HR*	simulated *HR*	kT (keV)
$< 2'$	–	0.70 ± 0.02	0.69 ± 0.003	$3.35^{+0.26}_{-0.24}$
$2' - 4'$	NE	0.67 ± 0.03	0.69 ± 0.003	$3.14^{+0.34}_{-0.30}$
	SE	0.73 ± 0.03	0.67 ± 0.004	$3.78^{+0.43}_{-0.38}$
	SW	0.68 ± 0.03	0.69 ± 0.004	$3.18^{+0.37}_{-0.32}$
	NW	0.71 ± 0.03	0.68 ± 0.003	$3.54^{+0.41}_{-0.36}$
$4' - 8'$	NNE	0.71 ± 0.03	0.69 ± 0.003	$3.45^{+0.39}_{-0.34}$
	ENE	0.64 ± 0.02	0.66 ± 0.003	$3.12^{+0.34}_{-0.30}$
	ESE	0.71 ± 0.03	0.66 ± 0.003	$3.75^{+0.41}_{-0.36}$
	SSE	0.69 ± 0.03	0.66 ± 0.003	$3.59^{+0.40}_{-0.35}$
	SSW	0.69 ± 0.03	0.68 ± 0.003	$3.35^{+0.39}_{-0.34}$
	WSW	0.66 ± 0.02	0.68 ± 0.003	$3.09^{+0.32}_{-0.28}$
	WNW	0.68 ± 0.02	0.69 ± 0.003	$3.18^{+0.29}_{-0.26}$
	NNW	0.65 ± 0.02	0.69 ± 0.003	$3.02^{+0.29}_{-0.26}$
$8' - 12'$	NNE	0.68 ± 0.03	0.69 ± 0.004	$3.19^{+0.44}_{-0.37}$
	ENE	0.63 ± 0.03	0.66 ± 0.004	$3.05^{+0.42}_{-0.35}$
	ESE	0.71 ± 0.03	0.66 ± 0.004	$3.65^{+0.52}_{-0.44}$
	SSE	0.68 ± 0.03	0.66 ± 0.004	$3.40^{+0.47}_{-0.40}$
	SSW	0.68 ± 0.03	0.67 ± 0.004	$3.41^{+0.47}_{-0.40}$
	WSW	0.64 ± 0.03	0.67 ± 0.003	$3.03^{+0.36}_{-0.31}$
	WNW	0.72 ± 0.03	0.68 ± 0.003	$3.60^{+0.38}_{-0.34}$
	NNW	0.69 ± 0.03	0.69 ± 0.003	$3.27^{+0.35}_{-0.31}$
$12' - 20'$	NNE	0.63 ± 0.03	0.67 ± 0.003	$2.98^{+0.38}_{-0.32}$
	ENE	0.65 ± 0.03	0.67 ± 0.003	$3.13^{+0.42}_{-0.35}$
	ESE	0.69 ± 0.03	0.66 ± 0.003	$3.50^{+0.48}_{-0.41}$
	SSE	0.72 ± 0.03	0.67 ± 0.003	$3.67^{+0.51}_{-0.43}$
	SSW	0.62 ± 0.03	0.67 ± 0.004	$2.92^{+0.46}_{-0.38}$
	WSW	0.65 ± 0.03	0.69 ± 0.003	$2.98^{+0.38}_{-0.33}$
	WNW	0.65 ± 0.03	0.68 ± 0.003	$3.02^{+0.34}_{-0.30}$
	NNW	0.63 ± 0.02	0.69 ± 0.003	$2.85^{+0.30}_{-0.27}$
$20' - 28'$	NNE	0.63 ± 0.04	0.67 ± 0.004	$3.00^{+0.57}_{-0.45}$
	ENE	0.63 ± 0.05	0.68 ± 0.005	$2.96^{+0.74}_{-0.55}$
	ESE	0.58 ± 0.05	0.69 ± 0.005	$2.56^{+0.61}_{-0.46}$
	SSE	0.63 ± 0.05	0.68 ± 0.006	$2.87^{+0.74}_{-0.55}$
	SSW	0.70 ± 0.06	0.67 ± 0.006	$3.50^{+0.96}_{-0.72}$
	WSW	0.77 ± 0.06	0.71 ± 0.005	$3.79^{+0.91}_{-0.71}$
	WNW	0.66 ± 0.06	0.69 ± 0.005	$3.04^{+0.82}_{-0.60}$
	NNW	0.60 ± 0.04	0.69 ± 0.004	$2.68^{+0.58}_{-0.44}$

Table 6.2 (continued)

radius	azimuth	data *HR*	simulated *HR*	*kT* (keV)
$28' - 36'$	NNE	0.72 ± 0.05	0.68 ± 0.005	$3.58^{+0.76}_{-0.61}$
	ENE	0.58 ± 0.09	0.68 ± 0.007	$2.60^{+1.36}_{-0.79}$
	ESE	0.79 ± 0.10	0.67 ± 0.006	$4.47^{+1.94}_{-1.31}$
	SSE	0.57 ± 0.08	0.66 ± 0.008	$2.66^{+1.20}_{-0.74}$
	SSW	0.55 ± 0.08	0.66 ± 0.008	$2.52^{+1.23}_{-0.74}$
	WSW	0.69 ± 0.07	0.68 ± 0.006	$3.38^{+1.08}_{-0.77}$
	WNW	0.60 ± 0.11	0.65 ± 0.007	$2.85^{+1.82}_{-0.99}$
	NNW	0.64 ± 0.11	0.66 ± 0.008	$3.08^{+1.86}_{-1.04}$

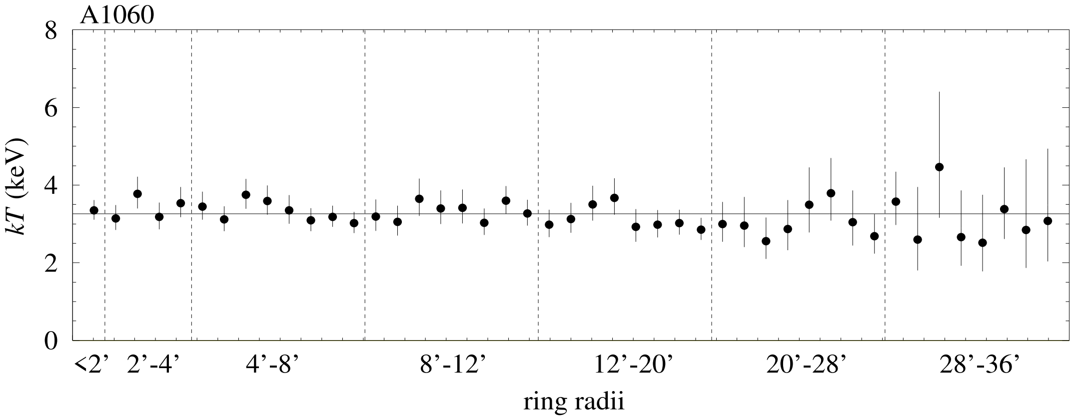

Figure 6.5: Azimuthal profiles of temperature in 7 annular regions for A1060. The error bars show 90% confidence levels. The ring radii are indicated in the abscissa and each ring is divided to 8 azimuthal sections with an opening angle of 45° (4 sections with 90° for the innermost ring of $2' - 4'$) in a counterclockwise direction from the north. The solid lines show the mean temperatures by constant-temperature fits.

We also have made a frequency histogram of the temperatures as shown in figure 6.6. The temperatures are calculated in one cell ($5'$) over the area where the statistical errors are within 25% that actually corresponds to about a radius of $30'$. The histogram is fitted with a Gaussian function. The mean temperature is 3.1 keV, and the standard deviation is 0.61 keV (19%). The deviation is smaller than the maximum statistical error taken here. Figure 6.7 shows temperature profiles along the two paths where path-A and B run from south-west to north-east direction, and from south-east to north-west direction, respectively. The south-east hot region is included in path-B. Actually, the profile for path-B seems to show some variation while the profile of path-A is almost flat. In order to look into the spectral feature, we have also performed spectral analysis as described later.

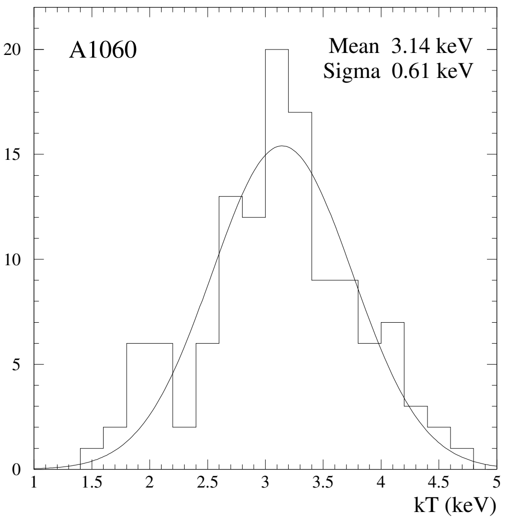

Figure 6.6: Frequency distribution of temperatures for A1060 fitted with Gaussian function.

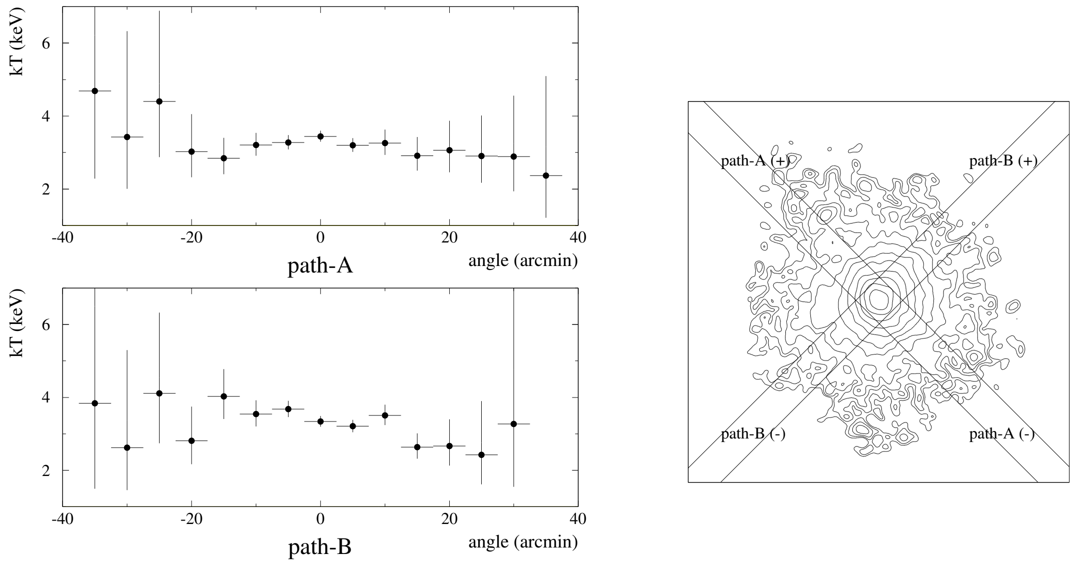

Figure 6.7: One-dimensional profiles of temperature for A1060 along the two paths shown in the right panel, along SW to NE direction (path-A) and SE to NW direction (path-B), shown as a function of the angle from the cluster center. The temperature in each bin is calculated for a $10' \times 5'$ rectangle. The error bars show 90% confidence levels.

6.1.2 Spectra

To look at the temperature features in terms of the pulse-height spectra, we accumulated the data for selected regions. The regions are shown in the right panel of figure 6.8. The south-east region of #2 indicates slightly higher temperature compared with the region #1, the significance should be confirmed. We assumed an absorbed MEKAL model and the response for an isothermal cluster, which do not require a priori knowledge of the temperature distribution (as in Honda et al. 1996). The spectra and the best-fit models are shown in figure 6.8, and the ratios between data and the best-fit model for the medium-temperature region #1 ("med") are shown in the bottom panel. The normalizations are arbitrarily scaled to help in a visual comparison. The results of the spectral fits are summarized in table 6.3. The errors are statistical and 90%-confidence levels for single parameter of interest. The difference in the best-fit temperatures are only 0.2 keV (7%) and the 90% error range of the temperatures and metal abundances between #1 and #2 overlap with each other. The temperature in the south-east region is smaller than that in figure 6.7. The difference is likely to be due to the integrated area. Since no other regions suggest a larger deviation in temperature, we conclude that the ICM in A1060 is consistent to be isothermal with an angular resolution of 10′ scale.

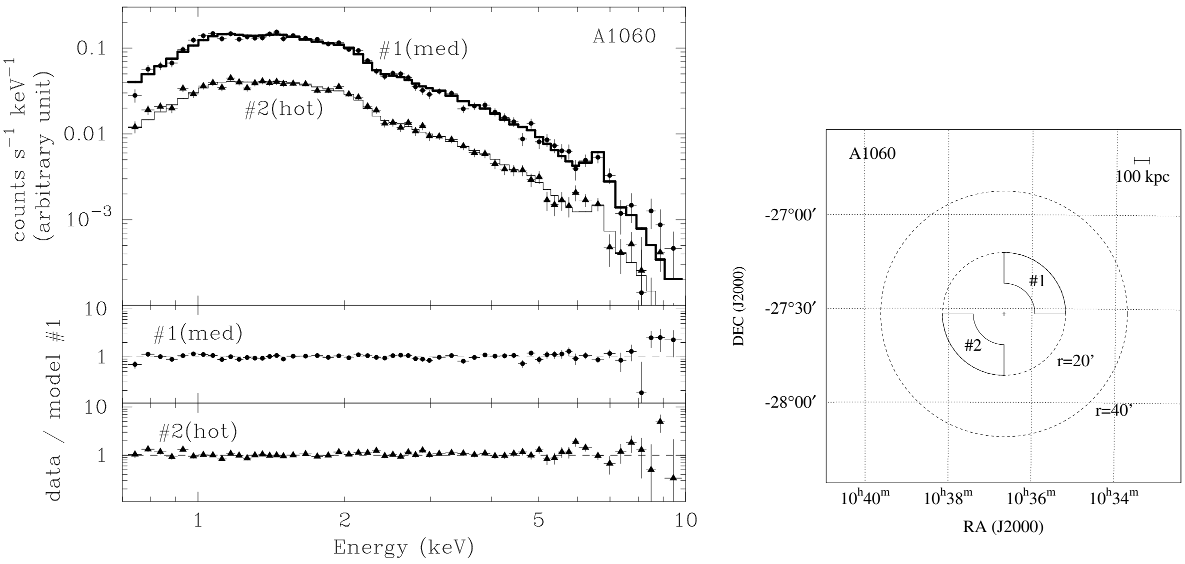

Figure 6.8: Pulse-height spectra for two selected regions in A1060 fitted with thermal models. The bottom panels show data-to-model ratios for a common model, which is the best-fit model of #1 ("med") shown by the thick line in the top panel. The right panel shows corresponding regions, in which the dashed circles show radii of 20′ and 40′.

Table 6.3: Spectral parameters for selected regions of A1060.

region no.*	$N_{\rm H}$	kT	Z	$\chi^2/d.o.f$
	(10^{20} cm^{-2})	(keV)	(solar)	
#1 (med)	3.5(fix)	$3.00^{+0.14}_{-0.13}$	$0.44^{+0.14}_{-0.12}$	67.0/55
#2 (hot)	3.5(fix)	$3.19^{+0.19}_{-0.18}$	$0.30^{+0.15}_{-0.13}$	60.1/55

* Corresponding regions are shown in figure 6.8

6.1.3 HCG 48

A compact group of galaxies, HCG 48 at a redshift of $z = 0.0094$, consists of only four galaxies: central elliptical galaxy IC 2597 (HCG 48 A), an Sa galaxy ESO 501-G 059 (HCG 48 B), an S0a galaxy (HCG 48 C) and an elliptical galaxy (HCG 48 D). Figure 6.9a shows the GIS image smoothed by a Gaussian function with $\sigma = 15''$ after background subtraction and exposure correction, overlaid on the optical image. The peak of X-ray emission does not correspond to the central elliptical galaxy (HCG 48 A), but to the southern Sa galaxy (HCG 48 B).

The pulse-height spectrum with a radius of $4'$ is shown in figure 6.9b. We used the public GIS blank-sky event for the background. We fit the spectrum with an absorbed MEKAL model where the Galactic absorption and metal abundance are fixed to the best-fit values of A1060 center ($N_{\rm H} = 3.5 \times 10^{21}$ cm^{-2}, $Z = 0.31$ solar) because of the low statistics. The obtained temperature is $3.3^{+0.8}_{-0.5}$ keV with $\chi^2/\nu = 11.7/10$, and the absorbed flux in the 0.5–10 keV is estimated to be 1.6×10^{-12} erg cm^{-2} s^{-1}. The similar temperature to that of A1060 is agreement with no significant structure in the temperature map. Since the spectrum is thought to include the surrounding cluster component of 3 keV, we have taken a spectrum at the same distance from cluster center in the same FOV as another background to examine intrinsic spectrum of HCG 48. The spectrum shows a higher temperature of $3.6^{+1.3}_{-0.8}$ keV with an absorbed MEKAL model or the photon index of 2.1 ± 0.2 with an absorbed power-law model. The X-ray emission is not likely from the hot gas associated with the group of galaxies, it might be possible from the HCG 48B component as an AGN.

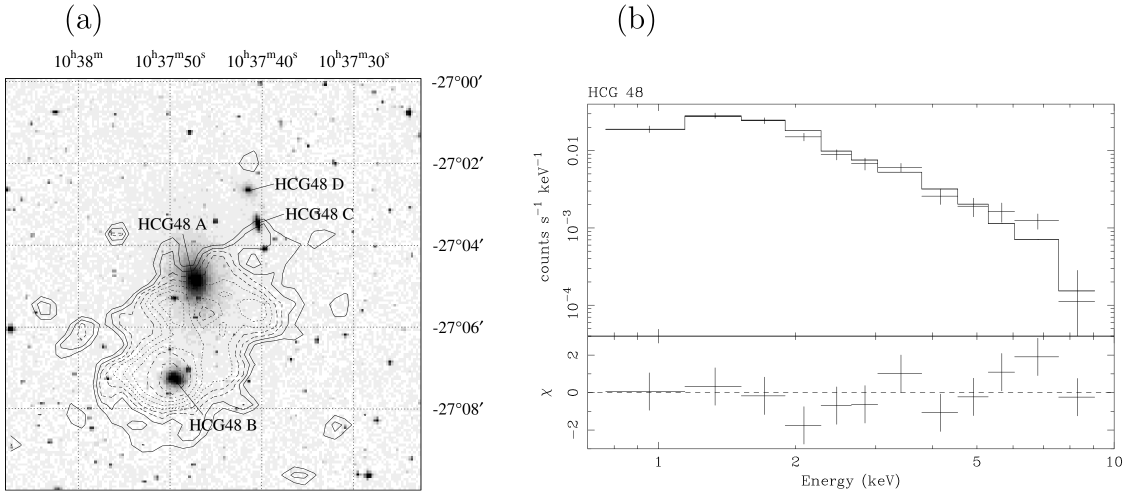

Figure 6.9: (a) GIS image of HCG 48 in the 0.7–7 keV band superposed on the optical image taken from Digitized Sky Survey supported by NASA *SkyView*. The X-ray peak corresponds to a Sa galaxy, ESO 501-G 059 (HCG48 B). (b) Pulse-height spectra of HCG 48 fitted with an absorbed MEKAL model.

6.2 AWM 7

Figure 6.10 shows the GIS2 image in the 0.7–7 keV energy band. The X-ray image is elongated in the east-west direction in parallel to the filament structure of Pisces-Perseus supercluster. AWM7 is located at 6° west of the Perseus cluster. Since their redshifts are similar (0.0172 and 0.0183), three-dimensional distance between the cluster centers is 12 Mpc. There are no obvious point sources. The right panel in figure 6.10 shows the surface brightness profiles projected on the RA and DEC axes, suggesting a very mild central concentration.

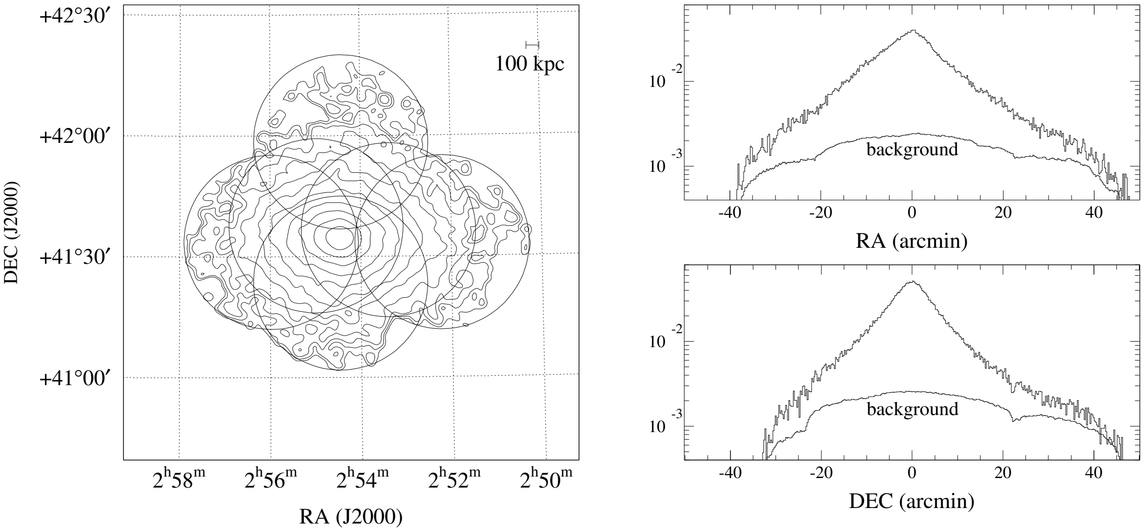

Figure 6.10: *left* – The GIS2 image of the AWM7 in the energy range 0.7–7.0 keV. Circles with radii of 22′ show the GIS field of view. *right* – The profiles projected on the RA (upper) and DEC (lower) axes and compared with the background.

6.2.1 Temperature structure

We have performed a simulation for a 3.6 keV isothermal cluster with the spectral model shown in table 5.4. The metal abundance gradient, extending to the whole cluster, is taken into account as described in chapter 4. The results of the ray-tracing simulation are shown in figure 6.11a and b. Both are derived in the same manner as in figure 6.3 for A1060. Figure 6.11a presents the fraction of the photon origins in the 7 concentric ring regions of $r = 0' - 4' - 8' - 12' - 20' - 28' - 36' - 44'$. In the central region, 80% of the detected photons have their origin in the corresponding sky region. For other regions, the fraction of the direct photons accounts for about 60% of the detected photons even in the $r = 36' - 44'$ ring. Figure 6.11b shows the simulated color-coded temperature map. Since the FOVs in the central region overlap each other, the simulation reproduces an

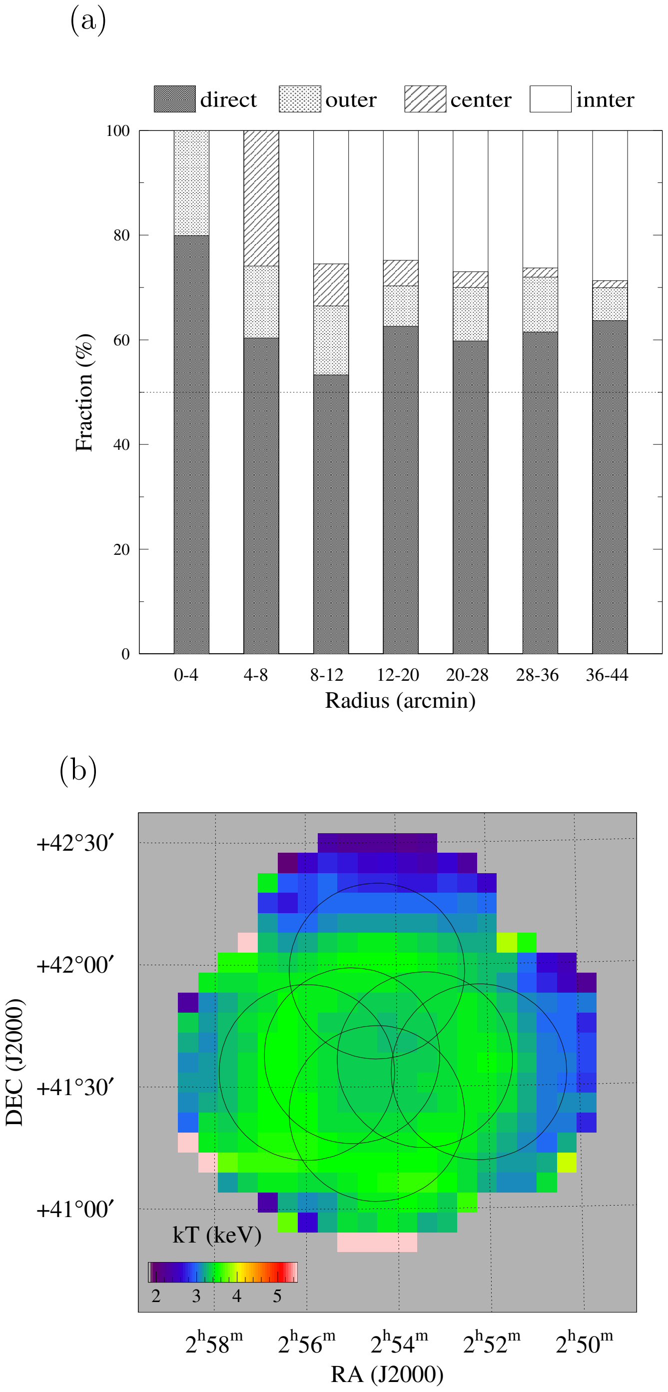

Figure 6.11: (a) Fractions of the photon origin and (b) color-coded temperature map for AWM7 estimated from the isothermal simulation.

isothermal temperature map. At the edge of the north pointing, the temperatures look slightly non-uniform with a difference of -0.6 keV from the input model.

Figure 6.12 shows the color-coded temperature map for the actual data superposed on the GIS brightness contours. The temperature fluctuation is less than 15% of the average value in the whole cluster. Especially, the central region within a radius of $20'$ is very isothermal. This result is consistent with the previous ones by Xu et al. (1997) and

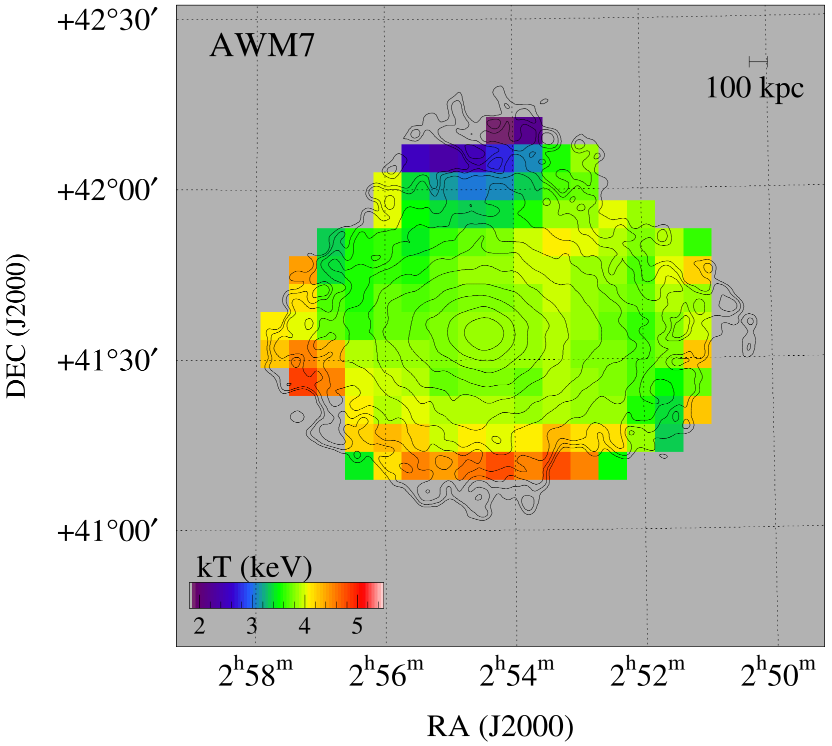

Figure 6.12: Color-coded temperature map for AWM7. X-ray intensity with the GIS2 is shown with contours.

Ezawa et al. (1997). In the previous X-ray results, the cool component exists barely in the central $r < 2'$ region where an excess of the surface brightness is seen (Neumann, & Böhringer 1995). However, there is no clear temperature drop at the central region. One reason is that the cool component is very weak in the GIS data, and the temperature after averaging over a $20' \times 20'$ region shows almost no signature in the temperature map. In the outer region, there are some structures near the north and south edges. The south region with an angular extent of $\sim 30'$ in the east-west direction is suggested to be hot with a temperature of 4.5 keV. On the other hand, the north region shows a low temperature around 2.5 keV.

The azimuthal variation of temperatures are shown in figure 6.13. The error bars show 90% confidence level. The fitting with a constant model gives a mean temperature of 3.82 ± 0.06 keV with $\chi^2/\nu = 55.5/44$. A temperature drop due to the cool component is seen in the central $r < 2'$ region only. If this central region is excluded, the reduced chi-square becomes significantly smaller, $\chi^2/\nu = 42.1/43$ with a mean temperature of 3.85 ± 0.06 keV. Both of the mean temperatures agree with the cluster average of 3.9 ± 0.2 keV with the central pointing obtained by Markevitch and Vikhlinin (1997). They also derived a two-dimensional temperature map for the central pointing and found it isothermal.

Table 6.4: The observed and simulated *HR* values and the corrected temperatures shown in fig 6.14 for AWM7.

radius	azimuth	data *HR*	simulated *HR*	kT (keV)
$< 2'$	–	0.72 ± 0.01	0.74 ± 0.002	$3.48^{+0.17}_{-0.16}$
$2' - 4'$	NE	0.78 ± 0.02	0.74 ± 0.002	$3.98^{+0.29}_{-0.26}$
	SE	0.75 ± 0.02	0.75 ± 0.003	$3.67^{+0.26}_{-0.24}$
	SW	0.80 ± 0.02	0.74 ± 0.003	$4.12^{+0.31}_{-0.28}$
	NW	0.77 ± 0.02	0.74 ± 0.003	$3.92^{+0.29}_{-0.26}$
$4' - 8'$	NNE	0.79 ± 0.02	0.74 ± 0.002	$4.04^{+0.30}_{-0.28}$
	ENE	0.77 ± 0.02	0.76 ± 0.002	$3.72^{+0.26}_{-0.24}$
	ESE	0.78 ± 0.02	0.75 ± 0.002	$3.88^{+0.27}_{-0.25}$
	SSE	0.79 ± 0.02	0.75 ± 0.003	$3.91^{+0.31}_{-0.29}$
	SSW	0.78 ± 0.02	0.76 ± 0.003	$3.86^{+0.32}_{-0.29}$
	WSW	0.77 ± 0.02	0.75 ± 0.002	$3.79^{+0.27}_{-0.25}$
	WNW	0.81 ± 0.02	0.75 ± 0.003	$4.21^{+0.32}_{-0.29}$
	NNW	0.75 ± 0.02	0.74 ± 0.003	$3.69^{+0.29}_{-0.27}$
$8' - 12'$	NNE	0.75 ± 0.03	0.76 ± 0.003	$3.54^{+0.37}_{-0.33}$
	ENE	0.79 ± 0.02	0.77 ± 0.003	$3.81^{+0.32}_{-0.29}$
	ESE	0.82 ± 0.02	0.77 ± 0.003	$4.07^{+0.35}_{-0.32}$
	SSE	0.79 ± 0.03	0.77 ± 0.003	$3.82^{+0.39}_{-0.35}$
	SSW	0.79 ± 0.03	0.77 ± 0.003	$3.81^{+0.38}_{-0.34}$
	WSW	0.81 ± 0.02	0.76 ± 0.003	$4.05^{+0.33}_{-0.30}$
	WNW	0.80 ± 0.02	0.76 ± 0.003	$3.94^{+0.33}_{-0.30}$
	NNW	0.81 ± 0.03	0.75 ± 0.003	$4.15^{+0.43}_{-0.39}$
$12' - 20'$	NNE	0.77 ± 0.03	0.77 ± 0.004	$3.55^{+0.45}_{-0.39}$
	ENE	0.77 ± 0.02	0.78 ± 0.003	$3.47^{+0.32}_{-0.29}$
	ESE	0.81 ± 0.02	0.78 ± 0.003	$3.83^{+0.35}_{-0.32}$
	SSE	0.80 ± 0.03	0.78 ± 0.003	$3.77^{+0.44}_{-0.39}$
	SSW	0.84 ± 0.03	0.78 ± 0.003	$4.12^{+0.45}_{-0.40}$
	WSW	0.80 ± 0.02	0.77 ± 0.002	$3.82^{+0.30}_{-0.27}$
	WNW	0.81 ± 0.02	0.77 ± 0.003	$3.98^{+0.35}_{-0.32}$
	NNW	0.77 ± 0.03	0.76 ± 0.003	$3.65^{+0.43}_{-0.38}$
$20' - 28'$	NNE	0.79 ± 0.06	0.79 ± 0.005	$3.59^{+1.00}_{-0.75}$
	ENE	0.79 ± 0.05	0.78 ± 0.005	$3.61^{+0.80}_{-0.64}$
	ESE	0.88 ± 0.05	0.79 ± 0.005	$4.53^{+0.92}_{-0.76}$
	SSE	0.94 ± 0.09	0.78 ± 0.007	$5.19^{+1.77}_{-1.32}$
	SSW	0.93 ± 0.08	0.79 ± 0.007	$5.05^{+1.48}_{-1.14}$
	WSW	0.80 ± 0.04	0.79 ± 0.004	$3.69^{+0.54}_{-0.46}$
	WNW	0.79 ± 0.04	0.78 ± 0.004	$3.70^{+0.62}_{-0.52}$
	NNW	0.86 ± 0.06	0.79 ± 0.005	$4.25^{+1.01}_{-0.80}$

Table 6.4 (continued)

radius	azimuth	data HR	simulated HR	kT (keV)
$28' - 36'$	NNE	0.53 ± 0.11	0.75 ± 0.008	$2.14^{+1.81}_{-0.90}$
	ENE	0.93 ± 0.15	0.76 ± 0.010	$5.57^{+3.69}_{-2.23}$
	ESE	0.80 ± 0.12	0.76 ± 0.011	$3.97^{+2.41}_{-1.43}$
	SSE	0.77 ± 0.19	0.77 ± 0.019	$3.59^{+4.33}_{-1.81}$
	SSW	0.83 ± 0.24	0.75 ± 0.017	$4.40^{+6.45}_{-2.49}$
	WSW	0.75 ± 0.07	0.76 ± 0.006	$3.52^{+1.20}_{-0.86}$
	WNW	0.81 ± 0.07	0.76 ± 0.006	$4.02^{+1.32}_{-0.97}$
	NNW	0.51 ± 0.10	0.76 ± 0.008	$2.02^{+1.46}_{-0.79}$

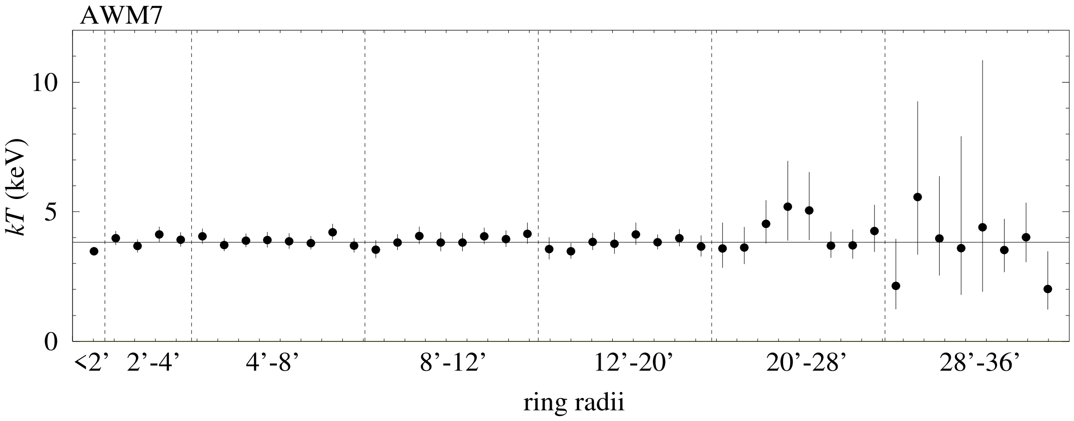

Figure 6.13: Azimuthal profiles of temperature for AWM7 in 7 concentric annular rings, in the same way as in figure 6.5.

The frequency histogram of the temperatures calculated for one cell is shown in figure 6.14. The distribution is for the data with relative statistical error to be less than 25% in a cell of $5' \times 5'$, which approximately corresponds to the central $r \sim 30'$ region. The histogram is fitted with a Gaussian function indicating the standard deviation to be 0.53 keV for a mean temperature of 3.81 keV. The rate of deviation to the mean of 14% is smaller than that of A1060. We have also examined the temperature profiles along two paths of north-south and east-west directions as shown in figure 6.15. The central region shows very little temperature drop of around 0.2 keV in both paths. The south and north regions at $20'$ off from the cluster center in path-B represent hot and cool as shown in the temperature map, but the statistics is very low. The temperatures along the east-west path are consistent with a constant value within the errors.

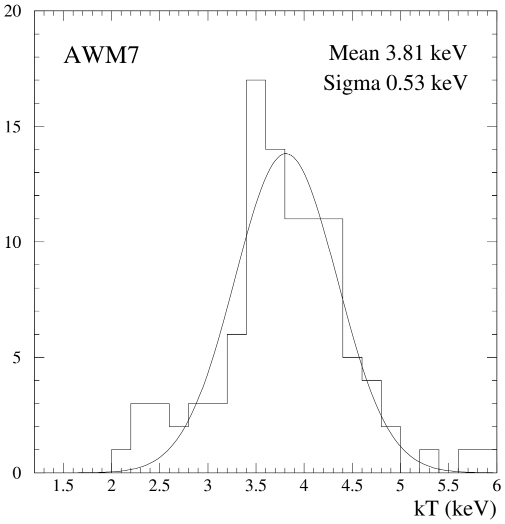

Figure 6.14: Frequency distribution of temperature for AWM7 fitted with Gaussian function.

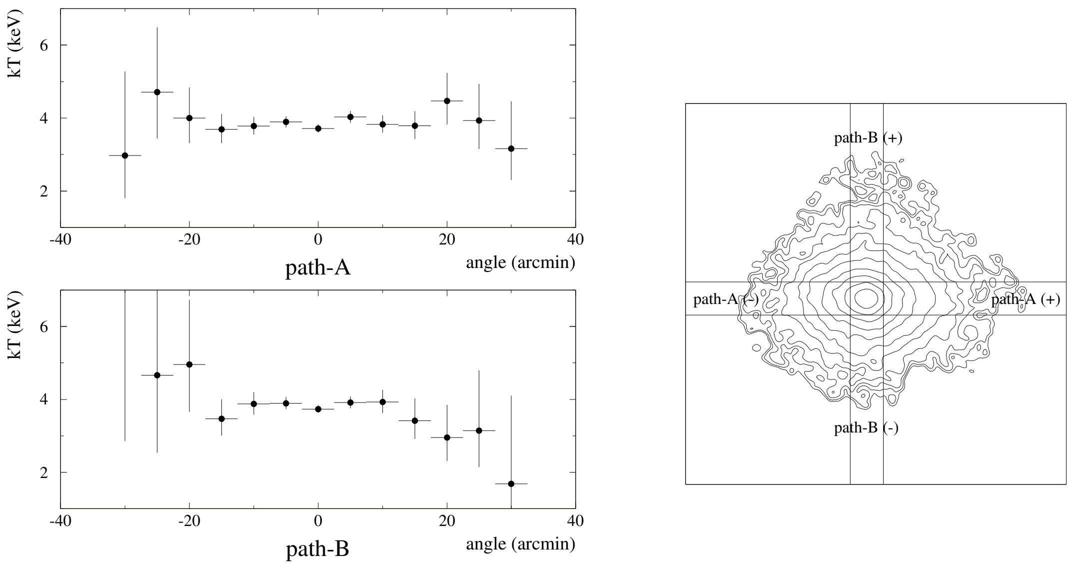

Figure 6.15: One-dimensional profiles of temperature for AWM7 along E to W direction (path-A) and S to N direction (path-B), shown as a function of the angle from the cluster center. The temperature in each bin is calculated for a $10' \times 5'$ rectangle. The right panel shows the calculated paths.

6.2.2 Spectra

The temperature map in figure 6.12 shows cool and hot features at about $20'$ north and south of the cluster center. We also fit the spectra for these regions (regions #1 and #2 in figure 6.16) with absorbed MEKAL models, and the data, best-fit models, and ratios to the best-fit model for the "cool" region #1 are shown in figure 6.16. As shown in table 6.5, the best-fit temperatures are $3.6^{+0.6}_{-0.4}$ keV for the north and $4.6^{+1.2}_{-0.7}$ keV for the south regions. The temperature difference is larger than the 90% error but less than the 95% limit, so this feature has a marginal statistical significance. The metal abundances in these two regions are consistent within the error.

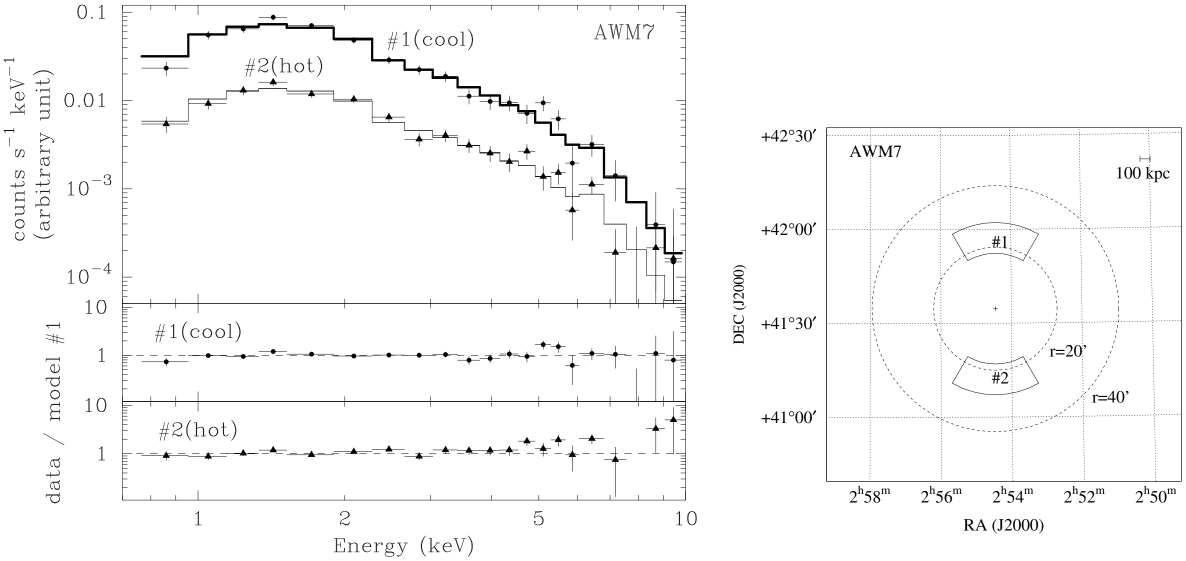

Figure 6.16: Pulse-height spectra for two regions (top panel) in AWM7, and the normalized ratios to the best-fit model of #1 (bottom panel) shown in the thick line in the top panel. The right panel corresponding regions of the spectra.

Table 6.5: Spectral parameters for selected regions of AWM 7.

region no.*	$N_{\rm H}$ (10^{20} cm^{-2})	kT (keV)	Z (solar)	$\chi^2/d.o.f$
#1 (cool)	8.7(fix)	$3.60^{+0.60}_{-0.44}$	$0.19^{+0.38}_{-0.19}$	22.5/18
#2 (hot)	8.7(fix)	$4.61^{+1.16}_{-0.70}$	$0.35^{+0.58}_{-0.23}$	24.2/18

* Corresponding regions are shown in figure 6.16

6.3 The Centaurus cluster

Figure 6.17 shows the X-ray image of the Centaurus cluster with the GIS2 in the 0.7–7 keV energy band. The extended emission around 15′ southeast from the cluster center is mainly caused by an artificial effect due to the XRT response, and also by an intrinsic structure as shown in figure 2.15. The X-ray emission is strongly peaked at the cD galaxy NGC 4696, and the central excess is characterized by a mixture of an intense hot and cool emission (Fukazawa et al. 1994; Allen and Fabian 1994; Ikebe et al. 1999). Strong metal concentration in the ICM, up to about 1.5 solar at the cluster center, is also seen, and the cD galaxy seems to play an important role in the central region.

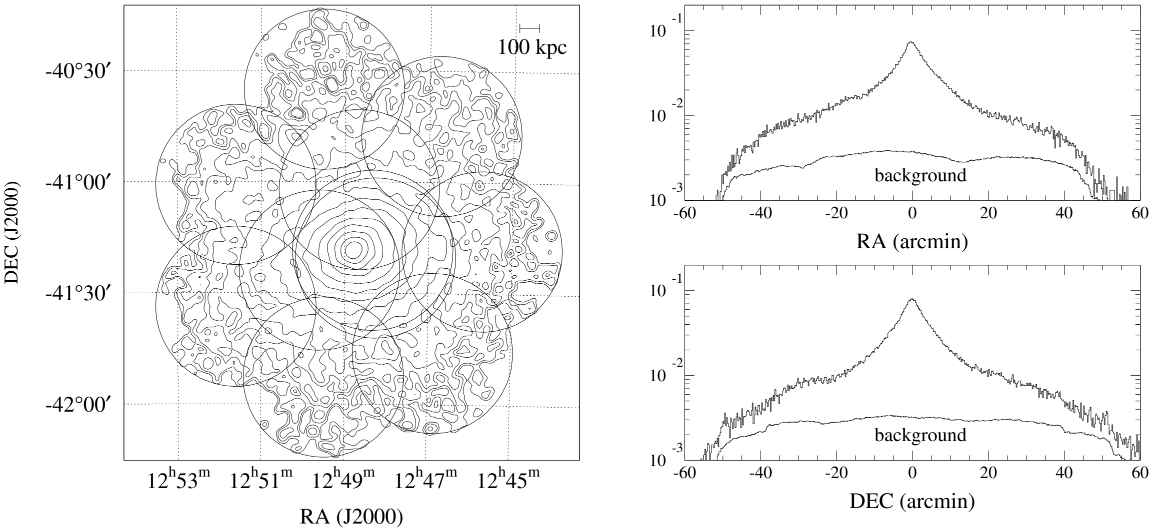

Figure 6.17: *left* – The GIS image of the Centaurus cluster in the energy range 0.7–7.0 keV. Circles with radii of 22′ show the GIS field of view. *right* – The profiles projected on the RA (upper) and DEC (lower) axes compared with the background.

6.3.1 Temperature structure

The results of isothermal simulation which includes the observed abundance gradient are shown in figure 6.18a and b. Figure 6.18a presents the fraction of the photon origins in the 7 concentric ring regions. The fraction in the $r = 4' - 8'$ region is strongly affected by photons from the central $r < 4'$ region, which account for 30% of the detected photons. Figure 6.18b shows the simulated color-coded temperature map. The apparent uneven temperature structure is caused by non-uniform coverage of the present mapping observations.

Figure 6.19a shows the temperature map for the observed Centaurus cluster without applying any correction to the central cool component. The temperatures, therefore,

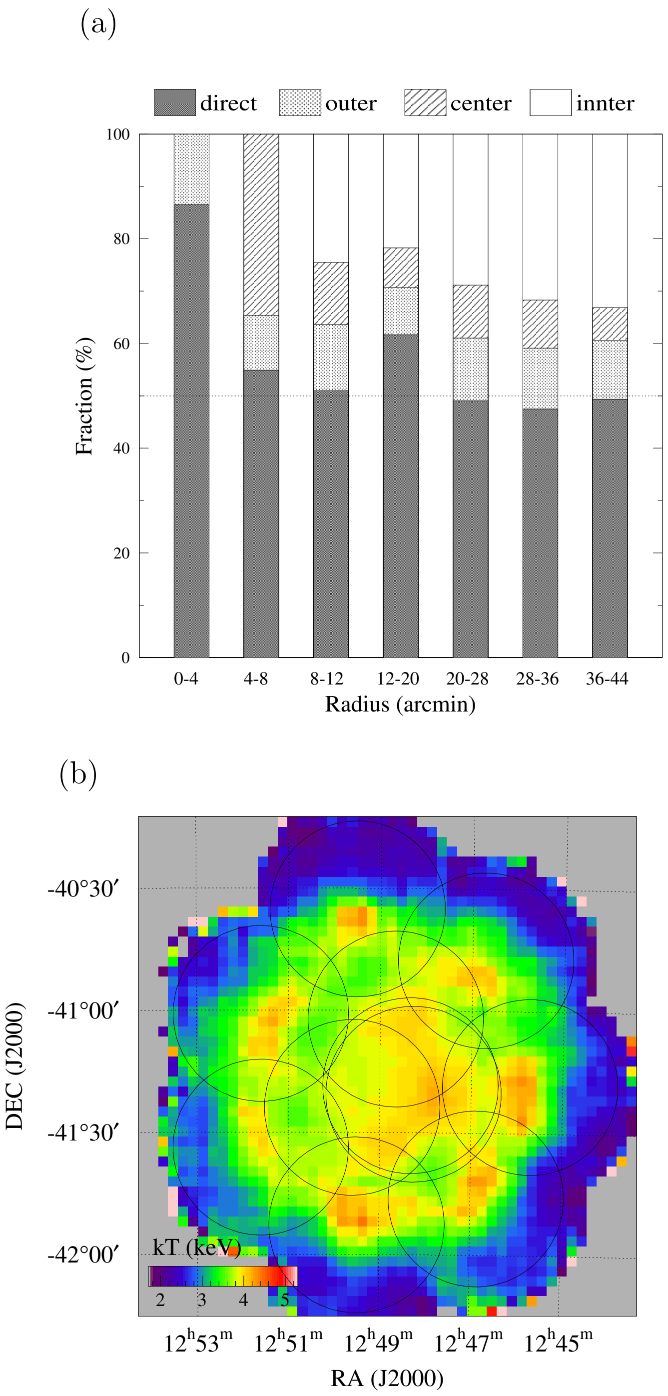

Figure 6.18: (a) Fractions of the photon origin and (b) color-coded temperature map for the Centaurus cluster estimated from the isothermal simulation.

correspond to the values for single-temperature fits. The central region within $r < 30'$ is characterized by a remarkable hot region at $\sim 15'$ south-east from the cluster center, which was already reported by Churazov et al. (1999). They have estimated the temperature by approximating the spectrum with a linear combination of 2 keV and 8 keV spectra. However, since no corrections have been made for the central cool component, the inner envelope of the reported hot region may well be the outer boundary of the cool component.

This point needs to be examined by applying correction for the cool component. Another interesting new feature is the extended cool regions at $40'$ north-west and north-east, indicating a temperature of close to 2 keV.

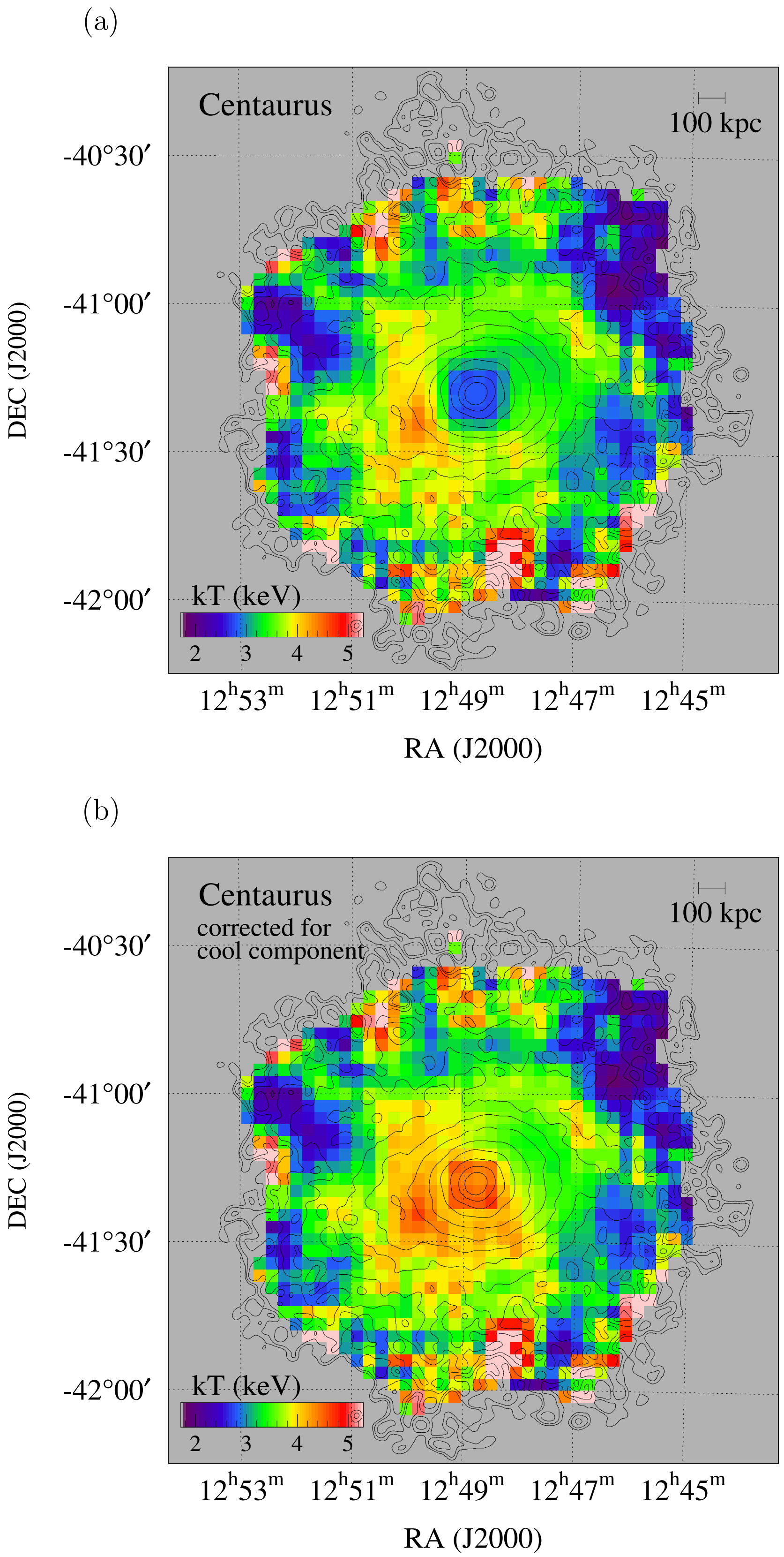

Figure 6.19: Color-coded temperature map for the Centaurus cluster (a) before, and (b) after the correction for the central cool component. X-ray intensity with the GIS2 is shown with contours.

Table 6.6: The observed and simulated *HR* values and the corrected temperatures for Centaurus cluster as shown in fig 6.21.

radius	azimuth	data HR	data $HR^\dagger$	simulated HR	kT (keV)	kT † (keV)
$< 2'$	–	0.52 ± 0.00	0.86 ± 0.01	0.79 ± 0.002	$2.41^{+0.05}_{-0.05}$	$4.55^{+1.60}_{-1.14}$
$2' - 4'$	NE	0.62 ± 0.01	0.88 ± 0.02	0.78 ± 0.003	$2.84^{+0.12}_{-0.11}$	$5.00^{+2.00}_{-1.39}$
	SE	0.60 ± 0.01	0.78 ± 0.01	0.78 ± 0.003	$2.73^{+0.11}_{-0.10}$	$4.02^{+1.38}_{-0.98}$
	SW	0.63 ± 0.01	0.81 ± 0.02	0.80 ± 0.003	$2.81^{+0.11}_{-0.11}$	$4.06^{+1.40}_{-0.99}$
	NW	0.65 ± 0.01	0.85 ± 0.02	0.80 ± 0.003	$2.91^{+0.12}_{-0.11}$	$4.43^{+1.63}_{-1.15}$
$4' - 8'$	NNE	0.73 ± 0.01	0.80 ± 0.01	0.80 ± 0.003	$3.36^{+0.17}_{-0.16}$	$3.95^{+0.22}_{-0.21}$
	ENE	0.73 ± 0.01	0.80 ± 0.01	0.79 ± 0.003	$3.49^{+0.17}_{-0.16}$	$4.03^{+0.21}_{-0.20}$
	ESE	0.73 ± 0.01	0.79 ± 0.01	0.78 ± 0.004	$3.57^{+0.18}_{-0.17}$	$4.04^{+0.22}_{-0.21}$
	SSE	0.72 ± 0.01	0.80 ± 0.02	0.80 ± 0.004	$3.32^{+0.18}_{-0.16}$	$3.97^{+0.24}_{-0.22}$
	SSW	0.74 ± 0.01	0.82 ± 0.02	0.80 ± 0.004	$3.48^{+0.18}_{-0.17}$	$4.21^{+0.25}_{-0.24}$
	WSW	0.73 ± 0.01	0.80 ± 0.01	0.81 ± 0.004	$3.34^{+0.17}_{-0.16}$	$3.91^{+0.22}_{-0.21}$
	WNW	0.73 ± 0.01	0.79 ± 0.01	0.81 ± 0.004	$3.30^{+0.16}_{-0.15}$	$3.76^{+0.20}_{-0.18}$
	NNW	0.69 ± 0.01	0.77 ± 0.01	0.81 ± 0.003	$3.10^{+0.15}_{-0.14}$	$3.67^{+0.20}_{-0.19}$
$8' - 12'$	NNE	0.77 ± 0.02	0.80 ± 0.02	0.79 ± 0.004	$3.83^{+0.27}_{-0.25}$	$4.07^{+0.30}_{-0.28}$
	ENE	0.79 ± 0.02	0.81 ± 0.02	0.81 ± 0.004	$3.78^{+0.24}_{-0.23}$	$3.95^{+0.26}_{-0.24}$
	ESE	0.83 ± 0.02	0.85 ± 0.02	0.79 ± 0.005	$4.32^{+0.29}_{-0.27}$	$4.55^{+0.31}_{-0.29}$
	SSE	0.82 ± 0.02	0.86 ± 0.02	0.81 ± 0.005	$4.10^{+0.31}_{-0.28}$	$4.41^{+0.34}_{-0.31}$
	SSW	0.80 ± 0.02	0.84 ± 0.02	0.83 ± 0.005	$3.70^{+0.28}_{-0.25}$	$4.03^{+0.32}_{-0.29}$
	WSW	0.80 ± 0.02	0.83 ± 0.02	0.84 ± 0.005	$3.61^{+0.24}_{-0.22}$	$3.83^{+0.27}_{-0.25}$
	WNW	0.76 ± 0.01	0.79 ± 0.01	0.84 ± 0.004	$3.36^{+0.19}_{-0.18}$	$3.54^{+0.21}_{-0.20}$
	NNW	0.78 ± 0.02	0.81 ± 0.02	0.82 ± 0.004	$3.64^{+0.23}_{-0.21}$	$3.87^{+0.26}_{-0.24}$
$12' - 20'$	NNE	0.78 ± 0.02	0.80 ± 0.02	0.81 ± 0.005	$3.71^{+0.29}_{-0.26}$	$3.86^{+0.31}_{-0.28}$
	ENE	0.79 ± 0.02	0.81 ± 0.02	0.79 ± 0.004	$3.92^{+0.26}_{-0.24}$	$4.11^{+0.28}_{-0.26}$
	ESE	0.82 ± 0.02	0.83 ± 0.02	0.79 ± 0.005	$4.21^{+0.29}_{-0.27}$	$4.38^{+0.30}_{-0.28}$
	SSE	0.80 ± 0.02	0.82 ± 0.02	0.81 ± 0.005	$3.82^{+0.29}_{-0.26}$	$3.99^{+0.31}_{-0.28}$
	SSW	0.80 ± 0.02	0.82 ± 0.02	0.81 ± 0.005	$3.80^{+0.31}_{-0.28}$	$4.03^{+0.34}_{-0.31}$
	WSW	0.79 ± 0.02	0.80 ± 0.02	0.83 ± 0.005	$3.56^{+0.24}_{-0.23}$	$3.68^{+0.26}_{-0.24}$
	WNW	0.75 ± 0.01	0.76 ± 0.01	0.82 ± 0.004	$3.32^{+0.20}_{-0.18}$	$3.43^{+0.21}_{-0.19}$
	NNW	0.75 ± 0.01	0.77 ± 0.02	0.82 ± 0.004	$3.34^{+0.22}_{-0.20}$	$3.42^{+0.23}_{-0.21}$
$20' - 28'$	NNE	0.67 ± 0.03	0.69 ± 0.03	0.79 ± 0.009	$2.98^{+0.46}_{-0.38}$	$3.11^{+0.50}_{-0.41}$
	ENE	0.72 ± 0.02	0.75 ± 0.03	0.78 ± 0.007	$3.35^{+0.40}_{-0.35}$	$3.60^{+0.45}_{-0.39}$
	ESE	0.79 ± 0.03	0.81 ± 0.03	0.78 ± 0.008	$4.06^{+0.51}_{-0.44}$	$4.30^{+0.55}_{-0.48}$
	SSE	0.77 ± 0.03	0.81 ± 0.04	0.78 ± 0.009	$3.81^{+0.59}_{-0.50}$	$4.20^{+0.69}_{-0.58}$
	SSW	0.76 ± 0.03	0.80 ± 0.03	0.79 ± 0.008	$3.65^{+0.53}_{-0.45}$	$4.01^{+0.61}_{-0.52}$
	WSW	0.69 ± 0.02	0.71 ± 0.03	0.80 ± 0.007	$2.99^{+0.35}_{-0.30}$	$3.11^{+0.37}_{-0.32}$
	WNW	0.76 ± 0.03	0.78 ± 0.03	0.79 ± 0.008	$3.64^{+0.46}_{-0.40}$	$3.84^{+0.50}_{-0.44}$
	NNW	0.81 ± 0.03	0.83 ± 0.03	0.81 ± 0.007	$3.93^{+0.49}_{-0.43}$	$4.16^{+0.54}_{-0.47}$

Table 6.6 (continued)

radius	azimuth	data *HR*	data *HR*†	simulated *HR*	*kT* (keV)	*kT* † (keV)
$28' - 36'$	NNE	0.75 ± 0.04	0.78 ± 0.04	0.77 ± 0.009	$3.76^{+0.69}_{-0.57}$	$4.00^{+0.76}_{-0.63}$
	ENE	0.68 ± 0.03	0.70 ± 0.03	0.83 ± 0.010	$2.80^{+0.45}_{-0.37}$	$2.91^{+0.49}_{-0.40}$
	ESE	0.76 ± 0.03	0.77 ± 0.04	0.80 ± 0.010	$3.52^{+0.57}_{-0.48}$	$3.61^{+0.60}_{-0.50}$
	SSE	0.73 ± 0.04	0.76 ± 0.05	0.82 ± 0.012	$3.21^{+0.71}_{-0.55}$	$3.40^{+0.78}_{-0.61}$
	SSW	0.83 ± 0.05	0.86 ± 0.05	0.81 ± 0.012	$4.12^{+0.92}_{-0.73}$	$4.46^{+1.03}_{-0.82}$
	WSW	0.69 ± 0.05	0.71 ± 0.05	0.82 ± 0.013	$2.88^{+0.73}_{-0.55}$	$3.03^{+0.80}_{-0.60}$
	WNW	0.63 ± 0.05	0.65 ± 0.05	0.79 ± 0.012	$2.69^{+0.67}_{-0.50}$	$2.80^{+0.73}_{-0.54}$
	NNW	0.71 ± 0.04	0.74 ± 0.04	0.80 ± 0.010	$3.18^{+0.59}_{-0.48}$	$3.40^{+0.67}_{-0.54}$

† Corrected for the cool component.

Figure 6.20a shows the azimuthal variation of the temperature for the 7 concentric rings. By fitting a constant model to the data of figure 6.20a, the isothermal model was rejected at the 99.99% confidence with a mean temperature of 3.15 ± 0.03 keV (reduced chi-square of χ^2/ν= 1110/44).

Frequency histogram of the temperature map derived for a cell size of $2.5'$ shown in figure 6.21a, in which no corrections are made for the cool component. Figure 6.21b shows the distribution when the cool component is subtracted, as described later. The temperatures are taken where the statistical error in a cell is less then 30%, hence the integrated region is within a radius of $\sim 30'$. The histogram is fitted with a Gaussian function, and the best-fit mean temperature and the standard deviation are 3.41 keV and 0.85 keV(25%), respectively. Though the temperatures in the central region are not corrected for the cool component in figure 6.21a, the standard deviation in the distribution is significantly larger than the previous 2 clusters.

Figure 6.22a shows the two one-dimensional profiles of temperature. The directions are from south-west to north-east direction (path-A) and from south-east to north-west direction (path-B) shown in figure 6.22c. The temperature in each bin is calculated for a $10' \times 5'$ rectangle region. The temperature drop in the center due to the cool component is clearly seen in both profiles. The south-east hot region corresponds to an offset angle of $10' - 20'$ in path-B. Therefore, the profile in path-B is asymmetric within a radius of $20'$ compared with the one in path-A.

6.3.2 Cool component

The temperature map in figure 6.19 is based on to the raw *HR* values before applying corrections for the central cool component. The map for the central GIS field ($r < 22'$) is essentially the same as the previous result by Churazov et al. (1999), who approximated the spectra with linear combination of 2 keV and 8 keV components. The hot region

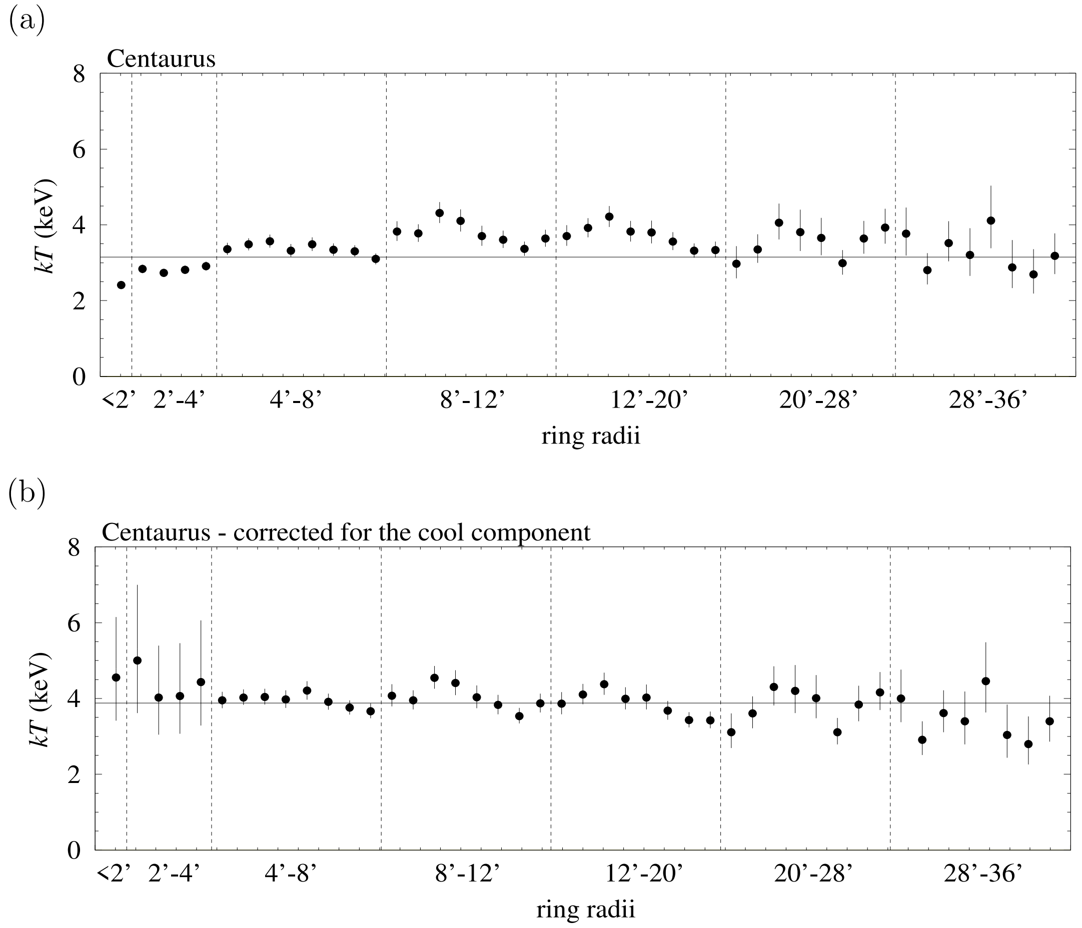

Figure 6.20: Azimuthal profiles of temperature for 7 annular rings (a) before, and (b) after the correction for the central cool component. The error bars in (b) are increased by including the systematic error of the cool-component intensity by 10%.

at $\sim 15'$ south east from the center is close to the second-brightest galaxy NGC 4709. Another interesting new feature is the extended cool region at $40'$ north west, indicating a temperature close to 2 keV.

Since our main interest is the structure of the hot component, which should reflect the dynamical history of the cluster, we subtracted the cool component in the central region from the data. The properties of the cool component in the Centaurus cluster have been extensively studied by Ikebe et al. (1999), who analyzed PSPC and GIS data jointly. Their model gives radial profiles of the emission measure and filling factor with a cut off radius of $R_{\rm cut} = 6'$, assuming a constant temperature, $kT_{\rm cool} = 1.4$ keV, for the cool component. Using this model and the ray-tracing simulation, we can estimate the radial count-rate profiles for the hard and soft bands, which were simply subtracted from the data. The central intensity of the cool component was estimated here from the ratio of the emission integrals of the two components given in table 3 of Ikebe et al. (1999), which showed the best-fit parameters for the spectrum within the central $3'$ region fitted with a 2-temperature MEKAL model. Note that the number of photons subtracted as the cool

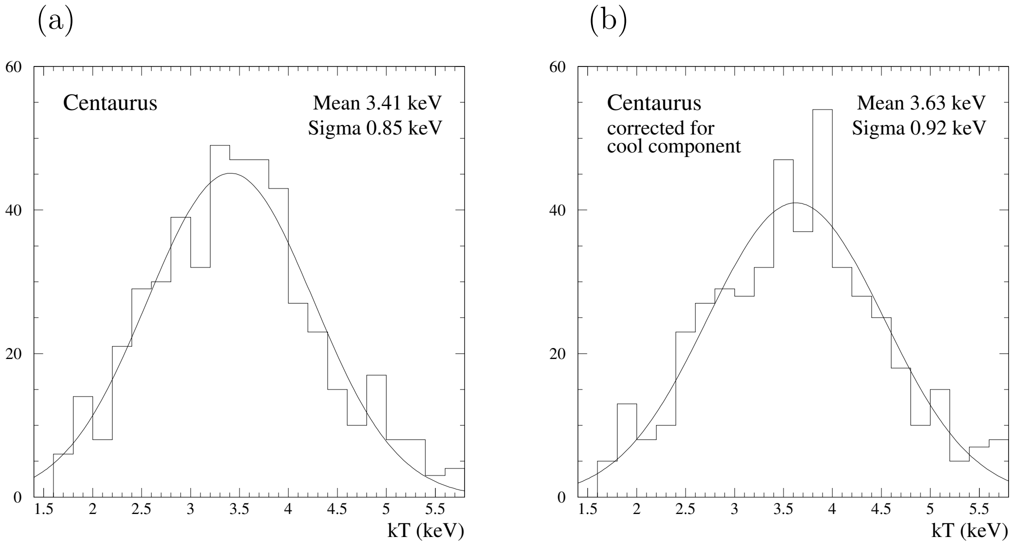

Figure 6.21: Frequency distribution of temperature for Centaurus cluster fitted with Gaussian function (a) before, and (b) after the correction for the central cool component.

component within the central 6′ was about a quarter of the total.

Figure 6.19b shows the resultant temperature map for only the hot component. The difference between figures 6.19a and b mainly appears within the central $\sim 8'$ region, as expected from the model profile of the cool component. The cluster center turned out to be fairly hot, and the obtained temperature (4.3 ± 0.4 keV) is close to the level in the south-east hot region. This temperature is consistent with the result ($4.2^{+0.8}_{-0.3}$ keV) by Ikebe et al. (1999). The azimuthally averaged temperatures are shown in figure 6.20b. The temperature variation is still significant even after the correction for the cool component. The mean temperature for the data in figure 6.20b fitted with a constant model increases by 0.7 keV to 3.88 ± 0.05 keV. Again, the isothermal model was rejected with 99.99% confidence, though the reduced χ^2 value became considerably smaller to $\chi^2/\nu = 125.8/44$. Figure 6.21b shows the frequency histogram. The mean temperature also rises to 3.63 keV, and the absolute value of standard deviation spreads to 0.92 keV(25%) by 8%. It is interesting that the standard deviation does not decrease, but increases. Figure 6.22b shows that the central temperature is fairly high in both two profiles. The asymmetry in path-B becomes more prominent while the profile of path-A is almost flat.

Since the corrections applied to the data assume the models with fixed parameters, systematic errors in the correction process need to be examined. To avoid complications due to model parameters, we simply varied the cool-component intensity by ±10%, by fixing its temperature and radial profile. This is an overestimation since the PSPC data can constrain the cool-component intensity with an accuracy of a few %. The 10% change causes a change in the hot-component temperature by 7% in the sense that stronger cool emission causes a hotter temperature. Since the systematic error is comparable to the

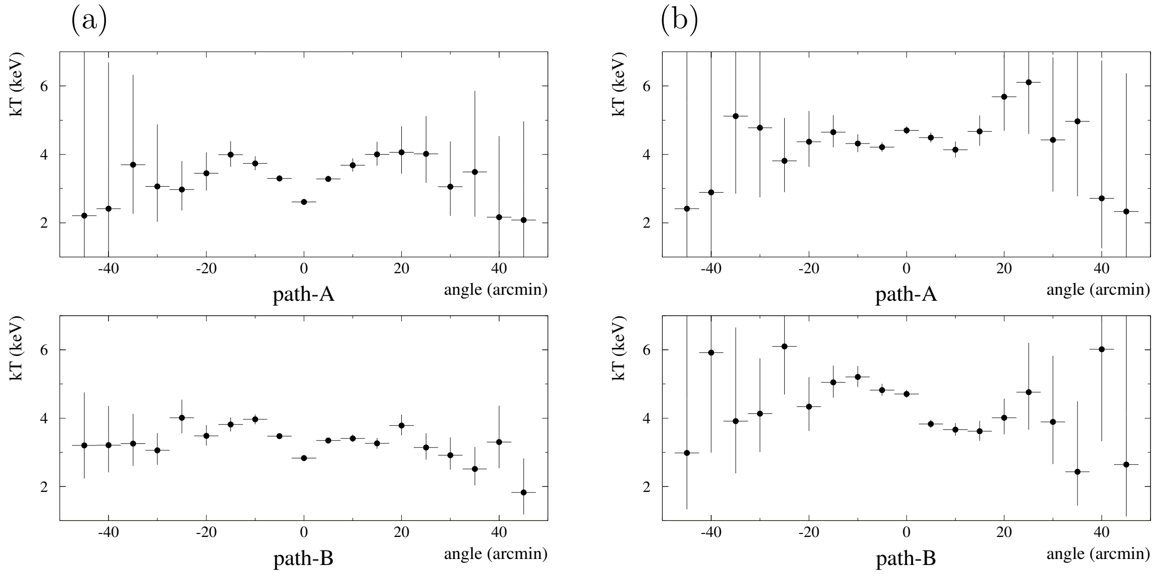

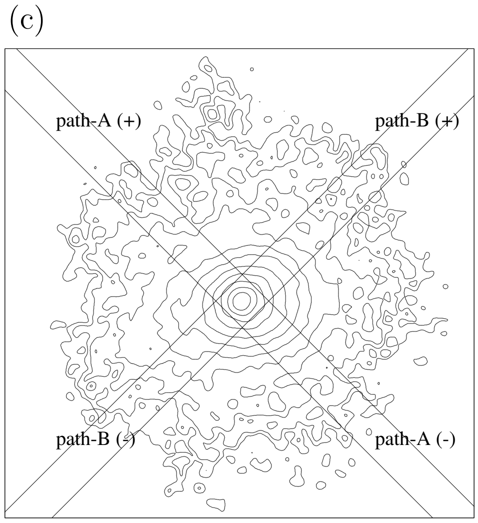

Figure 6.22: One-dimensional profiles of temperature for Centaurus cluster along SW to NE direction (path-A) and SE to NW direction (path-B), shown as a function of the angle from the cluster center. The temperature in each bin is calculated for a $10' \times 5'$ rectangle, (a) before, and (b) after the correction for the central cool component.

statistical error, we can say that the features in the temperature map have an accuracy of about 10%. The difference between the metal abundance of 1.0 and 0.2 solar, brings about the estimated temperature drop of 0.1 keV around 3.6 keV.

6.3.3 Spectra

To evaluate the significance of the hot and cool temperatures, the pulse-height spectra for 3 selected regions were compared. The selected regions, their spectra, and the ratios of each data to the best-fit model for #1 are shown in figure 6.23, and resulting parameters of spectral fits are shown in table 6.7. Region #2 in the south-east includes the hot region reported by Churazov et al. (1999), and the obtained temperature of 4.3 ± 0.2 keV is consistent with their result of 4.4 ± 0.2 keV. Region #1 is at a nearly symmetric to the hot region with respect to the cluster center, which should reduce the systematic effects in the temperature comparison. The obtained temperature of 3.5 ± 0.1 keV is close to the average value in the cluster excluding the hot and cool regions. At $30'$ north-west, a cool region is seen in the temperature map (region #3). The spectral fit shows the temperature to be $2.2^{+0.4}_{-0.3}$ keV, which is significantly lower than the mean temperature. Therefore, the hot and cool regions revealed in the temperature map are confirmed to be highly significant in terms of the spectral analysis.

Table 6.7: Spectral parameters for selected regions of Centaurus cluster.

region no.*	$N_{\rm H}$ (10^{20} cm^{-2})	kT (keV)	Z (solar)	$\chi^2/d.o.f$
#1 (med)	8.8(fix)	$3.52^{+0.09}_{-0.09}$	$0.38^{+0.07}_{-0.06}$	68.8/59
#2 (hot)	8.8(fix)	$4.30^{+0.17}_{-0.16}$	$0.31^{+0.09}_{-0.08}$	71.7/59
#3 (cool)	8.8(fix)	$2.24^{+0.35}_{-0.30}$	$0.08^{+0.41}_{-0.08}$	11.1/14

* Corresponding regions are shown in figure 6.23

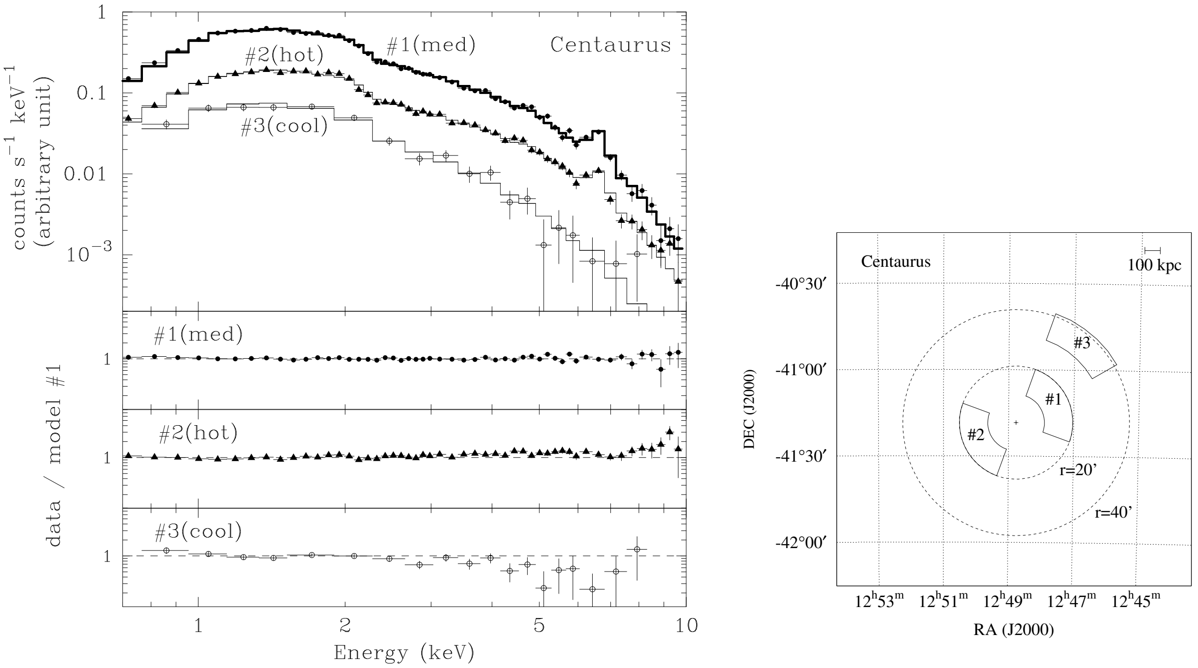

Figure 6.23: Pulse-height spectra (top panel) for the Centaurus cluster, normalized ratios to the best-fit model of #1 (bottom panel), and the selected regions (right panel).

6.3.4 Point sources

Point sources are recognized in the X-ray images with the PSPC and GIS data. The intensity and energy spectra of 3 brightest sources are examined here. The expanded GIS images for each source are shown in figure 6.24.

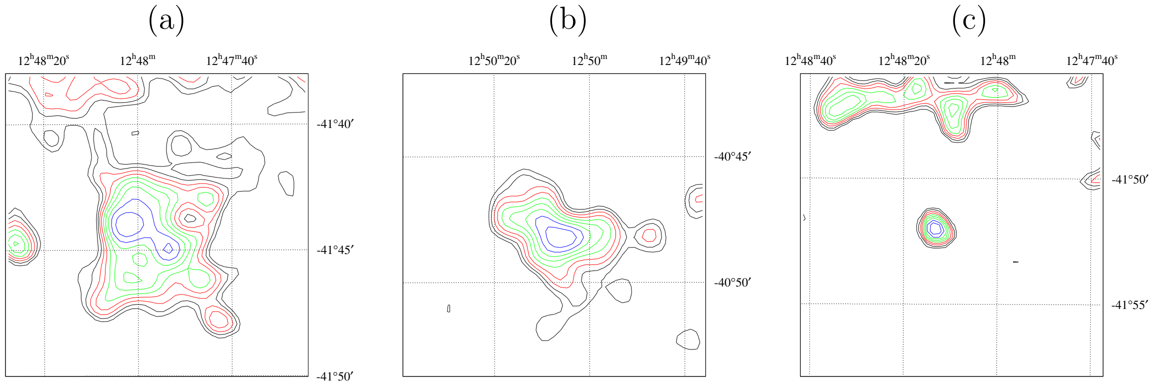

Figure 6.24: The GIS images of (a) 1RXS J124755.5-414356, (b) 1RXS J125007.3-404738 in the 0.7–7 keV band, and (c) CCC 032 in the 2–7 keV band. The image size is $12' \times 12'$ which corresponds to 214×214 kpc at the distance of the Centaurus cluster.

1RXS J124755.5-414356

Figure 6.25a shows the pulse-height spectrum with the GIS. The observed 0.5–10 keV flux is $F_{\rm X} = 4.6 \times 10^{-12}$erg cm^{-2}s^{-1}. The best-fit parameters with an absorbed MEKAL model or power-law+ MEKAL model are shown in table 6.8. Since the temperature obtained from MEKAL model fitting of 3.9 keV is not so different from the cluster temperature, the temperature map does not show any structure corresponding to this point source. We also fit with an absorbed power-law plus MEKAL model in which power-law model is for the 1RXS J124755.5-414356, and MEKAL model is regarded as the cluster component fixed with a temperature of 3.6 keV and a metal abundance of 0.3 solar. The best-fit photon index is 1.85, which is a typical value of AGNs.

1RXS J125007.3-404738

Figure 6.25b shows the pulse-height spectrum and table 6.8 shows the best-fit parameters. Fitting by an absorbed MEKAL model, a temperature of 3.3 keV which is almost the same as the cluster value is obtained. The observed 0.5–10 keV flux is $F_{\rm X} = 4.2 \times 10^{-12}$erg cm^{-2}s^{-1}. We also fit the spectrum with an absorbed power-law + MEKAL model as in the previous source. The best-fit photon index of 2.5 is not likely a AGN, the origin of X-ray emission is suggested to be thermal with a low temperature.

CCC 032

In figure 6.19, a small hot region is seen at $35'$ south of the cluster center. The extent before taking the running average is $\sim 2 \times 2$ pixels ($5' \times 5'$), which is comparable to that of a point source caused by the XRT response. The peak of the X-ray emission corresponding to the hot region is barely seen in the 0.7 – 7 keV band, however, the hard band image above 2 keV exhibits certainly a peak like a point source. The position is identified as CCC 032 (Jerjen and Dressler 1997); a galaxy of morphological type Im at a redshift $z = 0.00913$. The coordinate of CCC 032 (or DCL224) is (R.A., Decl.)$_{\rm J2000}$ = ($12^{\rm h}48^{\rm m}08.7^{\rm s}$, $-41^\circ 51' 48''$) at a redshift of $z = 0.00913$. The temperature derived by fitting the spectrum shown in figure 6.24c with an absorbed MEKAL model is ∼ 7 keV, which is consistent with the feature in the temperature map. Fitting with an absorbed power-law + MEKAL model gives a photon index of 1.4 for CCC 032, though the statistics is low. Since such small photon index suggests that this source does not emit by a hot gas, this galaxy might be an AGN.

Table 6.8: Spectral parameters for 1RXS J124755.5-414356, 1RXS J125007.3-404738, and CCC 032. $N_{\rm H}$ is fixed to the Galactic value 8.8×10^{20} cm^{-2}.

name	Model	kT/Γ (keV/)	Z (solar)	$\chi^2/d.o.f$
1RXS J124755.5-414356	MEKAL	$3.88^{+0.93}_{-0.65}$	$0.39^{+0.82}_{-0.39}$	22.0/22
	MEKAL + Power law	$1.85^{+0.86\,\dagger}_{-0.40}$	—	22.5/22
1RXS J125007.3-404738	MEKAL	$3.33^{+1.10}_{-0.73}$	$0.31^{+1.03}_{-0.31}$	21.2/23
	MEKAL + Power law	$2.49^{+1.69\,\dagger}_{-0.62}$	—	21.3/23
CCC 032	MEKAL	$7.4^{+40}_{-2.6}$	$0.45^{+3.2}_{-0.45}$	1.7/8
	MEKAL + Power law	$1.38^{+0.68}_{-1.38}$	—	1.7/9

† Errors are 90% confidence limit when the rest parameters are fixed to the best-fit value.

(a)

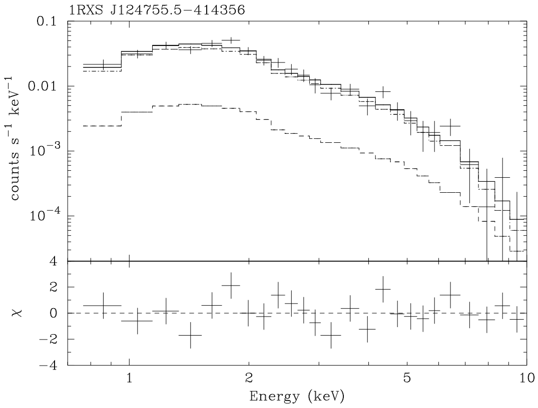

(b)

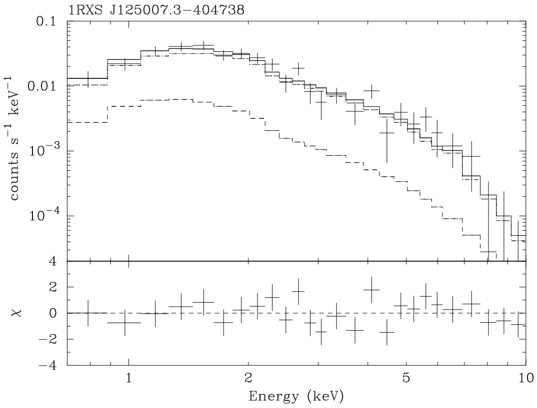

(c)

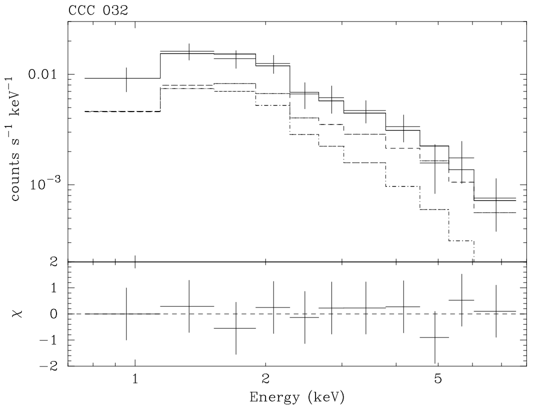

Figure 6.25: Pulse-height spectra of (a) 1RXS J124755.5-414356, (b) 1RXS J125007.3-404738, and (c) CCC 032 fitted with power-law + MEKAL model. The residual is shown in the bottom panels.

6.4 The Perseus cluster

Figure 6.26a shows the X-ray image with GIS2 combined with all 13 pointings in the 0.7 – 10 keV energy band. The circles show the GIS field of views with a radius of 22′. The image was smoothed by a Gaussian function with $\sigma = 1'$ after background subtraction and exposure correction. The observations covered almost 2° corresponding to 3.7 Mpc. The X-ray image with PSPC (figure 2.19) is elongated in the east-west direction in parallel to the filament structure of Pisces-Perseus supercluster. The GIS image also shows asymmetric emission along the east-west axis even with lower spatial resolution. A cD galaxy, NGC 1275, is located at the cluster center, showing strong surface brightness concentration with the cool component. There are two bright point sources seen in the south-west region. One is the well known narrow tailed radio galaxy IC 310 at a distance of 36.5′ from the cluster center. The other source further away at 55′ in the southwest is 1RXS J031525.1+410620. This X-ray bright source is not optically identified, and only catalogued in the bright source catalogue (1RXS) from the ROSAT all-sky survey. Figure 6.26b shows the projected surface brightness on to the RA and DEC axes with an offset from the cluster center. The excess of two point sources are seen in the profile of RA axis. The S/N of the Perseus cluster is the largest among the 4 clusters, and the statistics of the data is high even in the outermost pointing region.

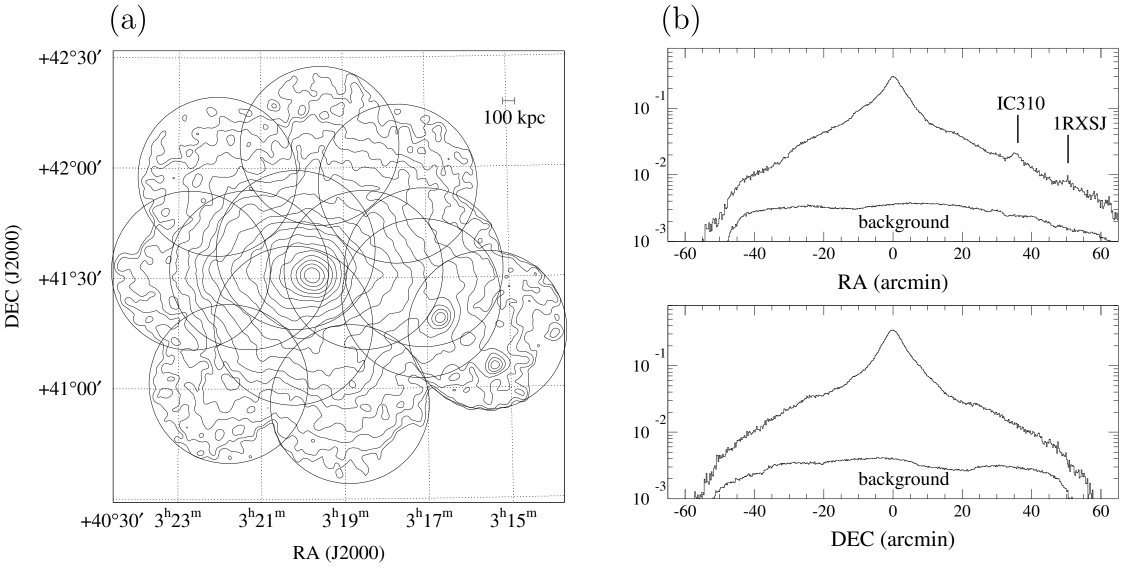

Figure 6.26: (a) GIS image of the Perseus cluster in the energy range 0.7–10 keV. Circles with radii of 22′ show the GIS field of view. (b) The profiles projected on the RA (upper) and DEC (lower) axes compared with the background.

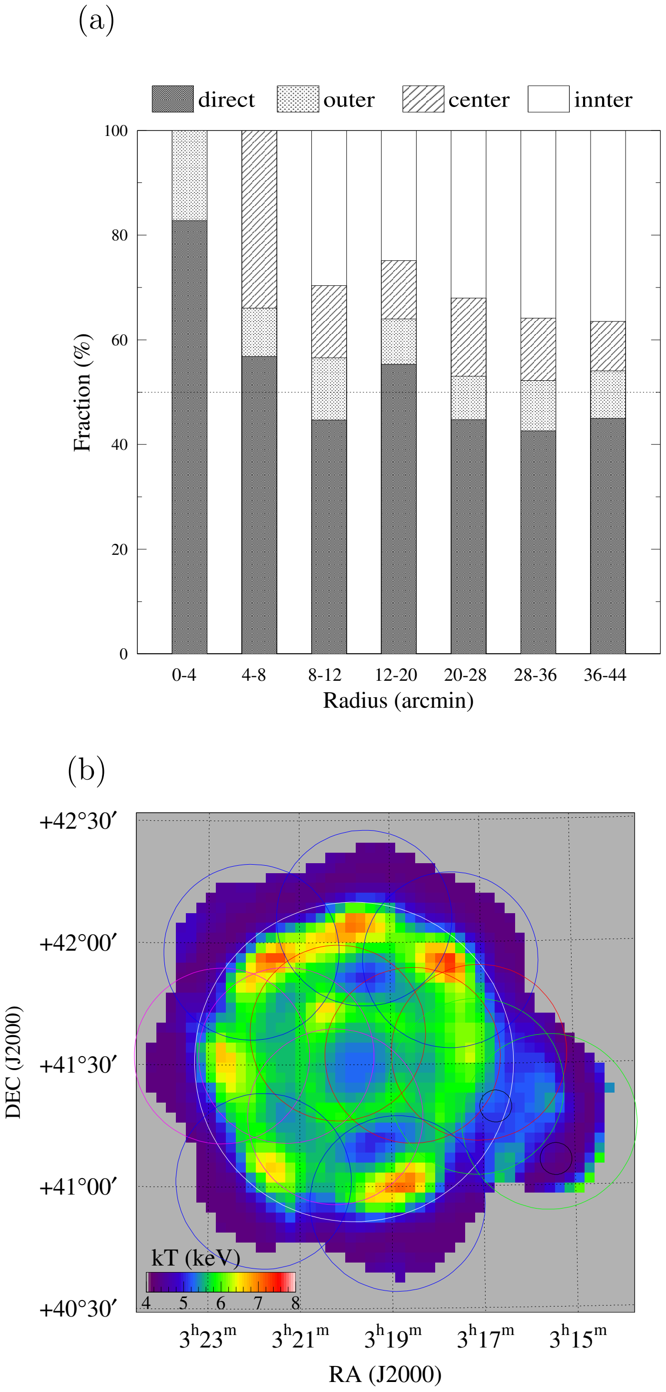

Figure 6.27: Fractions of the photon origin and color-coded temperature map for the Perseus cluster estimated from the isothermal simulation.

6.4.1 Temperature structure

We have carried out the simulation assuming that the input spectrum is a single-temperature MEKAL model with a temperature of 6.0 keV based on the PSPC image, and the significant abundance gradient reported by Ezawa et al.(2001) was included in the model. Figure 6.27a shows the fraction of photon origins in the 0.7–10 keV image combined with all pointings weighted by the exposure map. The whole region is divided into the 7

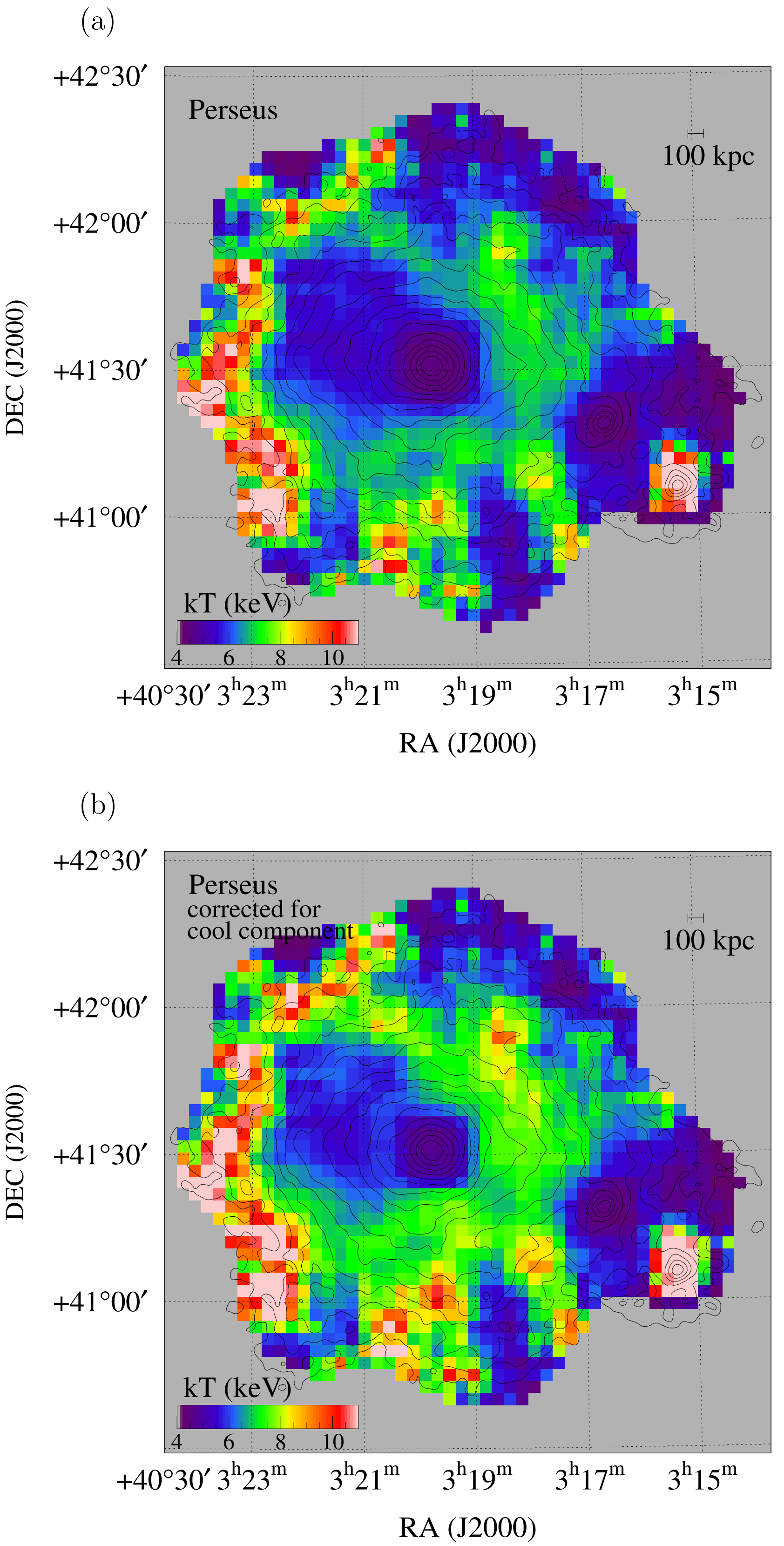

Figure 6.28: Color-coded temperature map for the Perseus cluster. X-ray intensity with the GIS2 is shown with contours. In panel (b), the cool component observed in $r < 30'$ is subtracted and only the hot-component structure is shown.

concentric rings of $r = 0' - 4' - 8' - 12' - 20' - 28' - 36' - 44'$. In all regions except for the central $r < 4'$ part, about a half of detected photons comes from the corresponding sky region, indicated as "direct" photons in the figure. The contaminating flux from the central bright region center contributes 30% in the next ring of $r`4' - 8'$ as high as in the case of Centaurus. We have produced the temperature map of the simulated isothermal cluster as shown in figure 6.27b. The shell-like structure with a temperature gap of more than 1 keV from the input temperature that results from the XRT response and the pointing configuration indicates the necessity of the correction for the XRT response.

Figure 6.28a shows the color-coded temperature map of the observed Perseus cluster after the correction of the XRT response and superposed on the GIS brightness contour map. Note that we use photons in the 2–10 keV energy band as a H in our hardness analysis for only this cluster as described in section 5. The Perseus cluster shows more complicated temperature structures than the Centaurus cluster. The most peculiar structure is a large cool region around $20'$ east of the cluster center, which is clearly extended with a diameter of about $\sim 30'$ (900 kpc) as if the gas is expanding away from its center. This cool region coincides with the known substructure in the surface brightness as recognized from the PSPC observations (Schwarz et al. 1992; Ettori et al. 1998). These results of the temperature map are generally consistent with the previous spectral results by Ezawa et al. (2001).

The other interesting feature in the temperature map is the ring-like hot region which almost encircles both the cool region and the cluster center. The eastern ridge, at $r \sim 40'$ from the center running north to south, seems particularly hot with $kT \gtrsim 10$ keV in a number of connected pixels. The rest of the ring-like feature indicates approximately the same temperature with $kT \sim 7$ keV. There are other soft regions: one small region in the south-south-west direction at $r \gtrsim 30'$, and an elongated region at the north-east edge. Neither of the regions show structures in the surface brightness distribution, suggesting that the low ICM temperatures in these regions do not accompany significant density contrast.

The central region within a diameter of $10'$ shows a marked softening of the spectrum with a temperature of 4.4 keV, as studied by Ezawa et al. (2001). They showed that 2 spectral components were needed to fit the spectra in the central region within $r = 20'$, but the hotter component itself also indicated a marked softening down to $kT = 5.7$ keV. The analysis and results after the cool component correction are described in section 6.4.2. Apart from the central concentration of the soft component, the two bright point sources, IC 310 and 1RXS J031525.1+410620, in the south-west region are clearly recognized in the temperature map. These sources are characterized by low ($\sim$ 4 keV) and high ($\sim$ 11 keV) temperatures, respectively, showing that the temperature map can effectively separate contributions from discrete sources. We have fitted their spectra and obtained parameters in more detail as described in 6.4.4.

Table 6.9: The observed and simulated *HR* values and the corrected temperatures for the Perseus cluster as shown in fig 6.30.

radius	azimuth	data HR	data $HR^\dagger$	simulated HR	kT (keV)	$kT^\dagger$ (keV)
$< 2'$	–	0.82 ± 0.00	0.86 ± 0.01	1.04 ± 0.002	$4.38^{+0.01}_{-0.00}$	$4.44^{+0.03}_{-0.03}$
$2' - 4'$	NE	0.86 ± 0.01	0.91 ± 0.01	1.04 ± 0.004	$4.44^{+0.05}_{-0.04}$	$4.68^{+0.12}_{-0.10}$
	SE	0.87 ± 0.01	0.92 ± 0.01	1.03 ± 0.004	$4.48^{+0.06}_{-0.05}$	$4.79^{+0.13}_{-0.11}$
	SW	0.84 ± 0.01	0.90 ± 0.01	1.03 ± 0.003	$4.42^{+0.04}_{-0.03}$	$4.65^{+0.10}_{-0.09}$
	NW	0.86 ± 0.01	0.93 ± 0.01	1.04 ± 0.003	$4.45^{+0.05}_{-0.04}$	$4.77^{+0.14}_{-0.12}$
$4' - 8'$	NNE	0.96 ± 0.01	1.05 ± 0.01	1.06 ± 0.004	$4.87^{+0.18}_{-0.15}$	$5.74^{+0.33}_{-0.29}$
	ENE	0.97 ± 0.01	1.03 ± 0.01	1.06 ± 0.004	$4.95^{+0.17}_{-0.15}$	$5.58^{+0.27}_{-0.24}$
	ESE	0.98 ± 0.01	1.05 ± 0.01	1.05 ± 0.004	$5.14^{+0.19}_{-0.17}$	$5.91^{+0.30}_{-0.27}$
	SSE	0.99 ± 0.01	1.08 ± 0.01	1.04 ± 0.004	$5.35^{+0.23}_{-0.20}$	$6.64^{+0.40}_{-0.36}$
	SSW	0.96 ± 0.01	1.06 ± 0.01	1.05 ± 0.004	$4.99^{+0.18}_{-0.16}$	$6.14^{+0.36}_{-0.32}$
	WSW	0.96 ± 0.01	1.05 ± 0.01	1.05 ± 0.004	$4.94^{+0.19}_{-0.16}$	$5.96^{+0.35}_{-0.32}$
	WNW	0.96 ± 0.01	1.04 ± 0.01	1.05 ± 0.004	$4.90^{+0.17}_{-0.15}$	$5.83^{+0.32}_{-0.29}$
	NNW	0.98 ± 0.01	1.07 ± 0.01	1.06 ± 0.004	$5.09^{+0.20}_{-0.17}$	$6.26^{+0.37}_{-0.33}$

Table 6.9 (continued)

radius	azimuth	data HR	data $HR^\dagger$	simulated HR	kT (keV)	$kT^\dagger$ (keV)
$8' - 12'$	NNE	1.08 ± 0.02	1.14 ± 0.02	1.12 ± 0.006	$5.54^{+0.40}_{-0.34}$	$6.26^{+0.55}_{-0.47}$
	ENE	1.07 ± 0.01	1.11 ± 0.01	1.10 ± 0.005	$5.66^{+0.31}_{-0.27}$	$6.19^{+0.39}_{-0.35}$
	ESE	1.04 ± 0.01	1.07 ± 0.01	1.08 ± 0.005	$5.41^{+0.28}_{-0.24}$	$5.81^{+0.34}_{-0.30}$
	SSE	1.09 ± 0.01	1.14 ± 0.02	1.09 ± 0.005	$6.02^{+0.38}_{-0.34}$	$6.80^{+0.50}_{-0.45}$
	SSW	1.12 ± 0.02	1.19 ± 0.02	1.10 ± 0.005	$6.38^{+0.47}_{-0.41}$	$7.57^{+0.64}_{-0.58}$
	WSW	1.10 ± 0.02	1.16 ± 0.02	1.08 ± 0.005	$6.34^{+0.43}_{-0.39}$	$7.45^{+0.59}_{-0.53}$
	WNW	1.11 ± 0.02	1.17 ± 0.02	1.08 ± 0.005	$6.37^{+0.46}_{-0.41}$	$7.48^{+0.62}_{-0.56}$
	NNW	1.09 ± 0.02	1.15 ± 0.02	1.09 ± 0.006	$5.95^{+0.44}_{-0.39}$	$6.93^{+0.62}_{-0.54}$
$12' - 20'$	NNE	1.10 ± 0.02	1.12 ± 0.02	1.11 ± 0.007	$5.88^{+0.47}_{-0.40}$	$6.21^{+0.54}_{-0.46}$
	ENE	1.03 ± 0.01	1.05 ± 0.01	1.08 ± 0.004	$5.43^{+0.23}_{-0.21}$	$5.61^{+0.26}_{-0.23}$
	ESE	1.05 ± 0.01	1.07 ± 0.01	1.07 ± 0.004	$5.73^{+0.25}_{-0.23}$	$5.96^{+0.28}_{-0.25}$
	SSE	1.13 ± 0.01	1.16 ± 0.01	1.09 ± 0.005	$6.78^{+0.44}_{-0.40}$	$7.24^{+0.49}_{-0.45}$
	SSW	1.11 ± 0.01	1.14 ± 0.01	1.05 ± 0.005	$6.91^{+0.45}_{-0.41}$	$7.54^{+0.52}_{-0.48}$
	WSW	1.10 ± 0.01	1.13 ± 0.01	1.07 ± 0.004	$6.43^{+0.33}_{-0.31}$	$6.96^{+0.39}_{-0.36}$
	WNW	1.13 ± 0.01	1.17 ± 0.01	1.07 ± 0.004	$7.07^{+0.41}_{-0.37}$	$7.79^{+0.48}_{-0.44}$
	NNW	1.12 ± 0.02	1.15 ± 0.02	1.06 ± 0.005	$6.90^{+0.50}_{-0.45}$	$7.63^{+0.60}_{-0.54}$
$20' - 28'$	NNE	1.07 ± 0.02	1.11 ± 0.02	1.06 ± 0.007	$6.19^{+0.58}_{-0.49}$	$6.93^{+0.72}_{-0.63}$
	ENE	1.02 ± 0.01	1.03 ± 0.01	1.06 ± 0.005	$5.51^{+0.29}_{-0.26}$	$5.74^{+0.33}_{-0.29}$
	ESE	1.07 ± 0.01	1.09 ± 0.01	1.07 ± 0.005	$6.11^{+0.36}_{-0.32}$	$6.46^{+0.41}_{-0.37}$
	SSE	1.09 ± 0.02	1.12 ± 0.02	1.05 ± 0.006	$6.69^{+0.53}_{-0.47}$	$7.18^{+0.60}_{-0.54}$
	SSW	1.07 ± 0.01	1.11 ± 0.02	1.03 ± 0.005	$6.69^{+0.49}_{-0.44}$	$7.42^{+0.58}_{-0.53}$
	WSW	1.12 ± 0.01	1.14 ± 0.01	1.08 ± 0.005	$6.66^{+0.43}_{-0.39}$	$7.03^{+0.47}_{-0.43}$
	WNW	1.14 ± 0.01	1.17 ± 0.02	1.08 ± 0.005	$7.02^{+0.48}_{-0.44}$	$7.60^{+0.55}_{-0.50}$
	NNW	1.09 ± 0.02	1.13 ± 0.02	1.05 ± 0.006	$6.75^{+0.58}_{-0.51}$	$7.57^{+0.70}_{-0.63}$
$28' - 36'$	NNE	1.14 ± 0.03	1.19 ± 0.03	1.15 ± 0.008	$6.00^{+0.73}_{-0.59}$	$6.70^{+0.92}_{-0.76}$
	ENE	1.08 ± 0.02	1.10 ± 0.02	1.10 ± 0.007	$5.79^{+0.54}_{-0.45}$	$6.07^{+0.61}_{-0.51}$
	ESE	1.14 ± 0.02	1.15 ± 0.02	1.10 ± 0.007	$6.71^{+0.69}_{-0.60}$	$7.06^{+0.76}_{-0.66}$
	SSE	1.15 ± 0.02	1.18 ± 0.03	1.08 ± 0.008	$7.48^{+0.88}_{-0.76}$	$8.00^{+0.98}_{-0.85}$
	SSW	1.17 ± 0.02	1.20 ± 0.02	1.12 ± 0.007	$6.96^{+0.73}_{-0.63}$	$7.59^{+0.85}_{-0.74}$
	WSW	1.03 ± 0.01	1.04 ± 0.01	1.04 ± 0.005	$5.97^{+0.42}_{-0.37}$	$6.21^{+0.45}_{-0.40}$
	WNW	1.10 ± 0.02	1.11 ± 0.02	1.10 ± 0.006	$6.15^{+0.54}_{-0.46}$	$6.37^{+0.58}_{-0.50}$
	NNW	1.16 ± 0.02	1.19 ± 0.03	1.13 ± 0.008	$6.65^{+0.77}_{-0.65}$	$7.22^{+0.89}_{-0.76}$

Table 6.9 (continued)

radius	azimuth	data *HR*	data *HR*†	simulated *HR*	*kT* (keV)	*kT*† (keV)
$36' - 44'$	NNE	1.06 ± 0.04	1.09 ± 0.04	0.96 ± 0.010	$8.19^{+1.63}_{-1.32}$	$9.04^{+1.88}_{-1.53}$
	ENE	1.12 ± 0.04	1.14 ± 0.04	1.00 ± 0.010	$8.71^{+1.71}_{-1.40}$	$9.44^{+1.91}_{-1.57}$
	ESE	1.12 ± 0.04	1.14 ± 0.04	0.97 ± 0.011	$9.49^{+2.01}_{-1.64}$	$10.21^{+2.20}_{-1.81}$
	SSE	1.06 ± 0.04	1.08 ± 0.04	1.02 ± 0.011	$6.84^{+1.35}_{-1.03}$	$7.22^{+1.48}_{-1.15}$
	SSW	0.99 ± 0.03	1.01 ± 0.03	0.99 ± 0.009	$6.02^{+0.87}_{-0.68}$	$6.37^{+0.99}_{-0.78}$
	WSW	0.90 ± 0.01	0.91 ± 0.01	1.02 ± 0.006	$4.71^{+0.22}_{-0.17}$	$4.79^{+0.24}_{-0.19}$
	WNW	0.97 ± 0.02	0.98 ± 0.03	0.99 ± 0.008	$5.76^{+0.71}_{-0.56}$	$5.96^{+0.77}_{-0.61}$
	NNW	0.98 ± 0.03	1.00 ± 0.03	1.01 ± 0.009	$5.57^{+0.85}_{-0.61}$	$5.87^{+0.96}_{-0.71}$
$44' - 60'$	NNE	0.69 ± 0.03	0.70 ± 0.03	0.75 ± 0.009	$5.06^{+1.06}_{-0.59}$	$5.20^{+1.18}_{-0.68}$
	ENE	0.80 ± 0.04	0.81 ± 0.04	0.79 ± 0.011	$6.42^{+1.65}_{-1.15}$	$6.66^{+1.77}_{-1.24}$
	ESE	0.97 ± 0.05	0.98 ± 0.05	0.83 ± 0.013	$9.85^{+2.98}_{-2.27}$	$10.33^{+3.16}_{-2.42}$
	SSE	0.81 ± 0.04	0.83 ± 0.04	0.86 ± 0.013	$5.43^{+1.38}_{-0.82}$	$5.62^{+1.51}_{-0.92}$
	SSW	0.77 ± 0.03	0.78 ± 0.03	0.82 ± 0.010	$5.33^{+1.06}_{-0.68}$	$5.51^{+1.17}_{-0.76}$
	WSW	0.93 ± 0.02	0.95 ± 0.02	0.97 ± 0.007	$5.56^{+0.61}_{-0.49}$	$5.84^{+0.69}_{-0.56}$
	WNW	0.87 ± 0.03	0.88 ± 0.03	0.88 ± 0.011	$5.91^{+1.21}_{-0.85}$	$6.14^{+1.32}_{-0.94}$
	NNW	0.76 ± 0.03	0.77 ± 0.03	0.82 ± 0.009	$5.06^{+0.86}_{-0.53}$	$5.17^{+0.93}_{-0.59}$

† Corrected for the cool component of $kT_{\rm cool} = 2.05$ keV.

The azimuthal variation of temperatures are shown in figure 6.29a. The *HR* values and derived temperature values are listed in table 6.9a. The maximum and minimum temperatures are about 10 keV and 4 keV. Fitting a model with a constant value to the data in figure 6.29a gives a mean temperature of 5.2 ± 0.02 keV with $\chi^2/\nu = 2323/60$. The error is estimated at $\Delta\chi^2 = 2.706$ using the statistical errors only. The large χ^2 value clearly demonstrates the significant temperature variation. The central temperature is consistent with the previous results of 4.4 ± 0.1 keV based on the spectral fitting within the central $4'$ by Ezawa et al. (2001). Note that in figure 6.29a and b, the 6th data point in the $36' - 44'$ ring shows a lower temperature and good statistics because of presence of IC 310.

Figure 6.30a shows a frequency histogram of temperatures fitted with a Gaussian function. The temperatures used in the distribution are taken as the statistical error is less than 20%, which corresponds to the data within a radius of about $40'$ (1.2 Mpc). The histogram interestingly breaks off at 4 keV and shows a tail-like distribution toward high temperatures. The best-fit Gaussian function gives a large standard deviation of 2.36 keV which corresponds to 49% of a mean temperature of 4.81 keV. Though these temperatures include a contribution from the cool component, such a distribution looks unusual while the histograms of other 3 clusters are almost symmetric.

Figure 6.31a shows the one-dimensional cutouts of temperature distribution along two

(a)

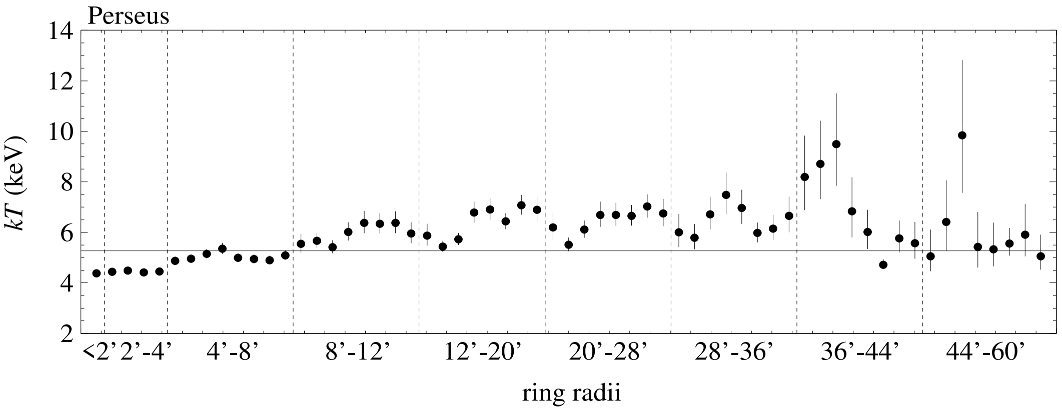

(b)

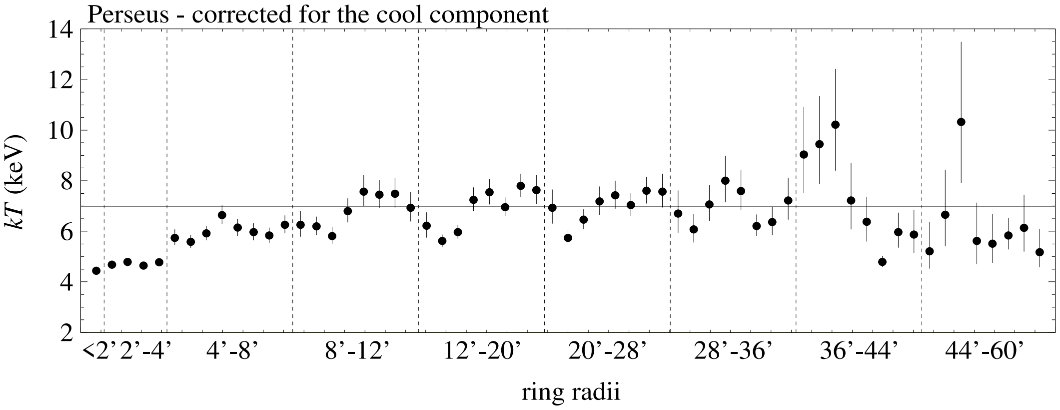

Figure 6.29: Azimuthal profiles of temperature for 9 annular rings for the Perseus cluster. Origin of the azimuth is in the north and the angle goes in counterclockwise way.

paths running in the north-south (path-A) and east-west (path-B) directions. The temperatures are calculated from the *HR* for each $5' \times 10'$ rectangular region, as indicated in figure 6.31c. The angular width of the central low-temperature region produced by the cool component seems more extended than that of the Centaurus cluster. The significant asymmetries are seen in both paths. The extended cool region in the east is recognized as a flat region between $-10'$ and $-20'$ along path-A. The very high temperature at the eastern edge ($-40'$ in path-A), the hot region in the south ($-30'$ in path-B), and the northern cool region ($+35'$ in path-B) can also be identified clearly. These one dimensional plots suggest that a significant change of the temperature occurs in a scale of $\sim 10'$ (300 kpc), even though the finer scale structure may be suppressed by the bin width of $5'$.

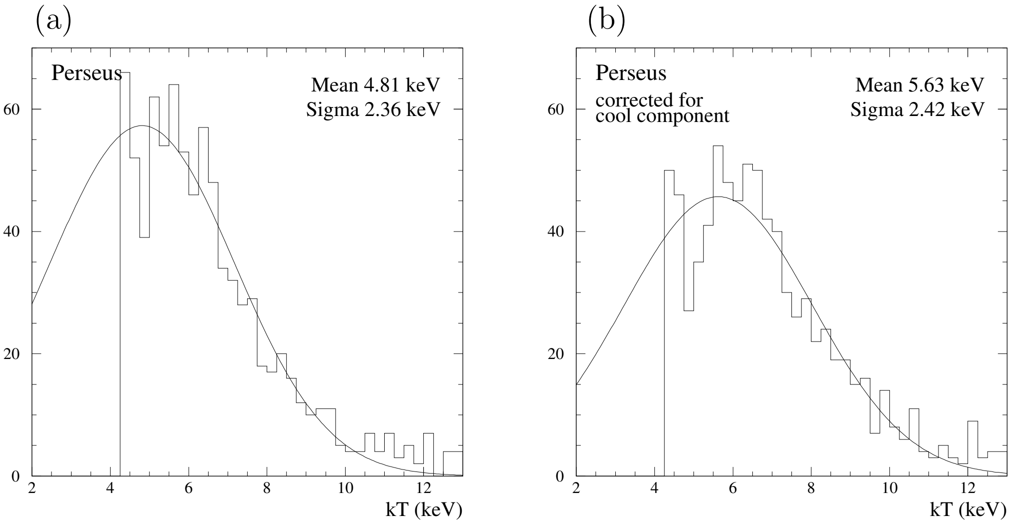

Figure 6.30: Frequency distribution of temperature for the Perseus cluster fitted with Gaussian function.

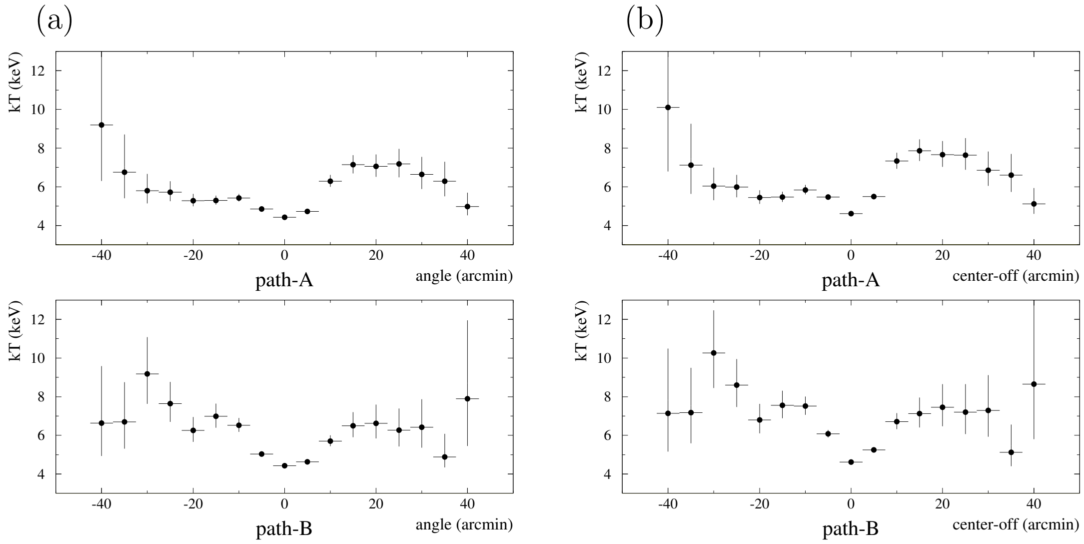

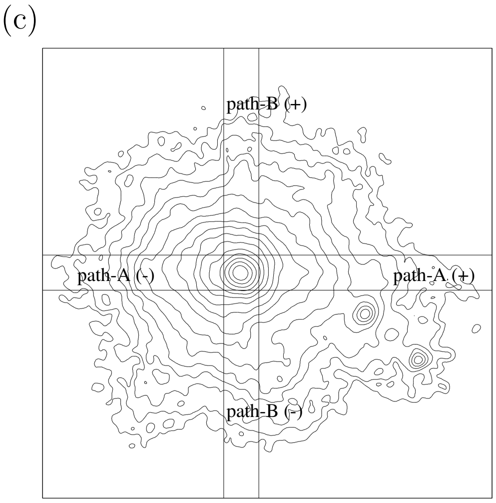

Figure 6.31: One-dimensional profiles of temperature for the Perseus cluster along SW to NE direction (path-A) and SE to NW direction (path-B) plotted as a function of the angle from the cluster center. The temperature in each bin is calculated for a $10' \times 5'$ rectangle. Data in (a) are before the correction for the cool component, and those in (b) are after it. The panel (c) shows the calculated paths.

6.4.2 Cool component

The Perseus cluster exhibits a strong cool component at the center. The spectrum from ASCA indicates that the temperature of the cool component is higher than that of the Centaurus cluster (Ezawa et al. 2001). We have attempted to subtract the cool component assuming a constant temperature of 2.05 keV which was derived from the central $r < 4'$ spectrum by Ezawa et al. (2001). The distribution of the cool component is approximated by a β-model based on the 2-β model fit of the surface brightness profile measured with the ROSAT PSPC as shown in 6.32. First, we fitted with a single β model to the profile of the outer $r > 10'$ region for the hot component. The best-fit parameters are $\beta_{\rm hot} = 0.64 \pm 0.01$, and $r_{\rm c,hot} = 10\farcm1 \pm 0\farcm3$. By fixing these parameters for the hot component, we obtained β model parameters for the cool component as $\beta_{\rm cool} = 1.16 \pm 0.01$, $r_{\rm c,cool} = 5\farcm0 \pm 0\farcm01$. However, the non-symmetric elongation of the X-ray image affects the distribution of the cool component significantly, because the cool component of the Perseus cluster extends out to around $30'$. We therefore took the observed PSPC image and multiplied it by the fraction of the cool component intensity derived by the 2-β model fit. We also introduced a cut off radius of $30'$, where the cool intensity becomes negligible sufficiently.

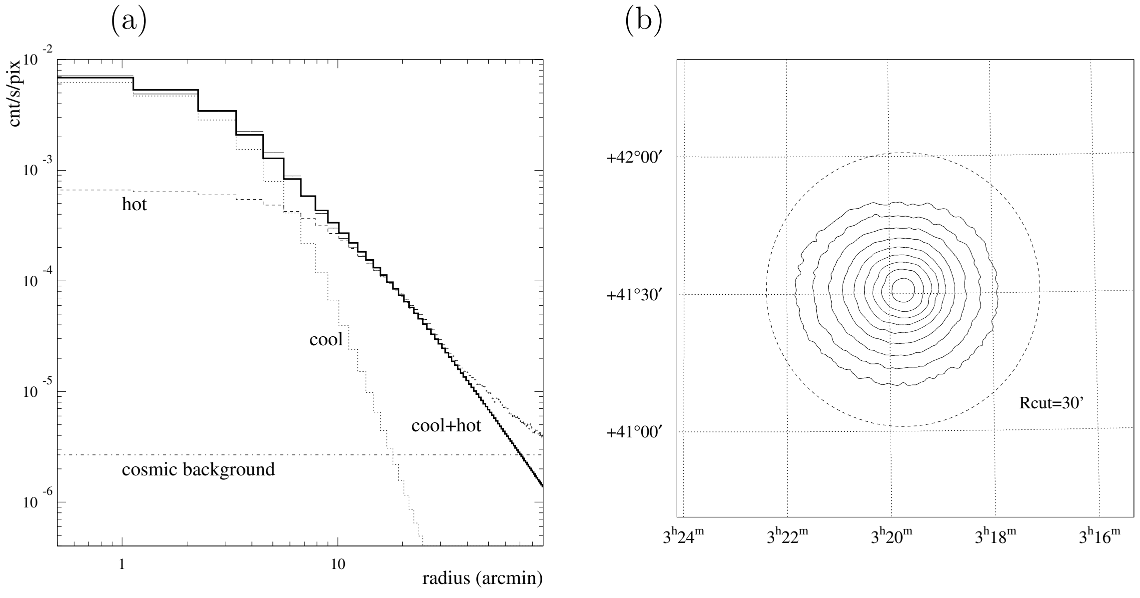

Figure 6.32: (a) The PSPC profile fitted with 2-β model after the particle background subtraction and the correction for the exposure and vignetting, and (b) X-ray image adopted for the cool component of the Perseus cluster.

Figure 6.28b shows the color-coded temperature map when the central cool component is subtracted. The temperatures naturally rise in almost the whole region. However, the central region indicates a lower temperature of 6.0 keV than the average even after the cool component correction. We also examined the azimuthal variation, the azimuthally averaged temperatures, the frequency histogram of the temperatures, and the one-dimensional profiles, all after the subtraction for the cool component. The results are shown in figure 6.29b, figure 6.30b, and figure 6.31b, respectively. The azimuthal temperature profiles in figure 6.29b show a wider variation than before. The mean temperature with a constant fit is 5.9±0.02 keV with the reduced chi-squared value of $\chi^2/\nu = 1769/60$. Again, the central $r < 4'$ region shows a low temperature around 5 keV. In the frequency histogram in figure 6.30b, the standard deviation becomes slightly larger to 2.42 keV when fitted with a Gaussian function. The ratio to the mean temperature of 5.63 keV is 43% which has decreased by 6%. The one-dimensional profiles in figure 6.31b show a clear temperature drop at the center, but the surrounding region rises up to 8 keV, significantly. The asymmetric shape becomes notable in both baths. The temperature in the cool region at $-20'$ from the center in path-A also increases to 6 keV.

6.4.3 Temperature and abundance maps from spectral fits

The temperature map calculated from the *HR* shows a complex structure. The temperatures vary in 5–9 keV with many fluctuations and there is also an extended cool region. Such a wide temperature range and the presence of the cool component hamper absolute determinations of temperature values and their structure, because the assumption of the isothermal cluster in the simulation oversimplifies the true situation. Also, the difference in the energy range between GIS and PSPC would cause some error in the ray-tracing simulation. Therefore, we attempt to derive another temperature map based on spectral fits to confirm the results of the *HR* analysis.

The combined GIS image for all pointings is divided into 7 × 7 cells with a size of $15' \times 15'$. The cell number allocations are shown in figure 6.33d. We have derived 41 pulse-height spectra, since the remaining 8 cells have zero (no observation) or very low (less than several hundred) photon counts. The lowest cluster flux compared with the background is about 1.3 for the cell #21. We fit the spectra with an absorbed MEKAL model in the 0.7–10 keV band. The best-fit parameters are shown in table 6.10. As in the previous *HR* analysis, $N_{\rm H}$ is fixed to the Galactic value of 1.4×10^{21} cm^{-2}. Figure 6.33a shows results from the single-temperature fit. For the cell #65 and #76, we applied an absorbed MEKAL + power-law model, because these regions include IC 310 and 1RXS J031525.1+410620, respectively. The photon indices of the power-law components are fixed to the best-fit values, $\Gamma = 2.1$ and 1.6 as shown in table 6.14, which are obtained from the spectral fitting for the point source only, as described later. The fractions of the point sources in the 0.7–10 keV band in the 2 cells, $F_{\rm ps}/F_{\rm tot}$, are 43% and 47% for IC 310 and 1RXS source, respectively.

For the central 9 cells, the large χ^2 values in table 6.10 clearly indicate the necessity of the cool component. The χ^2 values decrease considerably with a single-temperature model in the 3–10 keV band, or a 2-temperature model in the 0.7–10 keV band as shown

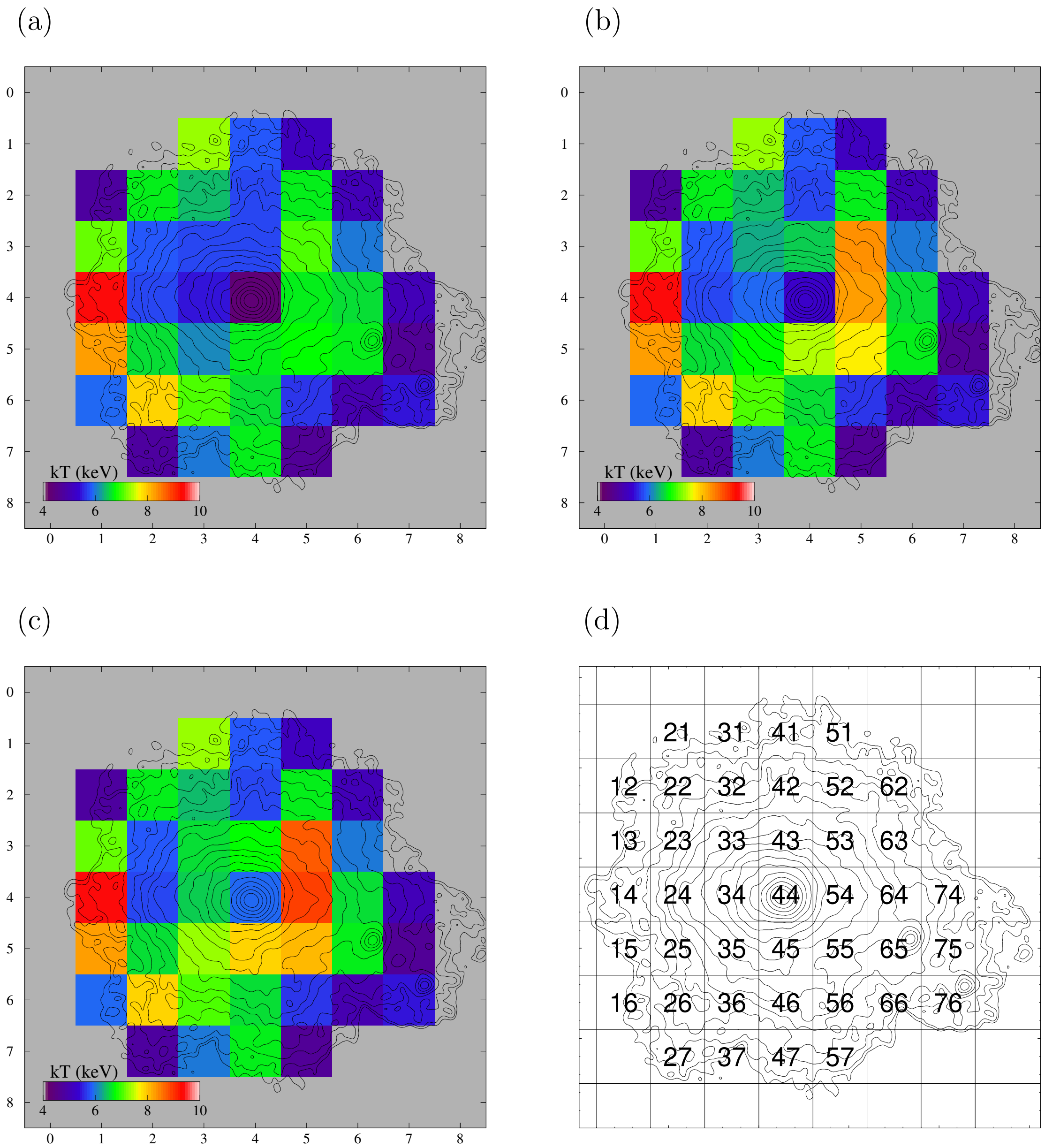

Figure 6.33: The temperature map obtained from the spectral fitting and the cell number corresponded in table 6.10, 6.11, and 6.12. (a) shows the temperatures fitted with a single temperature model. (b) and (c) differ on the central 9 cells from (a), fitted with a 2-temperature model and 2-temperature model with gain parameter, respectively.

in table 6.11 and 6.12. For the 2-temperature fit, the abundance for the cool component is fixed to the hot component one because there are no clear emission lines such as from Si, S, and Fe-L. For example, the previous χ^2/ν= 851.6/123 with the single temperature fit decreases to χ^2/ν= 260.43/121 with the 2-temperature model for the central cell #44. The temperature map obtained from the 2-temperature fit is shown in figure 6.33b. This shows that the immediate west from the center (#53–#55) is hotter than the surrounding region. The χ^2 value is, however, still large and the very high statistics requires us to

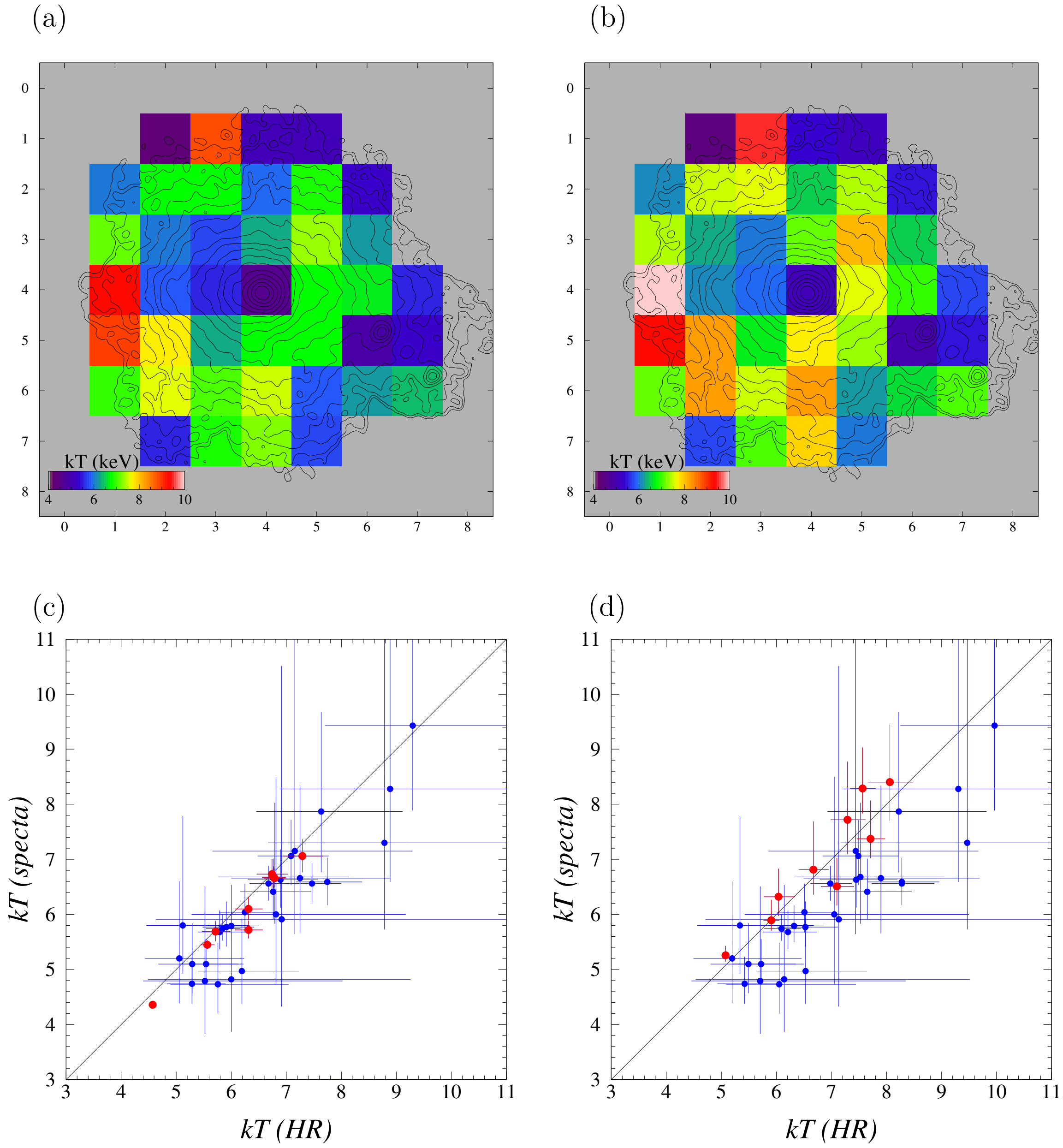

Figure 6.34: The panel (a) shows the temperature map obtained from the hardness ratio analysis with a size of $15' \times 15'$, and (b) is same as (a) but after correction for the cool component. The panel (c) and (d) show the distribution of temperatures obtained from the hardness ratio and from spectral fits with with a single and 2-temperature model, respectively. The error bars of the data are 90% confidence limit, and the red circles show the central 9 cells.

look into the systematic error in the GIS gain. The correction for such an effect becomes important only when the statistics is exceptionally high. The accuracy of the GIS gain is estimated to be about 1% based on the GIS calibration (Makishima et al. 1996). We find that the reduced χ^2 decreases by setting the gain parameter to 0.987–0.993 for all 9 cells as shown in table 6.13. For the central cell, however, the photon statistics is too high to obtain an acceptable spectral fit, indicating χ^2/ν=201.2/121. This may imply even 2-temperature model with a gain parameter is insufficient. The temperature map including the gain adjustment is shown in figure 6.33c, which is generally similar to the feature in figure 6.33b. We present all the pulse-height spectra together in appendix B.

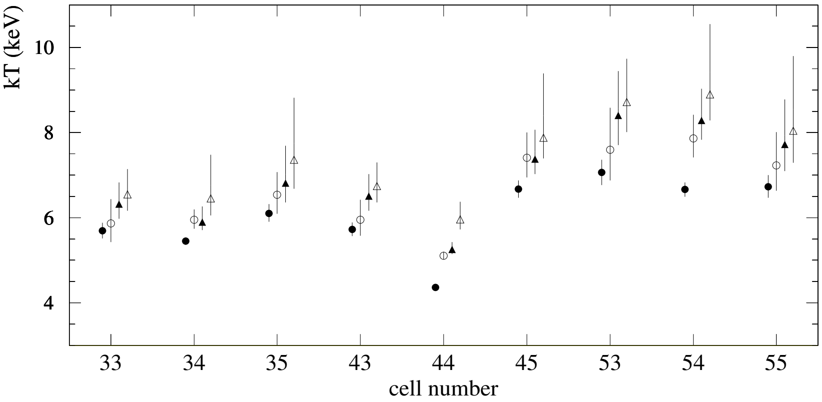

Figure 6.35: The best-fit temperatures in the central 9 cells fitted with the single temperature model in the 0.7–10 keV band (filled circles), in the 3–10 keV band (open circles), and with the 2-temperature model (filled triangles), with gain parameter (open triangles).

As shown in figure 6.33a, b and c, the absolute temperature of the hot component depends on the choice of spectral model in the central region due to the presence of the cool component. The necessity of the cool component is obvious based on the χ^2 value, but we should be careful about the introduction of the gain parameter, because the obtained values of the spectral parameters change quite sensitively for the 2-temperature fit. Figure 6.35 compares the derived temperatures of the hot component in the central 9 cells for various spectral models. Most of the temperatures rise in the order of the single-temperature fit, single-temperature fit in the 3–10 keV band, 2-temperature fit, and 2-temperature gain fit. We can also confirm that the relative values among the cells do not change largely, and that, except for the single temperature 0.7–10 keV fit (filled circles), the temperatures are mostly consistent with each other.

In order to compare with the temperatures calculated from the *HR*s, we have derived the temperature maps from the hardness ratio analysis method with a size of $15' \times 15'$ cell as shown in figure 6.34a and b. Figure 6.34b shows the data after the correction for the central cool component in the same way as described in previous subsection. The absolute temperature values looks different from figure 6.33, however, the whole features show relatively similar, for example the cool region around $20' - 40'$ east, hot region around $20'$ west, and very hot region at east edge. Figure 6.34c and d show the distribution of temperatures calculated from the *HR*s and obtained from the spectral fits excluding the cell #65 and #76, because these regions include IC 310 and 1RXS source.

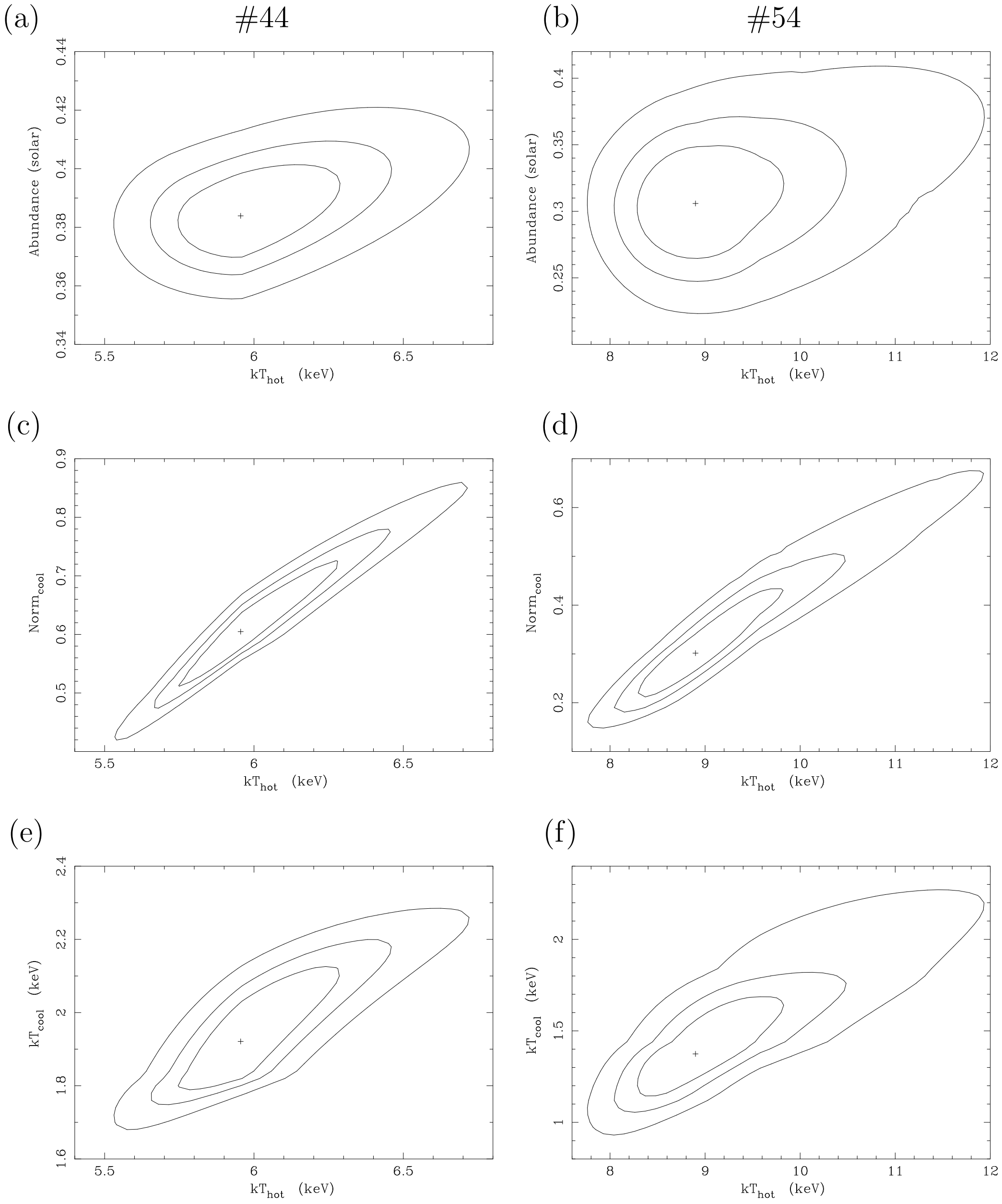

Figure 6.36: The confidence contours of (a,b) $kT_{\rm hot}$ versus abundance, (c,d) $kT_{\rm hot}$ versus normalization of the cool component, and (e,f) $kT_{\rm hot}$ versus $kT_{\rm cool}$, obtained from the 2-temperature gain fit of the cell #44 (left panels) and #54 (right panels). The contours show 68%, 90%, and 99% confidence levels.

The temperatures with spectral fits in figure 6.34d are the best-fit parameters with the 2-temperature fits as shown in table 6.12. We have confirmed that both temperatures are consistent within the 90% errors.

The increase of the hot component temperature also affects other parameters, such as the temperature and fraction of the cool component. To look into the correlation among the spectral parameters, we show confidence contours for the cell #44 and #54 in the 2-temperature gain fit in figure 6.36. The temperature for the cell #44 shows the largest

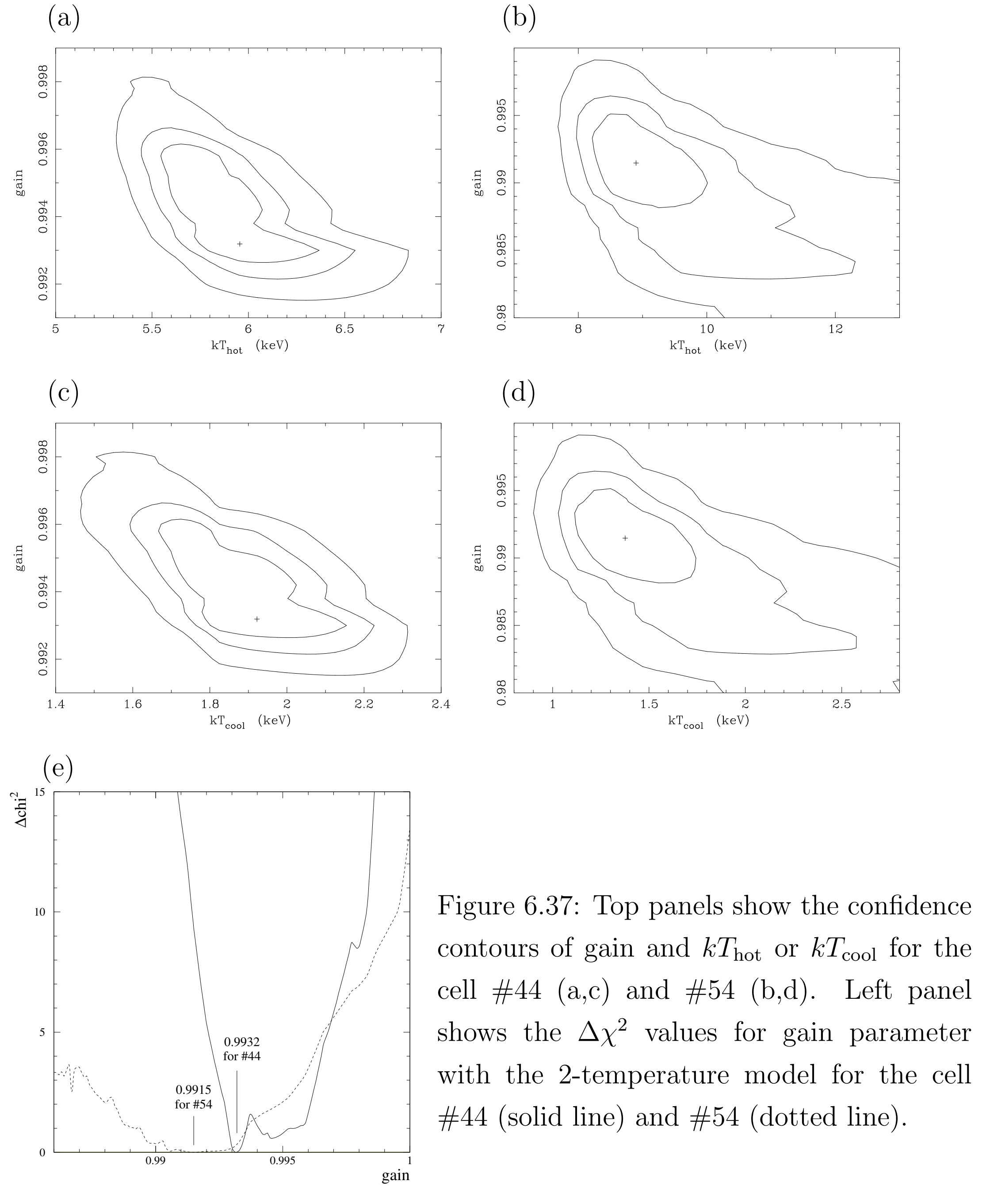

Figure 6.37: Top panels show the confidence contours of gain and $kT_{\rm hot}$ or $kT_{\rm cool}$ for the cell #44 (a,c) and #54 (b,d). Left panel shows the $\Delta\chi^2$ values for gain parameter with the 2-temperature model for the cell #44 (solid line) and #54 (dotted line).

increase by the introduction of the gain parameter, and the cell #54 is the second. There are obvious correlations between $kT_{\rm cool}$ and $kT_{\rm hot}$, and $Norm_{\rm cool}$ and $kT_{\rm hot}$, where $Norm_{\rm cool}$ is $10^{-14} \times EI/4\pi D^2$ at a distance of D and an emission integral EI. In the $kT_{\rm cool} - kT_{\rm hot}$ correlation, the fractional increase rate of $kT_{\rm cool}$ is about 1.6 times that of $kT_{\rm hot}$ for the cell #44. The metal abundance shows little dependence on the temperature. To examine the influence of the gain parameter, we also show the confidence contours between the gain parameter and temperatures for the same cell #44 and #54 in figure 6.37a-d. The confidence contours show some correlation between the gain and temperatures, indicating that the temperature changes by 10% for a change of the gain by 0.02. The errors related to the gain parameter are comparable to those of the other parameters. Figure 6.37e shows the variation of the $\Delta\chi^2$ value with the gain parameter. The $\Delta\chi^2$ curve for the cell #44 shows a sharp minimum, but the minimum is wider for the cell #54. Note that the $\Delta\chi^2$ value for gain=1.0 for the cell #44 is 59.2, which is a very significant deviation from the minimum.

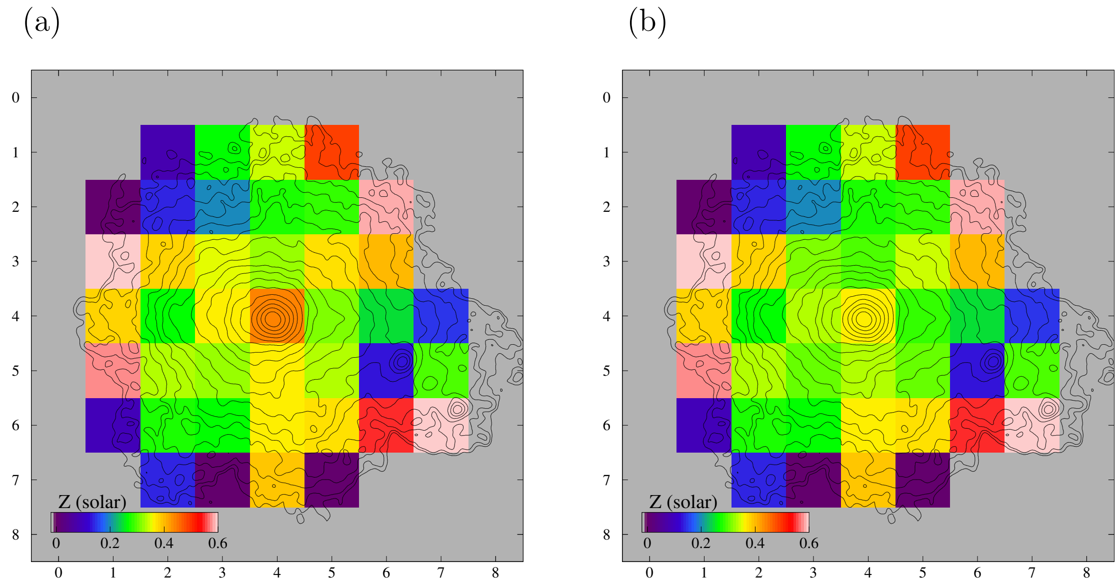

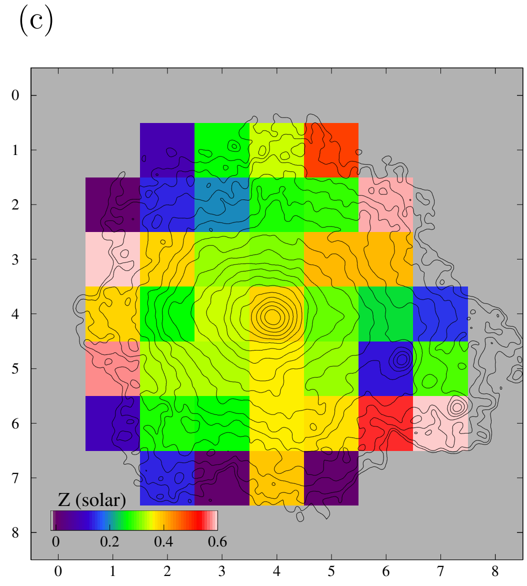

Figure 6.38: Color-coded abundance map for the Perseus cluster. X-ray intensity with the GIS2 is shown with contours. The assumed spectral models are; (a) single temperature 0.7–10 keV fit, (b) 2-temperature fit, and (c) with gain adjustment.

The temperature of the central cell #44 does not exceed 6 keV even with 2-temperature model as the temperature map has already shown. The east cool region in figure 6.33a becomes somewhat hotter in figure 6.33c, but the temperature is lower than the west region all the same. Around the cell #14 and #15, the temperature is high at $8 \sim 9$ keV as already seen in the *HR* temperature map (figure 6.28). Also, the outer north-east and south-east regions show considerably low temperatures around ∼ 5 keV again. Thus, we confirm the general consistency of the temperature maps derived from both *HR* analysis and spectral fits.

Figure 6.38 shows maps for metal abundance. The same fitting conditions apply for a, b, and c as in figure 6.33. Correlations between metal abundance and temperature, corresponding to the 3 fitting conditions, are shown in figure 6.39a, b, and c. We do not recognize a clear relation between the two parameters. Concerning the metal abundance, most of the regions show a moderate value of 0.3–0.4 solar with several high points at 0.5–0.6 solar. Since most of the high-abundance points are in the outer region with fairly large errors, this feature may be simply due to statistical fluctuation.

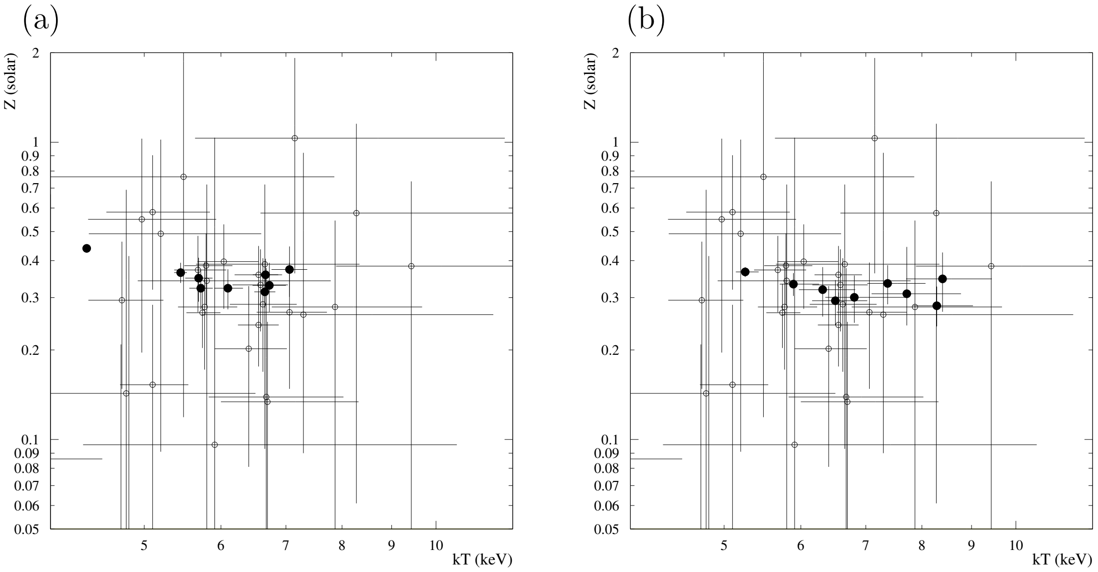

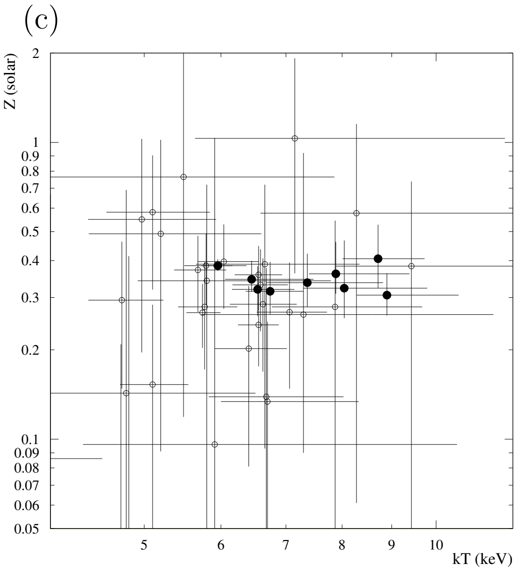

Figure 6.39: Distribution of temperatures and abundances based on spectral fitting with a single temperature model for (a). (b) and (c) are applied the results with (b) a 2-temperature, and (3) 2-temperature with a gain parameter model for the central 9 cells plotted with the filled circles.

In order to examine the correlation between the temperature and abundance, we fit the data for the 41 cells with a constant model. Figure 6.40 shows the results using the values obtained from 2-temperature gain fit. The data are arranged in the order of distance from the cluster center. The constant fit for the temperatures gives a mean value of 6.04 ± 0.06 keV with $\chi^2/\nu = 152.8/40$. Thus, the large χ^2 completely rejects the isothermality. For the abundance, we obtained the mean value of 0.34 ± 0.01 solar with $\chi^2/\nu = 66.25/40$. The constant value is rejected with a confidence level of 99.6%. We also fit the abundances with a linear model, and the χ^2 value become smaller to $\chi^2/\nu = 40.02/39$. This model is acceptable at the 90% confidence level and the central value is 0.376 solar. The metal abundance distribution, therefore, indicates a gentle gradient with the low metallicity in the outer region. This feature is consistent with the previous result by Ezawa et al. (2001). We also conclude that there is no obvious correlation between the temperature and abundance distribution.

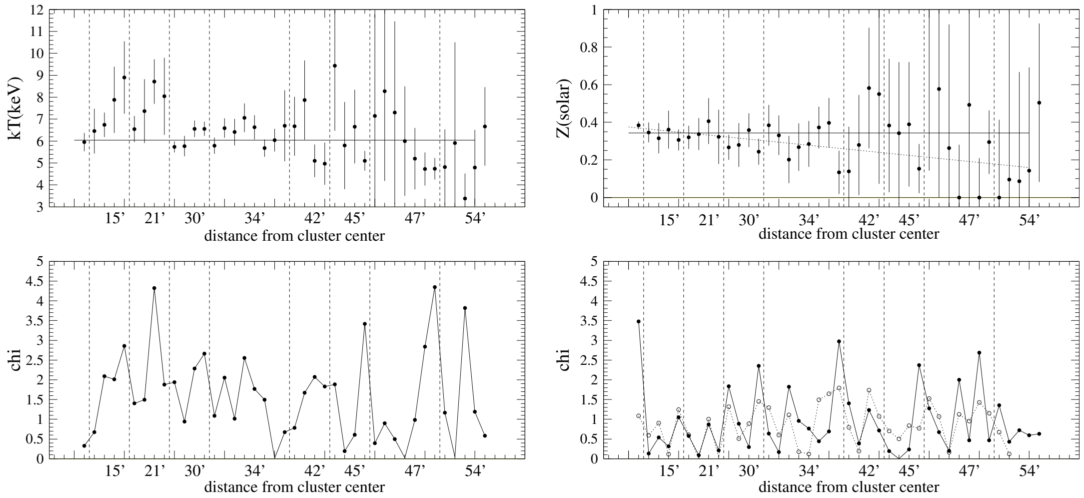

Figure 6.40: Constant fit for the distributions of temperature and abundance for the Perseus cluster derived from the spectral fits. The data are arranged in the order of the distance from the cluster center, so that the abscissa almost corresponds to the radius.

Table 6.10: Spectral parameters for each cell with the single-temperature MEKAL model in the 0.7–10 keV band, and $N_{\rm H}$ is fixed to the Galactic value $1.4 \times 10^{21} {\rm cm}^{-2}$.

No.	kT (keV)	Z (solar)	$\chi^2/d.o.f$
12	$4.82^{+1.72}_{-0.95}$	$0.00^{+0.41}_{-0.00}$	14.39/28
13	$7.15^{+4.63}_{-1.51}$	$1.03^{+0.89}_{-0.67}$	33.67/27
14	$9.43^{+2.97}_{-1.54}$	$0.38^{+0.35}_{-0.34}$	21.68/28
15	$8.28^{+4.10}_{-1.69}$	$0.58^{+0.58}_{-0.52}$	29.09/28
16	$5.91^{+4.60}_{-1.59}$	$0.10^{+0.94}_{-0.10}$	33.90/28
21	$3.38^{+1.14}_{-0.68}$	$0.09^{+0.58}_{-0.09}$	20.47/28
22	$6.68^{+1.35}_{-0.85}$	$0.14^{+0.24}_{-0.14}$	34.23/28
23	$5.79^{+0.37}_{-0.29}$	$0.38^{+0.11}_{-0.10}$	77.26/60
24	$5.74^{+0.25}_{-0.21}$	$0.27^{+0.07}_{-0.06}$	73.13/60
25	$6.59^{+0.44}_{-0.42}$	$0.33^{+0.10}_{-0.10}$	75.22/60
26	$7.87^{+1.80}_{-1.10}$	$0.28^{+0.27}_{-0.28}$	29.54/28
27	$4.79^{+1.72}_{-0.96}$	$0.14^{+0.55}_{-0.14}$	36.42/28
31	$7.30^{+4.16}_{-1.57}$	$0.26^{+0.66}_{-0.17}$	26.66/28
32	$6.41^{+0.60}_{-0.50}$	$0.20^{+0.13}_{-0.12}$	85.40/60
33	$5.69^{+0.19}_{-0.18}$	$0.35^{+0.06}_{-0.06}$	147.88/123
34	$5.45^{+0.08}_{-0.08}$	$0.36^{+0.03}_{-0.03}$	187.15/123
35	$6.10^{+0.22}_{-0.20}$	$0.32^{+0.05}_{-0.05}$	176.50/123
36	$7.06^{+0.66}_{-0.53}$	$0.27^{+0.13}_{-0.12}$	65.33/60
37	$6.00^{+2.50}_{-1.27}$	$0.00^{+0.28}_{-0.00}$	30.67/28
41	$5.80^{+1.99}_{-0.88}$	$0.34^{+0.38}_{-0.34}$	46.47/28
42	$5.77^{+0.47}_{-0.35}$	$0.28^{+0.12}_{-0.11}$	67.19/60
43	$5.72^{+0.17}_{-0.16}$	$0.32^{+0.05}_{-0.05}$	174.12/123
44	$4.36^{+0.03}_{-0.03}$	$0.44^{+0.01}_{-0.01}$	851.62/123
45	$6.67^{+0.20}_{-0.20}$	$0.36^{+0.05}_{-0.05}$	185.11/123
46	$6.56^{+0.38}_{-0.36}$	$0.36^{+0.09}_{-0.09}$	85.27/60
47	$6.66^{+1.68}_{-1.00}$	$0.39^{+0.33}_{-0.30}$	45.80/28
51	$5.20^{+1.40}_{-0.82}$	$0.49^{+0.53}_{-0.40}$	22.89/28
52	$6.63^{+0.55}_{-0.50}$	$0.28^{+0.12}_{-0.12}$	142.41/123
53	$7.06^{+0.30}_{-0.30}$	$0.37^{+0.07}_{-0.07}$	172.98/123
54	$6.66^{+0.17}_{-0.17}$	$0.31^{+0.04}_{-0.04}$	275.38/123
55	$6.73^{+0.27}_{-0.26}$	$0.33^{+0.06}_{-0.06}$	162.45/123
56	$5.68^{+0.39}_{-0.31}$	$0.37^{+0.11}_{-0.10}$	74.18/60
57	$4.73^{+0.76}_{-0.53}$	$0.00^{+0.21}_{-0.00}$	50.55/60

Table 6.10 (continued)

No.	kT (keV)	Z (solar)	$\chi^2/d.o.f$
62	$5.10^{+0.74}_{-0.53}$	$0.58^{+0.32}_{-0.26}$	81.90/60
63	$6.04^{+0.52}_{-0.37}$	$0.40^{+0.13}_{-0.12}$	71.65/60
64	$6.56^{+0.32}_{-0.31}$	$0.24^{+0.07}_{-0.07}$	84.06/60
65†	$6.70^{+1.62}_{-0.70}$	$0.13^{+0.12}_{-0.12}$	80.36/59
66	$4.97^{+0.96}_{-0.59}$	$0.55^{+0.48}_{-0.35}$	28.54/28
74	$5.10^{+0.45}_{-0.38}$	$0.15^{+0.13}_{-0.12}$	73.03/60
75	$4.74^{+0.49}_{-0.36}$	$0.29^{+0.17}_{-0.15}$	60.41/60
76†	$5.49^{+2.37}_{-2.86}$	$0.76^{+2.86}_{-0.65}$	28.81/27

† MEKAL + power-law fit as the ICM plus the point source component.

Table 6.11: Spectral parameters for the central 9 cells with the single temperature MEKAL model in the 3–10 keV band. $N_{\rm H}$ is fixed to the Galactic value $1.4 \times 10^{21}{\rm cm}^{-2}$. The metal abundance of the cool component is fixed to be the same as the hot component.

No.	$kT_{\rm hot}$ (keV)	Z (solar)	$\chi^2/d.o.f$
33	$5.86^{+0.58}_{-0.44}$	$0.32^{+0.06}_{-0.06}$	61.30/57
34	$5.95^{+0.24}_{-0.21}$	$0.33^{+0.03}_{-0.03}$	56.15/57
35	$6.54^{+0.53}_{-0.45}$	$0.29^{+0.05}_{-0.05}$	79.91/57
43	$5.95^{+0.47}_{-0.38}$	$0.27^{+0.05}_{-0.05}$	53.80/57
44	$5.10^{+0.09}_{-0.09}$	$0.35^{+0.02}_{-0.02}$	133.76/57
45	$7.41^{+0.60}_{-0.46}$	$0.33^{+0.05}_{-0.05}$	74.55/57
53	$7.60^{+0.98}_{-0.72}$	$0.33^{+0.07}_{-0.07}$	69.71/57
54	$7.87^{+0.55}_{-0.45}$	$0.27^{+0.04}_{-0.04}$	71.65/57
55	$7.23^{+0.79}_{-0.60}$	$0.29^{+0.07}_{-0.07}$	77.87/57

Table 6.12: Spectral parameters for the central 9 cells with the 2-temperature MEKAL model in the 0.7–10 keV band. $N_{\rm H}$ and abundance of the cool component are treated the same way as in table 6.11.

No.	$kT_{\rm hot}$ (keV)	$kT_{\rm cool}$ (keV)	Z (solar)	$F_{\rm cool}/F_{\rm tot}$ (%)	$\chi^2/d.o.f$
33	$6.32^{+0.51}_{-0.35}$	$0.81^{+0.34}_{-0.40}$	$0.32^{+0.06}_{-0.06}$	2.8	119.67/121
34	$5.89^{+0.37}_{-0.19}$	$1.03^{+0.39}_{-0.43}$	$0.33^{+0.03}_{-0.03}$	2.4	131.42/121
35	$6.81^{+0.88}_{-0.45}$	$1.14^{+0.76}_{-0.61}$	$0.30^{+0.06}_{-0.05}$	2.7	157.41/121
43	$6.51^{+0.51}_{-0.35}$	$0.97^{+0.28}_{-0.40}$	$0.29^{+0.05}_{-0.05}$	3.4	132.76/121
44	$5.26^{+0.17}_{-0.12}$	$1.38^{+0.12}_{-0.07}$	$0.37^{+0.01}_{-0.01}$	7.4	260.43/121
45	$7.38^{+0.69}_{-0.35}$	$1.04^{+0.46}_{-0.44}$	$0.34^{+0.05}_{-0.05}$	2.4	156.45/121
53	$8.40^{+1.04}_{-0.70}$	$0.96^{+0.33}_{-0.46}$	$0.35^{+0.08}_{-0.08}$	3.2	137.62/121
54	$8.29^{+0.74}_{-0.45}$	$1.12^{+0.23}_{-0.18}$	$0.28^{+0.04}_{-0.04}$	4.6	150.47/121
55	$7.72^{+1.06}_{-0.62}$	$1.34^{+0.58}_{-0.68}$	$0.31^{+0.14}_{-0.07}$	3.5	148.01/121

Table 6.13: Spectral parameters for the central 9 cells with the 2-temperature MEKAL model with a gain parameter in the 0.7–10 keV band. The same assumptions for $N_{\rm H}$ and abundance of the cool component as in table 6.11 are made.

No.	$kT_{\rm hot}$ (keV)	$kT_{\rm cool}$ (keV)	Z (solar)	gain	$F_{\rm cool}/F_{\rm tot}$ (%)	$\chi^2/d.o.f$
33	$6.55^{+0.60}_{-0.39}$	$0.90^{+0.54}_{-0.57}$	$0.32^{+0.06}_{-0.06}$	$0.990^{+0.010}_{-0.002}$	1.99	117.91/121
34	$6.45^{+1.02}_{-0.40}$	$1.74^{+1.53}_{-0.75}$	$0.35^{+0.05}_{-0.03}$	$0.993^{+0.005}_{-0.004}$	5.25	121.55/121
35	$7.36^{+1.46}_{-0.68}$	$1.83^{+3.55}_{-0.99}$	$0.34^{+0.09}_{-0.06}$	$0.987^{+0.007}_{-0.005}$	4.11	145.04/121
43	$6.74^{+0.56}_{-0.38}$	$1.13^{+1.92}_{-0.55}$	$0.32^{+0.08}_{-0.05}$	$0.989^{+0.005}_{-0.007}$	2.68	118.02/121
44	$5.96^{+0.42}_{-0.23}$	$1.92^{+0.20}_{-0.13}$	$0.38^{+0.02}_{-0.01}$	$0.993^{+0.003}_{-0.001}$	15.23	201.17/121
45	$7.88^{+1.51}_{-0.49}$	$1.43^{+2.42}_{-0.71}$	$0.36^{+0.10}_{-0.05}$	$0.990^{+0.004}_{-0.002}$	2.73	145.69/121
53	$8.71^{+1.02}_{-0.70}$	$1.11^{+0.53}_{-0.53}$	$0.41^{+0.12}_{-0.08}$	$0.988^{+0.009}_{-0.006}$	2.43	129.47/121
54	$8.90^{+1.65}_{-0.62}$	$1.38^{+0.49}_{-0.24}$	$0.31^{+0.06}_{-0.04}$	$0.992^{+0.004}_{-0.004}$	5.43	136.98/121
55	$8.04^{+1.75}_{-0.75}$	$1.51^{+1.30}_{-0.51}$	$0.32^{+0.14}_{-0.07}$	$0.993^{+0.003}_{-0.005}$	3.48	141.98/121

6.4.4 Point sources

There are 2 X-ray bright point sources at south-west in the Perseus cluster. Their intensity and energy spectra are examined here. The expanded GIS images in the 0.7–10 keV band are shown in figure 6.41.

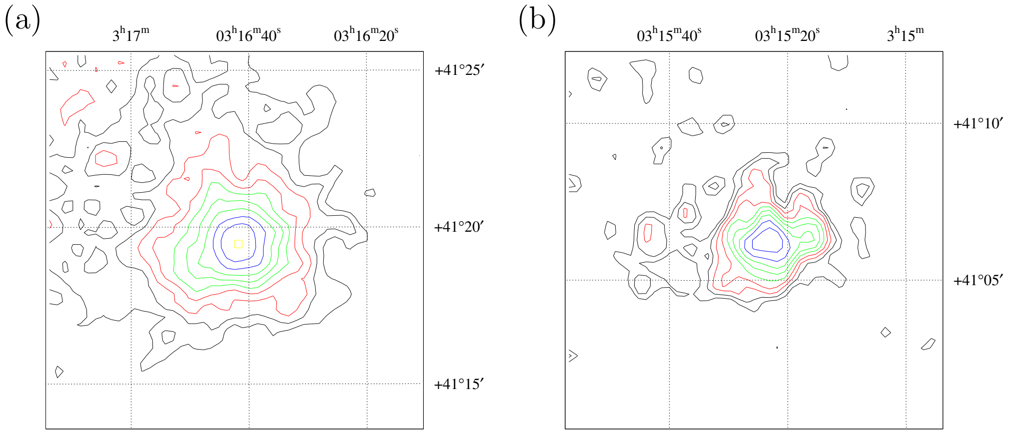

Figure 6.41: GIS image of (a) IC 310, and (b) 1RXS J031525.1+410620 in the 0.7–10 keV band. The image size is 12′ × 12′ which corresponds 370 × 370 kpc at the distance of the Perseus cluster.

IC310

IC310 is a head-tail radio galaxy at a distance of $z = 0.01888$ (Huchra et al. 1999) which is close to the Perseus, and the coordinate is $(\mathrm{R.A., Decl.})_{\mathrm{J2000}} = (3^{\mathrm{h}}16^{\mathrm{m}}42.9^{\mathrm{s}}, +41^\circ19'30'')$. The extent of the radio tail is as long as ~ 400 kpc $\sim 11'$ (Sijbring & Bruyn 1998). This source was also detected in the *SPARTAN-1* data, and the PSPC observation showed the X-ray luminosity to be $\sim 10^{43}$ erg s^{-1} (Schwarz et al. 1992), which is typical for a group of galaxies rather than a single elliptical galaxy.

Figure 6.42 shows the spectrum accumulated within a radius 5′. We took the data of around $r = 5' - 8'$ region for the background including the cluster component. The best-fit parameters with an absorbed MEKAL model or a power-law model are listed in table 6.14. The obtained temperature ~ 4 keV with MEKAL model is consistent with the *HR* results as shown in the temperature map in figure 6.28. The spectrum can also be fitted with a steep power-law model with the photon index of $\Gamma \sim 2.1$. The absorbed X-ray flux in the $0.5 - 10$ keV band is estimated to be $F_{\mathrm{X}} = 1.1 \times 10^{-11}$ erg cm^{-2} s^{-1}. The intrinsic luminosity is derived to be 0.8×10^{43} erg s^{-1} in the 0.5–2 keV energy band, which is consistent with the previous ROSAT result. Sambruna et al. (1999) has analyzed the ASCA spectrum, and fitted with a power law model, plus a Raymond-Smith model as the cluster component, including the galactic absorption. They derived the best-fit temperature of $kT = 5.6^{+2.5}_{-2.8}$ keV and $Z = 0.3$ for the Raymond-Smith model, and the photon index of $2.3^{+1.9}_{-0.4}$ for the power-law model. The difference from the present result is probably due to the background subtraction.

1RXS J031525.1+410620

This source is not optically identified, and the redshift is unknown. The pulse-height spectrum within a radius of $5'$ is shown in figure 6.42. The background is also taken from the surrounding $r = 5' - 8'$ region. The spectrum turned out to be very hard, and the obtained temperature with absorbed MEKAL model is about 16 keV, which is again consistent with the value in the temperature map. By fitting a power-law model, the photon index is obtained to be ~ 1.6, and the absorption of $N_{\rm H} \sim 10^{22}$ cm^{-2} is required, which is larger than the Galactic value. The observed X-ray flux is estimated to be 3.6×10^{-12} erg cm^{-2} s^{-1} in the 0.5 – 10 keV band. Assuming that the distance is the same as the Perseus cluster, the luminosity is calculated to be 0.7×10^{43} erg s^{-1}. The hard spectrum and the high luminosity are typical of AGNs, therefore, we suggest that this source is possibly an AGN.

Table 6.14: Spectral parameters for point sources in Perseus.

name	Model	$N_{\rm H}$ 10^{21}(cm^{-2})	kT/Γ (keV/)	Z (solar)	$\chi^2/d.o.f$
IC 310	MEKAL	1.4 (fix)	$3.5^{+0.5}_{-0.4}$	$0.44^{+0.4}_{-0.3}$	25.7/23
	Power law	1.4 (fix)	$2.1^{+0.1}_{-0.1}$	—	21.4/23
1RXS J031525.1+410620	MEKAL	$8.4^{+1.0}_{-0.6}$	16^{+84}_{-11}	$0.0^{+5.0}_{-0.0}$	20.2/22
	Power law	$10^{+1.5}_{-0.7}$	$1.6^{+0.7}_{-0.5}$	—	20.6/23

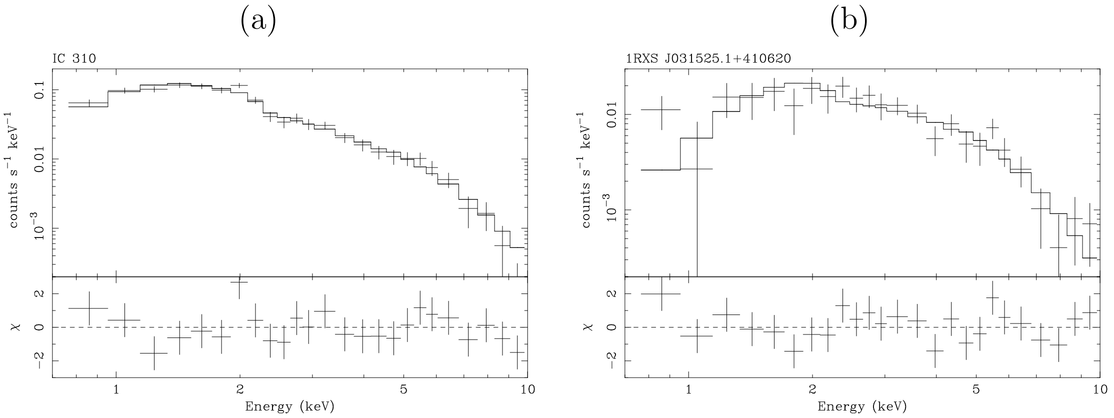

Figure 6.42: Pulse-height spectra of (a) IC 310 and (b) 1RXS J031525.1+410620 with the best-fit absorbed power-law models.

Chapter 7

Discussion

The ASCA mapping observations have revealed significantly different temperature features in the nearby bright 4 clusters, which show a fairly symmetric ICM distribution. The difference probably resulted from the past history of mergers. In this chapter, we attempt to perform quantitative discussion about the physical condition of the ICM, and consider the evolutional history for the 4 clusters, including other aspects such as metallicity distribution, galaxy distribution, and central cool component. The characteristics and estimated parameters for the 4 clusters are summarized in table 7.1.

7.1 Abell 1060

Temperature distribution: The temperature map of A1060 shows that the ICM is almost isothermal with $kT \sim 3.3$ keV over the whole cluster region ($r \sim 1.2$ Mpc). There is a slightly hotter region at $10'$ south-east which may possibly be resulted from a recent small merger. In fact, there is a possible small subgroup of NGC 3312, 3314a, and a small ring galaxy around the hot region. The difference of radial velocity to the cluster of about 1000 km s^{-1} would be enough to raise a temperature of ~ 0.2 keV. However, the temperature variation of less than 10% is too ambiguous to discuss the nature as the spectral analysis shows that the temperatures deviation is only 1.7σ. Also, a size and energy of the feature are too small to impact on the main cluster formation history. Therefore, we conclude that the isothermality is good in A1060. This indicates that A1060 has not experienced a major merger in the recent a few Gyr.

Metal distribution: Tamura et al. (1996) have reported the uniform metal distribution with a rather low level of 0.3 solar considering the other 3 clusters. The constancy of the metal abundance, as well as the constant temperature, suggests that the ICM in A1060 had been well mixed after an early starburst phase of $z > 1 \sim 2$ (Madau 1999) where metals have been injected into the ICM. If the mixing had occurred before the metal injection period and there was no mixing in the later phase, the metal mass density should follow galaxies and exhibit a large-scale metallicity gradient.

The absence of the metal concentration in the central region indicates that the cD galaxy has made little contribution to the metal enrichment of the ICM. In fact, the cD galaxy of A1060, NGC 3311, is smaller than those in typical bright cD clusters, and accordingly the central peak of the X-ray surface brightness and the accompanying cool component are the weakest among the 4 clusters presently studied.

Galaxy distribution: The above features, in particular the absence of the central sharp peak and the accompanying cool component, suggest that the formation process of A1060 has been rather slow. One reason could be that the number density of galaxies in the surrounding region is low. There is an empty space of about 60–70 Mpc extent in front and behind A1060 along the line of sight (Richter et al. 1982). The low matter density and the early mixing of the gas may have jointly acted to hold the growth speed of A1060.

Time scale: Let us investigate here various time scales which are relevant for the thermal conditions of the ICM. The time scale for radiative cooling is calculated from the central density, temperature, and the cooling function given by equation 2.17 The cooling function, $\Lambda(T, Z)$, depends on the temperature and metal abundance. We estimate the cooling time at the center of A1060 to be about 4 Gyr from the metal abundance of 0.3 solar, the temperature of 3 keV, the central density of 4×10^{-3} cm^{-3}, and the cooling function (Sutherland and Dopita 1993) with the assumption of $n_{\rm e} = n_{\rm i}$. The central cool gas would take $\sim$ 10 Gyr or more to build up substantially. This is comparable to the Hubble time, therefore it is natural that there is very little central cool component in A1060.

The time scale for thermal conduction is estimated by equation 2.22. Assuming that the scale length is 300 kpc, which is much longer than the mean free path $\lambda_{\rm e} \sim \lambda_{\rm i} = 1.2$ kpc, the conduction time scale with an electron density at 300 kpc is calculated to be 3×10^8 yr, which is considerably smaller than the cooling time and cluster age. In the outer region of the cluster, where the scale length would be $5 - 10$ times larger with reduced electron density by a factor of $5 - 10$, the conduction time $\sim$ 0.5 Gyr with $T/|\nabla T| = 1.2$ Mpc is still much shorter than the Hubble time. This, combined with the absence of strong mergers, can explain the constancy of the ICM temperature over the A1060 cluster.

The relaxation time to reach ionization equilibrium is fairly short and estimated to be $t_{\rm ie} \sim 8 \times 10^7$ yr at the cluster center (equation 2.20). Finally, the equipartition time $t_{\rm eq}$ between ion and electron is given by equation 2.21. For A1060, the time is estimated to be 3×10^8 yr.

All the time scales estimated at the cluster center can be compared as

$$t_{\rm cool} > t_{\rm H} > t_{\rm eq} \approx t_{\rm cond} > t_{\rm ie}, \qquad (7.1)$$

which indicates that a very good equilibrium state is reached in the gas, with no significant cooling.

Gas mass fraction: The gas fraction, $f_{\rm gas} = M_{\rm gas}/M_{\rm tot}$, is a good indicator to examine the cluster scale compared among clusters. We adopted here the virial radius as

$r_{180} = 1.23(T_{\rm X}/1{\rm keV})^{1/2}\ h_{50}^{-1}{\rm Mpc}$, which is given by Evrard, Metzler, & Navarro (1996). Assuming hydrostatic equilibrium, $\nabla P = -\rho\nabla\phi$, (here P, ρ and ϕ is the pressure, the mass density, and the gravitational potential), isothermal ($dT/dr = 0$), and spherical symmetry, the total gravitational mass is given as

$$M_{\rm tot} \ = \ -\frac{r^2}{G\rho(r)}\frac{dP}{dr} = -\frac{kTr}{G\mu m_{\rm p}}\frac{d\ln\rho(r)}{d\ln r} \tag{7.2}$$

where μ is the mean molecular weight, and $\rho(r)$ is the radial density distribution. The gas mass is also obtained by the following equation

$$M_{\rm gas}(< r) \ = \ \int_0^r \rho(r)4\pi r^2 dr\ . \tag{7.3}$$

Assuming a β-model profile, the gas fraction within the virial radius is estimated to be only ~ 0.06 from the best-fit parameters for the surface brightness profile with the PSPC data. Also, all of the scale parameter for A1060, such as X-ray luminosity, gas mass, and the size of X-ray emitting region, are much smaller than the other 3 clusters. It is only natural that the features should come to these when we consider that this cluster has grown slowly in rather low matter density region.

7.2 AWM7

Temperature structure: As for AWM 7, the second system studied here, the central region within a radius of $< 20'$ (~ 600 kpc) shows an isothermal ICM with $kT \sim 3.9$ keV. There are small temperature deviations near the north and south edges of the cluster with a statistical significance of about 2.4σ (see table 3) between the hot and cool regions. The north region (#1) shows a lower temperature than the central region, and vice versa for the south region. Except for these north and south structures, the constant temperature in the rest of the cluster space suggests that no significant mergers have occurred for the recent few Gyr.

Metal distribution: In contrast to A1060, a large-scale metallicity gradient has been found in AWM 7 (Ezawa et al. 1997). A possible scenario which can explain both the abundance gradient and the constant temperature would be that there has been no major merger in AWM7 since the period of initial metal enrichment. The metal enrichment from galaxies creates the abundance gradient because metals follow galaxy density and the diffusion process is estimated to be ineffective (see Metzler and Evrard 1994; Ezawa et al. 1997). If a gas mixing due to mergers would occur, the metal distribution would become uniform and does not trace the galaxy distribution. This excludes the recent gas mixing in AWM 7, and the good isothermality of the ICM also suggests that there have been no recent mergers in this cluster for a few Gyr.

Time scale: The cooling time estimated from the central density of 0.06 cm^{-3} (Neumann and Böhringer 1995) is 0.5 Gyr, which is shorter than the Hubble time and can explain that a significant amount of the cool gas has been accumulated during the prolonged non-merger period. The conduction time scale is estimated to be 1.0 Gyr for a scale length of 300 kpc. Considering the isothermality, this suggests that mergers have never occured within $\sim$ 1 Gyr, and to some extent conductive heat input from the hot component compensates the radiation loss. The time to reach ionization equilibrium is estimated to be $t_{\mathrm{ie}} = 10^{12} n_{\mathrm{e}}^{-1} = 2 \times 10^{7}$ yr. The equipartition time between ion and electron is 1×10^{8} yr. These time scales are compare as,

$$t_{\mathrm{H}} > t_{\mathrm{cond}} > t_{\mathrm{cool}} > t_{\mathrm{eq}} > t_{\mathrm{ie}}. \tag{7.4}$$

This relation explains the presence of the central cool component without strong concentration, which is partly affected by the conductive heat inflow probably and mergers in an early stage of evolution.

Tidal effect in the supercluster: Another distinctive feature of AWM 7 is the elongated X-ray image in the east-west direction. This elongation is nearly parallel to the large-scale filament of the Pisces-Perseus supercluster. There is, however, no significant temperature structure along this direction as seen in figure 6.12. Tidal deformation and directional mass accretion have been considered as possible origins of the elongated morphology (Neumann and Böhringer 1995). The tidal force, assuming that the Perseus is the source of tidal force and AWM 7 is orbiting around it, working on a unit mass is given by,

$$F_{\mathrm{tidal}} = GM_0 \left(\frac{1}{(D-R)^2} - \frac{1}{D^2} \right), \tag{7.5}$$

where, M_0 is the mass of the origin of the tidal force (Perseus cluster in this case), D is the center distance between the central and the orbiting objects, and R is the radius of the orbiting object (AWM 7). This force should be compared with the gravitational force of the orbiting object itself on a unit mass at a radius R,

$$F_{\mathrm{grav}} = \frac{GM}{R^2}, \tag{7.6}$$

where M is the mass of the orbiting object. Using the following values,

$$M = 3 \times 10^{14} M_{\odot},\ M_0 = 2 \times 10^{15} M_{\odot},\ D = 8.4\ \mathrm{Mpc},\ R = 800\ \mathrm{kpc}, \tag{7.7}$$

we obtain

$$F_{\mathrm{grav}} : F_{\mathrm{tidal}} \approx 74 : 1. \tag{7.8}$$

This indicates that the tidal force can deform the gas by less than 2%, which is a factor of 5–10 too small to cause the observed ellipticity. On the other hand, if the directional mass accretion takes the form of subcluster mergers, we would expect a clear temperature structure along the east-west direction. Since the tidal deformation itself would not cause large temperature variation, the constant temperature in AWM 7 suggests that the underlying dark matter may have an extended structure along the filament of the Pisces-Perseus supercluster.

7.3 The Centaurus cluster

Temperature distribution: The remarkable result in the present observations is the temperature distribution of the Centaurus cluster. We have shown that the hot region reported by Churazov et al. (1999) is largely extended and also covers the cluster center, which is seen after subtracting the cool component (figure 6.19b). Also, there are cool regions in the northeast and northwest toward the cluster edge. The spectral fits show that the temperatures in the hot and cool regions differ by a factor of about 2, and the deviations from the surrounding values are $\pm 20 - 30\%$. The observed temperatures for the hot regions in the Centaurus are consistent with this simple merger scenario.

The observed extent of this hot region is about 200 kpc in diameter. Taking the electron density to be 6×10^{-4} cm^{-3} (Ikebe et al. 1999) and the volume of a 100 kpc-radius sphere, the excess thermal energy in the hot region is estimated as,

$$E = 2\frac{3}{2}nkTV = 3 \times 10^{59} \left(\frac{\Delta kT}{1 \text{ keV}}\right) \text{ erg}, \tag{7.9}$$

where ΔkT denotes the temperature increase from the surrounding region. If a typical group of galaxies ($M \sim 10^{13} M_\odot$) collides with a velocity of 1000 km s^{-1}, its kinetic energy is 10^{62} erg. This is large enough to cause the observed temperature excess in the south-east hot region.

Galaxy distribution: Since both the central and the southeast hot regions in the Centaurus show similar temperatures, $kT \sim 4.3$ keV, they may have been heated in a single major merger. The radial velocity distribution of the member galaxies in the Centaurus cluster shows double peaks (Lucey et al. 1986). One is called as Cen30 which is the main group in the Centaurus cluster and consists of about 120 galaxies ($r < 3°$) with the mean velocity of 3041 km $^{-1}$ and the line-of-sight velocity dispersion of 586 km s^{-1}. The other is Cen45, consisting of 60 galaxies with the mean velocity of 4570 km $^{-1}$ and the velocity dispersion of 262 km s^{-1}. The central dominant elliptical galaxy in the Cen45 group, NGC 4709, is located just at the center of the south-west hot region. However, the galaxy distribution in the Cen45 is not concentrated in the hot region but extends further out to $r \sim 1°$.

The observed large line-of-sight velocity of Cen45, which is larger than the Cen30 one by 1500 km s^{-1}, may indicate the infall velocity of this subgroup. Lucey et al. (1986) in fact discuss that these two groups are at the same distance. Such a colliding velocity can raise the temperature by,

$$kT \sim \frac{3}{16}\mu m_{\mathrm{H}} v^2 \sim 3 \text{ keV}, \tag{7.10}$$

which could create the observed high temperatures. If this is the case, the Cen45 group is colliding into Cen30 from the near side. The expected energy shift for this velocity is about 30 eV at 6 keV, and future study of the relation between temperature and velocity of the gas would be able to show the details of the ongoing merger.

Time scale: The radiative cooling time at the cluster center with an electron density of 0.02 cm^{-3} (Ikebe et al. 1999) is about 0.5–1 Gyr. The conduction time scale is calculated to be 3.5 Gyr assuming the scale length to be 300 kpc, which is longer than the cooling time and a time to smooth out the temperature variation. It agrees that the temperature structure due to a merger of a few Gyr ago does not disappear yet. The relaxation time for ionization equilibrium is estimated to be $t_{\rm ie} = 10^{12} n_{\rm e}^{-1} = 2 \times 10^{7}$ yr. Assuming the temperature of 3.6 keV, The equipartition time between ion and electron is 1×10^{8} yr. These time scales are compared as,

$$t_{\rm H} > t_{\rm cond} > t_{\rm cool} > t_{\rm eq} > t_{\rm ie}, \tag{7.11}$$

which is consistent with the presence of the temperature structure and prominent cool component at the same time.

Central concentration of the metal and cool component: The short cooling time in the cluster center suggests that the cool component may have been built up very recently, after the major merger involving the central region. However, there is strong metal concentration in both the hot and the cool components (Fukazawa et al. 1994, Ikebe et al. 1999), exceeding 1 solar at the center. Based on this abundance feature, it looks difficult to build up the cool component after the last merger only, because galaxies distribution must have been disturbed and sharply peaked metal injection would be impossible. The cool gas is more likely to have been built up at least before the last merger which has caused the temperature variation.

The stellar mass within the central 50 kpc of the Centaurus cluster is estimated to be $2 \times 10^{12} M_{\odot}$ (Ikebe et al. 1999). Such a mass concentration, i.e. the formation of the cD galaxy, must have started in a very early time. Since the cool emission is generally associated with the cD galaxy in many clusters, this suggests that the cool component has been established all the way through the early starburst phase until the beginning of the major merger. In this case, the central cool component was probably massive enough to survive the merger, which caused shock heating and raised temperature by nearly 1 keV. If the centrally peaked gas distribution can survive, the metal concentration would also be maintained. Recently, Gómez et al. (2000) performed numerical simulations of head-on mergers in cooling-flow clusters. In cases where the initial cooling times are very small, even though the flows are once disrupted, the central cooling time remains less than the Hubble time and the flows are re-established in a few Gyr. These clusters would naturally be classified as cooling-flow clusters, even though they have experienced significant mergers. Regardless of the origin of the cool component, the Centaurus cluster may correspond to these cases of the survived cool components.

7.4 The Perseus cluster

Temperature structure: The Perseus cluster shows the most complex temperature structure among the 4 clusters studied here, as shown in figure 6.28 and 6.33. The temperature feature is not very similar to the Centaurus case, which was characterized by an extended hot region. The Perseus shows several regions with various temperatures in the 5–9 keV in a more complex manner.

The remarkable finding is the extended cool region with a low temperature of about 5 keV at $10' - 20'$ east from the cluster center. As seen in figure 1, this region has a diameter of about $20'$ (600 kpc). The same region was recognized in the ROSAT observations (Schwartz et al. 1992; Ettori et al. 1998) based on the substructure in the surface brightness. The residual image after subtraction of a β-model (contours in Fig. 1; also Schwarz et al. 1992) is very similar to the structure of the extended cool region. Ettori et al. (1998) discuss that there is possibly a group of galaxies merging into the main body of the cluster. Considering the size and temperature of the cool region, the merged body may well be an established poor cluster. No significant variation of metal abundance in this cool region suggests that the merged cluster was already enriched with metals to around 0.3 solar. This is the largest structure existing in the Perseus cluster, and the temperature map is shown to be a very effective way to reveal its whole structure.

Figure 6.28b also shows an interesting feature that a chain of hot regions seems to be surrounding the cool region discussed above. It could be that the collision of the group of galaxies, whose direction may be nearly in parallel to the line of sight, has caused shock heatings and created a large ring-like hot region. The diameter of the "hot ring" is as large as about 1° ($\sim$ 2 Mpc). The time scale to be isothermal for such large structure is several Gyr, which is longer than the dynamic time to have almost smooth surface brightness. That has also seen in cluster merger simulations (e.g. Takizawa 1999). Assuming that the hot region has a spherical shell structure with inner and outer radii of 500 kpc and 1 Mpc, respectively, its excess thermal energy is estimated to be 2×10^{62} erg. The necessary mass of the colliding system is then at least $2 \times 10^{13}\ M_\odot$ if the relative velocity is about 1000 km sec^{-1}. This suggests that a major merger with a small size cluster (such as Abell 1060) may have created the ring-like temperature structure.

Other structures in the temperature map are smaller and seemingly consisting of many blobs with a rough size of $10'$ (300 kpc). There are hot regions with $kT \gtrsim 8$ keV toward the southern and northeastern edges of the cluster. Low temperatures ($kT \sim 5$ keV) are seen at northwestern and southwestern edges, with the latter around IC 310. In the Virgo cluster, Shibata et al. (2001) reported that the spatial scale of hot and cool regions are around 300 kpc, which is more or less the typical size of groups of galaxies. The complex temperature structure in the Perseus cluster indicates that this cluster has experienced many times of subcluster mergers. If these temperature structures are maintained for more than 10^9 yr, as implied from the above time scale estimation, the present temperature feature is likely to be an accumulated result of subcluster mergers occurred during the recent several times 10^9 yr. These mergers may well have been the main building processes which have made the Perseus cluster into such a massive system, as suggested from numerical simulations of the cluster growth (Navarro, Frenk, and White 1995).

The distribution of the cool gas in the southwest near IC 310 looks as if the subcluster gas is blown away from the center of the Perseus. This suggests that the IC 310 subcluster is now falling into the main cluster, and the cool gas associated with the subcluster may be slowed down due to the ram pressure. We hope that observation with high angular resolution may lead to direct detection of shock features, such as sharp edges (Markevitch et al. 2000) observed with Chandra, and bring us a closed-up view of the dynamical processes in the cluster system.

Metal distribution: The large-scale metallicity gradient has been found by Ezawa et al. (2001). The gradual change over a large radial distance is similar to the AWM 7, but the central metallicity is lower than the AWM 7 level, even though the Perseus is much brighter and a richer system. This may be due to the resonance scattering of Fe Kα line (see Molendi et al. 1998). Since the cross section for a resonance scattering is roughly 10^{16} cm^2, the column density of Fe in the central 10 kpc region is roughly estimated as,

$$N_{\rm Fe} = 1.5 \times 10^{16} \left(\frac{n_{\rm gas}}{10^{-2}\ {\rm cm}^{-3}}\right) \left(\frac{D}{10\ {\rm kpc}}\right) \left(\frac{Z_{\rm Fe}}{4.7 \times 10^{-5}}\right)\ {\rm cm}^{-2}. \tag{7.12}$$

This suggests that the resonance scattering may have a significant effect on the measured intensity of Fe K-α line within a few arcmin from the center, unless bulk motion the gas shifts the line center by more than the thermal width. Recent finding of the marked reduction of line intensity toward the center of M87 by XMM-Newton (Böhringer et al. 2001) supports this possibility. If this effect, expected to be a factor of about 2, is corrected, the similarity with the AWM 7 becomes stronger, suggesting that the chemical evolution of the two clusters had progressed in a similar way.

Time scale: Let us briefly look at the time scales here. The radiative cooling time at the cluster center with an electron density of 0.02 cm^{-3} (Ettori et al. 1998) is about 3 Gyr. The rather long cooling time with the massive and extended cool component at the center implies that the recent merger that created the complex temperature structure partially disrupted the central concentration of the cool gas. The conduction time scale is calculated to be $\sim$ 2 Gyr for a length of 300 kpc, which is the cell size to obtain the temperature map based on the spectral fits. Thus, we estimate the time of mergers to be within recent 2 Gyr. The relaxation time for ionization equilibrium is estimated to be $t_{\rm ie} = 10^{12} n_{\rm e}^{-1} = 1 \times 10^7$ yr. Assuming the temperature of 6.0 keV, The equipartition time between ion and electron is 2×10^8 yr. By comparing all of them, the situation in the Perseus cluster is shown by,

$$t_{\rm H} > t_{\rm cool} > t_{\rm cond} > t_{\rm eq} > t_{\rm ie}. \tag{7.13}$$

The central cool component: The central cool component requires significantly high temperature of 2.0 keV compared with the typical value of the interstellar medium (ISM) in elliptical galaxies. This makes the interpretation of the cool gas in terms of the ISM in the cD galaxy difficult. As one goes out to larger radii, however, the best-fit cool component temperature somewhat drops to 1.0 keV while the fraction of the cool component decreases. Under a standard scenario of cooling flow models, such a temperature distribution is in an opposite sense, even though the hot-component trend may be a favorable one. Confirmation of the temperature and metallicity gradients is the subject of future observations from XMM-Newton or CXO. As discussed above, understanding the origin of the cool component is not straightforward and constitutes an important subject in the cluster research in the near future.

7.5 Implications on the cluster evolution

The observed temperature structures in the 4 clusters are jointly examined here, including the relation with the abundance distribution. The properties of the ICM and galaxies in the 4 clusters are summarized in table 7.1.

The present study is the first time that a systematic comparison of temperature structures between different richness classes are performed. Let us first look at the temperature structure excluding the central regions, which show highly different features in the cool component. Regarding the strength of the temperature fluctuation, the Perseus cluster shows the most dramatic temperature variation all over the cluster. The Centaurus follows it by showing the extended hot region. In spite of these highly significant fluctuations, AWM 7 and A1060 only indicate marginal evidence for the temperature variation in very limited spatial regions. Therefore, the first systematic trend based on this small sample is that the strength of the temperature fluctuation correlates with the cluster richness. We note that other rich clusters such as Coma and Ophiucus show strong temperature variation (Watanabe et al. 1999, 2001). Therefore, rich clusters seem to show more evidences of mergers than poorer clusters. This feature is consistent with the bottom-up scenario of the cluster formation, in which rich clusters are expected to be formed through a number of subcluster mergers. The present results have provided a strong evidence for the bottom-up formation of clusters.

Turning to the central emission, the Centaurus shows the highest concentration of the hot and cool gas in the center. This concentration is accompanied by the high metal abundance at the center, which exceeds 1.5 solar. No other clusters indicate such a high central abundance. The degree of the central concentration would depend on both the initial condition and the evolutionary history. A high initial density would naturally contribute to build up the central concentration, however mergers in an early phase may disturb the central region and the matter may spread out. Such a probability is also high in the case of high initial density. The Centaurus would have been formed under the right condition for a smooth growth of the central part, and have not experienced major mergers involving the central region. In this scenario, mergers in the Centaurus such as the one created the observed temperature structure would have started only recently. The central gas, established during the prolonged non-merger period, seems to be massive enough to have survived the strong merger.

The Perseus and AWM 7 indicate similar degree of central concentration in a relative sense. The central enhancements of the metal abundance are a factor of 2 or less. This suggests that, even though the Perseus is $6 - 7$ times more massive than AWM 7, relative disturbance due to subcluster mergers may be similar. It is interesting that these 2 clusters are closely located in the same supercluster filament, suggesting that the initial density fluctuation may be similar.

A1060 is the smallest system in the present sample, and the central concentration of matter is the weakest. The absence of strong temperature fluctuations implies that this cluster has not experienced strong mergers in the recent several Gyr. Therefore, mixing of the central region is not the reason to suppress the concentration. Instead, the observed low galaxy density in the surrounding region suggests that the growth speed of this cluster has been low as well as the low initial density. The metal abundance in A1060 is remarkable flat as a function of radius. This suggests that the ICM may have been mixed around the time of metal injection period. Such a mixing also affects to slow down the growth of the central region. Based on the above consideration, the evolution process of the 4 clusters are illustrated in figure 7.1. The process for each cluster is described below:

1. A1060 was formed in a low density environment, and after the starburst period, in which ICM was enriched with metals, the gas may have been mixed with mergers. For the rest of the time, this cluster has been in a quiet environment. Because of the low surrounding matter density, the evolution of A1060 is proceeding slowly.

2. AWM 7 was formed in a supercluster environment, and the initial matter density was higher than the A1060 case. The ICM was enriched in the starburst period, and no major merger has seriously influence the subsequent evolution of this cluster. The matter in the central region is building up with the higher rate than A1060.

3. The Centaurus cluster probably had a higher initial matter density in the cluster center than AWM 7, and the matter was fairly concentrated at the time of starburst without strong disturbance from mergers. The metals were efficiently produced at the cluster center, forming the observed peak in the metal abundance. Then, a strong merger has occurred recently, which has created the observed hot region but not disturbed the central matter structure.

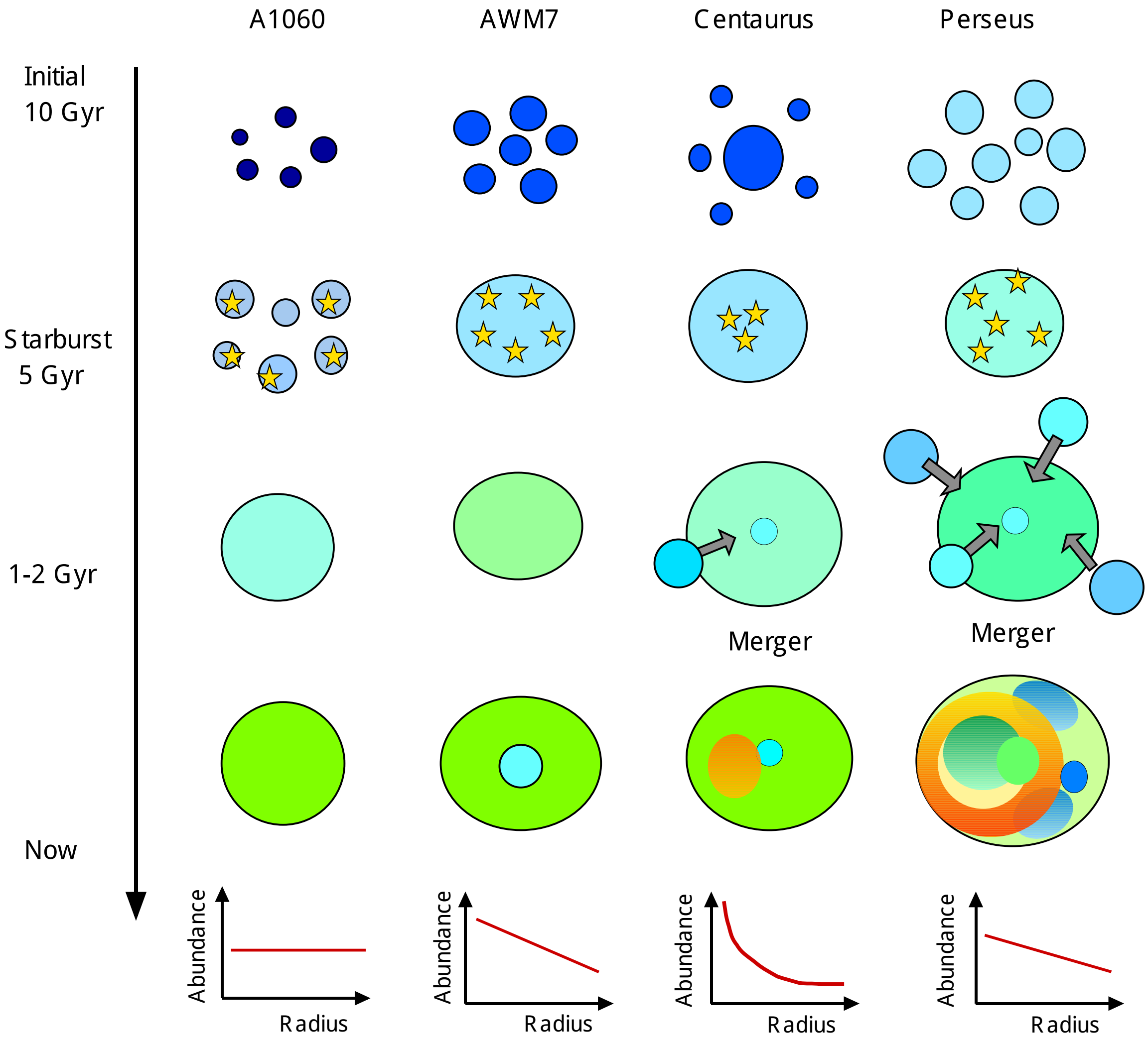

Figure 7.1: The schematic evolution history of the 4 clusters.

4. The Perseus cluster was formed in an environment similar to the AWM 7 one. This is a very rich cluster, but the X-ray radial profile and the metal abundance at the center indicate that the matter concentration is similar to the case of AWM 7. Therefore, the subsequent evolution through the starburst period has went in a similar way. The major difference from AWM 7 is the complex temperature structure as seen now. These mergers have occurred after the central matter concentration has been established, because the temperature structure within a radius of $10'$ seems very distinct from the surrounding region. However, the central concentration of the cool component and metal is moderate in contrast to that of Centaurus. Therefore, the recent strong mergers disrupt the central matter structure partially, not completely.

Finally, we suggest a preliminary way to explain the cluster formation process in the relation between temperature and metal distributions including two nearby rich clusters, Virgo and Coma. The temperature variation are divided into 3 classes relatively. A1060 and AWM7 are almost isothermal, Virgo and Centaurus show a significant hot region of a few hundred kpc, and Coma and Perseus show remarkably extended structure over 1 Mpc. Similarly, the observed metallicity profiles can be grouped into 3 types, i.e. almost uniform (A1060 and Coma), large-scale gentle gradient (AWM7 and Perseus), and central concentration (Virgo and Centaurus).

In figure 7.2, we plot a status of the 6 clusters based on these classification in a 2-dimensional plane of the relative intensity of temperature variation versus the strength of metallicity gradient. Initially, clusters have no structures in metallicity and temperature ($z \gtrsim 10$), and then the central components grow and create pronounced metal concentration during the starburst period ($z \sim 3-6$). This causes the upward movement in the plot, which would be steeper if cD galaxies have dominant effect, or would be smaller if cluster centers are disturbed by mergers in a fairly early period. Then, the strong mergers at some later stage tend to disrupt the cluster centers and distribute the metals over a wide region in the ICM. This makes the path downward, and at the same time the development of temperature structures moves the points rightward as indicated by the dashed line in figure 7.2.

The 6 data points suggest that Perseus and Coma are in a fairly evolved stage, and A1060 is in a relatively young stage. These features are broadly consistent with the evolutionary aspects inferred from optical observations, such as the density of galaxies. This scheme is crude and neglecting many factors that would significantly alter the evolution process. However, the general idea based on the combination of the metallicity and temperature distributions would still be useful in describing the history of the cluster evolution.

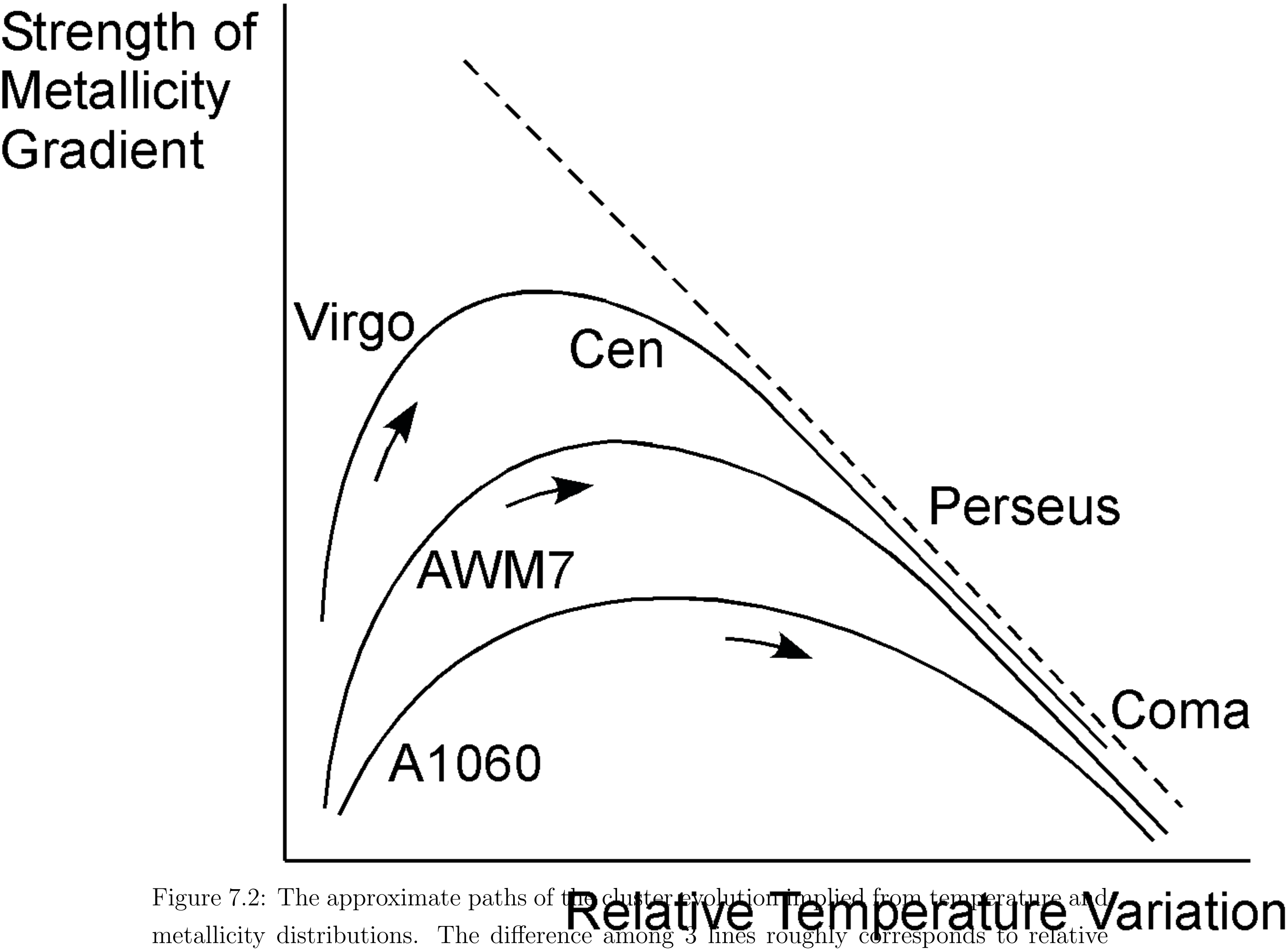

Figure 7.2: The approximate paths of the cluster evolution implied from temperature and metallicity distributions. The difference among 3 lines roughly corresponds to relative influence of the cD galaxies and frequency of mergers indicated by the dashed line.

Table 7.1: Summary of physical properties for the 4 clusters

	A1060	AWM7	Centaurus	Perseus
Temperature structure	none	none (north-south?)	hot (4 keV) & cool (2 keV)	complex (5–9 keV)
Metallisity gradient	none[a]	gentle[b], large-scale	sharp[c], concentrated	gentle[d], large-scale
Mean kT [keV]	3.3	3.9	3.6	7.0
$R_{\rm vir} (\equiv r_{180})$ [Mpc]	2.2	2.4	2.3	3.3
Central cool component	none[a]	1.6 keV[e] little	1.4 keV, strong[c] concentrated	$\lesssim 2$ keV, strong[d] extent
$n_{\rm e,0}$ [cm^{-3}]	0.004[a]	0.06[e]	0.02[c]	0.02[d]
Number of galaxies[e]	680	730	870	550
$M_{\rm gas}$ $(< r_{\rm vir})$ 10^{14} [$M_\odot$]	0.25	1.2	0.9	33.0
$M_{\rm tot}$ $(< r_{\rm vir})$ 10^{14} [$M_\odot$]	4.5	5.7	5.4	16.3
$f_{\rm gas}$ $(< r_{\rm vir})$	0.06	0.22	0.17	0.20
$t^{\dagger}_{\rm cool}$ [Gyr]	$\gtrsim 4$	0.5	1.0	2.8
$t_{\rm cond}$(300 kpc)‡ [Gyr]	0.3	1.0	3.5	1.8
$t_{\rm ie}$(300 kpc)‡ $\times 10^7$ yr	7.7	1.9	2.2	1.2
$t_{\rm eq}$(300 kpc)‡ $\times 10^8$ yr	3.3	1.0	1.1	1.6
Friends or family	Coma(richer) A1367(younger)	Perseus(richer) A262(poorer)?	none?	AWM7(poorer) A262(poorer)?

[a] Tamura et al. (1996, 2000) [b] Ezawa et al. (1997) [c] Ikebe et al. (1999). [d] Ezawa et al. (2001) [e] Neumann & Böhringer (1995). Richter et al. (1982), Koranyi & Geller (2000), Lucey et al. (1986), and Kent & Sargent (1983). † At the center. ‡ Assuming the scale length of 300 kpc and ρ(300 kpc).

Chapter 8

Conclusion

The multi-pointing observations from the ASCA GIS have presented two-dimensional temperature maps of four nearby bright clusters of galaxies: A1060, AWM 7, the Centaurus cluster, and the Perseus cluster. The extensive analysis has been performed for the hardness ratios and for the spectra in selected regions, and remarkable temperature structures have been obtained. The main points derived from the present work are summarized as follows.

1. A1060 and AWM 7 are found to be nearly isothermal from the center to the outer regions, indicating that there have been no major mergers in the recent several Gyr in these systems. The constant metallicity in A1060 suggests some mixing of the ICM around the time of metal injection period, while in AWM 7 such a mixing did not occur as suggested from the moderate central concentration of ICM and good correlation between metal mass density and galaxies.

2. The Centaurus cluster exhibits remarkable hot regions at $10' - 20'$ south-east from the cluster center and also at the central region. There are cool regions with a temperature of about half of the hot region toward the cluster edge. These results suggest that a strong merger has occurred in the recent a few Gyr, which has not disrupted the central gas concentration with the cool component. The sharp peak in the central gas suggests that the cluster has spent a long non-merger period before the start of the present merger.

3. The temperature map of the Perseus cluster shows even more complex structure over the whole region, with temperatures varying in $4 - 9$ keV. A ring-like hot region seems surrounding an extended cool region, which may be created by a collision of a smaller cluster into the main body. The metal abundances are mostly between 0.3 and 0.4 solar and show no significant correlation with temperature. This suggests that merging subclusters may have already attained an average metallicity.

4. Among the present sample, richer systems show larger fluctuation of temperature. This supports the bottom-up scenario of cluster formation in which rich clusters

have grown up through many subcluster mergers. Also, we have shown that the combination of X-ray morphology, temperature structure and metallicity distribution is a powerful method to look into the past history of individual clusters.

5. The present results have shown the importance of temperature structures in the study of dynamical evolution of clusters. In particular, even the clusters without much features in the morphology indicate some evidence of mergers. Therefore, the trace of dynamical evolution should remain in most of the clusters, which should be further studied with improved sensitivities.

Appendix A

The ROSAT Satellite

A.1 Overview

ROSAT (acronym for the German word *Röntgensatellit*, Trümper 1983) is a cooperative program between Germany, the USA, and the UK, launched on 1990 June. ROSAT consists of two telescopes, the X-ray Telescope (XRT) which covers the energy range 0.1–2.4 keV and the Wide Field Camera (WFC) which covers the energy range 0.07–0.188 keV. The XRT has two types of focal plane detectors, one is the Position Sensitive Proportional Counter (PSPC), and the other is the High Resolution Imager (HRI). The XRT mirror assembly is consisted of four nested Wolter-I mirrors with a focal-length of 2.40 m. Its mirror surfaces have a residual roughness of less than 0.3 nm, which made them the smoothest mirrors ever produced for a grazing-incidence telescope. This property is responsible for the excellent contrast of the ROSAT telescope. The PSPC provides a wide field of view ($\sim 2^\circ$ diameter), moderate energy resolution and a high spatial resolution in soft X-ray band ($0.2 - 2.5$ keV). The HRI, comprising two cascaded microchannel plates, provides a much higher spatial resolution ($\sim 2''$ diameter), but a smaller field of view and no energy resolution. The WFC is an EUV telescope, consisting of 0.525 m focal-length mirror assembly of three nested Wolter-Schwarzschild mirrors and microchannel plate (MCP). Since we utilized only the PSPC data in this thesis, we briefly describe the PSPC system. Further information on ROSAT is found in Briel et al. (1997).

A.2 Position Sensitive Proportional Counter (PSPC)

The PSPC is a multiwire proportional counter. The anode and cathode grids are contained in a gas-filled counter housing. The mutually perpendicular cathode grids determine the position of the events, while the anode grids determine the energy of the events. The entrance window consists of $\sim 1\mu$m film of polipropylen coated with carbon and lexan. Figure A.2(a) shows a window transmission of the PSPC, indicating a sharp break at 0.25 keV due to C K-edge of the window. The working gas consists of 65% Ar, 20% Xe, and

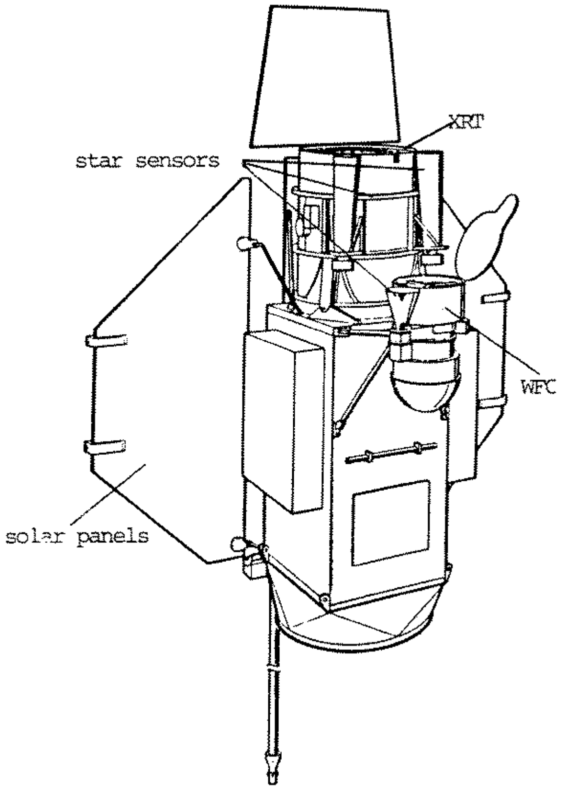

Figure A.1: Schematic view of the ROSAT spacecraft.(Briel et al., 1997).

Table A.1: Design parameters and performance of the PSPC

Energy band	0.2 – 2 keV (including XRT)
Energy resolution	$\Delta E/E \sim 0.43(E/0.93)^{-0.5}$
	$\sim$ 40% at 1 keV (FWHM)
Effective area	2° deg diameter
Entrance window	$\sim 1\mu$m plastic
Positional resolution	$\sim$ 30" at on-axis (FWHM) (including XRT)

15% CH_4. Due to a fall-off in the reflectivity of the XRT (see figure A.2(b)), the PSPC covers X-ray energy up to 2 keV. Figure A.3(a) shows PSFs of ROSAT XRT (m_σ) and PSPC (r_σ) as a function of angle from the optical axis. We can see that the PSPC has a better spatial resolution (less than $1'$ arcmin within $\sim 20'$ from the optical axis) than the ASCA detectors in sort X-ray bands.

A.3 Extended Source Analysis Software (ESAS)

The analysis of PSPC observations of extended sources is intrinsically more complex than that of point sources. In the latter case, provided the source is roughly centered in the field of view, event selection, vignetting correction, and exposure correction are

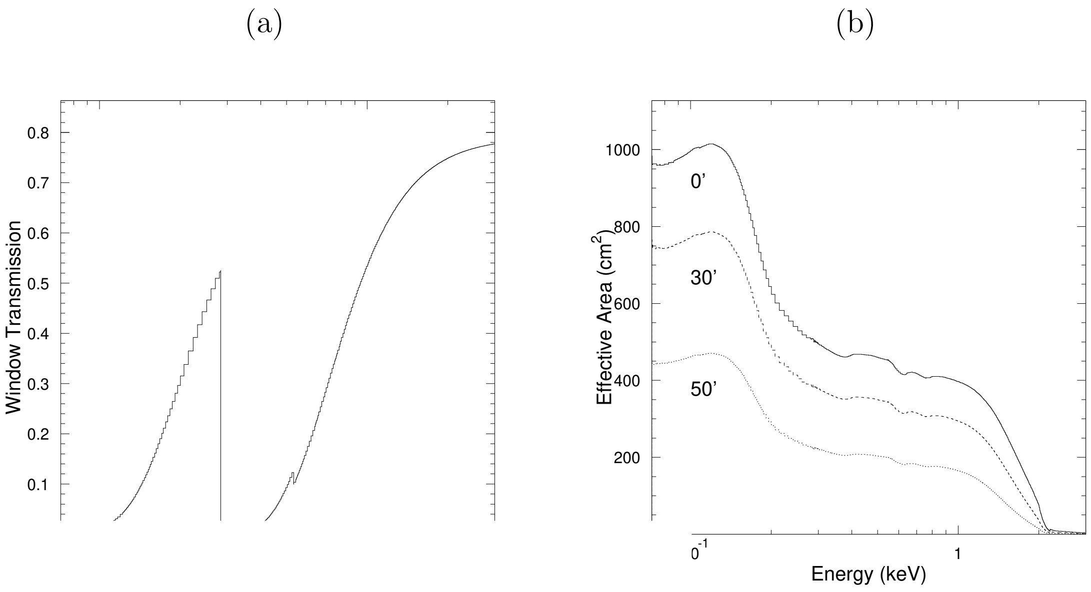
(a) (b)

Figure A.2: (a) The ROSAT PSPC-C entrance window transmission as a function of energy. (b) The effective area of the ROSAT XRT as a function of energy for off-axis angles 0, 30 and 50 arcmin.

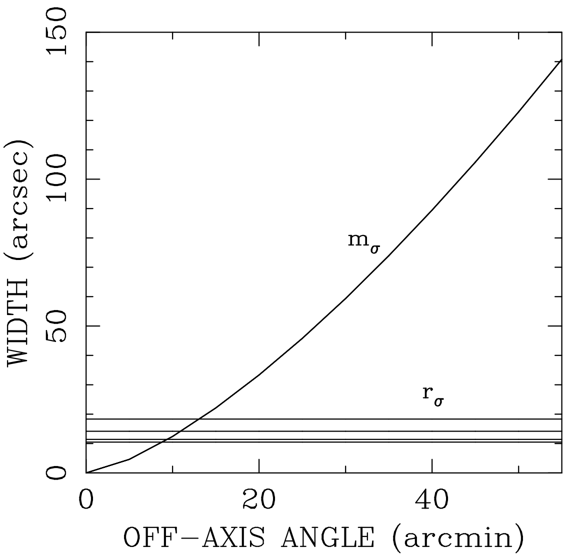

Figure A.3: The PSF of the ROSAT X-ray telescope (m_σ) and PSPC(r_σ). The 4 lines of PSPC components represent the PSF at different energy: 0.28, 0.50, 2.0 and 1.0 keV from top to bottom (Briel et al. 1997).

straightforward. A reasonable estimate of the background can be made from an annulus surrounding the sources. For extended sources, however, the background can vary significantly over the region of interest, requiring an independent assessment of its distribution over the detector. For studies of the diffuse background or features that might extend to the edges of the field of view or beyond, the integrated intensity of the background must be estimated from models of its various components. Furthermore, the telescope and detector quantum efficiencies vary over the field of view, requiring detailed corrections.

Extended Source Analysis Software (ESAS) package follows the methods outlined in Snowden et al. (1994) for such analysis of extended objects with PSPC. The data selection is carried out by looking into the time variation of the PSPC count rate in different energy bands, because the background rates and effective area of the detector depend on X-ray energy. The code can be found in the anonymous ftp area of legacy.gsfc.nasa.gov in the directory rosat/software/fortran/sxrb. The user's handbook is available here: http://heasarc.gsfc.nasa.gov/docs/rosat/cookbook/cookbook.html

A.3.1 Energy band definitions

Table A.2 contains pulse-height band which defined are specified in terms of the pulse-height invariant (PI) channels produced by the ROSAT Standard Analysis Software System (SASS; Gruber 1992). Figure A.4 shows the on-axis band-response curves as a function of energy for these ROSAT bands. The curves are derived from the pulse-height response model and quantum efficiencies (window transmission and gas stopping efficiency) of the PSPC, and from the XRT mirror effective area. In this thesis, we used the data of R4–R7 bands corresponding to 0.5 – 2.0 keV.

Table A.2: Broad energy band definitions

Band name	PI channels	SASS channels	Energy[a] (keV)
ROSAT Bands			
R1	8 – 19	1[b] – 5	0.11 – 0.284
R1L[c]	11 – 19	3 – 5	0.11 – 0.284
R2	20 – 41	6 – 10	0.14 – 0.284
R3	42 – 51	11 – 12	0.20 – 0.83
R4	52 – 69	13 – 15	0.44 – 1.01
R5	70 – 90	16 – 18	0.56 – 1.21
R6	91 – 131	19 – 23	0.73 – 1.56
R7	132 – 201	24 – 30	1.05 – 2.04
SASS Bands			
A	11 – 41	3 – 10	0.12 – 0.284
B	52 – 201	13 – 30	0.51 – 2.01
C	52 – 90	13 – 18	0.47 – 1.29
D	91 – 201	19 – 30	0.76 – 2.02
Total	11 - 235	3 – 33	—

[a] 10% of peak response. Bands with the same upper (or lower) channel boundaries can have different upper (or lower) energy limits because of the different width of the bands and the definition of the energy limits as a fixed fraction of the peak response.

[b] SASS channel 1 also includes PI channel 7.

[c] R1 band for low-gain observations.

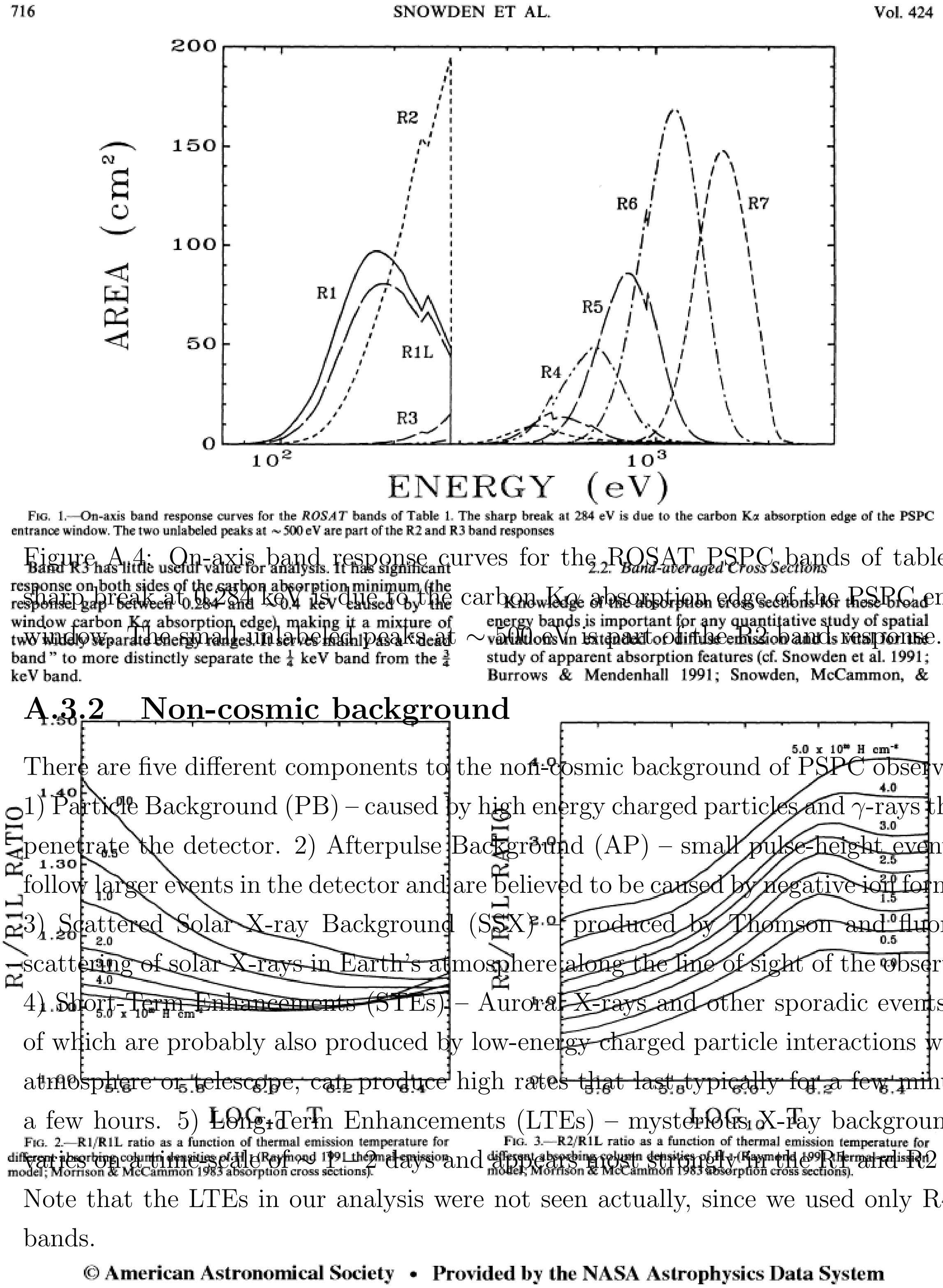

FIG. 1.—On-axis band response curves for the *ROSAT* bands of Table 1. The sharp break at 284 eV is due to the carbon Kα absorption edge of the PSPC entrance window. The two unlabeled peaks at ~500 eV are part of the R2 and R3 band responses

FIG. 2.—R1/R1L ratio as a function of thermal emission temperature for different absorbing column densities of H I (Raymond 1991 thermal-emission model; Morrison & McCammon 1983 absorption cross sections).

FIG. 3.—R2/R1L ratio as a function of thermal emission temperature for different absorbing column densities of H I (Raymond 1991 thermal-emission model; Morrison & McCammon 1983 absorption cross sections).

Figure A.4: On-axis band response curves for the ROSAT PSPC bands of table. The sharp break at 0.284 keV is due to the carbon Kα absorption edge of the PSPC entrance window. The small unlabeled peaks at ∼ 500 eV is part of the R2 band response.

A.3.2 Non-cosmic background

There are five different components to the non-cosmic background of PSPC observations: 1) Particle Background (PB) – caused by high energy charged particles and γ-rays that can penetrate the detector. 2) Afterpulse Background (AP) – small pulse-height events that follow larger events in the detector and are believed to be caused by negative ion formation. 3) Scattered Solar X-ray Background (SSX) – produced by Thomson and fluorescent scattering of solar X-rays in Earth's atmosphere along the line of sight of the observation. 4) Short-Term Enhancements (STEs) – Auroral X-rays and other sporadic events, most of which are probably also produced by low-energy charged particle interactions with the atmosphere or telescope, can produce high rates that last typically for a few minutes to a few hours. 5) Long-Term Enhancements (LTEs) – mysterious X-ray background that varies on a time scale of ∼ 1 – 2 days and appears most strongly in the R1 and R2 bands. Note that the LTEs in our analysis were not seen actually, since we used only R4 – R7 bands.

A.3.3 Data reduction

The procedures of data reduction and corrections are briefly summarized below. The name of programs are spelled with capital letters.

1. Initial time selection – VALID_TIMES : Apply a time selection to the accepted data to eliminate all periods where the Master Veto count rate averaged over ∼ 30 sec is greater than 170 counts s^{-1}.

2. Create light curves and model SSX light curves– RATE, AO : Determine the event count rates in the seven pulse-height bands and model particle background count rates in 30 s bins. Evaluate the nominal count rates of the scattered solar X-ray background.

3. Determine the SSX and LTE scale factors from the light curves – RATE_FIT : Fit the light curves with the following model function:

   $$I_i(t) = P_i(t) + (a_i + b_i \times t) \times SSX_c(t) + (c_i + d_i \times t + e_i \times t^2 + f_i \times t^3 + g_i \times t^4 \tag{A.1}$$

   $I_i(t)$ is the total event count rate for band i as a function of time, t in units of 10^5 seconds. Figure A.5 shows the fitted light curves of the RP800192 and RP800321 (center and east observations of the Centaurus cluster) in each R4 – R7 band. The various light curves display different non-cosmic background phenomena. The amplitude of background intensity in RP800192 fluctuates obviously more violent than that in RP800032. The R4 and R5 bands in particular to a more limited extent show the characteristic signature of scattered solar X-ray contamination.

4. Second time selection : The fitted light curves can be compared to the data to identify times of obvious STEs, which are apparent as deviations of the model from the observation light curve.

5. Determination of LTE contamination – LTE : The fitted polynomial coefficients from the program RATE_FIT are evaluated to determine the number of LTE events.

6. Cast the events and the exposure – CAST_DATA, CAST_EXP : Sort the events from the accepted time intervals into images in sky coordinates for the chosen bands. Using the livetimes, cast the efficiency weighted (vignetting-corrected) exposure for the chosen bands in sky coordinates for the accepted time intervals.

7. Determination of SSX/AP/PB contamination – TILT, FIT_AP, CAST_PART, CAST_SSX : Using the derived count rate versus time models for the SSX, LTE, PB, and AP for the chosen bands and accepted time intervals, cast the background counts in sky coordinates.

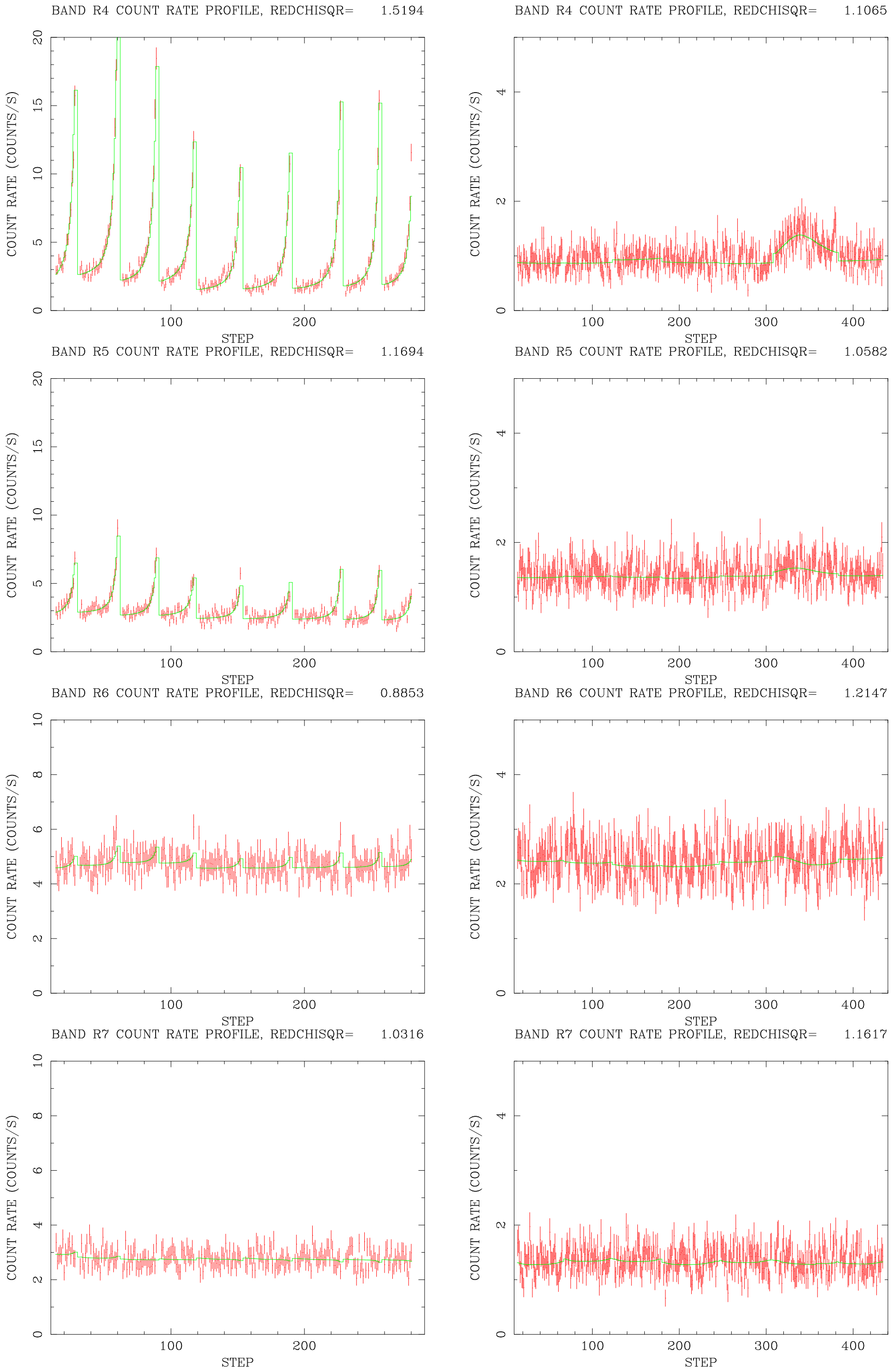

Figure A.5: The fitted light curves of the Centaurus cluster in each R4–R7 band corresponding to 0.5 – 2 keV band. The left and right panels show the data of RP800192 (center) and RP800321 (east) observations, respectively.

Appendix B

The GIS spectra of Perseus cluster

The spectra for the 41 cells with a size of $15' \times 15'$ to obtain the temperature map for the Perseus cluster are shown here (see subsection 6.4.3). The best-fit parameters are summarized in table 6.10–6.13. We show the spectra with the single-temperature MEKAL model in the 0.7–10 keV band for all cells in figure B.1. For the central 9 cells, we also carried out the single-temperature fit in the 3–10 keV band, 2-temperature, and 2-temperature gain fit in the 0.7–10 keV band, as shown in figure B.2, B.3, and B.4, respectively.

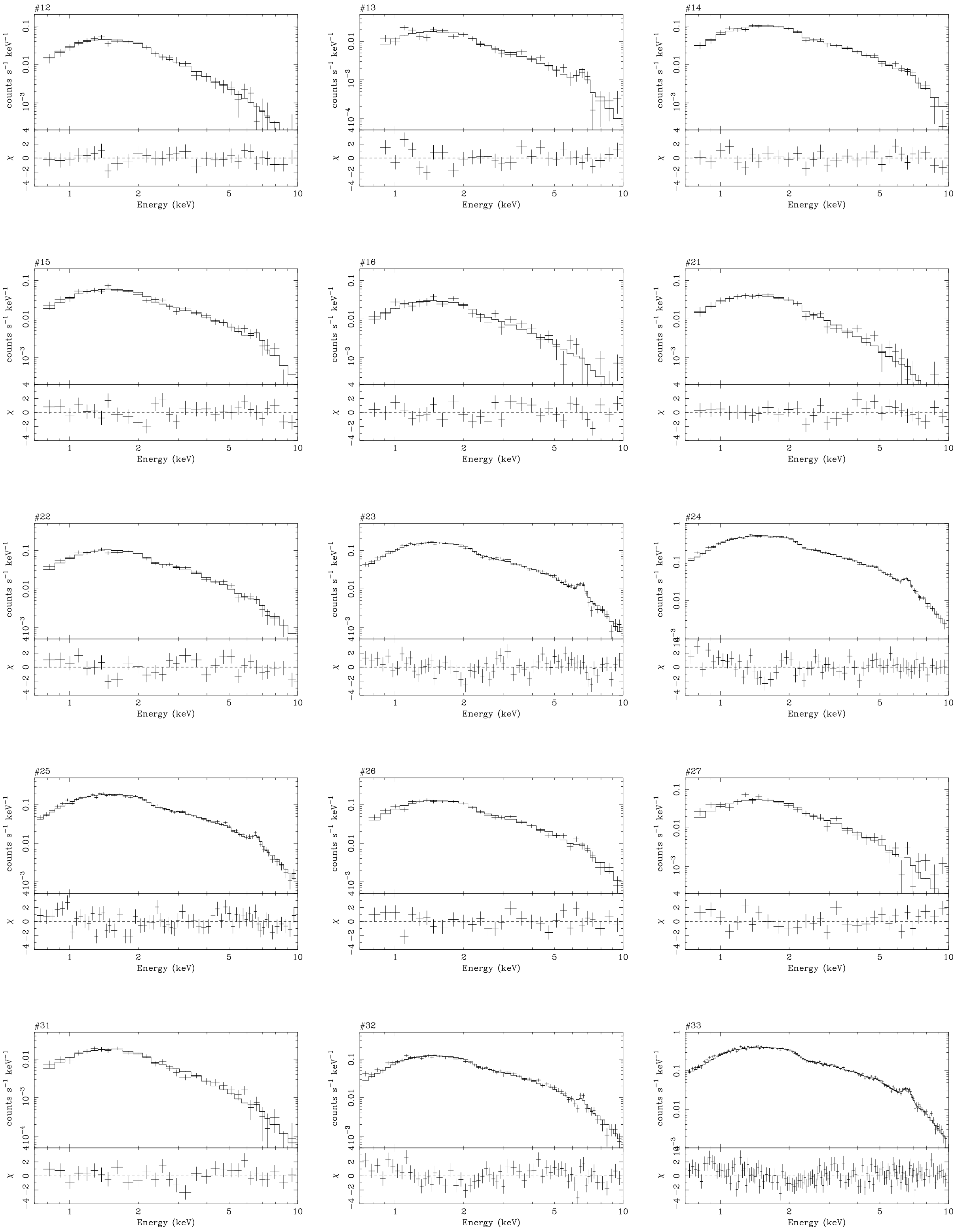

Figure B.1: Spectral fitting with the single-temperature MEKAL model in the 0.7–10 keV band for the 41 cells.

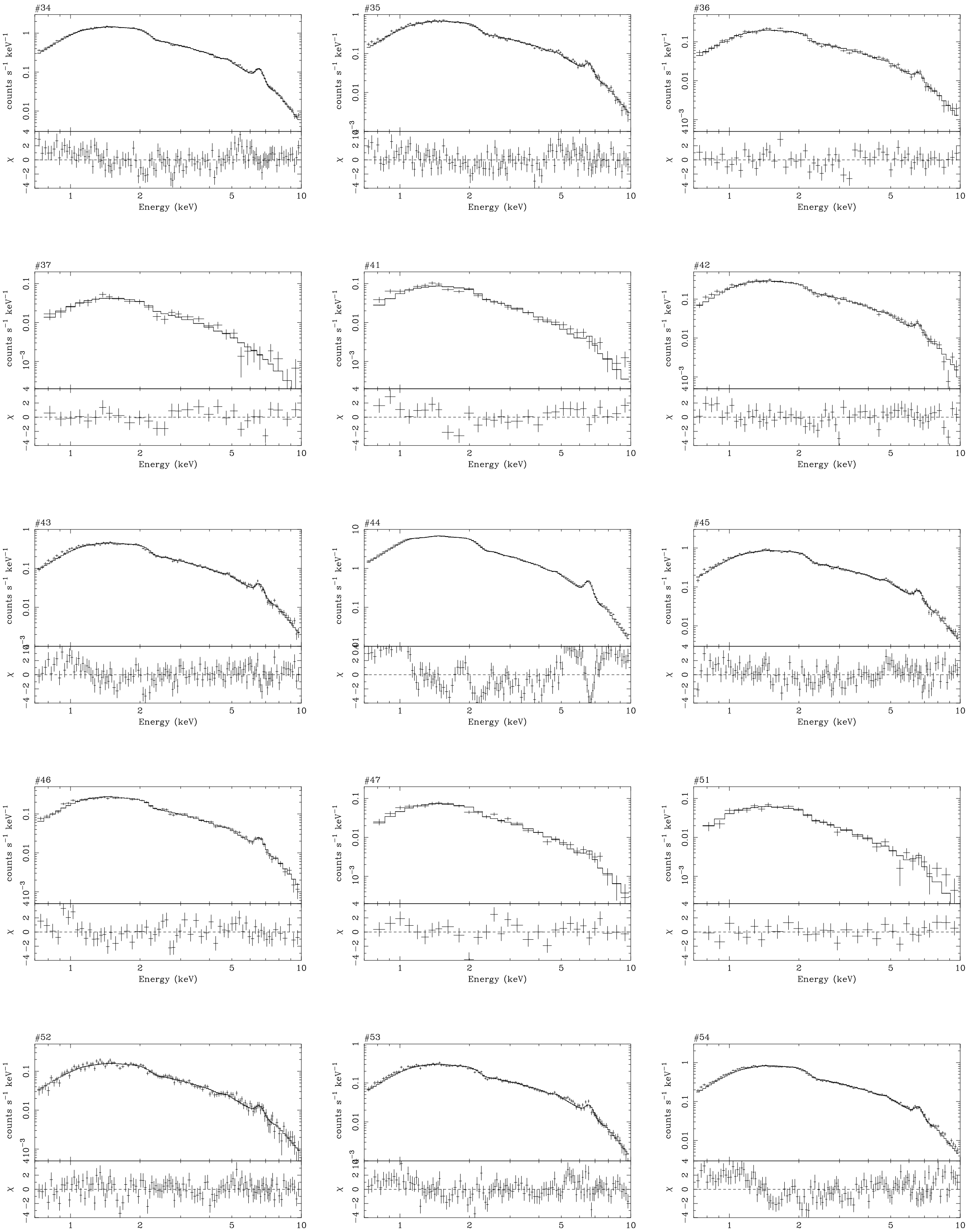

Figure B.1 (continued)

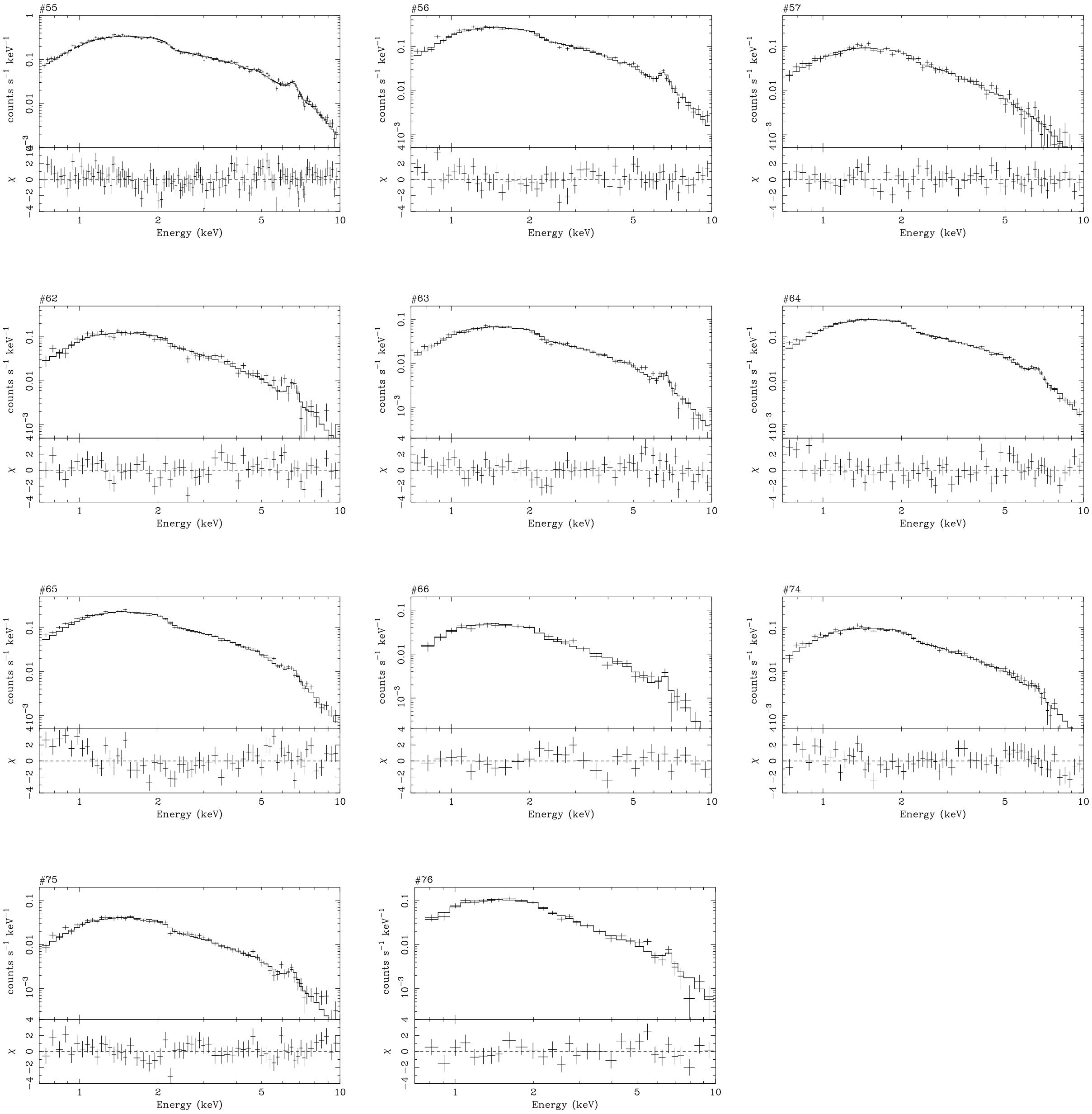

Figure B.1 (continued)

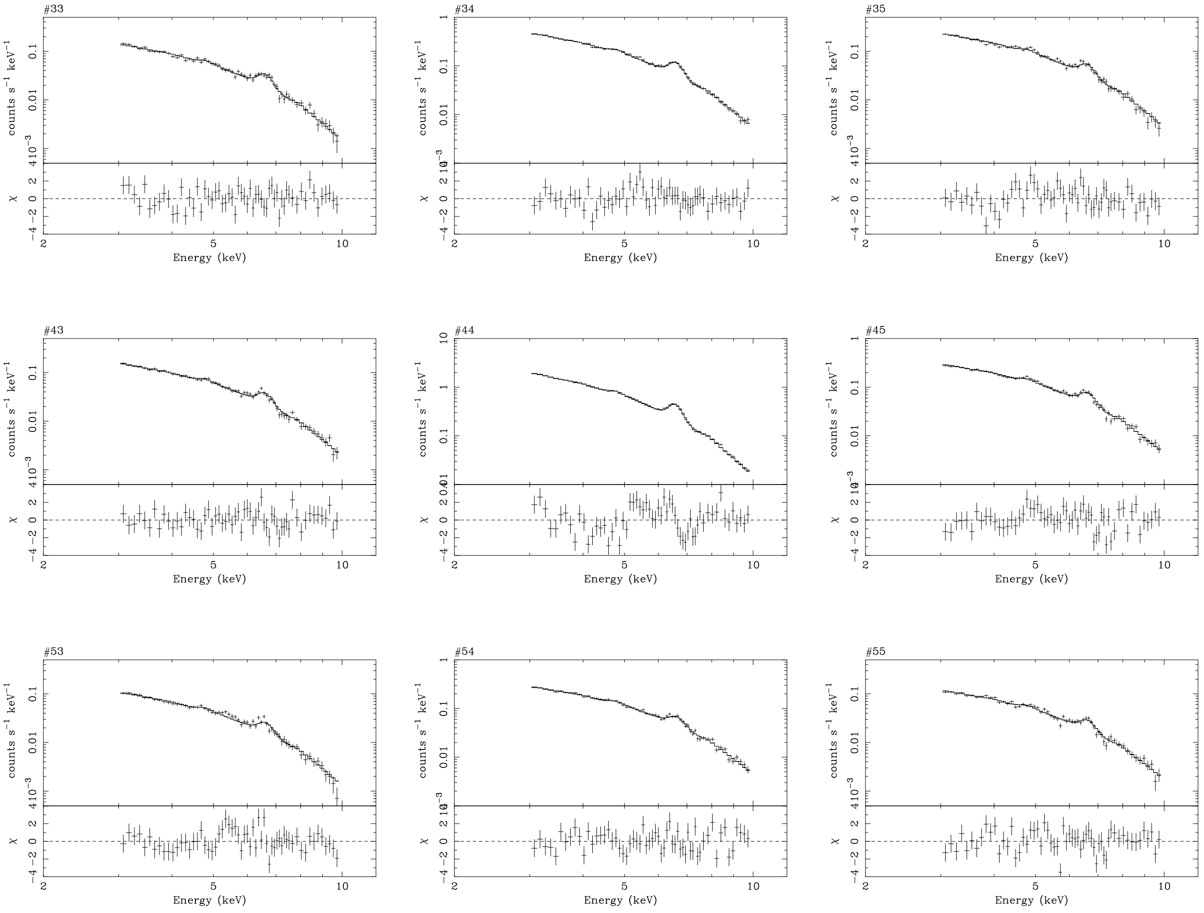

Figure B.2: Spectral fitting with the single-temperature MEKAL model in the 3–10 keV band for the central 9 cells.

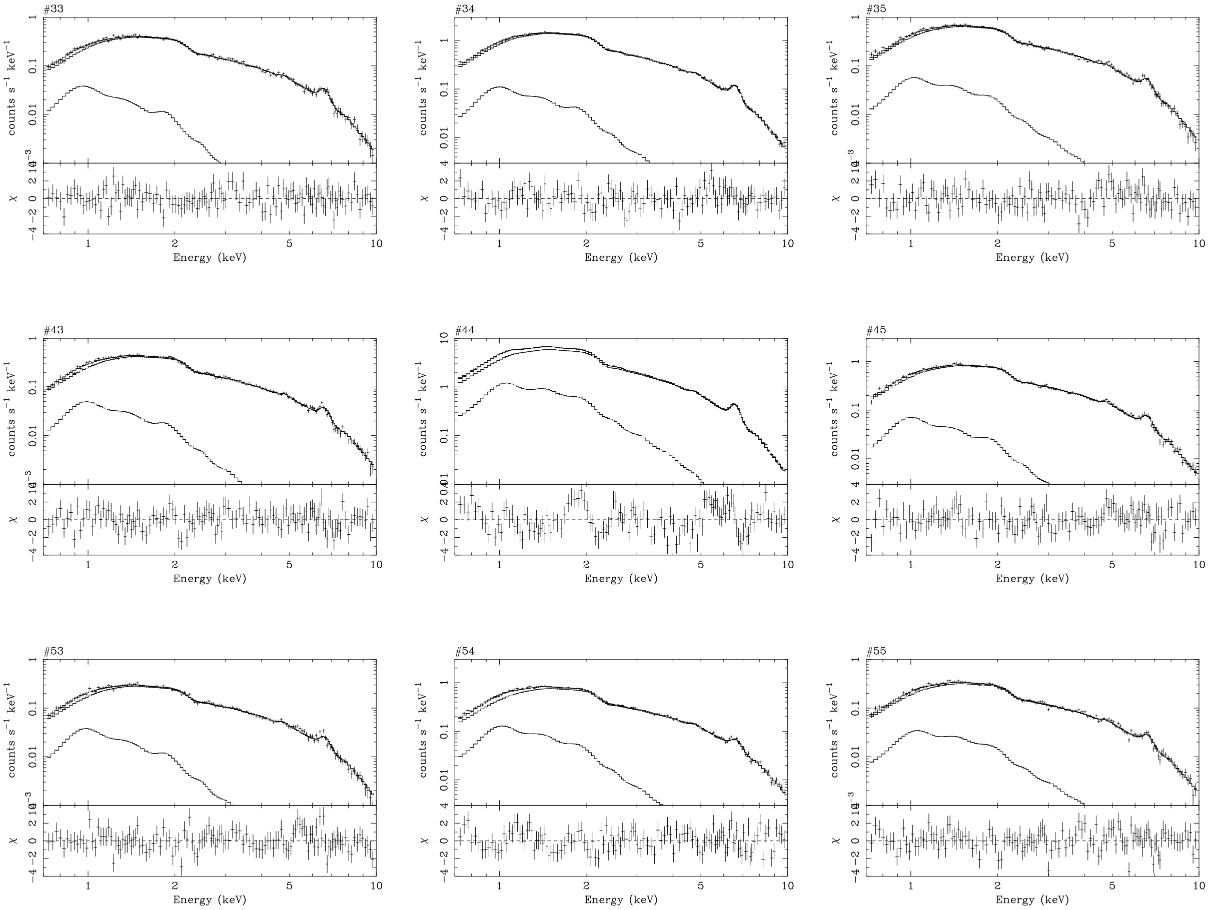

Figure B.3: Spectral fitting with the 2-temperature MEKAL model in the 0.7–10 keV band for the central 9 cells.

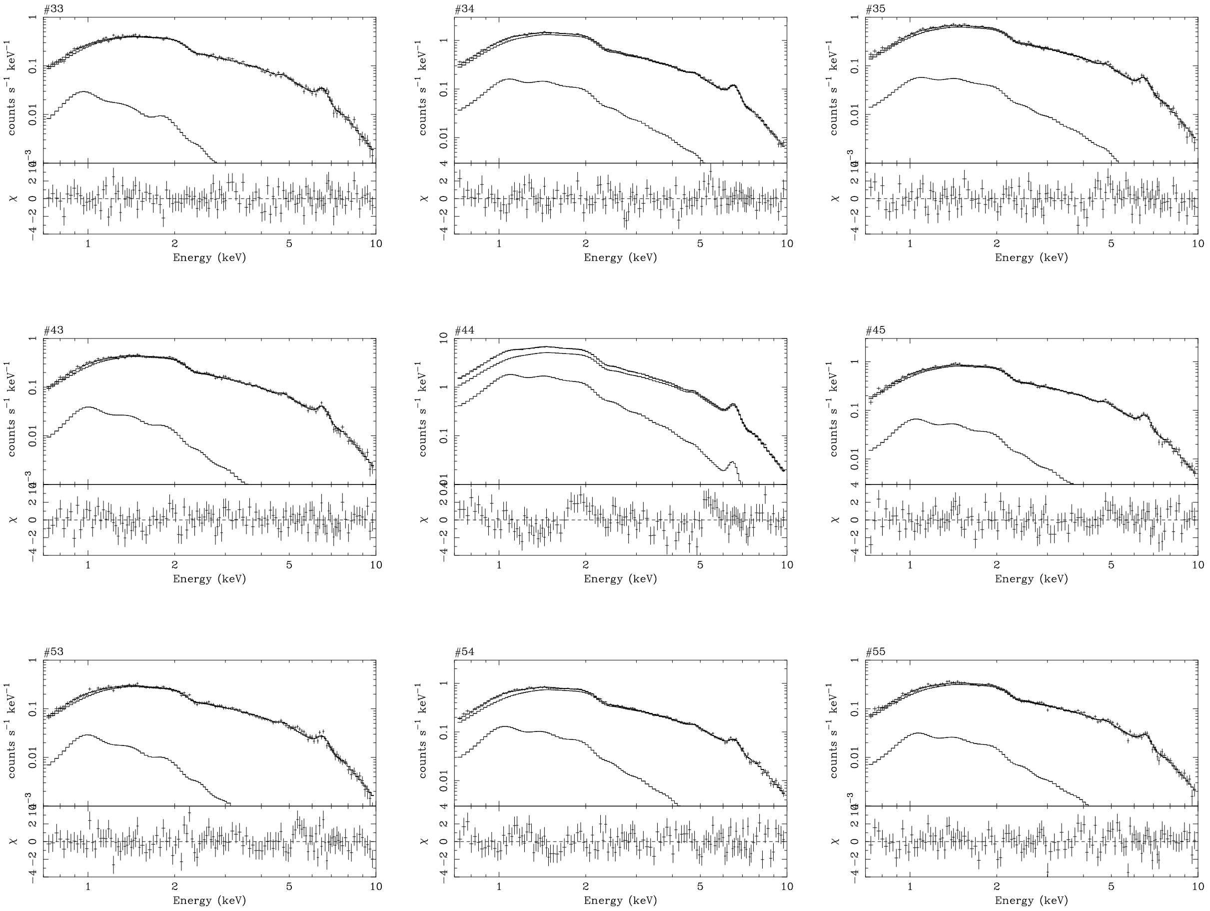

Figure B.4: Spectral fitting with the 2-temperature MEKAL model with the gain parameter in the 0.7–10 keV band for the central 9 cells.

Bibliography

[1] Abell, G. O., Corwin, H. G., Jr., Olowin, R. P. 1989, ApJS, 70, 1

[2] Albert, C., White, R. & Morgan, W., 1977, ApJ, 211, 309

[3] Allen, S.W., Fabian, A.C., Johnstone, R.M., Nulsen, P.E.J. & Edge, A.C., 1992, MNRAS, 254, 51

[4] Allen, S. W., & Fabian, A. C. 1994, MNRAS, 269, 409

[5] Anders, E. & Grevesse, N. 1989, Geochim. Cosmochim. Acta, 53, 197

[6] Arnaud, K. A., Mushotzky, R. F., Ezawa, H., Fukazawa, Y., Ohashi, T., Bautz, M. W., Crewe, G. B., Gendreau, K. C., et al. F. 1994, ApJ, 436, L67

[7] Arnaud, M., & Rothenflug, M. 1985, A&AS, 60, 425

[8] Arnaud, M., Aghanim, N., Gastaud, R., Neumann, D. M., Lumb, D., Briel, U., Altieri, B., Ghizzardi, S., Mittaz, J., Sasseen, T. P., & Vestrand, W.T. 2001, A&A, 365, L67

[9] Beers, T. C., Geller, M. J., Huchra J. P., Latham, D. W., & Davis R. J. 1984, ApJ, 283, 33

[10] Böhringer H. 1994, in Cosmological Aspects of X-Ray Clusters of Galaxies, ed. W.C. Seitter (Kluwer Academic Publishers, Dordrecht, Boston, and London) v441, p123

[11] Böhringer H., Belsole, E., Kennea, J., Matsushita, K., Molendi, S., Worrall, D. M., Mushotzky, R. F. et al. 2001, A&A, 365, L181

[12] Briel, U. G., et al. 1997, ROSAT User's Handbook, available from GSFC/NASA (legacy.gsfc.nasa.gov)

[13] Brunzendorf, J., & Meusinger, H. 1999, A&AS, 139, 141

[14] Burns, J. O., Rhee, G., Owen, F. N., Pinkney, J. 1994, ApJ, 423, 94

[15] Churazov, E., Gilfanov, M., Forman, W., & Jones, C. 1999, ApJ, 520, 105

[16] David, L. P., Jones, C. Forman, W. 1996, ApJ, 473, 692

[17] Dickey, J. M., & Lockman, F. J. 1990, ARA&A, 28, 215

[18] Edge, A. C. & Stewart, G. C. 1991, MNRAS, 252, 428

[19] Eke, V. R., Navarro, J. F., & Frenk, C. S. 1998, ApJ, 503, 569

[20] Ettori, S., Fabian, A. C., & White, D. A. 1998, MNRAS, 300, 837

[21] Ezawa, H., Fukazawa, Y., Makishima, K., Ohashi, T., Takahara, F., Xu, H., & Yamasaki, N. Y. 1997, ApJ, 490, L33

[22] Ezawa, H., Endo, T., Fukazawa, Y., Kikuchi, K., Takahashi, T. the Image Analysis Working group 1997b, ASCA News No.5, ed. ASCA GOF at NASA/GSFC, p. 23

[23] Evrard, A. E., Metzler, C. A. & Navarro, J. F. 1996, ApJ, 469, 494

[24] Ezawa, H., Yamasaki, N. Y., Ohashi, T., Fukazawa, Y., Hirayama, M., Honda, H., Kamae, T., Kikuchi, K., & Shibata, R. 2001, PASJ, 53, 595

[25] Fabin, A. C. & Pringle, J. E. 1977, MNRAS, 181, 5

[26] Fabian A.C. 1994, ARA&A, 32, 227

[27] Fabian, A. C., Arnaud, K. A., Bautz, M. W., & Tawara, Y. 1994, ApJ, 436, L63

[28] Finoguenov, A., & Ponman, T. J. 1999, MNRAS, 305, 325

[29] Finoguenov, A., David, L. P., & Ponman, T. J. 2000, ApJ, 544, 188

[30] Fitchett, M., & Merritt, D. 1988, ApJ, 335, 18

[31] Forman, W., Kellogg, E., Gursky, H., Tananbaum, H. & Giacconi, R., 1972, ApJ, 178, 309

[32] Fukazawa, Y., Ohashi, T., Fabian, A. C., Canizares, C. R., Ikebe, Y., Makishima, K., Mushotzky, R. F., & Yamashita, K. 1994, PASJ, 46, L55

[33] Fukazawa, Y., Ishida, M., & Ebisawa, K. 1997, ASCA News, 5, 3

[34] Fukazawa, Y. 1998, Ph.D. Thesis, The University of Tokyo

[35] Gehrels, N. & Williams, E. D. 1993, ApJ, 418, L25

[36] Giacconi, R., Murray, S., Gursky, H., Kellogg, E., Schreier, E., and Tananbaum, H. 1972, ApJ, 178, 281

[37] Gómez, P. L., Loken, C., Roettiger, K., & Burns, J. O. 2000, astro-ph/0009465

[38] Gruber, R. 1992, in Data Analysis in Astronomu IV, ed. V.Di Gesú et al. (New York, Plenum), 153

[39] Gursky, H., Kellogg, E., Leong, C., Tananbaum, H. & Giacconi, R., 1971, ApJ, 165, L43

[40] Hamabe, M. 1993, ApJS, 85, 249

[41] Honda, H., Hirayama, M., Watanabe, M., Kunieda, H., Tawara, Y., Yamashita, K., Ohashi, T., Hughes, J. P., & Henry, J. P. 1996, ApJ, 473, L71

[42] Huchra, J. P., Vogeley, M. S. & Geller, M. J. 1999, ApJS, 121, 287

[43] Ikebe, Y. 1995, Ph.D. Thesis, The University of Tokyo

[44] Ikebe, Y., et al. 1997, ApJ, 481, 660

[45] Ikebe, Y., Makishima, K., Fukazawa, Y., Tamura, T., Xu, H., Ohashi, T., & Matsushita, K. 1999, ApJ, 525, 58

[46] Ishisaki, Y. 1996, Ph.D. Thesis, The University of Tokyo

[47] Ishizaka, C. & Mineshige, S. 1996, PASJ, 48, L37

[48] Jerjen, H., Dressler A. 1997, A&AS, 124, 1

[49] Jones, C. & Forman, W. 1984, ApJ, 276, 38

[50] Kaastra, J. S. 1992, in An X-Ray Spectral Code for Optically Thin Plasmas (Internal SRON-Leiden Report, updated version 2.0)

[51] Kent, S. M., & Sargent W. L. W. 1983, AJ, 88, 697

[52] Kikuchi K., Furusho T., Ezawa H., Yamasaki N. Y., Ohashi T., Fukazawa Y., Ikebe Y. 1999, PASJ, 51, 301

[53] Kikuchi, K., Itoh, C., Kushino, A., Furusho, T., Matsushita, K., Yamasaki, N. Y., Ohashi, T., Fukazawa, Y., Ikebe, Y., Böhringer, H., & Matsumoto, H. 2000, ApJ, 531, L95

[54] Koranyi, D. M., & Geller, M. J. 2000, AJ, 119, 44

[55] Kowalski, M.P., Cruddace, R.G., Snyder, W.A. & Ulmer, M.P., 1993, ApJ, 412, 489

[56] Koyama, K., et al. 1984, PASJ, 36, 65

[57] Koyama, K., Takano, S., Tawara, Y. 1991, Nature, 350, 135

[58] Kriss, G. A., Cioffi, D. F., & Canizares, C. R. 1983, ApJ, 272, 439

[59] Kubo, H. 1994, Master Thesis, University of Tokyo

[60] Kunieda, H., Furuzawa, A., Watanabe, M., XRT Team 1995, ASCA News No. 3, ed. ASCA Guest Observer Facility at NASA/GSFC, p. 3

[61] Lucey, J. R., Currie, M. J., & Dickens, R. J. 1986, MNRAS, 221, 453

[62] Lynds, R. 1970, ApJ, 159, L151

[63] Madau, P. 1999, in After the Dark Ages: When Galaxies were Young, ed. S.S. Holt, E.P. Smith (AIP Press), 299

[64] Makishima, K., Tashiro M., Ebisawa K., Ezawa H., Fukazawa Y., Gunji S., Hirayama M., Idesawa E. et al. 1996, PASJ48, 171

[65] Markevitch, M., & Vikhlinin, A. 1997, ApJ, 474, 84 b

[66] Markevitch, M., Forman W.R., Sarazin C.L., Vikhlinin A. 1998, ApJ, 503, 77

[67] Markevitch, M., Vikhlinin, A., Mazzotta, P., VanSpeybroeck, L. 2000, X-ray Astronomy 2000 (astro-ph/0012215)

[68] Masai, K. 1994, ApJ, 437, 770

[69] Matilsky, T., Jones, C., and Forman, W. 1985, ApJ, 291, 621

[70] McMahon, P.M., Richter, O.-G., van Gorkom, J.H., Ferguson, H.C. 1992, AJ, 103, 399

[71] Metzler, C. A., & Evrard, A. E. 1994, ApJ, 437, 564

[72] Mewe, R., Gronenschild, E. H. B. M., & van den Oord, G. H. J. 1985, A&AS, 62, 197

[73] Mewe, R., Lemen, J. R., & van den Oord, G. H. J. 1986, A&AS, 65, 511

[74] Mitchell, R., and Mushotzky, R. F. 1980, ApJ, 236, 730

[75] Molendi S., Matt G., Antonelli L. A., Fiore F., Fusco-Femiano R., Kaastra J., Maccarone C., Perola C. 1998, ApJ, 499, 608

[76] Navarro, J.F., Frenk, C.S. & White, S.D.M., 1995, MNRAS, 275, 720

[77] Neumann, D. M. & Böhringer, H. 1995, A&A, 301, 865

[78] Ohashi, T., et al. 1996, PASJ, 48, 157

[79] Peres, C. B., Fabian, A. C., Edge, A. C., Allen, S. W., Johnstone, R. M., & White, D. A. 1998, MNRAS, 298, 416

[80] Peterson, J. R., Paerels, F. B. S., Kaastra, J. S., Arnaud, M., Reiprich, T. H., Fabian, A. C., Mushotzky, R. F., Jernigan, J. G., Sakelliou, I. 2001, A&A, 365, L104

[81] Rephaeli, Y. 1978, ApJ, 225, 335

[82] Rees, M. J. 1992, in Clusters and Superclusters of Galaxies, Proceedings of NATO Advanced Study Institute, ed. A.C. Fabian (Kluwer Academic Publishers)

[83] Richstone, D., Loeb, A., Turner, E. L. 1992, ApJ, 393, 483

[84] Richter O.-G., Materne J., Huchtmeier W. K. 1982, A&A, 111, 193

[85] Richter O.-G. 1987, A&AS, 67, 237

[86] Roettiger, K. et al. 1998, ApJ, 493, 62

[87] Sambruna, R. M., Eracleous, M., & Mushotzky, R. F. 1999, ApJ, 526, 60

[88] Sarazin, C. L. 1979, ApJ, 20, L93

[89] Sarazin, C. L. 1988, X-ray Emission from Clusters of Galaxies, Cambridge University Press

[90] Schwarz R. A., Edge A. C., Voges W., Böhringer H., Ebeling H., Briel U. G. 1992, A&A, 256, L11

[91] Serlemitsos P.J., Jalota L., Soong Y., Kunieda H., Tawara Y., Tsusaka Y., Suzuki H., Sakima Y. et al. 1995, PASJ47, 105

[92] Shibata R., Matsushita K., Yamasaki N.Y., Ohashi T., Ishida M., Kikuchi K., Böhringer H., Matsumoto H. 2001, ApJ, 549, 228

[93] Shu, F. H. 1992, The Physics of Astrophysics volume II. Gas Dynamics, University Science Books

[94] Sijbring D. & de Bruyn A. G. 1998, A&A, 331, 901

[95] Singh, K. P., Westergaard N. J., Schnopper H. W. 1988, ApJ, 330, 620

[96] Snowden, S. L., McCammon, D., Burrows, D. N., & Mendenhall, J. A. 1994, ApJ, 424, 714

[97] Snyder, W.A., Kowalski, M.P., Cruddace, R.G., Fritz, G.G., Middleditch, J., Fenimore, E.E., Ulmer, M.P. & Majewski, S.R. 1990, ApJ,365, 460

[98] Spitzer, L. Jr., 1956, Physics of Fully Ionized Gases, New York, Interscience

[99] Spitzer, L. Jr., 1978, Physical Processes in the Interstellar Medium, New Yorlk, Wiley

[100] Stark, A. A., Gammie, C. F., Wilson, R. W., Bally, J., & Linke, R. 1992, ApJS, 79, 77

[101] Stein, P., Jerjen, H. & Federspiel, M. 1997, A&A, 327, 952

[102] Sutherland R.S., Dopita M.A. 1993, ApJS, 88, 253

[103] Takahashi, T., et al. 1994, Why we need another Cyg X-1 observation, ASCA internal report, available from ISAS (ftp.astro.isas.ac.jp: /asca/report/xrt_US.ps)

[104] Takahashi, T., et al. 1995, ASCA News No. 3, ed. ASCA Guest Observer Facility at NASA/GSFC, p. 34

[105] Tamura, T., Day, C. S., Fukazawa, Y., Hatsukade, I., Ikebe, Y., Makishima, K., Mushotzky, R. F., Ohashi, T., Takenaka, K., & Yamashita, K. 1996, PASJ, 48, 671

[106] Tamura, T., Makishima, K., Fukazawa, Y., Ikebe, Y., & Xu, H. 2000, ApJ, 535, 602

[107] Tamura, T., Kaastra, J. S., Peterson, J. R., Paerels, F., Mittaz, J.P.D., Trudolyubov, S. P., Stewart, G., Fabian, A. C. et al. 2001, A&A, 365, L87

[108] Tanaka Y., et al. 1984, PASJ, 36, 641

[109] Tanaka, Y., Inoue, H. & Holt, S.S. 1994, PASJ, 46, L37

[110] Tarter, J. C. 1975, Ph.D. Thesis, University of California

[111] Trümper, J. 1983, Adv. Space Res., 2, 241

[112] Tsusaka, Y., et al. 1995, Appl. Opt., 34, 4848

[113] Tusru, T. 1992, Ph.D. Thesis, University of Tokyo

[114] Watanabe, M., Yamashita, K., Furuzawa, A., Kunieda, H., & Tawara, Y. 1999, ApJ, 527, 80

[115] Watanabe, M., Yamashita, K., Furuzawa, A., Kunieda, H., & Tawara, Y. 2001, PASJ, 53, 605

[116] White, S. D. M. 1976, MNRAS, 177, 717

[117] Xu, H., Ezawa, H., Fukazawa, Y., Kikuchi, K., Makishima, K., Ohashi, T., & Tamura, T. 1997, PASJ, 49, 9

[118] Yamashita, K. 1992, in Frontiers of X-ray Astronomy, ed. Y. Tanaka and K. Koyama (University Academy Press, Tokyo), p475

[119] Zel'dovich, Ya. B. & Raizer Yu. P. 1966, Physics of Shock Waves and High-Temperature Hydrodynamic Phenomena, Academic Press

Acknowledgments

First of all, I would like to express my special gratitude to Prof. T. Ohashi for his continuous support, leading and encouragement throughout the five years of my graduate course. I owe the finish in this thesis entirely to him. I also am deeply grateful to Dr. N. Y. Yamasaki. Her lucid guidance on astrophysics and data analysis helped me whenever I was thrown into confusion. I also greatly appreciate Dr. Y. Ishisaki for his powerful support on data analysis and experiments.

I am so much obliged to Prof. Y. Tawara, Prof. K. Masai, Dr. M. Takizawa, Dr. Y. Ikebe, Dr. K. Matsushita and Dr. S. Sasaki for valuable comments and discussions on theoretical aspects of clusters of galaxies. I am also deeply grateful to Dr. R. Shibata, Dr. M. Watanabe, and Dr. K. Kikuchi. They encouraged me to finish this work with useful advice and discussions on analysis methods.

I wish to thank members of our laboratory: Mr. H. Miyazaki, Ms. E. Rokutanda, Mr. A. Kushino, Mr. Y. Michikawa, Mr. T. Toramatsu, Mr. G. Fujimoto, Ms. C. Ito, Mr. T. Ishikawa, Mr. T. Kagei, Mr. T. Hiroike, and Ms. Y. Kawakami.

I appreciate all the members of ASCA team, GIS team, SimASCA W.G., SimARF team, and ASCA_ANL W.G. for spacecraft operation, calibration, data acquisition, and analysis support. I also appreciate Astro-E/XRS team; Prof. K. Mitsuda, Dr. R. Fujimoto, Dr. R.L. Kelley, and other GSFC and SHI people. It was indeed my pleasure that I was allowed to join the ground calibration experiments and launch operation as a member of the XRS team during the final year of Astro-E. I hope for the success of Astro-E2 mission from the bottom of my heart.

Finally, I thank my parents, sister, dog, relation, and friends for their hearty support and encouragement.